Driven interfaces in the Ising model

Thomas H. R. Smith

H. H. Wills Physics Laboratory
University of Bristol

A thesis submitted to the University of Bristol in
accordance with the requirements of the degree of
Ph.D. in the Faculty of Science

November 2010

Abstract

In this thesis we study, via Monte Carlo simulations, the structural and dynamic properties of interfaces in simple lattice models driven out of thermal equilibrium. Our main focus is a driven Ising lattice gas in both two and three dimensions, where an interface is stabilized by two parallel confining walls at the lower and upper (z) boundaries of the system. The boundaries in the other directions are taken to be periodic. Simulating using Kawasaki exchange dynamics, which conserve magnetisation or density locally, and introducing drive by biasing the transition rates in the x direction, a lateral current parallel to the interface plane is created. We find that the system reaches a non-equilibrium steady state, in which interfacial capillary-wave fluctuations are suppressed, and the magnetisation profile obeys the scaling form of an equilibrium system, but with a reduced wall separation; the interface width is also reduced. Static spatial pair correlations along the interface decay more quickly with distance under drive than in equilibrium, and for weak driving fields, can be rescaled to the equilibrim result, with a reduced correlation length. These results imply that the effect of drive upon the structure of the interface is the same as that of increasing the degree of confinement in equilibrium.

Turning to dynamics, we find that the space-time interface height correlation function shows evidence of thermal capillary wave transport in the drive direction, when the order parameter current profile has a component which is an odd function of distance z from the interface. This is the case for a linearly varying shear-like driving field $F(z)$, for example, but not for spatially uniform drive. Simulation results for a driven discrete Gaussian effective interface model, and a conservative, driven Blume-Capel (spin-1) model, also reveal transport of interfacial fluctuations, with the same criterion. We are able to measure the dispersion relations of the moving waves, and relate these to linear transport operators.

These results for the structure and dynamics hold in two and three dimensions for the Ising model. We compare our results to recent experimental and theoretical studies of driven interfaces, finding a mix of agreement and disagreement. In the $3d$ Ising model we also investigate the interplay between the drive and the equilibrium roughening transition, finding that the effective-confinement picture ceases to apply, but that transport still occurs. Finally, we report some explorations into intriguing instability-related phenomena discovered in the driven Blume-Capel model simulations.

For Dad

Acknowledgements

Firstly I would like to thank my supervisor Matthias Schmidt, for inspiring me with an interest in statistical physics, for many useful and enjoyable discussions, and patience with buggy code! Thanks to Anna Maciołek and Oleg Vasilyev for being excellent, dynamic collaborators and welcoming hosts. I am thankful to Bob Evans for help and support, and more generally to members of the department for their teaching during my undergraduate studies. An EPSRC grant for this research is gratefully appreciated, as is use of the Bristol HPC facilities. Thanks to my co-habitants of the "pink office": Morgan, Jon, Paul and Gavin, for helping to create such a lively and friendly working atmosphere. Thank you to my mum, who has always been so supportive, and my partner Carolyn for her patience with my monologues about physics, which helped solve many a problem!

Author's Declaration

I declare that the work in this thesis was carried out in accordance with the regulations of the University of Bristol. The work is original except where indicated by special reference in the text and no part of the thesis has been submitted for any other degree. Any views expressed in the thesis are those of the author and in no way represent those of the University of Bristol. The thesis has not been presented to any other University for examination either in the United Kingdom or overseas.

This thesis is based on the following papers:

T.H.R. Smith, O. Vasilyev, D.B. Abraham, A. Maciołek and M. Schmidt
Interfaces in Driven Ising Models: Shear Enhances Confinement
Phys. Rev. Lett. **101** 067203 (2008).

T.H.R. Smith, O. Vasilyev, D.B. Abraham, A. Maciołek and M. Schmidt
Interfaces in confined Ising models: Kawasaki, Glauber and sheared dynamics
J. Phys.: Condens. Matter **20** 494237 (2008).

T.H.R. Smith, O. Vasilyev, A. Maciołek and M. Schmidt
Lateral transport of thermal capillary waves
Europhys. Lett. **89** 10006 (2010).

T.H.R. Smith, O. Vasilyev, A. Maciołek and M. Schmidt
Laterally driven interfaces in the three-dimensional Ising lattice gas
Phys. Rev. E **82** 021126 (2010).

Contents

List of Figures

Chapter 1

Introduction

Man's desire to study and understand interfaces stems in the first instance from their presence all around us. Indeed, when we look around, surfaces and interfaces form almost all that we see. Study of interfaces is also *useful*. A primary modern example is the growing field of micro- and nano-fluidics, where surface-to-volume ratios can be several orders of magnitude larger than in macroscopic systems [1]. The consequential enhancement of interfacial effects may be exploited. Pinned micro-fluidic interfaces can be used to create an environment for chemical reactions to occur, for example to create polymer walls [1]. This is just one of many micro-fabrication processes depending crucially on interface behaviour – other examples include growth of silver nanowires [2] and microscopic polymer strings [3]. Of particular practical importance are interfaces in non-equilibrium systems – the vast majority of systems, both those occurring naturally, and those created by man, are not in thermal equilibrium, but possess currents. Non-equilibrium interfaces occur in applications such as crystal and dendritic growth, in deposition processes, and in the propagation of flame fronts [4], as well as in the aforementioned micro-fluidic systems (in such systems, fluids often need to be transported, so driven interfaces are particularly relevant).

Returning to a fundamental perspective, interfaces present an abundance of interesting problems, even in equilibrium: wetting [5], roughening [4], the effect of confined geometries [6, 7], fluctuations, and even the very definition of the interface itself [8, 9]. Driving out of equilibrium adds a whole new treasure-trove of investigative opportunities, for example phase separation under drive [10], interplay with the roughening transition (for example, non-equilibrium deposition processes and roughening in ^{4}He [4, 11]), and the effect of drive on the structure and dynamics of the steady-state interface. It is this last question

this thesis attempts to address, for some simple lattice models, via Monte Carlo (MC) simulations.

The understanding of interfacial behaviour has advanced by the now-standard combination of theory, experiment, and computer simulation. On the experimental side, the traditional methods are light and X-ray scattering, which give a Fourier-space description of the interfacial structure. Recently it has become possible to directly (i.e., in real space) observe interfaces of colloidal systems via confocal microscopy [12, 13], due to their very low surface tension and consequently slow dynamics. This approach is extremely attractive to those who live in real space! The studies carried out here are partly motivated by such an experiment [13], which we shall discuss later.

Theoretical approaches to the study of equilibrium interfaces may be classified into three categories or levels [14]. Firstly, microscopic theories attempt a "full" description of the system in question, by constructing a Hamiltonian for the individual degrees of freedom (e.g. molecules or Ising spins) and calculating the partition function. Thus bulk-interfacial coupling is automatically taken into account – this is the ideal approach, but of course is not usually practical for systems of interest or relevance. A notable exception is the two-dimensional Ising model, for which exact results are available. The second method is *density functional theory* [15]: one starts from an order parameter density field and constructs a free energy functional – minimization then yields the equilibrium properties (both bulk and interfacial). The difficulty is that the exact free energy functional is not usually known, so approximations must be made – the accuracy of the results depends on how sophisticated these approximations are, and how well they fit the model at hand. Nevertheless, results can be excellent. The third angle of attack is to treat only the interfacial degrees of freedom explicitly. One constructs an effective interface Hamiltonian which is a functional of the displacement $h(\mathbf{r})$ of the interface from a reference plane: $\mathcal{H} = \mathcal{H}[h(\mathbf{r})]$, where $\mathbf{r}$ is a vector parallel to the reference plane. Bulk degrees of freedom are supposed to have been integrated out (into the parameters of the Hamiltonian) – this is generally not explicitly done since then we would be back to the other two approaches! The relative simplicity of this approach is a great advantage, although capturing bulk-interfacial coupling is naturally problematic. Capillary wave theory, which we discuss in Sec. 2.3, is an example of this third approach.

The most dramatic change in recent times has been in computer simulation. Raw computing power has increased dramatically, while costs have dropped – the combination

of this "brute-force" advance, as well as the development of new algorithms, has meant that accurate, large-scale simulations of systems with interfaces are now possible. Approaches are diverse, from more (or less) realistic modelling of inter-particle and external potentials, and integration of the equations of motion, as in molecular dynamics, to more abstract lattice models simulated by Monte Carlo methods (and everything in between). One important advantage of computer simulations, at least currently, is the relative ease of obtaining results for non-equilibrium systems, as compared to via theoretical methods. This is in large part due to the lack of a general statistical-mechanical framework out of equilibrium, which is of course sought by workers in the field [16], and hopefully at some point will become a reality.

In the next chapter we discuss some important aspects of the theoretical description of equilibrium interfaces, which will be of use later.

Chapter 2

Theoretical background: equilibrium interfaces

The main focus of this chapter is to review the capillary wave theory description of interfacial fluctuations, and discuss its predictions. To prepare for this we first introduce some thermodynamics.

2.1 Gibbs dividing surface

It is useful to *define* the position of an ideal (sharp) dividing surface between two fluid phases separated by an interface. In this picture, the order parameter profile (density for a one-component fluid, or number density difference in components $n_a - n_b$ for an A-B binary mixture, or magnetisation for an Ising system) is step-like, changing abruptly from its bulk value in one phase to its value in the other. Of course, this is not really the case – rather, the Gibbs dividing surface is a useful way of defining the surface tension and excess surface densities of various quantities. In particular, the choice of dividing surface is made so that the surface tension is equal to the excess free-energy per unit area of the interface. To choose a concrete example for exposition, we consider a liquid-gas system in three dimensions, and following Ref. [17] start from

$$\begin{aligned} V_l n_l + V_g n_g + N_i &= N \\ V_l e_l + V_g e_g + E_i &= E \\ F_l f_l + F_g f_g + F_i &= F. \end{aligned} \tag{2.1}$$

Here the symbols V, N, E, F are volume, particle number, energy, and Helmholtz free energy. The lower case n, e and f are the corresponding densities (per unit volume). The subscripts g, l and i stand for gas, liquid, and interface, respectively. In fact we will seek $N_i = 0$, the criterion defining the Gibbs dividing surface. The Gibbs-Duhem relation is [17]

$$F = -PV + \sigma A + \mu N, \tag{2.2}$$

where P is the pressure, σ the surface tension, A the interfacial area, and μ the chemical potential (which is equal in the two phases in equilibrium). For the interface, this becomes

$$F_i = f_i A = \sigma A + \mu N_i, \tag{2.3}$$

as the interface has no volume here. Since no coordinates have been specified, we choose the dividing surface to be at $z = 0$, for convenience. We also assume that the system is isotropic and homogeneous in the directions parallel to the interface, so that the only density dependence is on z. Then the following equation defines the number of particles in the interfacial region (that is, the number of particles not accounted for by the assumption of a sharp step profile), N_i:

$$N_i = A \int_{-\infty}^{0} dz \left[n(z) - n_l \right] + A \int_{0}^{\infty} dz \left[n(z) - n_g \right], \tag{2.4}$$

where $n(z)$ is the true, inhomogeneous, number density. The Gibbs dividing surface corresponds to satisfying $N_i = 0$, and thus from (2.3), $f_i = \sigma$: the surface tension is the excess Helmholtz free-energy per unit area of the interface. Having set out some thermodynamics and defined an ideal dividing surface, we now turn to the statistical mechanics of the interface.

2.2 The order parameter profile and intrinsic interface

The Gibbs dividing surface is just one choice for the more general concept of an *intrinsic surface* $h(\mathbf{r})$ [8, 18, 19] defined to be the instantaneous boundary (i.e. in one particular configuration) between two phases. Here $\mathbf{r}$ are the $(d-1)$ coordinates parallel to the interface plane (as before, the perpendicular coordinate is z), in a d-dimensional system. As before we use the example of a liquid-gas system, with order parameter $n(z)$, the number density. The instantaneous microscopic density is, formally,

$$n(\mathbf{R}, t) = \sum_i \delta(\mathbf{R} - \mathbf{R}_i(t)), \tag{2.5}$$

where $\mathbf{R} = (\mathbf{r}, z)$. The average order parameter profile is then obtained by a phase-space average:

$$n(z, A) = \left\langle \frac{1}{A} n(\mathbf{R}, t) \right\rangle . \tag{2.6}$$

Using the intrinsic surface, we may define an *intrinsic density profile*:

$$\begin{aligned} \tilde{n}(z; h) &= \left\langle \frac{1}{A} \sum_i \delta(\mathbf{R} - \mathbf{R}_i + [0, 0, h(\mathbf{r})]) \right\rangle \\ &= \left\langle \frac{1}{A} n(\mathbf{R} + [0, 0, h(\mathbf{r})], t) \right\rangle . \end{aligned} \tag{2.7}$$

This is the statistical average of the particle density, relative to the reference surface defined by $h(\mathbf{r})$, and so depends on the choice of intrinsic surface. Averaging over the realizations of the intrinsic surface should then give the average profile defined in (2.6). The intrinsic profile $\tilde{n}(z)$ is, as its name implies, a property of the phase equilibrium itself, independent of the interfacial area, whereas the total profile $n(z)$ *does* depend on the system size. Density-functional type theories – the simplest of which is the venerable van der Waals [20, 21] theory of the interface, may be viewed as giving results representing the intrinsic profile; for a Lennard-Jones fluid near its triple point, van der Waals theory gives an interface width (the length scale over which the density goes from approximately that of one bulk phase to the other) of 2-3 molecular diameters [22], which is of the order of the bulk correlation length ξ_b. Thus the intrinsic profile is rather sharp, essentially a broadened step function [18]; for any *particular* dividing surface h, the density varies rapidly towards the bulk densities as we move away from the dividing surface. However, the surface $h(\mathbf{r})$ itself fluctuates, with an extent controlled by surface tension, system size, and external fields. The fluctuations of the dividing surface are thus the origin of the dependence of the full profile $n(z)$ upon system size – we investigate these in the next section.

Usually it is (reasonably) assumed that the intrinsic profile (2.7) obtained for a particular $h(\mathbf{r})$ is in fact *independent* of $h(\mathbf{r})$ [18]. Then we can make the relationship between the various quantities explicit, because the full profile will be given by a convolution of the intrinsic profile and the probability distribution of $h(\mathbf{r})$:

$$\begin{aligned} n(z, A) &= \int \tilde{n}(z - h) P(h)\, dh \\ &= \int \left\langle \frac{1}{A} n(\mathbf{R}, t \,|\, h) \right\rangle P(h)\, dh, \end{aligned} \tag{2.8}$$

where in the last line $\langle n(\mathbf{R}, t \mid h)\rangle$ means the averaged microscopic density for a given, fixed, $h(\mathbf{r})$. As mentioned, the intrinsic profile is calculable from density-functional theories – a natural question is whether one can access it in simulations or experiments – and whether doing so is useful. Measuring the intrinsic profile in a robust way is indeed desirable, from the point of view of constructing a coherent quantitative description of the interface profile [8, 19] – i.e., connecting density-functional results (microscopic) with those of the interface Hamiltonian approach (mesoscopic, capillary wave theory). Chacón *et al.* have developed an "intrinsic sampling method" [8, 19] which aims to find the intrinsic profile.

In this thesis our concern is the average behaviour, including the fluctuations of the intrinsic surface, so we do not need to employ elaborate methods to deconvolve the different contributions – to determine the profile, we simply measure the average of the density at each z coordinate. The question of how to define the intrinsic surface – the boundary between the two phases – remains. This will be discussed when we introduce the main simulation model in Chapter 7.

2.3 Capillary wave theory

We now assume we have some prescription for the location of the intrinsic surface $h(\mathbf{r}) = h(x, y)$ dividing two phases in a three-dimensional system, where x and y are coordinates in the lateral (interface) plane. Let the mean position of the interface be at $z = 0$, where z is the vertical coordinate, perpendicular to a flat interface. The function $h(\mathbf{r})$ will usually be referred to as the *interface height*. The objective of capillary wave theory (CWT) is to describe the thermal fluctuations of the interface, which cause it to distort, and wander in space – see Fig. 2.1 for an idealised illustration. We therefore construct an interface Hamiltonian $\mathcal{H}$, which gives the excess energy associated with these movements. This means that CWT falls into the third class of theories mentioned earlier – bulk degrees of freedom are not considered. The prediction of thermal fluctuations at a liquid-vapor interface seems to have first been made by Smoluchowski [23]. Mandelstam [24] then developed these ideas into a theory of thermal "capillary waves". This theory was then essentially rediscovered by Buff, Lovett and Stillinger [25] without reference to Mandelstam's work (although, interestingly, with passing reference to Smoluchowski). Subsequent work developed the theory more formally. Here we follow the treatments of Refs. [26–28].

The Hamiltonian $\mathcal{H} = \mathcal{H}[h(\mathbf{r})]$ consists of contributions due to work against surface

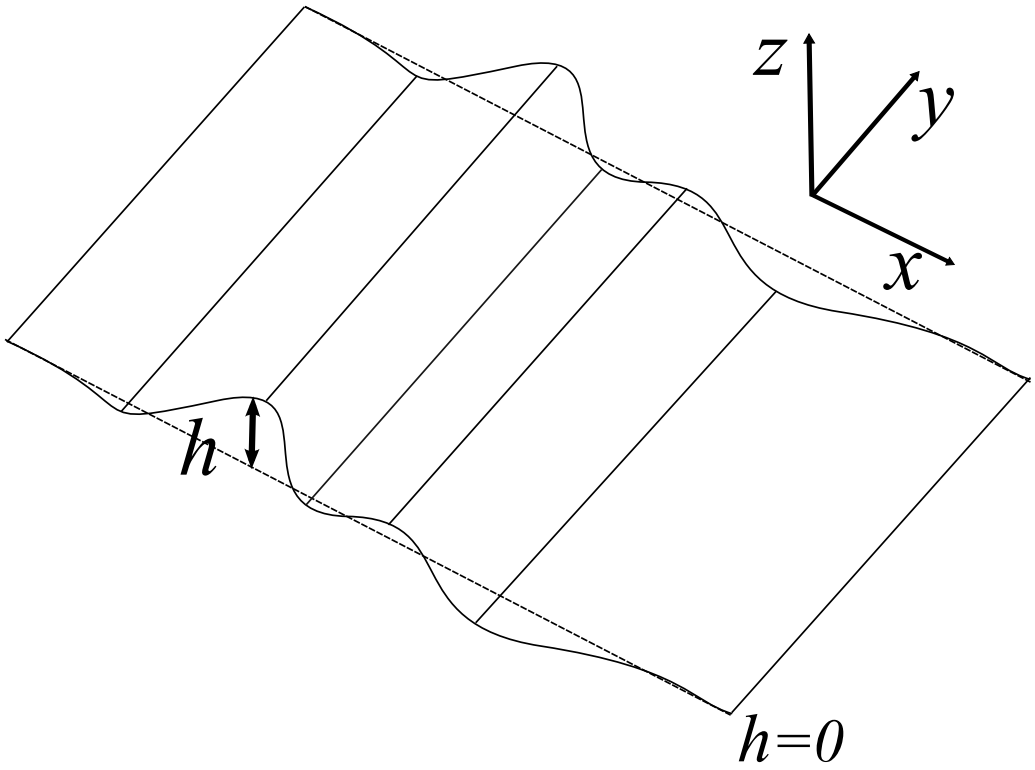

Figure 2.1: Interfacial fluctuation as treated by capillary wave theory, in a three-dimensional system. The undulations depicted here are idealised – in reality the amplitude may also of course change with y: $h = h(x, y)$.

tension, and work against external field(s). For clarity of exposition and continuity with the interfacial thermodynamics above, we consider a liquid-gas system in a gravitational field, and unconfined by walls. The description is readily generalized to other order parameters (e.g. for a spin system), or confined situations, as we will discuss later. For an infinitesimal area $dx\,dy$, the work against gravity required to create a "bump" of liquid phase of height $h(x, y)$ above $z = 0$ is

$$\begin{aligned}\Delta W_g &= dx\,dy \int_0^h dh'\, g(\rho_l - \rho_g) \\ &= \frac{1}{2} dx\,dy\, g(\rho_l - \rho_g) h^2. \end{aligned} \tag{2.9}$$

Here ρ_l and ρ_g are the mass densities in the bulk liquid and gas phases, respectively, and g is the acceleration due to gravity. Physically, to create a liquid "bump" of volume $dV = dx\,dy\,dh'$, one has to add mass $(\rho_l - \rho_g)dx\,dy\,dh'$ to the volume. The total work is then given by the integral up to the desired height h. The work against surface tension is due to increases in area [29] caused by distorting the interface surface from its ground (flat) state:

$$\Delta W_\sigma = \sigma dx\,dy \left(\sqrt{1 + |\nabla h(\mathbf{r})|^2} - 1 \right). \tag{2.10}$$

In CWT, the square root is simply approximated to first order – physically this means that local interface distortions are assumed to be small: $\frac{\partial h}{\partial x}$, $\frac{\partial h}{\partial y} \ll 1$. The full interface Hamiltonian is then

$$\mathcal{H} = \int\int dx\,dy \left(\frac{\sigma}{2} |\nabla h(\mathbf{r})|^2 + \frac{1}{2} g(\rho_l - \rho_g) h^2 \right), \tag{2.11}$$

where the integrals cover the whole interface area. As argued by Bedeaux and Weeks [27], $\mathcal{H}$ should come about when short-wavelength degrees of freedom present in the full Hamiltonian for the system have been integrated out. It is possible to make this concept more precise by considering the columnar picture of Weeks [9]. The system is viewed as an array of columns, each of transverse dimensions $\sim \xi_b$, the bulk correlation length. The partition function can then be written as a sum of *constrained* partition functions, each with a particular set of column heights $\{h_i\}$. These constrained functions can be used to define an interface Hamiltonian, whose continuum limit is (2.11). This picture is sensible when distortions of the interface on the scale of ξ_b are not allowed, since the height is constant within a column – thus providing a natural short-wavelength cutoff in the theory. For further details of this approach see Ref. [9]. We now take $h(\mathbf{r})$ to be

periodic on a square of side L and expand it in a Fourier series:

$$h(\mathbf{r}) = \sum_{\mathbf{k}=\mathbf{k}_{\min}}^{\mathbf{k}_{\max}} h_{\mathbf{k}} \exp(i\,\mathbf{k}\cdot\mathbf{r}), \tag{2.12}$$

where $\mathbf{k} = (k_x, k_y)$. We discuss the limits of the sum in a moment. Using Parseval's identity, we can then write (2.11) in Fourier space:

$$\mathcal{H} = \frac{1}{2}L^2 \sum_{\mathbf{k}=\mathbf{k}_{\min}}^{\mathbf{k}_{\max}} |h_{\mathbf{k}}|^2 \left(g(\rho_l - \rho_g) + \sigma k^2\right), \tag{2.13}$$

where $k = |\mathbf{k}|$. The low wave vector limit in the sum is set by the system size: $k_{x,\min}, k_{y,\min} = 2\pi/L$, corresponding to the longest wavelength mode allowed. From the previous discussion, the upper limit should correspond to the length scale below which the interfacial description does not apply, i.e., $k_{\max} \approx 2\pi/\xi_b$. This is also consistent with the requirement of small local gradients. Eqn. (2.13) is quadratic in the Fourier height components $h_{\mathbf{k}}$, so we can invoke the equipartition theorem: the thermally averaged energy associated with each mode is $k_B T/2$, where T is the temperature and k_B the Boltzmann constant. Hence

$$\left\langle |h_{\mathbf{k}}|^2 \right\rangle = \frac{k_B T}{\sigma L^2} \frac{1}{k^2 + \xi_{\parallel}^{-2}}, \tag{2.14}$$

where the angles indicate an ensemble average. Using equipartition is equivalent to performing the Gaussian integrals involved in the explicit calculation of $\left\langle |h_{\mathbf{k}}|^2 \right\rangle$ – the Gaussian nature of the Boltzmann factors means that the average is straightforward to calculate. Eqn. (2.14) introduces an important new quantity with the dimensions of length:

$$\xi_{\parallel} \equiv \sqrt{\frac{\sigma}{g(\rho_l - \rho_g)}}. \tag{2.15}$$

$\xi_{\parallel}$ is the *lateral correlation length*, or *capillary length* – as the name implies, it measures the range of correlations along the interface. This is a crucial length scale in the problem, and will appear in all the results for quantities of interest. Armed with the Fourier space description of $\mathcal{H}$, we are now in a position to calculate observables of interest.

2.3.1 Interface width

We first calculate the width w of the interface. This may be defined as the root-mean-square height displacement: $w \equiv \sqrt{\langle h^2 \rangle}$. To aid calculation, we convert the sum over

wave vectors to an integral, using the density of modes in Fourier space. This yields an integral which can be done by inspection; the result is

$$w^2 = \frac{k_B T}{4\pi\sigma} \ln\left[\frac{k_{\max}^2 + \xi_\parallel^{-2}}{k_{\min}^2 + \xi_\parallel^{-2}}\right] \qquad (d = 3). \tag{2.16}$$

Eqn. (2.16) has interesting asymptotic properties. Firstly, if gravity is turned off, then $\xi_\parallel \to \infty$, so $w^2 \sim \ln(k_{\max}/k_{\min})$, which diverges as $\ln(L)$ as $L \to \infty$. This means that in zero gravity, the interfacial width is infinite in the thermodynamic limit. Secondly, if $L \to \infty$ first, then

$$\begin{aligned} w^2 =& \frac{k_B T}{4\pi\sigma} \ln(k_{\max}^2 \xi_\parallel^2 + 1) \\ \sim& \ln(\xi_\parallel), \qquad L \to \infty,\ g \to 0,\ (d = 3) \end{aligned} \tag{2.17}$$

Thus whichever way we take the limits $g \to 0$, $L \to \infty$, the width is divergent – put another way, the order parameter (density) profile is completely "washed out", $d\rho/dz = 0$.

This prediction is in contrast to that of density-functional approaches, where one obtains a width which is finite in the limit of infinite system size and zero gravity. As mentioned above, one may view these microscopic theories as giving profiles representative of the intrinsic profile, incorporating bulk fluctuations, while in CWT we are instead describing the fluctuations of the dividing surface. Making this statement precise is not easy, due to the question of the choice of cutoff $k_{\max}$, whose exact value is still somewhat arbitrary, and the question of exactly which fluctuations are incorporated into the two approaches, in order to avoid "double-counting". Further discussion of these issues may be found in Ref. [30], where the authors use a density-functional theory to then construct an improved interfacial Hamiltonian.

We now return to the capillary wave predictions. The analysis above may be carried out for systems in any dimension – for a two-dimensional system ($1d$ interface: a line) one finds for the width

$$w^2 = \frac{k_B T \xi_\parallel}{2\pi\sigma} \left[\arctan(\xi_\parallel k_{\max}) - \arctan(\xi_\parallel k_{\min})\right] \qquad (d = 2). \tag{2.18}$$

In the limit $L \to \infty$ the second term vanishes. In the limit of small g, we can approximate the first arctan term by its asymptotic value $\pi/2$, since $\xi_\parallel \gg k_{\max}^{-1}$ in this limit. Then we have

$$w^2 \sim \frac{k_B T}{4\sigma} \xi_\parallel, \qquad L \to \infty,\ g \to 0,\ (d = 2) \tag{2.19}$$

Thus the width is again divergent in the infinite system, zero gravity limits; the divergence as $g \to 0$ is much stronger than in three dimensions – linear as opposed to logarithmic. This suggests that capillary-wave fluctuations are much stronger in $2d$, and that $d = 3$ is the marginal dimension (logarithmic divergence). Indeed this is confirmed if one treats the problem in arbitrary dimension d [27] – for $d > 3$, the width is *independent* of $\xi_\parallel$, and so remains finite in the thermodynamic limit, in agreement with mean-field results.

2.3.2 Height correlation function

The spatial height-height correlation function gives information about the interfacial structure on the two-point level:

$$C(\mathbf{r}) \equiv \left\langle \frac{1}{L^2} \int d\mathbf{r}'\, h(\mathbf{r}')h(\mathbf{r}'+\mathbf{r}) \right\rangle, \tag{2.20}$$

where the integral is over the whole interface, and the angles denote an ensemble average. Note that since $\langle h \rangle = 0$, C should decay to zero for $r \to \infty$ without the subtraction of a $\langle h \rangle^2$ term. We can show that (2.14) are coefficients of the Fourier series expansion of this function. Firstly, by definition,

$$C(\mathbf{r}) = \left\langle \frac{1}{L^2} \int d\mathbf{r}' \sum_{\mathbf{k}} h_{\mathbf{k}} e^{i\mathbf{k}\cdot(\mathbf{r}'+\mathbf{r})} \sum_{\mathbf{k}'} h_{\mathbf{k}'} e^{i\mathbf{k}'\cdot\mathbf{r}'} \right\rangle \tag{2.21}$$

Since h is real, taking the complex conjugate of it leaves it invariant, so we have

$$\begin{aligned}
C(\mathbf{r}) &= \left\langle \frac{1}{L^2} \int d\mathbf{r}' \sum_{\mathbf{k}} h_{\mathbf{k}} e^{i\mathbf{k}\cdot(\mathbf{r}'+\mathbf{r})} \sum_{\mathbf{k}'} h^\star_{\mathbf{k}'} e^{-i\mathbf{k}'\cdot\mathbf{r}'} \right\rangle \\
&= \left\langle \frac{1}{L^2} \int d\mathbf{r}' \sum_{\mathbf{k},\mathbf{k}'} h_{\mathbf{k}} h^\star_{\mathbf{k}'} e^{i\mathbf{k}\cdot\mathbf{r}} e^{i(\mathbf{k}-\mathbf{k}')\cdot\mathbf{r}'} \right\rangle \\
&= \left\langle \frac{1}{L^2} \int d\mathbf{r}' \sum_{\mathbf{k}} h_{\mathbf{k}} e^{i\mathbf{k}\cdot\mathbf{r}} \sum_{\mathbf{k}'} h^\star_{\mathbf{k}'} e^{i(\mathbf{k}-\mathbf{k}')\cdot\mathbf{r}'} \right\rangle \\
&= \left\langle \frac{1}{L^2} \sum_{\mathbf{k}} h_{\mathbf{k}} e^{i\mathbf{k}\cdot\mathbf{r}} \sum_{\mathbf{k}'} h^\star_{\mathbf{k}'} \int d\mathbf{r}'\, e^{i(\mathbf{k}-\mathbf{k}')\cdot\mathbf{r}'} \right\rangle \\
&= \left\langle \sum_{\mathbf{k}} h_{\mathbf{k}} e^{i\mathbf{k}\cdot\mathbf{r}} \sum_{\mathbf{k}'} h^\star_{\mathbf{k}'} \delta_{\mathbf{k}\mathbf{k}'} \right\rangle \\
&= \sum_{\mathbf{k}} \left\langle |h_{\mathbf{k}}|^2 \right\rangle e^{i\mathbf{k}\cdot\mathbf{r}}.
\end{aligned} \tag{2.22}$$

In going from the fourth to the fifth line, we used the resolution of the Kronecker delta in terms of an integral (see Ref. [31] Chapter 5). Thus the Fourier coefficients of the correlation function expansion are just the expectation values of the absolute values (squared)

of the Fourier coefficients for the height. This is useful, because we can substitute using (2.14), and convert to an integral:

$$C(\mathbf{r}) = \frac{k_B T}{\sigma L^2} \frac{L^2}{4\pi^2} \int_{k_{\min}<|k|<k_{\max}} \frac{d\mathbf{k}}{k^2 + \xi_{\|}^{-2}} e^{i\mathbf{k}\cdot\mathbf{r}} \tag{2.23}$$

To proceed, a transformation to polar coordinates is made. In the limit $k_{\min} \to 0$, $k_{\max} \to \infty$, the required integrals may be found in tables [32]. Sending the lower limit to zero is not a problem, since one is interested in the limit of infinite system size anyway. However, we explicitly stated earlier that CWT does not apply for all k – fluctuations on the scale of the bulk correlation length cannot be treated. Therefore we cannot simply send $k_{\max}$ to infinity in good conscience. Mathematically, the integral is divergent for $r = 0$ in dimensions $d \geq 3$. Physically, $C(0) = \langle h^2 \rangle$ should give the squared interface width (see the previous section), and so should only diverge when $\xi_{\|}$ becomes infinite. The resolution is to regularize the integral by introducing a shifted spatial variable [27, 33, 34], where the shift is related to the length scale corresponding to $k_{\max}$. Then the upper limit on the integral may be sent to infinity, because for k greater than $k_{\max}$, the rapid oscillations of the integrand ensure no contribution. The result for a three dimensional system is

$$C(r) = \frac{k_B T}{2\pi\sigma} K_0 \left(\sqrt{\left(\frac{r}{\xi_{\|}}\right)^2 + \lambda^2} \right), \tag{2.24}$$

where K_0 is the modified Bessel function of the second kind, and $\lambda \approx 1/(k_{\max}\xi_{\|})$ is the shift [27, 35]. The presence of λ ensures that the correlation function does not diverge at zero separation. For small arguments, $K_0(z)$ diverges as $-\ln(z)$, while in the other limit, there is exponential decay; the capillary length $\xi_{\|}$ controls the range of correlations.

2.3.3 Confinement

In the previous sections, we have considered an unconfined liquid-gas interface in a gravitational field. In the simulations described later, we wish to model a *confined* interface, where the system is constrained by two (upper and lower) walls at some separation L_z – see Fig. 2.2a for an illustration. Such systems are relevant experimentally, particularly with the growth of nano-fluidics, mentioned earlier, as well as being of theoretical interest due to the new behaviour resulting from interactions between walls, interface and bulk. To describe this situation, CWT should be modified to take into account the presence of the walls. Since we shall be simulating a spin system in zero external (static) magnetic

field, the gravitational potential term is not applicable. Instead, we know that the interfacial fluctuations will be limited by the walls, due to entropic effects: excursions of the interface to the vicinity of one wall are entropically unfavourable, because the interface has less freedom to fluctuate in this position (it cannot pass the impermeable wall), as compared to further away. Thus it is natural to add a potential to the Hamiltonian $\mathcal{H}$ to model this effect. Consider a potential $V(h)$ which we expand in powers of h about the mean position $\bar{h}$:

$$V(h) = V(\bar{h}) + (h - \bar{h}) \left(\frac{dV}{dh} \right)_{h=\bar{h}} + \frac{1}{2}(h - \bar{h})^2 \left(\frac{d^2V}{dh^2} \right)_{h=\bar{h}} + \dots \tag{2.25}$$

The first derivative is zero at the mean position, so ignoring the constant term, the leading contribution is

$$\frac{1}{2}h^2 \left(\frac{d^2V}{dh^2} \right)_{h=0}, \tag{2.26}$$

where we have let the mean position lie at $h = 0$ (as in the preceding discussion of CWT). Recalling the gravitational contribution Eqn. (2.9) to the unconfined CWT Hamiltonian, we see it is of the same parabolic form as Eqn. (2.26). Thus for any potential which we can expand as in (2.25) (with non-zero second derivative at $h = 0$), we will obtain a leading h^2 dependence on the interface height. Now we may write the CWT Hamiltonian in a general form using (2.26):

$$\mathcal{H} = \int d\mathbf{r} \left\{ \frac{\sigma}{2} |\nabla h(\mathbf{r})|^2 + \frac{1}{2}h^2 \left(\frac{d^2V}{dh^2} \right)_{h=0} \right\}. \tag{2.27}$$

In this form we may apply the theory laid out previously to any situation which may be modelled by some appropriate choice of the potential $V(h)$. We may immediately identify the lateral correlation length by comparing (2.27) and (2.11), and using (2.15):

$$\xi_{\parallel}^{-2} = \frac{1}{\sigma} \left(\frac{d^2V}{dh^2} \right)_{h=0}, \tag{2.28}$$

and the results for the width and height correlations apply unchanged.

An accepted explicit form of potential in $d = 3$ [7, 36, 37] for walls which have a short range interaction with the bulk phases is

$$V_{3d}(h) \propto \exp\left(-\kappa \left(L_z/2 + h\right)\right) + \exp\left(-\kappa \left(L_z/2 - h\right)\right), \tag{2.29}$$

where the $h = 0$ plane is taken to be at the midpoint between the walls – each term represents the contribution from one wall (we have assumed that the effects of each wall

are separable in this way). The constant κ is the decay rate for the potential away from the walls; in mean-field theory $\kappa = 1/\xi_b$ [36, 38]. Expanding in powers of h (or using (2.26)), the first non-constant term goes as h^2, as expected:

$$V_{3d}(h) \propto \exp\left(-\kappa L_z/2\right) \kappa^2 h^2. \tag{2.30}$$

For this potential, the explicit form of the lateral correlation length is

$$\xi_\parallel \propto \sqrt{\frac{\sigma}{2}} \kappa^{-1} \exp(\kappa L_z/4), \qquad (d=3) \tag{2.31}$$

corresponding to Eqn. (2.15) in the unconfined case. Notice that $\xi_\parallel$ scales exponentially with the wall separation. We can now see the behaviour of the interface width in a confined system; for $d = 3$, in the limit $L \to \infty$ (long lateral dimension), using (2.17) we have

$$\begin{aligned} w^2 &= \frac{k_B T}{4\pi\sigma} \ln(k_{\max}^2 \xi_\parallel^2 + 1) \\ &\propto L_z, \qquad (k_{\max}\xi_\parallel)^2 \gg 1. \qquad (d=3) \end{aligned} \tag{2.32}$$

In $d = 2$, an appropriate potential from the walls is [7]

$$V_{2d}(h) \propto \frac{1}{(L_z/2-h)^2} + \frac{1}{(L_z/2+h)^2}, \tag{2.33}$$

giving, via (2.28),

$$\xi_\parallel \propto L_z^2 \qquad (d=2). \tag{2.34}$$

The leading contribution to the interface width (2.18) for $L \to \infty$ will then be

$$w^2 \sim \xi_\parallel \sim L_z^2 \qquad (d=2). \tag{2.35}$$

In both cases, the interfacial width scales as a power of the wall separation L_z; the dependence is stronger in $d = 2$ than in $d = 3$. Note that in both cases the limit $L \to \infty$ has been taken – if one wants to access this regime in a finite (simulation) system, care is required to ensure that $L \gg L_z$. We will see evidence of crossover between regimes in the $3d$ results presented later.

Before moving on, some of the great variety of phenomena that occur in confined situations should be mentioned. The nature of the wall-particle interactions is important in determining the phase behaviour of confined systems. For example, in colloid-polymer mixtures, where phase separation into a colloid-rich (liquid-like) phase and a polymer-rich (vapour-like) phase can occur for suitable system parameters, confinement by simple hard

walls can bring about an effective attraction of the colloids to the walls. This is due to the depletion effect – when colloids are closer than about twice the polymer radius of gyration to the walls, it is entropically favourable for the polymers to evacuate this area, and for the colloids to move next to the wall, since the polymers will have more freedom to explore different configurations. Monte Carlo simulations of the Asakura-Oosawa model of colloid-polymer systems [39, 40] confined between hard walls have shown capillary condensation [41] of the colloidal liquid to occur, due to this effect – that is, the wall attraction is able to stabilise the colloidal-liquid phase at statepoints which in bulk would be colloidal-gas (the binodal is shifted).

Subsequent studies have considered the same system, but with different colloid-wall interactions. Vink *et al.* [42] found that it was possible to essentially cancel the depletion effect by making the walls *repel* colloids at short ranges, with an appropriate choice of the strength of the repulsive potential. Fortini *et al.* [43] considered semi-permeable walls, where the polymers may pass a small distance, but the colloids may not; this is like an infinite repulsive colloid-wall potential. In this limit, capillary evaporation, the opposite of condensation – stabilisation of the gas phase within the liquid region of the bulk phase diagram, was observed. *Asymmetric* walls, which each have different interactions with the colloid, are of particular interest. Parry and Evans [38] studied the phase behaviour of a generic fluid (or Ising magnet) confined between walls with opposing fields, via a Landau free energy functional. In the semi-infinite system ($L_z = \infty$, walls infinitely far apart), complete wetting, an infinitely thick layer of the phase favoured by the wall, occurs at a temperature T_w, where the transition may be of first or second order depending on the surface field. In the confined system, for temperatures above T_w but below bulk criticality, coexistence between two phases occurs, separated by an interface with average position midway between the walls [38, 44]. The location of T_w may be altered by changing the magnitude of the wall fields, and may be sent arbitrarily far below the bulk critical temperature for large enough fields. As the temperature passes through T_w, an interface localization-delocalization transition occurs – for $T < T_w$, the interface becomes localized to the vicinity of one wall; this transition has been studied in Ising [7, 45] as well as colloid-polymer [46] systems.

From the above overview, it should be clear that a rich array of phenomena can occur in confined fluid systems – far more than may be explained properly here, and instead the reader is referred to review articles [47, 48] covering both Ising-like and colloid-polymer

systems.

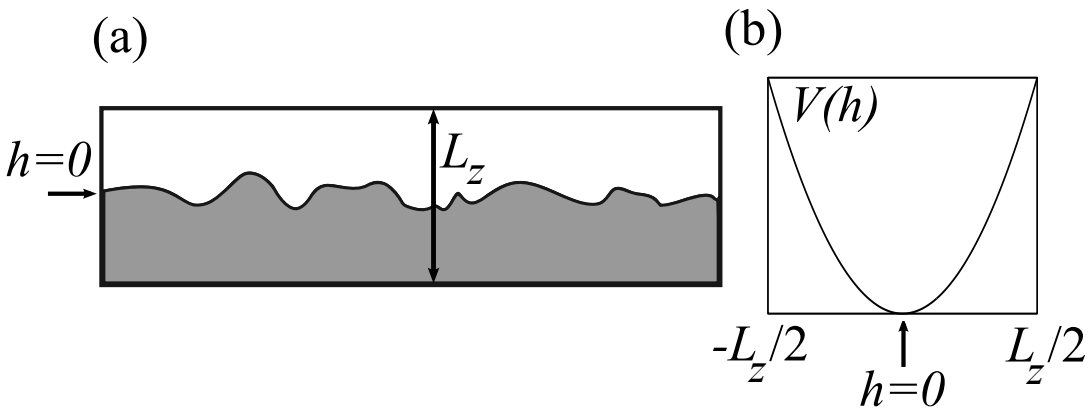

Figure 2.2: (a) Confined system with an interface – this could be a two-dimensional system, or a slice through a three-dimensional one. (b) Parabolic potential $V(h)$ with a minimum at the mean interface position, midway between the walls.

Chapter 3

The Ising Model

3.1 History and definition

The Lenz-Ising model is unquestionably an important model in condensed matter physics – indeed, it is rather difficult to avoid it in some guise or another. This last statement is a clue to why the model is so widely used – when cast in different ways, the Ising model captures the essence of many problems on an idealized level. The most obvious (and the original) of these is ferromagnetic behaviour; others include the description of binary alloys, liquid-gas systems, and more generally "cooperative phenemona", i.e. complex, non-trivial collective behaviour exhibited by a system of many simple components. A brief discussion of some of these applications of the Ising model will be given in the following.

The key characteristics of the Ising model as known today were conceived by Wilhelm Lenz, and his student, Ernst Ising, in the 1920s. These are the assumption of elementary magnets on a lattice which may turn over or *flip* between two orientations, the existence of interactions which favour alignment of these magnets, and that these interactions are short-ranged. The reader might notice that in the first sentence of this chapter we used the term "Lenz-Ising model", then reverted to the much more common "Ising model"; as pointed out by Niss [49] (the historically curious reader might be interested to read this nice account of the history of the Ising model, as well as its sequel [50]) the former name was actually preferred by Ising, and is probably the fairer, since Lenz introduced the "flipping" assumption in a paper in 1920 (Ising's thesis came in 1924), and must certainly have contributed to the further details of the model. In any case, we revert to simply "Ising model" hereafter, for familiarity and brevity (quite possibly the reason for

the shorter name's popularity!). Let us now define the basic model.

On lattice sites i, of which there are N in total, sit "spins" σ_i, which may take values ± 1. In the magnetic picture, the two states correspond to actual spin states of an electron: oriented "up" and "down" respectively. Nearest-neighbour spins on the lattice interact via a coupling constant J with units of energy. Two aligned spins contribute $-J$ to the internal energy of the system; opposite spins contribute $+J$. Thus if $J > 0$, aligned spins lower the energy and the system is ferromagnetic. We shall not consider antiferromagnetic Ising models (where $J < 0$), which are also studied. We also ignore quantum-mechanical effects – in any case, for the lattice-gas mapping we consider later, these are negligible. The whole system may also sit in an external field B, which couples to all the spins. All this may be described mathematically by the Ising Hamiltonian

$$H\left[\{\sigma_i\}\right] = -J \sum_{\langle ij \rangle} \sigma_i \sigma_j - B \sum_i \sigma_i, \tag{3.1}$$

where the angles indicate that the first sum is only over nearest-neighbour (interacting) pairs. The dependence on the values of the spin variables is explictly indicated on the left hand side here. The lattice may possess any number of dimensions d, the most relevant of which, $d = 3$, is also the trickiest to deal with. For the most part we will consider $2d$ square lattices and $3d$ simple cubic lattices in the following.

In equilibrium statistical mechanics, given the Hamiltonian and nature of the lattice (dimensionality, geometry, boundary conditions), in principle one can proceed to calculate the partition function in the thermodynamic limit, and from this, obtain results for all static observables as derivatives of it. In practice, this is only possible under certain conditions. For example, in one dimension, the Ising model is solvable with or without a field [17]; indeed the solution of the one-dimensional model was the primary topic of Ising's 1924 thesis and paper of the following year. In two dimensions on a square lattice, an exact solution is only available for the case $B = 0$ [51] – the celebrated Onsager result. Rudolf Peierls had proved the existence of ferromagnetism in the $2d$ Ising model at low temperatures in 1936, but did not have a solution. Kramers and Wannier, in 1941, had found the critical temperature T_c where ferromagnetism sets in, but Onsager was able to find the partition function. In three dimensions, no exact solution has been found at all. Despite this, much is known in two and three dimensions from approximate theoretical approaches, for example mean field theory, series expansions and renormalization group methods [17, 52, 53], and from Monte Carlo simulations [54–56]. We now ask – what have

these varied methods helped to discover that makes the Ising model so interesting?

3.2 Phase transition

The most important feature of the Ising model is the existence (or lack thereof, depending on dimensionality) of a second-order phase transition (in the thermodynamic limit) from a state of zero average magnetisation to one with a non-zero *spontaneous* magnetisation m_{sp}, in the limit of the external field B going to zero. Firstly we define the thermally-averaged magnetisation per site:

$$m \equiv \frac{1}{N} \left\langle \sum_i \sigma_i \right\rangle, \tag{3.2}$$

where the angles indicate an ensemble/thermal average over all states available to the system. Equilibrium statistical mechanics prescribes Boltzmann probabilities,

$$p_s = \frac{e^{-\beta H_s}}{Z} \tag{3.3}$$

for the states s – that is, weighted according to their energy, with lower energy states being more probable. Here $\beta \equiv 1/k_{\mathrm{B}}T$, where T is the temperature of the system, and k_{B} the Boltzmann constant. H_s refers to the Hamiltonian (3.1) evaluated for state s. The normalisation factor Z is of course the partition function:

$$Z(\beta) = \sum_s e^{-\beta H_s}, \tag{3.4}$$

where the sum is over all states. The Helmholtz free energy F is related to the natural logarithm of the partition function:

$$F = \langle E \rangle - T \langle S \rangle = -k_{\mathrm{B}} T \ln Z, \tag{3.5}$$

where $\langle E \rangle$ and $\langle S \rangle$ are the expectation values of the energy (Hamiltonian) and the entropy, respectively. In equilibrium, F attains its minimum value. Expectation values of observables, such as (3.2), of a system in equilibrium may be obtained by performing an ensemble average, that is, a weighted average over all states:

$$\langle A \rangle = \sum_s A_s \, p_s = \frac{1}{Z} \sum_s A_s \, e^{-\beta H_s}, \tag{3.6}$$

where A is an arbitrary observable, and A_s is the value of A in the state s. In passing we remark that (as mentioned above) properties of the system, such as magnetisation per

site, may also be written as derivatives of the partition function (or equivalently, the free energy):

$$\begin{aligned} m =& \frac{1}{Z} \sum_s \left(\frac{1}{N} \sum_i \sigma_i \right) e^{-\beta H_s} \\ =& \frac{1}{\beta N} \frac{\partial \ln Z}{\partial B}. \end{aligned} \tag{3.7}$$

Returning to the spontaneous magnetisation, we can now define this as (noting the order of the limits)

$$m_{\mathrm{sp}} = \lim_{B \to 0} \lim_{N \to \infty} m. \tag{3.8}$$

The *thermodynamic limit* of an infinite system, $N \to \infty$, has been taken here. The quantity m_{sp} is the *order parameter* for the Ising transition, since it is zero in the disordered, high temperature, phase, and non-zero in the ordered phase. Interpreting (3.8) physically, the external field is made arbitrarily small, but the system retains unequal numbers of up and down spins on the average. If this is the case, the up/down symmetry has been broken, and *spontaneous symmetry breaking* has occurred: although for $B = 0$ the Hamiltonian (3.1) is invariant under the operation of flipping all spins, $H[\{\sigma_i\}] = H[\{-\sigma_i\}]$, the expectation value of the magnetisation, m_{sp}, is not invariant since it is non-zero. The limit $N \to \infty$ is crucial for theoretical work, since in a finite system, there is *no* true phase transition, because the partition function Z and the resultant free energy remain analytic [31]. This is why the order of the limits in Eqn. (3.8) was important – if we had taken the field to zero before taking the thermodynamic limit, then the magnetization would just be zero. Fortunately all this does not mean studying finite systems (as done in simulation) is useless; one has a pseudo-phase transition, where although truly $m_{\mathrm{sp}} = 0$, the distribution is strongly double-peaked at two values equal in sign but opposite in magnitude.

The existence of a transition and its properties depend on the dimensionality of the lattice. In one dimension, there is no transition for $T > 0$, but in two or more dimensions, a non-zero critical temperature T_c marks the transition point. In two dimensions on the square lattice, $k_B T_c/J = 2/\ln(1+\sqrt{2}) = 2.269\ldots$ [51] (exact), while in $3d$ on the simple cubic lattice $k_B T_c/J = 4.5115\ldots$ [57] (from Monte Carlo simulations). Since the transition is second-order, the spontaneous magnetisation (a first derivative of the free energy) tends continuously to zero from below T_c, while the susceptibility at constant temperature $\chi_T = (\partial m/\partial B)_T$ diverges. The divergence is a power-law, $\chi \sim |T - T_c|^{-\gamma}$ where $\gamma > 0$ is the *critical exponent* for the susceptibility. Other divergent quantities (see

below) have associated critical exponents.

The critical properties of the $2d$ and $3d$ Ising models have been extensively studied – not only to understand the model itself, but due to the idea of *universality* [31, 58], which tells us that all systems in the same "universality class" possess the *same* critical exponents. The $3d$ Ising universality class encompasses $d = 3$ systems with a single scalar order parameter and short-range interactions, and so covers many systems, for example simple liquids. This is an important example of the relevance of the Ising model outside ferromagnetism – by studying the $3d$ Ising model, we can predict the critical exponents of classical liquids, without bothering about the details of the chemistry. As mentioned above, no exact solution has been found for the $3d$ Ising model (the transfer matrix method by which the $2d$ model may be solved encounters technical difficulties [17]). However, very accurate estimations of the critical temperature and exponents are possible, via renormalization group (RG) methods, series expansions, and Monte Carlo methods. The RG approach is based on the idea of integrating out degrees of freedom (spins in the Ising model) to produce a new system with "block" degrees of freedom which interact via altered coupling constants. This picture is originally due to Kadanoff [59]; subsequently Wilson [60] developed this concept quantitatively, casting it in the form of differential equations. This enabled the prediction of critical properties with accuracies comparable to series expansion methods [61]; Wilson's work was (and still is) important in many other areas – for example, it provided a resolution to the Kondo problem in condensed matter physics. High temperature series expansions are based upon the idea of expanding the expectation value of some observable about the $T = \infty$ state; a graphical representation naturally emerges [17], and graphs can be evaluated to, in princple, arbitrary order, to obtain highly accurate results after summing. The analysis is, however, difficult, so precise results are not available for all quantities for all models of interest. Discussion of Monte Carlo methods, the third method listed, we defer to Chapter 6.

Below the critical point, where there is a spontaneous magnetisation, phase separation occurs, and the most probable states are those with macroscopically large regions of $+1$ or -1 spins, separated by interfaces. In the ferromagnetic picture, these are regions with opposite magnetisation, separated by domain walls. As temperature decreases, the magnetisation increases, and as $T \to 0$, $m_{\mathrm{sp}} \to \pm 1$, depending on the sign of the field as it goes to zero in the limit Eqn. (3.8). Thus at very low temperature the system is nearly all 'up' or 'down'. As the temperature is increased up to near T_c, the magnetisation vanishes

as a power law: $m_{\rm sp} \sim |T - T_c|^{\beta}$: the majority of one species becomes smaller. For the $2d$ Ising model, $\beta = 1/8$ (independently of the lattice type, as for all critical exponents – an example of universality). As the critical point is approached, spatial correlations grow, and right at T_c, correlated regions of up and down spins exist at all length scales: that is, the bulk correlation length $\xi_b \to \infty$ as $\xi_b \sim |T - T_c|^{-\nu}$, where ν is another (positive) critical exponent. In fact, the various critical exponents are related via scaling relations, and the correlation length divergence is responsible for the susceptibility and specific heat divergences. This is because ξ_b is the characteristic length scale in the system, and controls the singular part of the free energy. For fuller explorations of scaling and critical properties the reader is referred to Refs. [17, 31, 53, 62].

3.3 Conserved order parameter Ising model

An important specialisation of the "vanilla" Ising model, and one which we shall make great use of later, is the *conserved order parameter* (COP) Ising model. As the name implies, this variant constrains the magnetisation to be a chosen constant. Thus the ensemble of states available to the system is restricted – for example, if one chooses $m = 0$, then only states where there are equal numbers of up and down spins are permitted. The external field B, which couples to the spins in the Hamiltonian (3.1), now simply contributes a constant term when $\sum_i \sigma_i$ is fixed, so we can ignore it.

The conserved order parameter Ising model also exhibits a phase transition [63], at the same critical temperature as the normal model, but due to the constraint, there can be no overall magnetisation. Thus, below T_c the system again phase separates, but as $T \to 0$, the different regions become larger (and there are thus fewer individual islands of one sign). This is because the internal energy cost of interfaces, $2J$ per unit length relative to an unbroken bond, becomes increasingly important at low T, relative to entropic contributions to the free energy.

Why should one care about the COP Ising variant? We answer this question in the next section, where the lattice gas isomorphism of the Ising model is introduced.

3.4 Mappings of the Ising model: relevance outside magnetism

The other applications of the Ising model alluded to at the beginning of this chapter may be reached by simple mappings of variables from the magnetic language to the one of interest. We first consider the *lattice gas* equivalence, which will be of use later in making contact with fluid interfaces. Let us define a lattice gas model, forgetting for the moment any connection to the Ising model. We may allow the lattice to be in principle of arbitrary dimension and type, although we will only be concerned with $2d$ square and $3d$ simple cubic lattices. Each site of the lattice may be occupied by a single particle ($n_i = 1$), or unoccupied ($n_i = 0$), where n_i is the occupation number of the site, and defines its state. Let there be N sites in all. We imagine that the particles will interact via two-, three-, and higher body potentials, as well as experience an external field. This may be represented by the Hamiltonian

$$H_{\mathrm{LG}} = \sum_{i}^{N} U_{\mathrm{ext}}(i) n_i - \frac{1}{2} \sum_{i,j}^{N} U_2(i,j) n_i n_j + \ldots, \tag{3.9}$$

where $U_{\mathrm{ext}}(i)$ is the external potential, U_2 is the pair interaction, the ellipses represent three-body and higher interactions, and the half prevents double-counting. We now make the assumption of nearest-neighbour interactions, so that $U_2(i,j) = U_2 = \text{const.}$ if i and j are nearest-neighbours, and $U_2(i,j) = 0$ otherwise. We also neglect three-body and higher interactions, to arrive at

$$H_{\mathrm{LG}} \approx \sum_{i}^{N} U_{\mathrm{ext}}(i) n_i - U_2 \sum_{\langle ij \rangle} n_i n_j, \tag{3.10}$$

where the second sum is now over nearest-neighbours. With this simplified Hamiltonian, we can make an exact equivalence with the Ising model (comparing with (3.1), it already has the same form). We define

$$\begin{aligned} n_i &= \frac{1}{2}(\sigma_i + 1) \\ \Rightarrow \sigma_i &= 2n_i - 1, \end{aligned} \tag{3.11}$$

so that a particle is equivalent to a '+' spin state, and a hole to a '-'. Substituting (3.11) into (3.10), we have

$$\begin{aligned} H_{\mathrm{LG}} =& \frac{1}{2}\sum_i(\sigma_i+1)U_{\mathrm{ext}}(i) - \frac{U_2}{4}\sum_{\langle ij\rangle}(\sigma_i\sigma_j+1+2\sigma_i) \\ =& \text{ const.} + \frac{1}{2}\sum_i \sigma_i U_{\mathrm{ext}}(i) - \frac{U_2}{4}\sum_{\langle ij\rangle}\sigma_i\sigma_j - \frac{U_2}{4}\frac{2}{2}z\sum_i\sigma_i, \end{aligned} \tag{3.12}$$

where z is the coordination number of the lattice; for example a $2d$ square lattice has $z = 4$. A factor of $1/2$ in the last term prevents double-counting after converting the pair sum to a single one. The constant terms not involving the spin variables just set the zero of energy, and will just introduce a multiplicative factor into the partition function. In (3.12), the term involving U_{ext} represents a field varying at each lattice site. For simplicity, we now set $U_{\mathrm{ext}} = 0$. The grand canonical partition function for the lattice gas is then

$$\begin{aligned} \Xi(T,\mu,N) =& \sum_{\{\sigma_i\}} \exp\left[-\beta(H_{\mathrm{LG}}(\{\sigma_i\}) - \mu N_p)\right] \\ =& \sum_{\{\sigma_i\}} \exp\left[-\beta\left(-\frac{U_2}{4}\sum_{\langle ij\rangle}\sigma_i\sigma_j - \frac{U_2 z}{4}\sum_i\sigma_i - \mu\sum_i\frac{1}{2}\sigma_i + \text{const.}\right)\right] \\ =& \sum_{\{\sigma_i\}} \exp\left[-\beta\left(-J\sum_{\langle ij\rangle}\sigma_i\sigma_j - B\sum_i\sigma_i\right) + \text{const.}\right] \\ =& Z_{\mathrm{Ising}} \times \text{const.} \end{aligned} \tag{3.13}$$

where μ is the chemical potential, and N_p is the number of particles in a given configuration. The outer sums are over all states (all numbers of particles from $N_p = 0$ to $N_p = N$ are included). In the third line we have identified

$$\begin{aligned} J &\equiv U_2/4 \\ B &\equiv zU_2/4 + \mu/2, \end{aligned} \tag{3.14}$$

and thus found that the *grand canonical* partition function of the lattice gas is equivalent to the *canonical* partition function of the Ising model. The phase transition in the Ising model occurs at $B = 0$, or in the lattice gas language at a chemical potential of $\mu = -zU_2/2$.

We can also say that the lattice gas in the *canonical* ensemble is equivalent to the COP Ising model. In the canonical ensemble, $N_p = \text{const.}$, so that after mapping, the terms involving $\sum_i \sigma_i$ are also constants. Then the only non-constant term is the spin-spin

interaction term, and

$$Z_{\mathrm{LG}}(T,N,N_p) = \sum_{\{\sigma_i\}_{N_p}} \exp\left[-\beta\left(-J\sum_{\langle ij\rangle}\sigma_i\sigma_j + \text{const.}\right)\right], \tag{3.15}$$

where the configurational sums only include the states corresponding to the constraint of fixed N_p. This is just the partition function for the COP Ising model, to within a constant factor. All this demonstrates the primary use of the COP Ising model - we can use it as an *idealised liquid-gas type system in the canonical ensemble.* For example, one can simulate a COP Ising model below its critical temperature, and interpret the results in terms of a phase separated liquid-gas system. The results may be viewed in either the magnetic or lattice gas "language" interchangeably; the simplicity of the fundamental mapping (3.11) makes conversion of observables quite transparent. For example, the particle-particle spatial (disconnected) correlation function is

$$\langle n_i n_j\rangle = \frac{1}{4}(\langle\sigma_i\sigma_j\rangle + 1), \tag{3.16}$$

differing from the disconnected spin-spin correlator only by a constant.

In the thermodynamic limit, statistical ensembles become equivalent – this is because the relative fluctuation in an observable reduces as the number of degrees of freedom in the system increases [17]. For example, in the grand canonical lattice gas, the fluctuations in the particle number N_p scale as $\sqrt{\langle(N_p - \langle N_p\rangle)^2\rangle}/\langle N_p\rangle \sim 1/\sqrt{N}$. Thus the canonical and grand canonical lattice gas, and consequently the normal and COP Ising models, become equivalent in the thermodynamic limit. In simulations, this limit is of course inaccessible, and the inequivalence in finite systems can have important effects, as we will see later.

The appeal of lattice gas models, such as the Ising lattice gas just described, lies in the relative simplicity compared to a continuum system – particles may only sit at discrete positions. Of course, if one wishes to describe, say, a particular liquid-gas system in detail, this imposition makes the model rather unrealistic. However, when looking at more general properties, such as critical behaviour, phase separation, or as we shall do, fluctuations of an interface, a simple generic system can be an advantage – we can hope to find features common to many systems. This "universality-oriented" approach is of course a commmon theme in condensed matter physics – we wish to discover the *essential* features underlying any particular phenomenon, so that we can understand a seemingly diverse range of systems under a single physical description.

The Ising Hamiltonian may also be used to describe binary alloys, systems of two types of metal atoms, A and B, in a lattice structure. Sites may be occupied by either an 'A' atom, or a 'B' (allowing empty sites corresponds to a three-state system, so would not be equivalent to the Ising model, but rather a Blume-Capel model – this will be discussed later). The site variables are mapped to Ising spin variables, and similar arguments apply for the Hamiltonian as in the case of the lattice gas. A classic example of this type is β brass, an alloy of copper and zinc. This exhibits an Ising transition from an ordered state, where the Cu atoms sit on one (cubic) sublattice of a bcc lattice, and the Zn on the other, to a disordered state where they are equally likely to sit on either sublattice. Aside from these *exact* mappings, the Ising model has been used in many other non-magnetic contexts. One interesting recent example [64] is a study of networks within the brain, where correlation networks extracted from magnetic resonance imaging scans of human brains were compared to networks constructed from simulation data of the $2d$ Ising model. The authors found that many properties of the networks were "indistinguishable" for the choice of simulation temperature $T = T_c$. This is quite striking – the Ising model is rather simple, yet shows the same behaviour at criticality as the hugely complex human brain. As the authors point out, the collective behaviour of the $\sim 10^{10}$ neurons is the important factor, rather than the finer biological details – this is the same idea as *universality* in statistical physics. Many more examples of the relevance of the Ising model outside its original field exist, from driven lattice systems [65] (the subject of Chapter 4), to applications in quantum chromodynamics (QCD) [66], to more outlandish and inter-disciplinary connections such as immunological networks [67].

3.5 Ising interfaces

In this work we are specifically concerned with the properties of the planar interface of a phase-separated, conserved order parameter, Ising system. The first question is – how can such an interface be induced? The answer lies in the choice of boundary conditions on the edges of the lattice. Taking the example of a COP Ising model with $-1 < m < +1$ and $T < T_c$ on a $2d$ square lattice, if all four boundaries are periodic, and the system size is sent to infinity in both directions, then there is no preferred direction for an interface to lie along, so all orientations will occur. However, if we impose *walls* of fixed spins at, say, the top and bottom edges of the system, then we create a strong energetic bias against

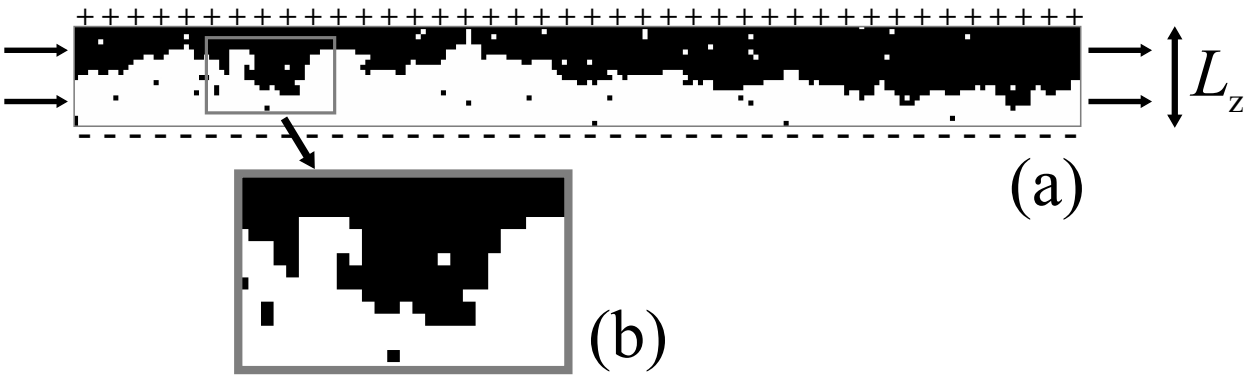

Figure 3.1: (a) A phase-separated Ising system (simulation snapshot) confined between walls of opposing spins at separation L_z. The x boundaries are periodic. (b) Zoomed section of the interface: a "beak-like" overhang, and "bubbles" are visible.

configurations with contact of many spins of opposite sign to the wall, with it. If one wall consists of all '+' spins, and the other all '−', then the system will separate into two phases divided by a single planar interface, lying horizontally on the average – see Fig. 3.1a. Note that in the figure, the '+' phase lies in the upper half of the system – strictly, given the lattice gas mapping '+' → particle, this means that the high density phase is in the upper half. However, since the mapping may be trivially swapped around, restoring the natural order, this is really a matter of taste. We will adopt the convention of Fig. 3.1a in the simulation models. Additional interfaces would cost energy $2J$ per unit horizontal length, so in equilibrium they are not favourable. (We note that if the walls are of the same sign, there will be a minimum of two interfaces). The other boundaries, perpendicular to the average interface plane, are still assumed to be periodic. Indeed, this is the choice made for the simulations presented later. In this way all parts of the interface are able to move in the vertical direction (although the constraint $m = \text{const.}$ prevents the free "wandering" of the whole interface that is possible for non-conserved systems. This is relevant in the context of choice of simulation dynamics, which we discuss later in Chapter 6; see also [68]). Another approach is to *pin* the interface by introducing walls of fixed spins at the left and right edges as well, where each wall is partly composed of '+' spins and partly of '−'. This additional energetic restriction may be used to force the interface to have a non-zero average tilt angle. For the present work, where drive and particle flux will be present, the periodic choice is more suitable, as should become clear when we explain the model in Chapter 7.

Figure 3.2: A discrete Gaussian or SOS-type configuration. The overhangs and bubbles present in the full Ising model are not present, allowing for an unambiguous definition of the interface height.

3.5.1 The solid-on-solid and discrete Gaussian models

Investigating interfaces in the Ising model is made problematic by its nature as a microscopic model, where the degrees of freedom describe the whole system, not just the interface. Of course, this feature is an advantage in that the interface is not artificially "baked-in", but appears as result of the phase behaviour of the model. However, not only is a fully microscopic model hard to deal with analytically, but also there is no immediate unambiguous definition of the dividing surface between phases for a given system configuration. Even though, in a system with appropriate boundary conditions as described above, on a large scale there are clearly two "bulk" regions with an interface in between, there are always "bubbles" or "intruders" of one phase in the other for $T > 0$. Although there will be a continuous dividing surface (we consider a $3d$ system) of broken bonds midway between the upper and lower walls, this can possess "overhangs" where the dividing surface passes a point (x, y) in the lateral plane at two z values – see Fig. 3.1b. This prevents the vertical position of the surface from being a single-valued function of $\mathbf{r} = (x, y)$, so one cannot use it to define a height function $h(x, y)$. Of course, one can *coarse-grain* the Ising system to be able to define such a function, and indeed we will do this in the simulations described later, but there is also merit in investigating limits of the Ising model where an interface-height description arises naturally.

The *solid-on-solid* (SOS) model may be obtained as the infinite vertical coupling limit of the *anisotropic* Ising model. The latter is the same as the isotropic Ising model introduced earlier, but the coupling J is now allowed to vary in the different axis directions. For current purposes, we let the couplings in the lateral (interfacial) plane be equal, and be denoted by simply J; in $d = 3$, this means that couplings in x and y directions are

the same. We denote the coupling in the perpendicular direction by J_z. The Hamiltonian is then as before, Eqn. (3.1), but with J replaced by a direction-dependent coupling J_{ij}. Now we let $J_z \to \infty$. What are the consequences? Firstly, the ground-state ($T = 0$) energy becomes infinite, but this can simply be subtracted since it is a constant [69]. Secondly, configurations with "intruders" become disallowed, since the presence of extra broken z-bonds implies an infinite free energy cost. Similarly, overhangs are forbidden – in all, we have enforced the system to have a single-valued integer height function $h(\mathbf{r})$ at all lateral positions $\mathbf{r}$; formally, the bulk critical temperature is infinite in the SOS limit. An example configuration (taken from an MC simulation) is given in Fig. 3.2. Effectively, we have reduced a d-dimensional Ising model of spins σ_i to a $(d-1)$-dimensional problem of integer height variables (columns) h_i. The Hamiltonian for this system can be written

$$H_{\mathrm{SOS}}\left[\{h_i\}\right] = \frac{J}{2}\sum_{\langle ij\rangle}|h_i - h_j| - B\sum_i h_i, \tag{3.17}$$

where the first term counts the energy cost of broken bonds due to height differences of neighbouring columns. Hereafter we will set $B = 0$, since as in the Ising model, we will not consider the effect of a static external field. In a simulation, the effect of such a field is to grow or shrink the heights as a function of time, and thus move the interface position. We will briefly discuss some work on such non-equilibrium SOS interfaces in Chapter 6.

A closely related model is the *discrete Gaussian* (DG) model, whose Hamiltonian reads

$$H_{\mathrm{DG}}\left[\{h_i\}\right] = \frac{J}{2}\sum_{\langle ij\rangle}(h_i - h_j)^2 - B\sum_i h_i, \tag{3.18}$$

differing only by the replacement of the moduli of the height differences by their squares. As the name implies, this yields Gaussian configuration probabilities, which are analytically convenient. One expects the qualitative features of the DG and SOS models to be the same at low temperatures [70, 71], since the energy costs of height differences 0, ± 1 are the same in both models, and at low temperatures, height differences are typically small.

The DG model is essentially the discrete version of the capillary wave model, discretized in both lateral positions and heights; thus we expect it to display many of the same characteristics. One important exception is the presence of a finite-temperature *roughening transition* in the $2d$ DG (and SOS) models, which does not occur in continuum. The roughening transition will be discussed Sec. 3.5.4. Note that allowing a continuum of height

values gives the *unweighted Gaussian model* [71], which does not display a roughening transition.

3.5.2 Two-dimensional systems

For two-dimensional Ising systems with an interface, several exact results are available, since the transfer matrix technique may be applied. The underlying idea in the transfer matrix approach is to write the partition function as a trace of a product of matrices:

$$Z = \operatorname{Tr} V^L, \tag{3.19}$$

where V is a matrix, and L is the linear dimension of the lattice (which will go to infinity in the thermodynamic limit). Using the properties of matrix algebra, the trace of V^L may be expressed as a sum of the L^{th} powers of the eigenvalues. Then in the thermodynamic limit $N \to \infty$, only the largest eigenvalue contributes, so the problem of finding the partition function is reduced to the task of finding the largest eigenvalue of V. Of course, this is certainly not trivial! (V is not symmetric, and may be infinite-dimensional). However, the problem is tractable, at least for certain cases. A useful and elegant method is to cast the problem in a quantum-mechanical way, and apply known transformations from that field (such as the Jordan-Wigner transformation, which converts the problem into an interacting fermion problem). This "spinor approach", see for example Schultz *et al.* [72], was used in Refs. [73–75]; a very approachable account may be found in Ref. [17].

The case of all boundaries being '+' spins was solved using the transfer matrix technique by Abraham and Martin-Löf [73] some time ago; this solution was later adapted [74, 75] to the case of *opposing* upper (+) and lower (−) walls at a finite separation, with the lateral dimension infinite ("strip-like" geometry). Specifically, let the x and z directions be parallel and perpendicular to the walls, respectively. Let the length of the system in the x-direction be L_x, and let the wall separation be L_z. In Ref. [75], the magnetisation profile $m(z)$ and interfacial width w were calculated exactly for semi-infinite strips, that is, $L_x \to \infty$ with L_z finite, for several values of L_z and temperature. This geometry creates a *confined* system, where the walls play an important role. In fact, in theoretical work the more general concept of a *surface field* is used – fields which act on the surface layers of the lattice to bias the spins there in a particular orientation. Fully fixed walls of opposite sign then correspond to infinite surface fields of opposite sign. Varying the surface fields allows one to investigate wetting and interface localization-delocalization transitions

[7, 45, 76, 77]. Note that this system is quasi one-dimensional; since the lower critical dimension of the Ising model is two, the strip has no *true* phase transition. Rather, below the bulk critical temperature, the system is in the "soft-mode" phase ($T > T_w$, recalling the discussion in Sec. 2.3.3; $T_w = 0$ for fixed walls) predicted by Parry and Evans [38] with a $+-$ interface midway between the walls.

For low temperatures, the profiles in Ref. [75] were found to agree well with SOS model results, as expected, since the SOS model as defined above should describe low-temperature Ising interfaces well. Profiles are characterized by values close to ± 1 near the walls, with a smooth, monotonic variation in between. For low temperatures, the profiles are sharp, since fluctuations are small, and the magnitude of the bulk spontaneous magnetisation $m_{\rm sp}$ is large. As temperature increases, the profiles become more diffuse. This is due to the long-wavelength capillary-wave fluctuations discussed earlier, which being thermal in nature, grow in strength as temperature is increased. The interfacial width – defined earlier as the r.m.s. interface height, $w = \sqrt{\langle h^2 \rangle}$, increases in parallel; the local and global position of the interface "wanders" between the two walls, exploring the whole region. Indeed, the scaling plots in Ref. [75] indicate that $w \propto L_z$ in confined two dimensional Ising systems – the interface intrepidly explores all perpendicular space. This result is the same dependence we obtained in the confined version of CWT, see Eqn. (2.35), providing support to the assertion that capillary waves are the dominant contribution to the interfacial behaviour above microscopic scales. We note that the width may be alternatively defined as the second moment of the gradient of the profile (as in fact was done in Ref. [75]; this definition requires no coarse-graining – see Sec. 9.3.2), but as we will see later, which definition we use has only a minor quantitative effect on simulation results for nearly all quantities. The r.m.s. height definition is perhaps the more easy to picture physically.

The finite-size scaling relations for the magnetisation profile are also of interest. For an equilibrium fluid or Ising magnet confined between two walls, Fisher and de Gennes [78] proposed a scaling relation for the density or magnetisation profile. For fixed walls of spins, and zero bulk field, this reads [75]:

$$m(z, T, L_z)_{\rm eq} = m_{\rm b}(T)\tilde{\mathcal{M}}_{\rm eq}\left(\frac{z}{\xi_b(T)}, \frac{L_z}{\xi_b(T)}\right) = m_{\rm b}(T)\mathcal{M}_{\rm eq}\left(\frac{z}{L_z}, \frac{L_z}{\xi_b(T)}\right), \qquad (3.20)$$

where $\xi_b(T)$ is the bulk correlation length as before, and $m_{\rm b}(T)$ is the spontaneous magnetisation for a bulk (infinite in all directions) system. $\tilde{\mathcal{M}}_{\rm eq}$ and $\mathcal{M}_{\rm eq}$ are finite-size scaling

functions: $\mathcal{M}_{\rm eq}(u,w)$ is obtained from $\tilde{\mathcal{M}}_{\rm eq}(\tilde{u},w)$ by changing the first scaling variable $\tilde{u} = uw$. We have appended the various functions with "eq" subscripts for consistency with later notation, although not necessary in this purely equilibrium context. Eqn. (3.20) implies that the shape of the magnetisation profile depends on a common scaling function of two variables, which are the perpendicular coordinate z, and the wall separation L_z, in units of the bulk correlation length. The temperature enters the scaling variables only through its influence on $\xi_b(T)$. The shape of the scaling function (and thus the profile) can be altered by changing the wall separation at fixed T or by changing the temperature at fixed L_z (or of course, varying both simultaneously). For semi-infinite $2d$ strips with opposing walls, scaling of the form (3.20) was found [75]. We will later construct an analogue of this finite-size scaling form in driven, *non-equilibrium* Ising systems.

The correlation length along the interface, $\xi_\parallel$, has also been calculated for $2d$ Ising systems [74]. Below T_c and away from the critical regime, $\xi_\parallel \sim L_z^2$. Combining this with the above result for the width, we have $w^2 \sim \xi_\parallel$. These relations between the width, lateral correlation length, and wall separation are the same as that predicted by capillary wave theory, see Eqns. (2.18) and (2.34), and also from the SOS model [38]. This result, together with the agreement of the dependence of w on L_z, shows that for low temperatures, away from criticality, the full Ising model exhibits the same large scale behaviour as that of a simple interface Hamiltonian – capillary wave theory. This is an excellent endorsement as to the qualitative correctness of CWT, and shows that in confined phase-separated Ising systems long-range CW-type fluctuations are dominant for this non-critical temperature regime. This makes sense – as discussed previously, CWT does not treat correlations on length scales $\mathrm{O}(\xi_b)$ or smaller, so should not be expected to describe the critical region, where ξ_b becomes large. Equally, the SOS description cannot apply there, since the SOS model has no equivalent critical point. For further comparison of SOS and CWT results with transfer matrix calculations for the Ising model, see Refs. [74, 75].

3.5.3 Three-dimensional systems and tests of predictions

Equivalent exact results for confined interfaces in the $3d$ Ising model are not available, since as mentioned above, the approach used in $2d$ fails [17]. However, progress can be made via interface Hamiltonians, and by studying simpler lattice models (e.g., SOS). Studies of discrete random surface models (including the SOS) [79] show rather different behaviour to that in two dimensions. Instead of wholescale wandering, the interface interacts with the

walls via "needle-like" structures. These needles or spikes allow the interface to explore more configurations, increasing the entropy, and thus lowering the free energy. Their creation costs internal energy, and a balance is reached at equilibrium. A rigorous analysis gives $w^2 \propto L_z$ and $L_z \propto \ln \xi_\parallel$, so that $w^2 \propto \ln \xi_\parallel$, in agreement with CWT, see Eqns. (2.31) and (2.32).

These predictions can, and have been, verified by Monte Carlo simulations. Kerle *et al.* [80] analyzed data from $3d$ Ising simulations with opposing surface fields, finding agreement with the theoretical predictions for a good range of values of L_z. Simulation studies of the $2d$ Ising system [7] have also found good agreement with CWT and the exact results described above. What about more realistic model systems, or indeed real systems? Refs. [36, 80] presented the first experimental evidence for the predicted dependence of the interface width on film thickness, in a binary mixture of copolymers. Binder *et al.* [37] carried out Monte Carlo simulations of polymer blends, finding agreement with CWT at large length scales. Vink *et al.* [81] verified CWT predictions at large length scales in simulations of the Asakura-Oosawa (AO) model of colloid-polymer systems, and observed the breakdown of CWT at short length scales, where bulk fluctuations become important.

3.5.4 The roughening transition

So far we have described the behaviour of interfaces (be they in fluids or in lattice models), on large length scales $\gg \xi_b$, as being governed by capillary-wave fluctuations – that is, elastic distortions of the interface, controlled by surface tension. When this is true, the predictions of CWT hold – in particular, in the limit of infinite system size and zero gravity (or other confining field), the interface width diverges; the system is said to be in the *rough* state. However, for certain systems it is now known that there is another regime, the *smooth* state, where the interfacial width is always finite, and that a transition temperature known as the *roughening temperature* T_R delimits the phases. What sort of systems exhibit the roughening transition? Our analysis of *continuum* capillary wave theory earlier showed no evidence of any transition point; the dependence of the width on temperature was smooth, and the state was always rough. Indeed, liquid-gas systems, which are also continuous, do not exhibit a roughening transition; rather, only systems which are spatially *discrete* show roughening [4], such as the Ising model, or its idealisations, the SOS and DG models. Dimensionality is also crucial – the Ising model only has a finite T_R for $d = 3$ (and therefore a $2d$ SOS model); in $d = 2$, the interface is always rough. For $d > 3$ the

interface is always smooth (as it is in CWT [27]).

The idea of a roughening transition originated with Burton and Cabrera [82, 83], in the context of crystal growth. Their argument, which we give below (for a nice summary see also Ref. [70]), is physically appealing and plausible – by considering layers of the simple cubic $3d$ crystal lattice as $2d$ square-lattice Ising systems, they argued that a transition should occur near the critical temperature T_c^{2d} of the $2d$ Ising model, which is approximately $(1/2)T_c^{3d}$. Specifically, imagine an anisotropic (see Sec. 3.5.1) $3d$ Ising system on a simple cubic lattice at low temperature; then the interface will typically be not too far from its flat ground state. The elementary excitations consist of a spin of the lower phase appearing in the layer just above the mean interface plane, or a spin of the upper phase appearing just below (of course, one can also frame this in the lattice-gas language, as appropriate for crystal growth). The associated energy cost is $4J$, where J is the coupling constant in the x and y directions – quite significant. Within either of these layers, the interactions are just those of the $2d$ square-lattice Ising model. If we increase the temperature, when we pass T_c^{2d}, the magnetisation vanishes, so that in each of the two layers there are equal numbers of '+' and '-' spins on the average. At this point, nucleating a spin on either layer ceases to cost any free energy, and the interface is no longer smooth; the width diverges.

This argument is clearly not exact – the approximation of independent $2d$ Ising layers breaks down before the roughening transition is reached. However, it is consistent with the observation that $2d$ Ising interfaces are always rough – the interface would be viewed as a $1d$ Ising model, for which there is no critical point, and $\langle m \rangle = 0$ for any $T > 0$. The argument also suggests that the coupling in the z-direction, J_z, should not matter, since it did not appear in the energy cost for creating excitations [70]. This naturally leads one to study roughening in the simpler SOS and DG models, where $J_z \to \infty$ (see Sec. 3.5.1); indeed this is where much effort has been directed.

The existence of the roughening transition is now established for the $3d$ Ising and $2d$ SOS and DG models via a combination of theoretical and simulation work. It turns out that the transition is of the Kosterlitz-Thouless [84] class, also exhibited by the XY lattice model. Indeed, the SOS and XY models may be related by a duality transformation [85]. For some time, however, it was not clear whether the transition really existed. Weeks *et al.* [86] performed low-temperature expansions of the $3d$ simple cubic Ising model, finding a divergence of the interface width at a temperature slightly above T_c^{2d}. Chui and Weeks

[87] used the renormalization-group methods of Kosterlitz and José *et al.* [88] on a discrete Gaussian model to find the roughening transition and study its dynamics. Monte Carlo studies of roughening in the SOS and DG models were carried out by Swendsen [70], providing good evidence for its existence; however, MC simulations are tricky due to finite-size corrections which only decay logarithmically with increasing system size [89]. More recent studies have attempted to overcome this problem, and accurate values of T_R in the $3d$ simple cubic Ising system are now available [89, 90]: $T_R \approx 0.54 T_c^{3d}$.

Apart from the interfacial width, what are the other physical properties of the roughening transition? The lateral correlation length $\xi_{\|}$ is another quantity of interest: it is finite for $T < T_R$, and diverges exponentially with temperature as $T \to T_R$ [4, 91]. In a renormalization-group (RG) approach, where one considers successive rescalings to larger and larger length scales, on scales smaller than $\xi_{\|}$, the interface is actually *rough*, and free to fluctuate. On scales $> \xi_{\|}$ the interface is smooth; in the RG picture, the strength of the "lattice potential" which inhibits fluctuations diverges under iteration of the RG equations. The roughening temperature corresponds to a fixed point of the RG "flow" (differential) equations. More details of this approach may be found in Ref. [4], and for more general RG ideas see Ref. [31]. The roughening transition will be relevant in this thesis when we study the $3d$ driven Ising model; in particular, the interplay of the action of the drive with the roughening transition is interesting, although the tricky nature of the transition makes this challenging.

Chapter 4

Driven lattice models

4.1 Introduction

In the previous two chapters we have focused on *equilibrium* systems, where the Gibbsian statistical-mechanical framework may be applied. The key point is that the probability distribution of the states in an equilibrium system is known – the probabilities are proportional to the Boltzmann factor $e^{-\beta H}$, where H is the Hamiltonian, as explained in Sec. 3.2. By contrast, for non-equilibrium systems, the distribution is not generally known, and there is no general prescription for finding it. This immediately makes the statistical mechanics of non-equilibrium systems both difficult and interesting!

This sets up a daunting problem – we should ask what a sensible approach to investigating non-equilibrium systems might be. Firstly we should recognise the difference between systems which are evolving, and those in a non-equilibrium steady state. The former includes systems which are heading towards a final equilibrium state (having, for example, been quenched from some higher temperature), as well as those which are not, and may either attain a non-equilibrium steady state distribution, or evolve indefinitely. The latter is thus a restricted class, where the system can never relax to equilibrium, but where instead the (generally unknown) probability distribution has become time-independent. In this thesis we will be almost exclusively concerned with this regime (in simulations we also have access to the evolutionary behaviour, when desired).

An overarching aim must be to try and the find *universal* features which seemingly disparate systems share, which may eventually help to unearth some underlying statistical-mechanical framework, *à la* Gibbs. Therefore it seems wise to look at models which are

simple, with "just enough" features to be non-trivial; also, it would be useful to be able to take an "equilibrium limit" and return to a known model. The Katz-Lebowitz-Spohn (KLS) model [65, 92], named after its inventors, conforms to these ideals, and has therefore been extensively studied from its inception right up to the present day. Indeed, the main model we investigate in this thesis is a slight generalization of the KLS model, and much of the next few sections will aid its later introduction.

4.2 The Katz-Lebowitz-Spohn model

The KLS model is a non-equilibrium version of the conserved order parameter Ising lattice gas, which we have discussed in Sec. 3.4. Thus most of the model is already familiar: the Hamiltonian is just the Ising one, Eqn. (3.1), and we impose the restriction of a fixed overall magnetisation, as discussed in Sec. 3.3: this means we can take the static magnetic field $B = 0$, since this term is a constant in the COP Ising model. As a reminder, in the lattice gas language, we have fixed the overall particle number or total density, and work in the canonical ensemble.

The new feature is an external driving field, which affects the transition rates between different states of the system by biasing the movement of particles in a particular direction. For suitable boundary conditions this creates a particle current and drives the system into a non-equilibrium steady state. The KLS model is an example of a "driven diffusive system", a term frequently encountered in the literature: the competition of diffusive and driven dynamics is a key feature. Although designed primarily to be simple and minimal, the KLS model does bear a relationship to real physical systems. Part of the original motivation for the model was to describe superionic conductors [93] in the presence of a static electric field. In these materials, an abundance of vacant lattice sites causes one or more species of ion to be highly mobile, leading to large conductivities. In a static field the ions create a constant current, which the KLS model mimics. Additionally, in superionic systems the conductivity can be strongly temperature-dependent, which points to the existence of an order-disorder phase transition. Thus, a driven model with a phase transition – the KLS model – seems to be a good candidate for describing such materials. However, we stress that this connection is only really an aside (for our purposes): these superionic materials are of course much more complex than a simple Ising lattice gas, and many display *repulsive* interactions between ions, unlike the standard (attractive) KLS

model [93, 94]. We now discuss some relevant general theory for non-equilibrium lattice systems.

4.2.1 Master equations, transition rates and detailed balance

Since the external field in the KLS model will enter through transition rates, we need a dynamical description of statistical-mechanical systems. Such a description may be provided by writing a *master equation* [55, 94] which relates the probabilities of states and the transition rates between them:

$$\frac{dp_\mu}{dt} = \sum_\nu \left[R_{\nu\to\mu}\, p_\nu - R_{\mu\to\nu}\, p_\mu \right]. \tag{4.1}$$

Here the p_μ are the probabilities of individual microscopic configurations, and the $R_{\mu\to\nu}$ are the transition rates. Eqn. (4.1) says that the rate of change of probability of a state μ is equal to the net current into or out of it; the first term in the sum is the flux into μ, the second is the outward flux. Of course, since the p_μ are probabilities, they should be appropriately normalised: $\sum_\mu p_\mu = 1$.

A steady state is defined by the condition that the left hand side of (4.1) is zero for all states μ, so that there is no net current into or out of a state. So far this formalism applies to both equilibrium and non-equilibrium steady states. If the system is to be in equilibrium, then the probability distribution must be Boltzmann, so that

$$\frac{p_\mu}{p_\nu} = e^{-\beta(H_\mu - H_\nu)}, \tag{4.2}$$

where H_μ is the Hamiltonian evaluated in state μ. The steady state condition and the correct probability distribution may be ensured by imposing the condition of *detailed balance* [54, 55, 94]:

$$\frac{R_{\nu\to\mu}}{R_{\mu\to\nu}} = \frac{p_\mu}{p_\nu} = e^{-\beta(H_\mu - H_\nu)} \qquad \text{for all pairs } \mu, \nu. \tag{4.3}$$

The first equality is just the condition that each term in the sum in Eqn. (4.1) is zero; clearly this is sufficient to make the LHS of (4.1) zero also. The second equality uses the known probability ratio (4.2); therefore if the rates obey this, the system will reach equilibrium (here we assume ergodicity holds [54] for the system of interest). Detailed balance says that not only is the overall current into or out of a state zero, but that this is also true for all *individual* pairs of states – a strong condition!

For a non-equilibrium steady state, the probability distribution is not known, and (4.2) does not hold. We may still choose the *rates* to satisfy the exponential ratio in (4.3), since this makes contact with equilibrium rates, and furthermore will have the correct equilibrium limit. Indeed, this is done in the KLS model, as outlined in the next section. Before moving on, we note that the steady state master equation is really a set of linear equations, so if we specify the rates $R_{\mu\to\nu}$ then we could in principle solve this system for the probabilities p_μ. The problem is that this is not computatationally practical except for very small systems (in terms of number of states), in the same way that evaluating the partition function directly is not possible. This direct, exact, approach can however be useful for checking results from other methods, such as simulations.

4.2.2 Microscopic dynamics

The above discussion is general in the sense that we have not specified *physically* how a system transitions from one state to another; we have only given the mathematical rates. Some dynamics must be chosen, and in doing so we must ensure that the conserved magnetisation condition is never violated.

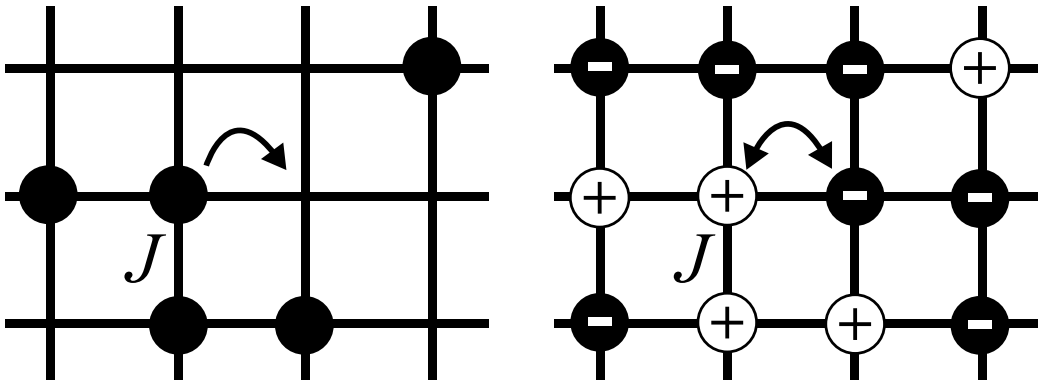

Figure 4.1: Illustration of Kawasaki dynamics on a $2d$ square lattice, in (a) lattice gas and (b) Ising spin representations. In (a), the particle hops to the right, breaking two bonds and creating one, with net cost $+U_2$, in the notation of Sec. 3.4. In (b), a '+' and a '−' spin exchange positions; the net cost is $+4J$. Since $J = U_2/4$, the energy changes are the same, as they must be.

The dynamics used in the standard KLS model are Kawasaki-type *exchange* dynamics [55, 95], which are illustrated in Fig. 4.1. An elementary transition consists of the exchange of two nearest-neighbour spins on the lattice; in the lattice gas picture, this corresponds

to a particle moving to a nearest-neighbour unoccupied site. Clearly this satisfies the magnetisation-conservation condition. Note that since *two* spins move in a Kawasaki exchange, the transition rates will depend on the nearest neighbours of both spins, via the energy change $H_\mu - H_\nu$ in (4.3). An important feature is that particles only move *locally*; they do not "teleport" across the lattice – this helps to make the model somewhat more physically realistic on a microscopic level than it would be with non-local dynamics. Adding the effect of the driving field (see below) is also most natural with local exchange dynamics.

The issue of choice of dynamics is most relevant in Monte Carlo simulations, and we will return to it later in Chapters 6 and 7, where we will also show the implementation of Kawasaki dynamics in a simulation.

4.2.3 Driving field and rates

The driving field in the KLS model alters the rates $R_{\mu\to\nu}$, which in equilibrium were functions of the energy difference between states: $R_{\mu\to\nu} = R\left(\beta(H_\nu - H_\mu)\right) \equiv R(\beta\Delta H)$. Physically, the idea is to bias particle movements in a particular direction, and suppress movements in the opposite direction. In the other mutually perpendicular directions, exchanges occur with normal equilibrium rates. In the standard KLS model, the driving force field is taken to be spatially *uniform*, and temporally constant – the simplest choice. Additionally, the field acts along one axis direction, say x. Denoting the field by F, we define a work term which will enter the transition rates for exchanges in the x direction:

$$\Delta W = -J\,F\,(\sigma_i - \sigma_j)/2, \tag{4.4}$$

The subscripts i and j identify the exchanging spins' positions; in a $2d$ system, we take the coordinates to be $i = (x, z)$, $j = (x+1, z)$. Thus for positive F and $\sigma_i = +1$, $\sigma_j = -1$, we obtain $\Delta W = -J\,F < 0$, so that this exchange is *enhanced* – it has a negative work term associated with it. Thus for this convention, '+' spins (particles) will tend to move in the positive x direction. Conversely, '+' movements in the negative x direction are *suppressed*. Note that since there are just two spin states, this implies that the opposite is true for '−' spins – they are biased to move in the negative direction. Having defined the work term, the modified transition rates will take the form

$$R_{\mu\to\nu} = R\left(\beta(\Delta H + l\Delta W)\right), \tag{4.5}$$

where l simply "turns on" the second term for exchanges in the x direction, $l = 1$, and turns it off for other directions, $l = 0$.

An important effect of the presence of the uniform (in space and time) drive is that particle-hole (Ising) symmetry is violated – the system is not invariant under flipping all spins. However, the combined 'CP' symmetry, under the operation $\sigma_i \to -\sigma_i$ and reflecting $x \to -x$, remains intact. Similar symmetry considerations will prove to be important in the present study, when we investigate capillary wave dynamics under drive in Sec. 9.5.

At this point, we have specified the interactions, inherited from the COP Ising model, and the dynamics – Kawasaki spin exchanges with a bias due to the force field. What remains to be specified are the boundary conditions, and a specific functional form of the transition rates $R_{\mu\to\nu}$. We defer the former to the next section; for the rates, the usual choice in the KLS model are the well-known Metropolis rates, introduced by Metropolis *et al.* in the 1950s [96], which here take the form

$$R_{\mu\to\nu} \propto \min\left\{1, \exp(-\beta(\Delta H + l\Delta W))\right\}. \tag{4.6}$$

The min function ensures that the transition probability is never greater than unity; its presence makes the rates look like rather a strange choice from an analytic perspective. The "blame" lies with simulators, since this choice is efficient in terms of acceptance ratios [55]; we will return to this in Chapter 6. Physically, Metropolis rates mean that energetically favourable transitions *always* occur, while those costing energy have a Boltzmann-like probability of happening. For $\Delta W = 0$, Metropolis rates satisfy detailed balance [54, 55], so a system evolving according to these rates will attain equilibrium. For non-zero driving force, detailed balance may be violated, depending on the boundary conditions imposed, as we now discuss.

4.2.4 Boundary conditions

In the KLS model, the standard choice of boundary conditions is to make all boundaries periodic. This means that there will be a particle current through the system, in the direction of the driving field, and that the system is translationally invariant in this direction. Crucially, the choice of periodic boundaries in this direction ensures that the system is non-equilibrium – the driving field cannot be subsumed into the definition of the Hamiltonian. In order to do so, we would require a term like $\sum_i F\, x\, \sigma_i$ [92] (i.e., writing the field as a gradient of a potential $\mathbf{F} = -\nabla V(x)$); however, this fails across the

periodic boundaries. Therefore detailed balance, Eqn. (4.3), is violated, since the rates include a non-Hamiltonian component. Note that we *could* incorporate the field into the Hamiltonian for closed (wall) boundaries in the field direction – then the system would be in equilibrium, and we would be modelling something like sedimentation under gravity. The choice of boundary conditions in the other lattice directions is more free, and may be altered to suit a specific investigation – for example, using walls to model confined systems.

4.2.5 Summary of some selected results

As discussed above, directly solving the steady-state master equation is not feasible for systems of reasonable size. For the KLS model, the main methods of study are therefore a coarse-grained Langevin approach, and Monte Carlo simulations. In the former, one constructs a Landau-Ginzburg Hamiltonian for the system from the usual kind of symmetry arguments [17, 31], and then studies the resulting Langevin equation [97] of motion for the order parameter, which includes a functional derivative of the Hamiltonian with respect to the order parameter, as well as a noise term, and a term to model the driving field [94]. *Microscopic* theoretical studies, by contrast, take the form of dynamic mean field theories, where small clusters of lattice sites are considered, and the probability distributions of these clusters are derived [94, 98, 99]. This approach has given some good qualitative results for the phase diagram, but cannot deal with inhomogeneous states, which means that it is inappropriate for the study of interfaces.

As revealed by simulations and these dynamic mean field theories, the Ising order-disorder transition is retained in the KLS model at all driving strengths, for the choice of fixed magnetisation $m = 0$ (fixed density $\rho = 1/2$). We will discuss this choice exclusively, since it is by far the most-studied case, as the equilibrium critical point can be reached for $F = 0$. In two dimensions, the critical temperature increases monotonically with F until it saturates at roughly 1.4 times the (Onsager) equilibrium bulk critical temperature, for infinite drive. The same trend has been found in $3d$ via simulations [100], albeit with a slower increase of $T_c(F)$. The critical behaviour of the KLS model has been extensively studied by field theoretic renormalization group methods, and the critical exponents have been calculated [101]. Since this topic is well beyond our current scope, the reader is directed to [94] and references therein. Below T_c, as in the Ising model, the system phase separates and macroscopic interface(s) are formed, their number depending on the geom-

etry and boundary conditions. Interfaces are always observed to orient themselves *along* the drive direction (x, in the convention above), and never in the the perpendicular direction(s). This makes sense on an intuitive level – an interface initially lying perpendicular to the drive may easily be broken up by a current passing normal to it. Thus in a fully periodic $2d$ system, the steady state has two phases with an upper and a lower interface separating them, lying along the x direction. If instead '+' and '−' walls are imposed at the top and bottom, as discussed in Sec. 3.5, there will be just one interface, located midway between the walls.

Here we are most interested in the structure and dynamics of interfaces in steady states. Happily this has been the subject of several simulation and theoretical works, for the KLS model. Leung *et al.* [102, 103] carried out Monte Carlo simulations of the $2d$ KLS model in the sub-critical regime. At the top and bottom boundaries, + and − walls were used, respectively, with an approximately square geometry, not strongly confined. Leung *et al.* noted that owing to the local particle number conservation imposed by Kawasaki dynamics, the evolution of the system was rather slow, since particles must be transported "step-by-step" in order to change the large-scale configuration of the interface. This was also found to be the case in the present study, with long simulation runs required (see Chapter 9) to first reach a steady state, and then to gather good statistics. In Ref. [103], the magnetisation profile $m(z)$ (density profile $\rho(z)$ in lattice gas language) between the walls was found to become much *sharper* upon increasing the applied drive: $|m(z)|$ stayed close to unity much further away from the walls as compared to the equilibrium profile, and thus changed sign much more sharply. This indicates that the interface is less rough when drive is applied: capillary-wave like fluctuations are suppressed. Leung *et al.* also investigated the spatial and temporal correlations of the interfacial height (where the height was defined by a coarse-graining method), and the finite-size scaling of the interfacial width. From the behaviour of the latter quantity, they speculated that the interface would in fact be *smooth* in the thermodynamic limit – i.e., the width would tend to a finite value as the system size is increased. This is a striking example of the differences between equilibrium and non-equilibrium systems – recall from the discussion in Sec. 3.5.4 that equilibrium interfaces are always *rough* in $d = 2$ ($T_R = 0$), so that the width diverges in the thermodynamic limit. A subsequent simulation study [104], again in an unconfined system, of the Fourier transform of the height correlation function, $C(k) \equiv \left\langle |h_{\mathbf{k}}|^2 \right\rangle$, showed $C(k) \sim 1/k^{0.67}$, markedly different from the $1/k^2$ equilibrium (unconfined) capillary-wave

behaviour, Eqn. (2.14) with $\xi_{\|} \to \infty$. The behaviour in the driven case is consistent with a smooth interface, since the squared interfacial width w^2 can be thought of as just the zero-separation value of the (real-space) height correlation function, i.e. $C(\mathbf{r} = \mathbf{0})$, and thus proportional to $\int \left\langle |h_{\mathbf{k}}|^2 \right\rangle dk$ (see Eqn. (2.23)), with the usual cutoff considerations. This quantity is finite even in the thermodynamic limit $L \to \infty$; contrast Eqn. (2.19), the $d = 2$ CW result.

Although these studies were exclusively two-dimensional, the authors expected the trend of interface smoothening to extend to three dimensions. This was motivated by a heuristic argument for the mechanism of the smoothening: the driving field reduces the time scale for the decay of long wavelength interfacial modes, and thus acts to destroy such fluctuations, creating a *smooth* interface on these length scales. This is rather analogous to the roughening transition, see Sec. 3.5.4. Microscopically, their picture is one of particles being driven along x continually, preventing the (slow) formation of large (in the z dimension) deformations. Such an argument applies equally in $3d$ as $2d$, and is physically appealing, although making it more precise on a microscopic level turns out to be difficult. Leung and Zia [104] also interpreted the smoothening in terms of an effective interface stiffness, which grows on large length scales, and thus resists the same types of long-wavelength fluctuation.

On the theoretical side, one starts with the bulk dynamical (Langevin) equation, and derives an equation for the interface from this [105–107] – inevitably, approximations are required. Yeung *et al.* [107] investigated the stability of the interface under drive; in particular, they found that driving along the interface (that is, in the usual way as introduced above) can suppress fluctuations. Zia and Leung [106] studied a *randomly* driven variant of the KLS model, where the direction of the drive changes randomly in time between the positive and negative x directions. For this form the Ising symmetry, which is lost for uniform drive as discussed above, is restored, and there is no current through the system on the average. In Ref. [106], suppression of interface roughness was found for the randomly driven model, with a $1/k$ decay of $C(k)$; this was subsequently observed in simulations [104]. Analytic results for the correlations in the standard (uniformly driven) case are not available, although Zia *et al.* [108] have argued that the violation of the fluctuation-dissipation theorem (in both the standard KLS model and the random one) leads to a modification of $C(k)$ and is thus the *common* source of roughness suppression.

These studies of the KLS interface are invaluable as a reference point for the current

work, and we will return to them later when we come to discuss the results. They do, however, form only a small part of the body of work on driven diffusive systems. Many other strange and surprising phenomena have been discovered, especially in the sub-critical regime. For instance, Boal *et al.* [109] modified the ($d = 2$) KLS model by imposing *open* x-boundaries (i.e., those oriented perpendicular to the drive) in Monte Carlo simulations. Particles enter through one of these boundaries, and exit at the other, so there is a chemical potential gradient in the system, in addition to the uniform driving field. As we have seen, the field tends to create interfaces (for $T < T_c$) oriented along it, so that there is a density gradient in the perpendicular direction. The chemical potential gradient has the opposite effect – it creates a density variation along x. Competition of these forces at low temperatures produces "finger-like" or "icicle" structures in the system, which are rather different to the normal KLS steady state. The number of fingers, and their angle with respect to the drive, is controlled by the drive strength and the chemical potential gradient – the drive will break up an interface perpendicular to it, but the boundary conditions do not permit the drive's preferred parallel orientation. A compromise is reached at the angle observed in the simulations. Further discussion of chemical potential gradients in lattice systems, and their interplay with driving fields, may be found in [94].

Other studies of the sub-critical KLS driven lattice gas have investigated topics such as the dynamics of phase separation after a quench from a random '$T = \infty$' state [10]. The system initially forms thin stripes along the drive direction, which then grow and coalesce via a combination of evaporation at the interfaces, and diffusion through the bulk of a stripe. Recently the finite-size scaling of the interfacial width, and its time evolution in the critical regime, were also studied [110]. For much more information and many references on the KLS model and its variants, see the comprehensive review Ref. [94], as well as a short "taster" review [111].

Finally, besides the KLS model and variants thereof, investigations into other driven lattice models exist in the literature. Chan and Lin [112] devised a sheared $2d$ Ising model with conserved order parameter, and studied the variation of critical temperature and critical fluctuations with the strength of the applied shear. In their model, the drive was not implemented as a modification of the transition rates, but instead by periodically shifting whole rows of spins by different distances according to their vertical coordinate. In between these "shear steps", standard equilibrium MC exchange dynamics were applied. The authors found the critical temperature to increase when shear was applied, and critical

fluctuations were suppressed. This perhaps seems more obvious than for the KLS model, since the discrete shear step clearly and suddenly destroys inter-row correlations – this is perhaps a weakness of the model. However, since the MC rates themselves are not modified, the model is in some senses simpler than the KLS-type approach. Also, by decoupling the shear flow and thermal evolution, one can use non-conserved dynamics if so desired; see [113] for an example of this.

Chapter 5

Experiments

Fluctuations at fluid interfaces have been studied experimentally for a long time, by the techniques of light [114] and more recently X-ray scattering [115, 116]. These methods return Fourier-space information, such as the structure factor; one can obtain a real-space description via a Fourier transform. However, information on individual particle positions is lost, so one cannot see what the interface "really looks like". Observing the interface directly in real space, as a complementary source of information, is therefore desirable – not only for the benefit of theorists and simulators who may be more at home in real space, but also as a tool to capture microscopic events such as coalesence of droplets [117].

Is this a realistic prospect? To answer this we invoke capillary wave theory (CWT) (Sec. 2.3), which as we have discussed, provides a good description of interfacial fluctuations. The key length scales are the interfacial width (or "roughness"), and the lateral correlation length $\xi_{\parallel}$. If the roughness is too small and the correlation length too long, then direct visual observation is not possible. For molecular liquids, this is the case – the roughness is on the order of nanometres, while the correlation length is a few mm, so their ratio is of order 10^{-6} [12]. However, if these length scales can be tuned such that the roughness is increased and the correlation length decreased to appropriate scales for visual observation, then we will be in luck. This is precisely what can be done in colloidal systems [12, 118].

Colloids are loosely defined as particles with sizes in the range $\sim$ 10 nm to 1 μm; when immersed in a solvent, a colloidal dispersion is formed. These are extremely useful – canonical examples include milk, paint, and blood. Here we consider in particular mixtures of colloids and polymers; in such systems, phase separation may occur for appropriate

densities of the constituents. This transition is entropically driven [119] – the presence of polymers causes an effective "depletion" attraction between the colloids, "pushing out" polymers and allowing them more configurational freedom. The system thus separates into a colloid-rich (polymer-poor) "liquid" phase and a colloid-poor (polymer-rich) "gas", separated by an interface. For our purposes, the relatively large size of colloidal particles is key – the surface tension σ of a phase separated system scales with the colloidal diameter d as $1/d^2$ [120]. But from CWT we know that $\xi_\parallel \propto \sqrt{\sigma}$ (Eqn. (2.15)), and $w \propto 1/\sqrt{\sigma}$ (Eqn. (2.16)). Thus by increasing the size of particles, one can simultaneously *increase* the roughness and *decrease* the correlation length. In this way, Aarts *et al.* [12] were able to bring both into the μm range, allowing visual observation of a phase-separated colloid-polymer system by confocal microscopy. Additionally, the greatly reduced surface tension *increases* the characteristic decay time for capillary-wave fluctuations [121] $\tau \propto \sigma^{-1/2}$, up to the order of seconds for the system in question. This means that the *dynamics* of capillary waves are also accessible experimentally – for example one can measure the time-displaced height correlation function. In Ref. [12], the colloids (the widely used poly(methly methacrylate), PMMA) were fluorescently tagged so that the phases could be distinguished. Using this technique, the authors were able to capture striking images of the interface, and analyze these to test the predictions of CWT in the system, finding agreement.

This leads us to one of the initial motivations for the work presented here: a subsequent experiment by Derks *et al.* [13, 118], where the same colloid-polymer system was prepared, but this time placed in a shear cell and driven *out of equilibrium*. The authors studied the static height-height correlation function, Eqn. (2.20), obtaining results for the width of the interface w and lateral correlation length $\xi_\parallel$. The dynamic height-height autocorrelation function (temporally-displaced, equal position) was also measured, in order to obtain characteristic decay times for height fluctuations. The *central* result of the paper is however visible from images of the experimental system itself [13] – under shear, the colloid-polymer interface becomes significantly smoother, i.e., capillary wave fluctuations are suppressed. The effect was observed to be greater for higher shear rates. The width measurements support the visual impression: the width reduces when shear is applied to the system. As the authors pointed out, suppression of thermal capillary waves by shear in a real system is rather counter-intuitive (and therefore interesting) – for example, wind at a water surface *creates* (macroscopic) waves.

A natural question is whether this phenomenon is just specific to the experimental system used, or whether it is a more general feature of non-equilibrium fluid interfaces. This question provided the initial basis for the investigations presented in this thesis. A hint that this phenomenon might not just be specific to the experimental system was already available from the simulations of Leung *et al.* [102, 103] (Sec. 4.2.5), where smoothening was found in the driven Ising lattice gas (KLS model). These results were, however, for a $2d$ system, while the experimental system is of course three-dimensional. Also, the driving field is uniform in the KLS model, but the form of the field could conceivably be important in determining the interface structure and dynamics (as we shall see, this is indeed the case for the dynamics). Finally, larger and more accurate simulations have been made possible in the 20 years since the Leung study. For these reasons, a new investigation with greater scope was certainly worthwhile. Furthermore, very recently, a theoretical study of a sheared fluid interface in $d = 3$ was conducted [122], using the framework of fluctuating hydrodynamics. In that work, Thiébaud and Bickel compared their findings to the experiment of Derks *et al.* and to MC simulations [123] – we shall discuss this in Chapter 10. This third independent point of comparison is valuable, and is encouraging evidence of continued activity in this field.

As mentioned, Derks *et al.* measured the static height correlation function – note that this was $C(x, y = \text{const})$ in the notation of Sec. 2.3, because the focal plane of the microscope is rather thin ($< 1\mu$m), so it picks up a $2d$ "slice" of the full $3d$ system. They found that the experimental data could be fitted by the Bessel function CWT form (in fact Eqn. (2.24), but without the shift λ) rather well, by using the correlation length $\xi_{\parallel}$ and the pre-factor as fitting parameters. This is remarkable – CWT is only expected to be valid in equilibrium, which the sheared colloid-polymer mixture is not. The $\xi_{\parallel}$ extracted from the fits was found to *increase* with applied shear, as was the effective "surface tension" from the pre-factor.

The dynamic height-height autocorrelation function,

$$C(\mathbf{r} = 0, t) = \langle h(\mathbf{r}', t')h(\mathbf{r}', t' + t)\rangle,$$

measures the average correlation between interface heights at the same point in space, but separated in time by an interval t. The typical decay time τ_{cap} of this function in equilibrium is the "capillary time" – the lifetime of capillary wave fluctuations. In [13], the decay times of the equilibrium system were measured, and used with hydrodynamics

results for CW dynamics [124] to obtain decay times τ_q for individual Fourier modes. It was then argued that the shear affects only modes with a decay time $\tau_q > \dot{\gamma}^{-1}$, where $\dot{\gamma}$ is the shear rate (which has units of inverse time); physically, the slow modes are "washed away" by the current along the interface. Finally, this relation was applied to a calculation of an effective non-equilibrium surface tension $\sigma(\dot{\gamma})$, which was found to increase under shear, in agreement with the surface tension obtained from the fits of the static height correlations. The physical ideas of large, slow fluctuations being washed away, and the increase in effective stiffness remind us of the arguments of Refs. [103] and [104], which are appealing. However, since the surface tension is a free energy, which is an *equilibrium* notion, caution is required in the interpretation of the quantity measured in experiment.

In summary, the experiment described above is very intriguing, and led to the initial simulations in the present work. However, it should be emphasised that we do not seek to model such a complex fluidic system accurately, but rather investigate non-equilibrium interfaces on a more generic and hopefully more fundamental level.

Chapter 6

Monte Carlo Methods

6.1 Introduction

The term "Monte Carlo methods" forms a rather large umbrella over a wide variety of specific applications, from condensed matter physics, to electrical engineering, to financial markets [125] and many more. The unifying feature is the use of random numbers to perform sampling and so to compute quantities of interest. In condensed matter physics, these are observables of a system – for example, energy, order parameter, two-body correlation functions, etc. The use of random sampling sets Monte Carlo (MC) methods apart from molecular dynamics, where the equations of motion of the system are numerically integrated forward in time [54].

The general prescription for an MC simulation of a condensed matter system is as follows. Firstly the system is prepared in some initial state, and parameters (temperature, etc.) are chosen. The system is then evolved from one state to another via some choice of simulation dynamics, and observables may be measured periodically in order to perform averages. Generally MC simulations use *importance sampling*: the system's states are sampled according to the desired probability distribution (which for an equilibrium system, is Boltzmann). This (natural) choice makes MC simulations powerful – we do not try to sample *all* states of a system during a simulation (if we could, we may as well just calculate the partition function directly – the huge number of states makes this impractical, e.g., 2^N for an Ising system with N spins), but rather we sample the more likely states more often, since these contribute the most to observable averages. Indeed, the vast majority of possible states will never be visited at all in an MC simulation, yet the results can still

be extremely accurate.

States are generated as a *Markov chain*, possessing the key property that the transition probability from a state μ to a state ν depends only on these configurations, and not on the past history of the system [54, 55]. The condition of detailed balance, which we have discussed in Sec. 4.2.1, ensures that the Markov process reaches a steady state probability distribution, rather than a limit cycle [55]. For an equilibrium simulation, this distribution is of course Boltzmann; out of equilibrium, it is generally unknown. The other requirement for equilibrium is *ergodicity*: the system must be able to reach any allowed state from any initial state. This condition has to be proved for individual MC algorithms [55].

For the moment we consider equilibrium systems. Since detailed balance, Eqn. (4.3), only fixes the ratio of transition rates, some freedom is allowed in choosing their specific form. We now rewrite the transition rate $R_{\mu\to\nu}$ in the form

$$R_{\mu\to\nu} = s_{\mu\to\nu} A_{\mu\to\nu}, \tag{6.1}$$

where $s_{\mu\to\nu}$ is the "selection probability", which specifies the probability of choosing ν as the candidiate for the new state, and $A_{\mu\to\nu}$ is the "acceptance probability", which is the likelihood that the transition is actually accepted. In a simulation, the idea is to explore the state space efficiently, so the acceptance probability should be made as large as possible, while still obeying detailed balance and normalisation. The famous Metropolis algorithm [96] is a particular choice of $s_{\mu\to\nu}$ and $A_{\mu\to\nu}$, which is both rather simple, and reasonably efficient, in the sense that the acceptance ratio is chosen optimally, given the enforced selection probability. Specifically, one chooses a uniform selection probability, so that if there are N states, $s_{\mu\to\nu} = 1/N$. The acceptance ratio has already been given on the RHS of Eqn. (4.6); it is:

$$A_{\mu\to\nu} = \min\left\{1, \exp(-\beta(\Delta H))\right\}. \tag{6.2}$$

ΔH is the change in internal energy resulting from the transition. According to (6.2), moves which lower the system's energy are *always* accepted, while other moves are accepted with a Boltzmann factor probability. This is the optimal choice for the selection probability given [55]. For the Ising model, the Metropolis algorithm is usually implemented via the simplest choice: *single spin-flip* dynamics, where the new state is obtained by flipping one spin on the lattice (in principle many spins could be flipped, since this still obeys the $1/N$ selection probability, but cluster algorithms [54, 55] are a better approach if one wishes to go down this avenue).

Here we are interested in the conserved order parameter (COP) Ising model (or lattice gas) introduced in Sec. 3.3. For this model, *flipping* a single spin is not permitted, since this changes the overall magnetisation. Instead one can employ Kawasaki *exchange dynamics*, which were introduced in Sec. 4.2.2. Since an elementary move consists of exchanging a nearest-neighbour pair, the selection probabilities are not $1/N$, but $2/zN$, where z is the number of nearest neighbours of a site, the lattice coordination number (4 for a $2d$ square lattice). This number comes about because there are N choices for the first site, and z for the second, but the pair can be chosen in either order. This $s_{\mu\to\nu}$ is still uniform, so for the acceptance probability, the Metropolis form (6.2) is again optimal. This constitutes the Kawasaki algorithm for an MC simulation of the COP Ising model.

6.2 Non-equilibrium Monte Carlo

Although the majority of MC simulation studies are focused on systems in thermal equilibrium, a significant number consider non-equilibrium systems. As discussed in Sec. 4.1, this class includes systems approaching equilibrium, as well as those which are driven such that they reach a non-equilibrium steady state. For example, studies of the COP Ising lattice gas approaching equilibrium from a high-temperature quench [126] have advanced our understanding of the dynamics of phase separation in fluids. The KLS model (Sec. 4.2) is an example of a system reaching a non-equilibrium steady state, with a variety of interesting phenomena.

The key issue in non-equilibrium MC is the choice of dynamics. Generally one is interested in observing not only static observables, but quantities which depend on the dynamics, such as currents, or time correlation functions – for *equilibrium* MC, static observables such as the energy or the pair correlation function are frequently the only quantities of interest. For this reason, the dynamics must be chosen to be at least somewhat physically realistic, so that these dynamic observables are meaningful. In particular, some of the rather efficient algorithms which have been developed for equilibrium systems, such as cluster algorithms for the Ising model, involve non-local movements of spins, i.e. "teleportation" across the lattice, and are thus unsuitable. Additionally, often the dynamics should be conservative – for example, in the KLS model, two spins have to be exchanged in order to implement the effect of the driving field. This means that the choice of algorithm is generally much more restriced than if one is only interested

in static equilibrium properties. In the KLS model, the dynamics are of the Kawasaki exchange type, with Metropolis acceptance ratios, extended to incorporate the driving field. Kawasaki exchange dynamics are both local and conservative, and are therefore physically reasonable for a simulation of a driven diffusive model such as the KLS model, or indeed of phase separation in the equilibrium Ising lattice gas.

The problem with this restriction to local, conservative algorithms is one of efficiency – they are *slow* to evolve the system through phase space. A particle hopping to a neighbouring lattice site corresponds to a very small displacement in phase space – to move the system a significant "distance" requires many individual hops, and therefore takes a long time. In the case of spinodal decomposition in the COP Ising model, the typical domain size grows as $t^{1/3}$ [55], compared to $t^{1/2}$ for even the single-spin flip (i.e., non-conservative) algorithm. Thus observing the latter stages of separation takes a relatively large computational effort. This also applies to driven systems such as the KLS model, although the presence of an external field will alter the situation. Furthermore, in a fully phase-separated COP Ising system with an interface, the dynamics become even slower – the majority of nearest neighbours in the bulk are spins of the same sign, so exchanges between these do not change the configuration. Thus evolution must primarily proceed via the interface, which is also slow, because detaching a spin from its bulk phase costs energy. This was experienced by Leung *et al.* [102, 103] in their simulations of the steady-state interface of the KLS model, as discussed earlier.

Apart from the distinction between conservative and non-conservative, and local and non-local dynamics, there also exists a classification for transition rates into *soft* and *hard* [127–130]. If we consider rates with both internal energy and external (static) magnetic field energy terms, then for "soft" rates, $A_{\mu\to\nu}$ factorizes into separate contributions due these sources, while for "hard" rates, it does not. Rikvold and Kolesik [127–129] studied SOS and Ising interfaces growing (i.e., moving vertically) in MC simulations under both soft and hard rates, and found significant differences in the structure and mobility of the interface depending on the type of rate used. For example, the average height difference between neighbouring columns in the SOS model depends strongly on the static magnetic field B for hard rates, but is independent of it for soft rates. The authors make the point that when conducting MC simulations of non-equilibrium interfaces, the choice of rates, as well as the choice of dynamics (as discussed above) matters. In our case, the situation is somewhat different, since we will not consider a static external magnetic field, but rather

a KLS-like field. However, an analogous classification is possible [131].

Another issue relating to choice of simulation dynamics is the non-equivalence of ensembles in finite systems. In the thermodynamic limit, the canonical and grand canonical ensembles become equivalent, so that static observables attain the same average values. However, we can only simulate a finite system, so this equivalence is not exact. Thus even for an *equilibrium* simulation, the choice of dynamics can have an effect. As shown later in Sec. 9.4, the difference is especially pronounced for systems with an interface, where the extra freedom of interface wandering allowed by non-conserved Glauber (spin-flip) [132] dynamics can significantly affect values of *static* observables, as compared to using Kawasaki dynamics.

Chapter 7

The main model

We now define the primary model that has been investigated in this work. Consider a conserved order parameter Ising model (lattice gas) on a $2d$ square lattice, or $3d$ simple cubic lattice. We fix the magnetisation $m = 0$ ($\rho = 1/2$), so that there are equal numbers of up and down spins, and in equilibrium, the critical point is accessible. We consider only sub-critical temperatures, and avoid close proximity to the critical point, since the associated phenomena would drastically complicate the situation. The static external field term, which simply shifts the zero of the energy in the COP Ising model, is set to zero. The lattice has dimensions $L_x \times L_z$ ($2d$), or $L_x \times L_y \times L_z$ ($3d$). Periodic boundary conditions are applied in the x and (if applicable) y directions. Spin lines (layers) in $2d$ ($3d$) are located at half integer z coordinates

$$z = -\frac{L_z - 1}{2}, -\frac{L_z - 3}{2}, \cdots -\frac{1}{2}, \frac{1}{2}, \cdots \frac{L_z - 1}{2}, \tag{7.1}$$

for a total of L_z layers; we will take L_z to be even. The z boundaries consist of walls of fixed spins $\sigma = +1$ at the top ($z = (L_z+1)/2$) and $\sigma = -1$ at the bottom ($z = -(L_z+1)/2$) edges of the lattice. As discussed earlier, for sub-critical temperatures, these boundary conditions induce an interface aligned parallel to the x-y plane on the average, with the '+' phase in the upper half of the volume, $z > 0$. We focus on slit-like ($2d$) or slab-like ($3d$) lattice geometries, with $L_x \gg L_z$ in the $2d$ system, and $L_x, L_y \gg L_z$ with $L_x = L_y$ in the $3d$ system, so that the system is confined between the two walls, and the scaling length scale for the interfacial width is $L_z \equiv L_\perp$ (Sec. 2.3.3). As discussed in Chapter 2, confined systems are relevant experimentally, are rich theoretically, and useful exact results are available for the $2d$ confined (infinite-strip) Ising model, providing an important reference

point.

Time evolution of the system proceeds under Kawasaki spin-exchange dynamics, which, as discussed earlier, conserve magnetisation or density locally (and globally). These dynamics are modified by an external force field $\mathbf{F}(z) = [F_x(z), F_y(z), 0]$ which acts on the system, driving in the x-y plane. This field alters the Monte Carlo acceptance rates, to produce a modified Metropolis rate as in the KLS model,

$$p = \min\{1, \exp[-\beta(\Delta H + \Delta W)]\}. \tag{7.2}$$

As usual $\beta = 1/k_{\mathrm{B}}T$ is the inverse temperature (the Boltzmann constant will be set to unity), and ΔH is the change in internal energy from the proposed exchange. ΔW is the work done by or against the external force field; for $\Delta W = 0$, the above rate reduces to the standard Metropolis one, which samples thermal equilibrium states. We are interested in the case of non-zero ΔW, when the system will reach a non-equilibrium steady state. The system is immersed in a heat bath at constant temperature T, into which the work done is dissipated. The driving field is related to the work term by

$$\Delta W = -J\ \boldsymbol{\delta} \cdot \mathbf{F}(z)(\sigma_i - \sigma_j)/2, \tag{7.3}$$

where i and j label the positions of the spins:

$$\begin{aligned} i &= (x, y, z), \\ j &= (x + \delta_x, y + \delta_y, z + \delta_z) \end{aligned} \tag{7.4}$$

and $\boldsymbol{\delta}$ is the displacement vector between spins i and j:

$$\begin{aligned} \boldsymbol{\delta} &\equiv (\delta_x, \delta_y, \delta_z) \\ &= (\pm 1, 0, 0) \quad \text{or} \quad (0, \pm 1, 0) \quad \text{or} \quad (0, 0, \pm 1), \end{aligned} \tag{7.5}$$

where the last equality holds because only nearest-neighbour exchanges are allowed. Note that since $F_z \equiv 0$, then $\Delta W = 0$ when the two spins are displaced in z – the exchange occurs with the equilibrium rate. These modified Kawasaki dynamics simulate the competition between diffusive motion and driven motion in the system.

At this point there is still a lot of freedom in choosing the specific form of the driving field – there are, in principle, two components $F_x(z)$ and $F_y(z)$, both functions of z. We will thus consider a few simple choices for the field, motivated by those which are likely to be the most relevant experimentally, and by what has been studied before. Our main

focus will be the case of 'shear-like' *linear* variation of the driving field with z, and the field acting in the x-direction only, such that the field components are

$$\begin{aligned} F_x(z) &= \gamma z, \qquad \text{(shear-like drive)} \\ F_y(z) &= 0, \end{aligned} \tag{7.6}$$

where γ is the field gradient in z. With this choice, exchanges along x are enhanced or suppressed, while exchanges in both the y and z directions proceed with equilibrium rates ($\Delta W = 0$). We also study the closely-related case of a V-shaped spatial dependence,

$$\begin{aligned} F_x(z) &= \gamma \left| z \right|, \qquad \text{(V-shaped drive)} \\ F_y(z) &= 0, \end{aligned} \tag{7.7}$$

such that the drive acts in the *same* direction throughout the system. These choices are motivated by an attempt to model experimentally-realisable situations – for example a sheared colloidal system. In an experiment, one applies a force to the walls of the shear cell, rather than throughout the bulk – hydrodynamic interactions then set up a velocity profile. In the Ising model, by contrast, there is no inertia and there are no hydrodynamic interactions. In the $2d$ system, we do also consider the case of driving purely in the layers next to the walls, to mimic the experimental situation:

$$\begin{aligned} F_x(z) &= \pm f_w, \quad z = \pm(L_z - 1)/2 \qquad \text{(boundary drive)} \\ F_x(z) &= 0, \text{ elsewhere} \\ F_y(z) &= 0, \end{aligned} \tag{7.8}$$

such that the layer next to the upper wall is driven with constant field $+f_w$, the layer next to the lower wall is driven with field $-f_w$, and the exchanges at all other z values occur with equilibrium rates. As we shall see, there is no *bulk* current in this case, as expected; however, the boundary field still has an effect on the structure of the system. We also consider other forms of drive. To make a connection to the KLS model, spatially uniform drive in the x direction,

$$\begin{aligned} F_x(z) &= f = \text{const.} \qquad \text{(uniform drive)} \\ F_y(z) &= 0, \end{aligned} \tag{7.9}$$

is a natural choice to study. In addition we consider a "step-like" driving field, which swaps direction at the mean interface position, $z = 0$:

$$F_x(z) = f \cdot \mathrm{sgn}(z) \qquad \text{(step-like drive)}$$
$$F_y(z) = 0. \tag{7.10}$$

These five forms of driving field are illustrated in Fig. 7.1. A first glance reveals that the bulk driving forms (i.e., all except the boundary drive) are all either even or odd in z. Indeed, the symmetry of the field will turn out to be crucial for the dynamics of the interface. The parameters γ, f_w and f control the strengths of the various forms of drive, and the properties of the interface will depend strongly on their values.

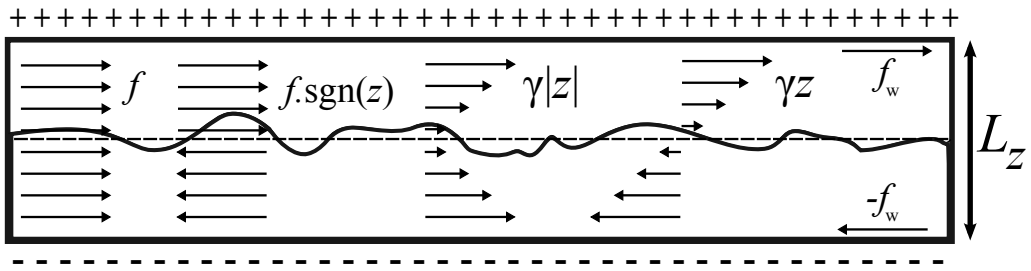

Figure 7.1: Illustration of the drive variants in the driven Ising model, as defined in the text. From left to right: uniform, step-like, V-shaped, shear, and boundary drive. The midline of the system is indicated with a dashed line, and a schematic interface is sketched.

With the driven dynamics fully specified, we can now construct the list of actions that constitute a single time-step in the MC simulation. We work in spin language:

1. Choose a random spin i, the first candidate exchangee.

2. Choose a random nearest-neighbour of i (j), the other candidate exchangee.

3. Compute ΔH, ΔW, and use these in the Metropolis rate (7.2) to decide whether to accept the exchange.

4. If the move is accepted, swap the values σ_i and σ_j. If not, do nothing.

The above ignores efficiency considerations – for example, if the chosen spins i and j actually have the same values, then their exchange has no effect on the system configuration, so we can skip steps $3-4$. Note that we *cannot* exclude such choices from occuring when

using a nearest-neighbour algorithm, if we wish the $F = 0$ case to be equilibrium: excluding like-spin pairs from the candidates has been shown to violate detailed balance [133]. For a system with N lattice sites, completing the above sequence N times corresponds to one *Monte Carlo sweep* (MCS) of the lattice – this is a standard unit of time in MC simulations, since on the average, each spin is visited once in step 1 per MCS.

MC simulations of the above model have been carried out in $2d$ and $3d$, for a variety of system sizes, temperatures, and driving strengths, from equilibrium to strongly driven. The simulations were implemented using both the simple single-spin algorithm, as well as a more advanced multispin method [55, 126]. We explain the meaning of this term, and set out the algorithmic details, in the next chapter, and present results in Chapters 9 and 10. At this point we introduce a closely related secondary model which has also been investigated.

7.1 The driven Blume-Capel model

The Blume-Capel (BC) [134–136] model may be thought of as a spin-one version of the Ising model (which is spin-1/2), or as a (crude) lattice model of an AB binary mixture. In the BC model spins therefore have three states, $\sigma = +1, -1, 0$; in the binary mixture picture, the ± 1 states correspond to species A and B, and the 0 state corresponds to the absence of a particle at that lattice site. This is a fundamental change to the model: the Ising up-down symmetry is broken, and richer phenomenology is possible – for example, the BC model exhibits a tri-critical point which divides a first-order transition line and a line of continuous (critical) transitions from the paramagnetic to the ferromagnetic state.

The general Hamiltonian for the Blume-Capel model is

$$H_{\mathrm{BC}}\left[\{\sigma_i\}\right] = -J \sum_{\langle ij \rangle} \sigma_i \sigma_j + D \sum_i \sigma_i^2 - B \sum_i \sigma_i, \tag{7.11}$$

with $\sigma_i = \pm 1, 0$. The new term compared to the Ising model is the "crystal-field coupling" with $D \geq 0$, which favours the presence of $\sigma = 0$ spins and gives an equal penalty D for the ± 1 spin states. Often in the literature the magnetic field term involving B is not included in the definition of the Hamiltonian, and is assumed to be zero implicitly. Here, as for the Ising model, we will be interested in *fixed* numbers of all three spin states (fixed numbers of species A and B), so in fact both the second and third terms are simply constant anyway. The form of the Hamiltonian is then precisely Ising. As an aside we note

that the BC model is actually a special case of the Blume-Emery-Griffiths (BEG) model, which has an additional "biquadratic" (spin-squared coupling) term in the Hamiltonian [137].

At $D = 0$, $B = 0$, the BC model exhibits an order-disorder transition at a critical temperature $k_{\rm B}T_c/J \approx 1.69$ on a $2d$ square lattice, and at $k_{\rm B}T_c/J \approx 3.19$ on a simple cubic lattice [138]. With the restriction of fixed numbers of each spin species, much of the rich phase behaviour of the full BC model is inaccessible, but this is not the focus here. Studies of the phase diagram and critical properties may be found in Refs. [135–139].

Here we study a $2d$ *driven* BC model to a) serve as a somewhat better model of driven binary mixtures than the Ising model, by allowing for vacancies, and b) to test whether results found in the driven Ising model have wider applicability, or are just special to that system. As mentioned, we fix the number of $\sigma = +1$ and $\sigma = -1$ spins (which in turn fixes the number of $\sigma = 0$ spins); equivalently in the binary mixture picture, we fix ρ_a and ρ_b, the densities of the A and B species. We consider the same sort of (confined) geometries as in the driven Ising model, and apply the same boundary conditions. Together with the choice of temperature $T < T_c$, this induces phase separation with an interface lying parallel to the x direction, in a similar way to the Ising case. Simulations were again done using Kawasaki exchange dynamics with a work term ΔW to account for the drive, as in the Ising system. An important difference, however, concerns the choice of the driving direction for the ± 1 spin species. In the Ising model, there are just two states, so if, say, $+$ spins are driven in the positive x direction, $-$ spins must go the other way. However, in the BC model we may *co-drive* the $+$ and $-$ species in the *same* direction, by virtue of the vacancies. For co-drive, the appropriate work term is

$$\Delta W_{\rm co} = -J\ \boldsymbol{\delta} \cdot \mathbf{F}(z)(\sigma_i^2 - \sigma_j^2). \tag{7.12}$$

Note that now $+/-$ exchanges occur with *equilibrium* rates, and only $+$/vacancy and $-$/vacancy exchanges are subject to drive. Of course, we may choose to apply the drive as in the Ising model ("counter-drive"), where the ± 1 spin species are driven in opposite directions; then the work term is just (7.3). We will study both the counter- and co-driven cases in Sec. 9.8.

7.2 The driven discrete Gaussian model

The third model we consider is a driven version of the discrete Gaussian (DG) model introduced in Sec. 3.5.1. We consider a $1d$ DG model, so that the system consists of a one-dimensional array of heights h_i, modelling the interface in a $2d$ Ising system. In the DG Hamiltonian (3.18) we set the static external field $B = 0$, and we enforce conservation of the total height: $\sum_i h_i \equiv 0$. The choice of constant, zero, ensures that the zero-temperature (flat) interface lies at $h = 0$. Analogously to the other models, simulation dynamics then consist of particle movements from one column i to a nearest-neighbour column j. The source column loses a unit of height: $h_i \to h_i - 1$, which moves to the neighbour: $h_j \to h_j + 1$. We again use modified Metropolis rates, with a work term ΔW due to the drive. The work couples to the height variables in the DG model; to produce a linear shear-like variation of driving strength with height, to drive in the x direction, we use

$$\Delta W = -(x' - x)\frac{[h(x) + h(x')]}{2} J\gamma, \tag{7.13}$$

where x and x' are the source and destination column positions, respectively. This form uses the *mean* of the heights in the two columns to determine the work; of course, other choices are possible – e.g., just one of the heights. We will come back to this briefly in Sec. 9.6. A spatially uniform drive may be set up with the work term

$$\Delta W = -(x' - x)Jf, \tag{7.14}$$

and so forth. The internal energy change term ΔH depends on the the heights at x, x', and their other nearest neighbours (each column has two nearest neighbours in the $1d$ model), which we denote x_n and x'_n:

$$\Delta H = 3\left[1 + h(x') - h(x)\right] + h(x_n) - h(x'_n) \tag{7.15}$$

A simulation time-step then consists of the following actions:

1. Choose a random column i, the candidate source column.

2. Choose a random nearest-neighbour of i (j), the candidate destination.

3. Compute ΔH, ΔW, and use these in the Metropolis rate (7.2) to decide whether to accept the move.

4. If the move is accepted, decrement the height h_i, and increment h_j. If not, do nothing.

The DG model is less computationally expensive than the COP Ising lattice gas to simulate for a long time, and so a simple single-spin (see Chapter 8) implementation proved sufficient to obtain good quality data. Finally, note that it is easy to substitute the SOS Hamiltonian (3.17) for the DG one, and simulate a driven SOS model – indeed we investigate this possibility in Sec. 9.6.

Chapter 8

Computational details

We now give details of the "specialized" computational techniques used in the driven Ising model simulations, namely the multispin coding method, and parallelization via domain decomposition. We first address multispin coding.

8.1 Multispin methods

Multispin coding is a computational technique which can speed up Monte Carlo simulations for some systems (typically spin systems, as the name implies). Essentially it follows the single instruction, multiple data (SIMD) paradigm, although no special instructions (e.g., Streaming SIMD Extensions [SSE]) are required, only standard bitwise operations (AND, OR, NOT, XOR) and shifts. The idea is to hold the state of several degrees of freedom (spins) within a single unsigned integer variable, and update their values simultaneously using the mentioned bitwise operators, in order to evolve the system(s). In fact there are two main approaches to using this underlying idea: either the spins in the variable may all belong to the *same* system, in which case multispin coding allows one to simulate a larger system, or they may belong to *different* systems (of the same dimensions) which are evolved in parallel (though of course, not identically). The latter approach allows us to average observables over all systems in the "multispin ensemble", and thus gain improved statistics (which would otherwise require very long runs). This second technique has also been termed "multilattice coding" [54]. Here we concentrate on this method; for more information on the single-system technique we refer to [55].

Multispin coding is only applicable to a restricted class of systems. The degrees of

freedom must take discrete values (preferably as few as possible) – the values must be representable in just a few bits. Assuming this is the case, one can attempt to create a multispin version of the desired simulation algorithm (for example, single spin-flip, spin exchange, or even a cluster algorithm). This is not necessarily straightforward, and naturally, more complex algorithms are more difficult to transcribe to multispin "language". A single time-step in a multispin algorithm always involves more instructions than a simple single-spin version, and so for an especially complex algorithm, the gains may be outweighed by the overheads. Perhaps more importantly, additional complexity introduces bugs in code, and experience has shown that these bugs can be subtle and hard to find. Nevertheless, multispin coding is a powerful and elegant technique, and with carefully planned algorithms accompanied by a single-spin implementation as a check, it can be very beneficial. Additional words of caution may be found in Ref. [55].

The Ising model is the ideal candidate for multispin coding, since the spins take just two values ± 1, which means one spin corresponds to a single bit. This has the dual benefits of simplifying the algorithm, and maximising the number of systems in the multispin ensemble: on a 64-bit CPU and operating system, we can efficiently simulate 64 systems at once. A multispin version of the Metropolis spin-flip algorithm for the two-dimensional Ising model may be found in textbooks [55]; equilibrium Kawasaki dynamics in two dimensions have also been implemented [126]. Here we extend the algorithm detailed in Ref. [126] to include the effect of the driving field F, in order to simulate the driven Ising lattice gas model defined in the previous chapter.

8.2 Equilibrium multispin Kawasaki dynamics

To introduce the method, we first cover the equilibrium case, following and expanding on [126]. Our goal is to construct a variable p_{eq} whose bits are one with the correct Metropolis acceptance probability, for each system. Once we possess this variable, the actual spin exchanges may be carried out by the operation

$$\begin{aligned} S_1' &= S_1 \oplus p_{\mathrm{eq}} \\ S_2' &= S_2 \oplus p_{\mathrm{eq}}, \end{aligned} \tag{8.1}$$

where S_1 (S_1') and S_2 (S_2') refer to the initial (final) values of the variables containing the two spins being exchanged, and $\oplus$ is the exclusive-or (XOR) bitwise operation, which

returns 1 if the two argument bits are unlike, and 0 if they are the same. Each bit in S_1 and S_2 corresponds to a *different* system, but at the *same* spatial location. The bits of $p_{\rm eq}$ must be generated such that all the systems evolve independently. We now introduce auxiliary variables P_i and Q_i (abbreviating nearest-neighbours to "nns"):

P_i: bits 1 if *at least* i nns of S_1 are anti-parallel to S_1, excluding S_2.

Q_i: bits 1 if *at least* i nns of S_2 are anti-parallel to S_2, excluding S_1.

For a $2d$ square lattice, i takes values $1, 2, 3$; for a $3d$ simple cubic lattice, $i = 1, \ldots 5$. We also define the variables R_i, which have each bit 1 with probability $\exp(-4\beta J)$; i runs over the same numbers as for the P_i and Q_i. Gemmert *et al.* [126] show how to obtain the variables P_i and Q_i from the spin configuration; this is done in the following way. One constructs variables A_i and B_i,

$$A_i = S_1 \oplus N_{1,i},$$

$$B_i = S_2 \oplus N_{2,i},$$

where the $N_{1,i}$ ($N_{2,i}$) are the nearest neighbours of S_1 (S_2), excluding the other exchangee S_2 (S_1). The P_i and Q_i then follow by a series of bitwise AND and OR operations on the A_i and B_i; in the $2d$ square-lattice case, the optimal procedure obtains them in six operations [126]. Once the P_i and Q_i variables have been calculated, the acceptance probability variable $p_{\rm eq}$ can be computed using the following formula in the $2d$ case:

$$p_{\rm eq} = (S_1 \oplus S_2) \wedge (P_1 \vee Q_3 \vee R_1) \wedge (P_2 \vee Q_2 \vee R_2) \wedge (P_3 \vee Q_1 \vee R_3). \qquad (d = 2) \quad (8.2)$$

Here the symbols $\wedge$ and $\vee$ represent the bitwise AND and OR operations, respectively. In the following we talk in terms of a single bit, although of course all bits are operated on at the same time. The first set of parentheses simply filters out the cases where the relevant bit of S_1 and S_2 is the same. The second set evaluates to one if either S_2 has three anti-parallel neighbours, or S_1 has at least one anti-parallel neighbour, or if the relevant bit of R_1 is one. Now, if the bit of Q_3 is one, then the same is true for Q_2 and Q_1, so we immediately see that in this case, the bit of p will be set. This is because the *maximum* ΔH for this case is zero, which is always accepted under Metropolis rates.

The same argument applies if the relevant bit of P_3 is one – then all the brackets again give one. If neither P_3 nor Q_3 have the bit set, then the exchange may occur, but requires one or more of the R variables to have the appropriate bit set. As an example, consider

the case where the bit of P_2 is one; then the exchange depends on the last bracket – it requires either Q_1 or R_1 to have their bit set. If Q_1 has the correct one-bit, then we know that S_2 has at least one anti-parallel neighbour, and S_1 has at least two. This means that $\max(\Delta H) = 0$, so the exchange suceeds. If however Q_1 is not set, then we know that S_2 has *no* anti-aligned spins, so $\Delta H = +4$. Thus the Metropolis exchange probability is $\exp(-4\beta J)$, which is just the probability that R_1 has its bit set. Thus we see that p_{eq} has its bits one with the correct probability for this case. The same argument can be applied to all other cases; when multiple R_i are required, this corresponds to the Metropolis probabilities $\exp(-8\beta J)$ and $\exp(-12\beta J)$, using the identity $\mathrm{prob}(a \wedge b) = \mathrm{prob}(a)\mathrm{prob}(b)$, for two bits a and b, where prob() gives the probability of its argument being one.

In three dimensions, the form of the algorithm is exactly the same, with more P_i, Q_i and R_i to account for the greater number of neighbours. The acceptance probability is just

$$\begin{aligned} p_{\mathrm{eq}} =& (S_1 \oplus S_2) \wedge (P_1 \vee Q_5 \vee R_1) \wedge (P_2 \vee Q_4 \vee R_2) \wedge (P_3 \vee Q_3 \vee R_3) \wedge \\ & (P_4 \vee Q_2 \vee R_4) \wedge (P_5 \vee Q_1 \vee R_5). \qquad (d = 3) \end{aligned} \tag{8.3}$$

Having computed p_{eq}, the exchange operation on the bits of S_1 and S_2 can be carried out according to Eqn. (8.1) – we have then completed a step of the Kawasaki MC algorithm outlined in the previous chapter, but on many systems at once.

8.3 Driven multispin algorithm

We now modify the above algorithm to include the effect of the work ΔW done by the driving field F. First of all we recall that exchanges perpendicular to the drive direction occur with equilibrium rates, so for these cases (8.2) or (8.3) apply. We now consider exchanges in the driving direction, where new expressions are needed. Due to the form of the Metropolis rates, which plateau at 1 for $\Delta H + \Delta W \leq 0$, we consider the cases where the first-chosen spin S_1 is moving *against* and *with* the field, separately. One might initially think that we could avoid this by simply swapping the identities of S_1 and S_2, but recall that *each bit* of these variables is a spin in an independent system – an against-drive move in one system may be a with-drive move in another. Thus the full exchange operation will actually consist of a "superposition" of the two cases. We first consider against-drive moves.

8.3.1 Against-drive S_1 moves

In this case, $\Delta W > 0$, so that the exchange probability is reduced compared to the equilibrium case. Consider the specific case where the bit of Q_1 for the system we are considering is zero. Then, depending on the P_i, $\Delta H = 0, +4, +8, \ldots$, up to $+12(+20)$ for $d = 2$ ($d = 3$). When we incorporate the drive, the resultant $\Delta H + \Delta W > 0$. Thus the exchange never automatically succeeds, so we can write the against-drive exchange probability variable p_a as a simple bitwise AND with the equilibrium variable p_{eq}:

$$p_a = p_{\mathrm{eq}} \wedge V_0, \tag{8.4}$$

where V_0 has bits one with probability $\exp(-\beta\Delta W)$. This is the simplest case; if the bit of Q_1 is set (but that of Q_2 is not, for now), then ΔH *may* be negative, so $\Delta H + \Delta W$ may be also. Additional terms are required to handle this possibility – we cannot simply bitwise AND with V_0. A suitable expression for p_a in $d = 3$ is

$$p_a = p_{\mathrm{eq}} \wedge \left\{ \left[\overline{Q_1} \wedge V_0\right] \vee \left[Q_1 \wedge \overline{Q_2} \wedge ((P_5 \wedge V_1) \vee (\overline{P_5} \wedge V_0))\right] \right\}, \tag{8.5}$$

where $\overline{Q_1}$ (for example) represents the bitwise NOT operation, and V_1 has bits one with probability $\min[1, \exp(-\beta(-4 + \Delta W))]$. The first term in the {...} encapsulates the previous case, where Q_1 was not set; the second term handles the new case, where Q_1 is set, but the $Q_{>1}$ are not. In equilibrium, for this situation, only when P_5 is set is $\Delta H < 0$ – therefore if P_5 is off, then the expression is like (8.4) (last term). When P_5 *is* set, then the V_1 variable gives the appropriate probability of success.

This line of logic may be continued to cover the remaining cases, i.e., the other Q_i having the appropriate bit set. For example, when Q_2 is set, there are now *two* cases where automatic acceptance ($\Delta H + \Delta W \leq 0$) is possible, and we require another auxiliary variable like V_1, which has bits one with probability $\min[1, \exp(-\beta(-8 + \Delta W))]$. The structure of the expression is a series of sub-expressions which each handle a different physical configuration of spins; the results of these sub-expressions are OR'ed ($\vee$) together to produce the final result. The full acceptance probability expression for against-drive moves may be found in Appendix A.

8.3.2 With-drive S_1 moves

Now the exchange probability is larger than in the equilibrium case. This means that the above approach of extending p_{eq} with additional terms via a bitwise AND no longer

works. Instead we generate the with-drive probability variable p_w independently. The general structure of the expression is the same as before: sub-expressions handling different physical cases, which are OR'ed together. For the case where Q_1 is not set, we have (again for $d = 3$):

$$\begin{aligned} p_w =&(S_1 \oplus S_2) \wedge \left\{\overline{Q_1} \wedge \right. \\ &\left[(P_5) \vee (\overline{P_5} \wedge P_4 \wedge U_1) \vee (\overline{P_4} \wedge P_3 \wedge U_2) \vee (\overline{P_3} \wedge P_2 \wedge U_3) \vee \right. \\ &\left.\left. (\overline{P_2} \wedge P_1 \wedge U_4) \vee (\overline{P_1} \wedge U_5)\right]\right\}, \end{aligned} \tag{8.6}$$

where the U_i have bits 1 with probability $\min[1, \exp(-\beta(4i - \Delta W))]$. Each inner set of parentheses handles a different P_i case; the first deals with P_5 set, in which case the exchange automatically succeeds. In the second, P_4 is set, but P_5 not; now $\Delta H = +4$, so we AND with U_1 to get the correct exchange probability. The other parentheses follow similarly.

When Q_1 is set, but not Q_2, both the cases P_5 set and P_4 set correspond to automatic exchange success. We thus replace the first expression in parentheses in (8.6), (P_5), with $P_5 \vee P_4$, and "shift along" the variables $U_{1\ldots4}$; U_5 now does not appear, since ΔH is at most $+16$ in this situation. The expression that handles both cases is then

$$\begin{aligned} p_w =&(S_1 \oplus S_2) \wedge \\ &\left\{\left[\overline{Q_1} \wedge ((P_5) \vee (\overline{P_5} \wedge P_4 \wedge U_1) \vee (\overline{P_4} \wedge P_3 \wedge U_2) \vee (\overline{P_3} \wedge P_2 \wedge U_3) \vee \right.\right. \\ &\left.(\overline{P_2} \wedge P_1 \wedge U_4) \vee (\overline{P_1} \wedge U_5))\right] \vee \\ &\left[\overline{Q_2} \wedge Q_1 \wedge ((P_5 \vee P_4) \vee (\overline{P_4} \wedge P_3 \wedge U_1) \vee (\overline{P_3} \wedge P_2 \wedge U_2) \vee \right. \\ &\left.\left.(\overline{P_2} \wedge P_1 \wedge U_3) \vee (\overline{P_1} \wedge U_4))\right]\right\}. \end{aligned} \tag{8.7}$$

The first and second lines are just (8.6); the third is the new part. Now that the structure is defined, the full expression which deals with all cases can be built up simply; this is given in Appendix A.

We now have the exchange probabilities for both against- and with-drive moves of S_1; what remains is to combine these to produce the final p for use in (8.1) (with p_{eq} replaced by p). To do this we need knowledge of the relative positions of S_1 and S_2. We now assume that the driving field acts in the x direction only (since this is true of the forms of field defined previously), and that it is directed in the positive x direction. We label the variable of the pair which has the smaller x coordinate by S_l ("left"), and the other by S_r

"right"); if the x coordinates are the same, the choice of labelling does not matter. Thus for example if S_1 is positioned to the left of S_2, we identify S_l with S_1 and S_r with S_2. Now the appropriate test can be applied to each spin in the ensemble by creating "with-drive" and "against-drive" masks, M_w and M_a: the former has bits one only in positions where the bit of S_l is set, and the latter has bits one only in positions where S_r is set. We can arrange this via

$$\begin{aligned} M_w &= S_l \wedge \overline{S_r} \\ M_a &= \overline{M_w}. \end{aligned} \tag{8.8}$$

Finally, we can construct the full exchange probability variable p:

$$p = (M_w \wedge p_w) \vee (M_a \wedge p_a). \tag{8.9}$$

Note that if we wish to swap the field direction, we can simply take the bitwise NOT of M_w and M_a; this makes it easy to implement a shear-like drive, for instance. This concludes the specification of the driven multispin Kawasaki algorithm; what we have not covered is the generation of the various random variables required. Recall that we need variables R, V_i, U_i which have *their bits set* with several different probabilities. A thorough discussion of how to tackle this problem may be found in Ref. [55]; essentially one starts from the "easy" case, where the bits are set with probability 1/2. An integer pseudo-random number generator is a suitable source for this; in this project the primary generator used was a C++ implementation [140] of the Mersenne Twister algorithm [141], which is a reliably uniform generator with an extremely long period, and good speed. The results were also checked with other generators [142]. Random unsigned integer variables obtained from the generator can then be combined appropriately to generate the desired probabilities [55].

8.4 Parallelisation

In three dimensions, the sheer number of lattice sites makes even simple systems such as the Ising model computationally demanding. This is especially true for the present case: long runs are required in systems with an interface evolving under the local, slow, Kawasaki dynamics. Additionally, while the multispin algorithm will prove to be valuable in obtaining precise results for observables, a single Monte Carlo step does take significantly

longer (approximately twice as long) than with a single-spin implementation. For these reasons the $3d$ driven Ising simulations were parallelised, both by domain decomposition for running the actual MC algorithm, and also separately for data processing.

Domain decomposition, as the name implies, is the technique of splitting the lattice up into several sub-domains [55], which are then worked on (semi-)independently by different threads/processes/cluster notes (depending on the details of the parallelisation employed). In the ideal case, the real ("wall-clock") time taken for a simulation of given length is reduced by a factor N_t, where N_t is the degree of parallelisation (number of threads, or similar). Of course, in practice, this is not the case, because the different sub-domains are not entirely independent, so that there is some degree of synchronization overhead. Therefore, when implementing parallelisation via domain decomposition, we wish to keep this overhead small, whilst still producing a correct MC algorithm. The choice of how the lattice is divided up, and the number of sub-domains used, affects the overhead. For the driven Ising system being simulated here, the basic (Kawasaki) dynamics are local, so communication and synchronization between sub-domains is only necessary at the boundaries between them. We therefore wish to keep the inter-domain contact boundary area-to-domain volume ratio small; of course, there is a trade-off here, because *minimizing* this quantity corresponds to just one sub-domain! In practice, testing is required to determine a good balance.

In any case, for the driven Ising system with x and y boundaries periodic, a simple and efficient choice for *how* to effect the decomposition is to divide the lattice along x. Then, for an $L_x \times L_y \times L_z$ lattice (recall $L_z \ll L_x,\ L_y$), the contact area is $L_y L_z$ per sub-domain, and sub-domains are of dimensions $(L_x/N_t) \times L_y \times L_z$. The parallelisation must then be implemented such that at least in equilibrium, detailed balance and ergodicity are respected. One method to do this, as explained in [55], is to not perform any exchanges for which ΔH depends on the value of a spin in a neighbouring sub-domain. The other ("interior") spins can be exchanged without any synchronization or communication with other sub-domains. Then, periodically, the borders of the domains are translated, so all the spins are given the chance to be updated (otherwise the algorithm would be non-ergodic). In fact, here we do not do this, but instead allow all spins to be exchanged, and perform the necessary synchronization if neighbouring domains choose to update spins at or near their border at the same time. This approach was taken in view of the presence of drive (and therefore current) in the system: if the border regions are fixed, then a "build-up" of

spins at a border could take place, which would be contrary to the aim of the microscopic dynamics.

In the approach used, each domain runs in its own thread, and neighbouring pairs of domains share a locking primitive [143] (chosen to be a spinlock, after testing different solutions), which is used to provide mutual exclusion during the update of lattice sites near their border. The parallelised algorithm for each sub-domain proceeds as follows:

1. Choose a random spin i, the first candidate exchangee.

2. Choose a random nearest-neighbour of i (j), the other candidate exchangee.

3. If either of these is in a border region, then acquire the appropriate lock. This prevents the neighbouring domain from updating spins in the sensitive region until the lock is released. If the lock is currently held by the neighbour domain, the thread will block here until it can acquire it.

4. Calculate the acceptance probability and carry out the exchange if it is accepted (this could be a multispin implementation, or a single-spin – it makes no difference at this level).

5. If a lock was acquired, release it.

Due to the vagaries of the operating system scheduler and the hardware, the threads will not all run at exactly the same speed (measured in MC steps per unit time). If some threads lag behind significantly, the driven dynamics begin to be affected. Therefore in the implementation, the threads are periodically made to wait at a *barrier* [143] synchronization object. When all threads have reached this barrier, the "local" MC time in each is known to be synchronized. The interval between barrier synchronizations is chosen as a balance between efficiency and minimizing any effect on the dynamics. If the interval is too long, "build-ups" similar to that mentioned above may occur; we have observed that this has a small but observable effect on interface time correlation functions. In practice, one must carry out preliminary tests, by comparing data from a single-threaded run with that from a parallel run, to ensure there are no anomalies.

The barrier is also a convenient point to measure observables required from the simulation. When using a multispin algorithmic core, a large amount of data is produced (i.e., 64 systems' worth). This means that a relatively large amount of processing must

be done in order to calculate observables – therefore this part of the program was also parallelised. A classic producer-consumer approach was used, with a pool of threads being "fed" a lattice configuration snapshot periodically, which could then be used to calculate any observable of interest. Different observables were divided among the threads in the pool in a reasonably fair way, such that the more computationally expensive observables were shared out. For the actual calculations, the multispin data were "demultiplexed" into separate single-spin lattices for processing – although for some quantities, direct calculation from the multispin state is possible, it is extremely inconvenient, or impossible, for others.

This concludes the details of the computational methods used. The simulation code was written in C++, making use of the Blitz++ [144], Boost [145], FFTW [146], RapidXML [147] and CImg [148] libraries, as well as the previously-mentioned random number library [140]. We now turn to the results of the Monte Carlo simulations.

Chapter 9

Results in two dimensions

We first discuss the two-dimensional driven Ising lattice gas. All simulations were done on a $2d$ square lattice. For the majority of the simulations, $L_x = 200$ was chosen for the lateral system length, with the wall separation distance L_z varying from 10 to 40, allowing a variety of aspect ratios and degrees of confinement. Some results are also shown for systems with larger L_x; simulations were carried out at up to $L_x = 1250$. As mentioned earlier, the fixed total magnetisation was chosen to be $m = 0$. Simulations were carried out at $T/T_c^{2d} = 0.75, 0.85, 0.95$, where $T_c^{2d} = 2.269\ldots$ is the bulk equilibrium $2d$ Ising critical temperature [51]. In this chapter we abbreviate T_c^{2d} to T_c, since we exclusively discuss two-dimensional systems. The time required to reach a steady state was measured by carrying out test runs of several different lengths, and comparing the results to determine whether they agreed to within statistical errors. The initial state was chosen to be the $T = 0$ ground state, i.e. all '+' ('−') in the upper (lower) half of the system – since the system is expected to phase separate, this choice should reduce the time to reach a steady state. Quenching from a random ($T = \infty$) initial configuration was also tested, and confirmed to give the same steady state. The pre-measurement period in the "production" runs was then chosen to be the minimum time required as determined by these tests, plus a significant extra amount, in order to be safe. The time to reach a steady state was found to vary significantly with applied drive, being longest for *zero* drive, i.e., equilibrium. This longest steady state time was 10^8 Monte Carlo sweeps (MCS), where as defined earlier, 1MCS corresponds to $N = L_x \times L_z$ trial moves – one per spin, on the average. Measurements were then taken over another 10^8 MCS in the steady state, a sufficient length of time to produce good statistics (especially when combined with the multispin

method) for all observables.

Statistical errors were estimated primarily by the bootstrap technique [55, 149], a flexible method which can handle errors on observables which have more than one correlated element, as well as providing a reliable error estimate when measurements are taken more frequently than the autocorrelation time for a particular observable in the system. The bootstrap method is one of a family of "resampling" methods, where one repeatedly calculates the relevant observable from samples taken from the full data set, and calculates the standard error of these results; this converges to the true standard error. The blocking technique [150, 151] was also experimented with. Finally, in some cases, quantities were averaged over multiple runs, in which case the usual direct error calculation method was applied (checking consistency between independent runs also provides a test of the accuracy of the error estimations). For most observables and parameter sets, the statistical errors are rather small (and highly consistent between different runs), with the multispin method proving to be a great help – indeed, when checking results with a single-spin algorithm, the errors and variance between runs were found to be much greater.

9.1 Simulation snapshots

We first present some simulation "snapshots" to give the reader an idea of what the system really looks like. In Fig. 9.1 we show snapshots of steady state systems in equilibrium, and under both moderate and strong shear-like drive.

Comparing Fig. 9.1a-c, the most striking change when the system is driven is that the interface becomes *smoother*; in the $\gamma = 2$ case, the smoothening is quite dramatic. The large fluctuations present on the equilibrium interface seem to be destroyed by the drive (although they are for a single time, these snapshots are representative of the steady state behaviours). At this point we can already say that the interface of a system driven by the shear-like drive is "less rough" than its equilibrium counterpart. Indeed, these snapshots are rather reminiscent of the experimental system of Derks *et al.* [13]. We next develop this quantitatively, via the various observables which probe the system's structure. First we address the current in the system, since this provides a good introduction to the action of the drive.

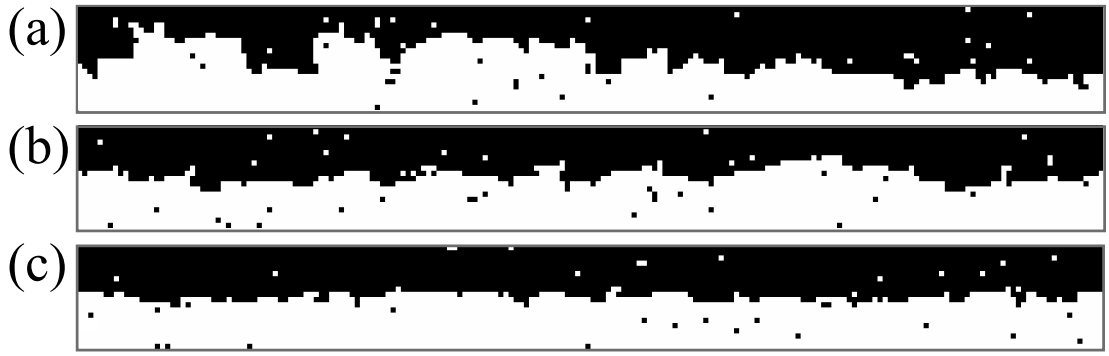

Figure 9.1: Snapshots taken in the steady state from MC simulations of an $L_x = 200$, $L_z = 20$ system at temperature $T/T_c = 0.75$. (a) Equilibrium, no drive applied: the interfacial fluctuations are strong. (b) Shear-like drive of moderate strength, $\gamma = 0.5$: the largest fluctuations present in (a) are absent here. (c) Strong shear-like drive with $\gamma = 2.0$: the interface is now quite smooth.

9.2 Current profile

Driving in the x direction creates a non-vanishing current profile $j^x(z)$ in this direction (parallel to the walls). We define the full (vector) order parameter current profile as

$$\mathbf{j}(z) = \mathbf{j}_+(z) - \mathbf{j}_-(z) \tag{9.1}$$

where the $\mathbf{j}_\sigma(z)$ are the current profiles of the ± 1 spin species. The x-component $j^x_\sigma(z)$ of $\mathbf{j}_\sigma(z)$ is the net number of spins of that species moving in the positive x direction per unit time (MCS) at perpendicular coordinate z. The Ising symmetry means that the current profile can also be written as $\mathbf{j}(z) = 2\mathbf{j}_+(z)$; the definition (9.1) may be applied to systems lacking the Ising symmetry, such as liquid-gas or liquid-liquid interfaces, or the Blume-Capel model. This definition also generalizes to three dimensions.

In Fig. 9.2 we display results for the current profile as a function of the scaled variable $\tilde{z} \equiv 2z/L_z$, for equilibrium and for various types and strengths of drive. When no drive is applied, the system reaches a thermal equilibrium steady state, with zero average current for all $\tilde{z}$. For the boundary-driven case, the current is localized at the walls and vanishes in the middle of the system. This lack of a bulk current highlights the lack of hydrodynamic interactions in our system – only in layers where the drive is applied locally can there be a non-zero current. In the shear-like drive case $j^x(\tilde{z})$ varies smoothly with $\tilde{z}$, see Fig. 9.2a. For small values of γ, a near-linear behaviour is observed. For strong drive the current

saturates upon approaching the walls, and $|j(\tilde{z})|$ displays pronounced maxima either side of the mean interface position ($\tilde{z} = 0$) at the center of the system. This change in shape can be explained by recalling that the observed current depends on not only drive strength, but also on carrier density (particle-hole or ± 1 pairs). For the larger values of γ, the interface is less rough (as we saw in Fig. 9.1), and so there are fewer particle-hole pairs available for exchange at z values far from the centre of the strip (this point will be reinforced by the magnetisation profiles shown in the next section). Therefore, despite the smaller driving strength near the centre, the large carrier density can "win" and produce maxima at these locations.

Fig. 9.2b shows the form of the current for the other drive types. For a spatially uniform drive, the current takes the same sign throughout the system. Despite the homogeneity of the field, the current displays a maximum at the centre of the system (the mean interface position). As for shear, this reflects the greater carrier density in this region. Indeed, for the $f = 0.5$ and $f = 1.0$ cases shown, by only three or four lattice spacings away from the maximum the current has decayed significantly and plateaued, indicating that the carrier density is essentially constant in the rest of the system for these parameters. This suggests a sharp magnetisation profile, which is indeed the case (see next section). The data for the step field of strength $f = 0.5$ follow the uniform drive data closely for $\tilde{z} > 0$, deviating only slightly at the middle of the system. Due to the symmetry of the field, the current then swaps sign around $\tilde{z} = 0$ (the connecting line, as with all lines in the figure, is purely a guide to the eye). The current profile for the V-shaped field looks rather odd at first, but comparing with the data for shear-like drive in Fig. 9.2a, one sees that they really have the same shape for $\tilde{z} > 0$ (and are reflections of one another for $\tilde{z} < 0$), apart from the points directly next to the midline. Indeed, plotting the data together shows close agreement. Due to the even symmetry, a strange "valley" shape is induced around the midline of the system for the V-shaped field.

These trends extend to larger system sizes: Fig. 9.3 shows results for an $L_x = 450$, $L_y = 30$ system at $T/T_c = 0.75$. At small shear-like drive strength γ, the current is very close to linear; for stronger drive, maxima develop near the middle of the strip, as before. The magnitude of the current also attains similar values to those in the smaller system.

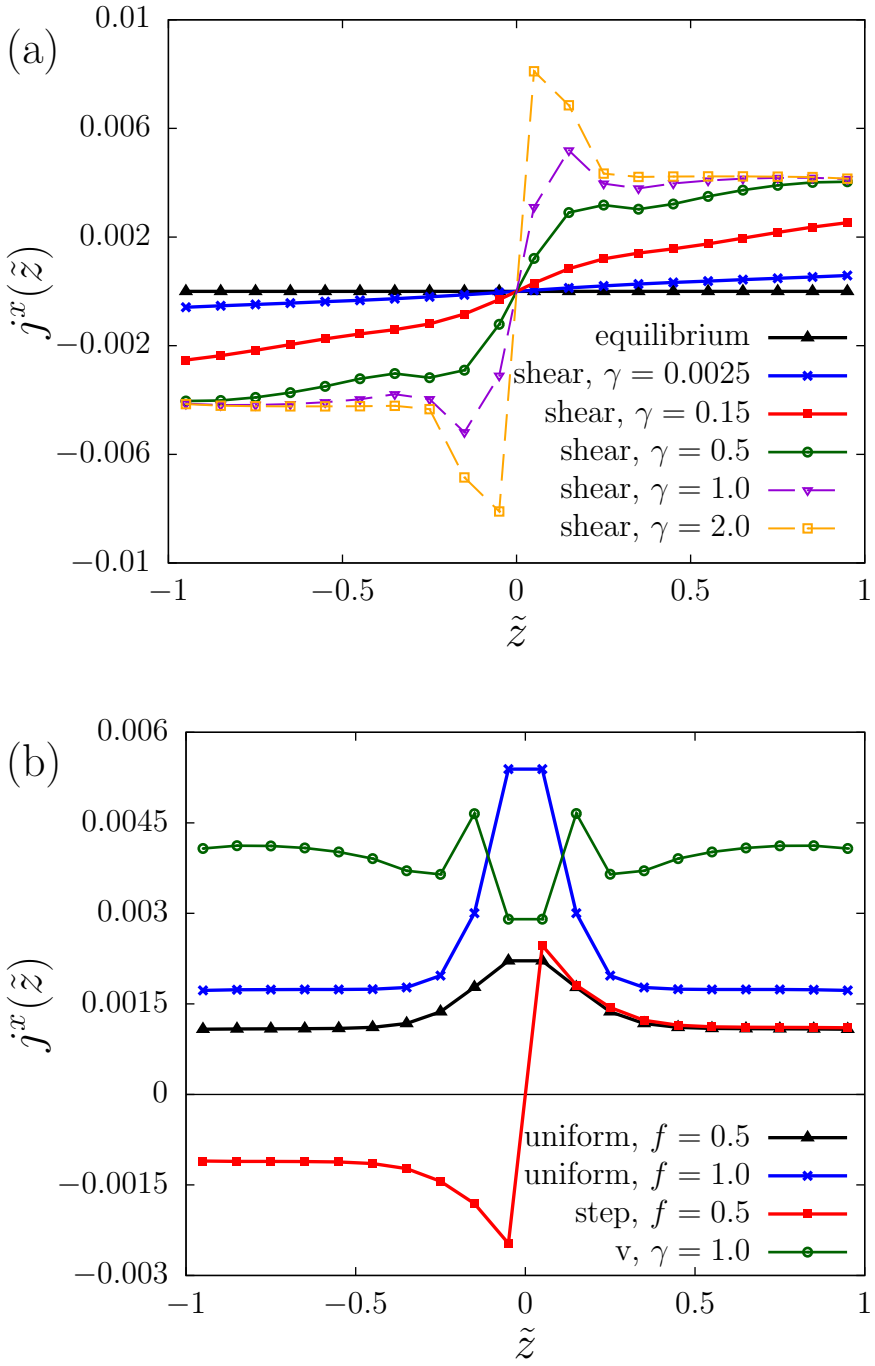

Figure 9.2: Current profiles $j^x(\tilde{z})$ for an $L_x = 200$, $L_z = 20$ system at temperature $T/T_c = 0.75$. Error bars are of order or smaller than the symbol size. (a) Results for equilibrium (where the current is zero), and several values of shear-like drive strength γ. (b) Results for other drive types: spatially uniform drive, step-like drive, the V-shaped drive, as introduced in Chapter 7.

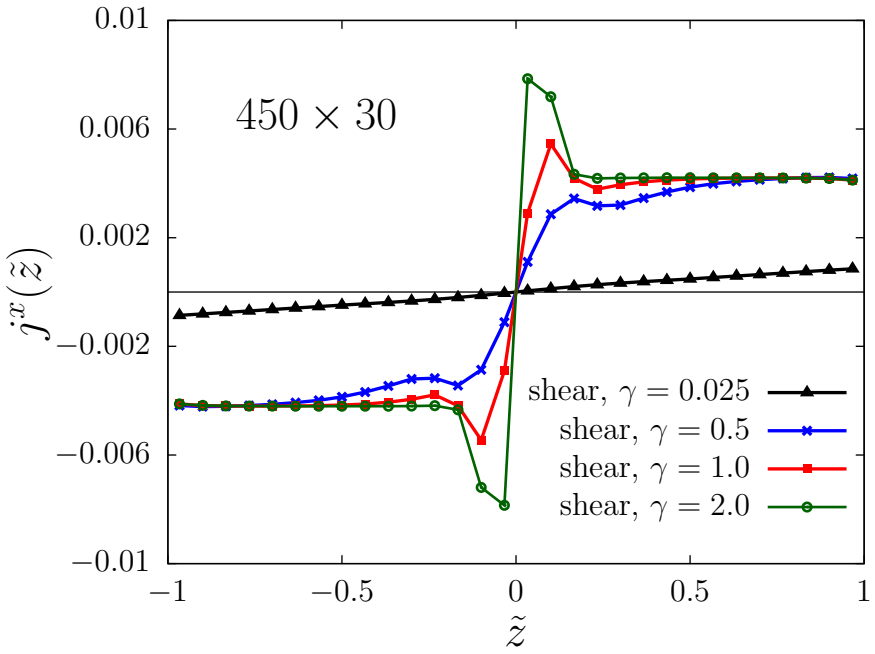

Figure 9.3: Current profiles $j^x(\tilde{z})$ for a system of dimensions $L_x = 450$, $L_z = 30$ at temperature $T/T_c = 0.75$. Results are shown for several values of shear-like drive; there is good agreement with the data from the smaller 200×20 system, both in shape and amplitude.

9.3 Statics: interface structure

9.3.1 Magnetisation profile

We now turn to the static, structural properties of the driven Ising system, starting with the magnetisation profile between the lower and upper walls, $m(z)$; in lattice-gas language, this is the density profile. In two dimensions, this is calculated as

$$m(z) = \frac{1}{L_x} \left\langle \sum_x \sigma(x,z) \right\rangle , \tag{9.2}$$

where the angles denote a time average in the steady state. For each z, $m(z)$ is just the average magnetisation in that layer. In a phase-separated system $m(z)$ changes sign across the interface, and attains values close to $+1$ (-1) near the upper (lower) walls. In Fig. 9.4 we plot the magnetisation profile, scaled by the spontaneous (bulk) magnetisation of the infinite system m_b, as a function of the scaled variable $\tilde{z}$. Recall from Sec. 3.5 that in $2d$ in equilibrium, exact results for the magnetisation profile are available for the infinite-strip geometry $L_x \to \infty$, L_z finite. For large enough aspect ratio L_x/L_z in the simulation system, the equilibrium simulation data should follow this closely – indeed from the inset of Fig. 9.4a we see that this is the case for $L_x = 200$, $L_z = 20$, corresponding to an aspect ratio of 10. The agreement is not perfect even for this reasonably large aspect ratio; this is due to the nature of the Kawasaki dynamics; we discuss this issue in Sec. 9.4. Going to larger aspect ratios does improve the agreement, but then either larger systems are required, which are slower to simulate, or one must use a rather small L_z, which gives few data points to work with along the z axis.

For the equilibrium system, we see that the variation of $m(\tilde{z})$ with $\tilde{z}$ is rather slow, and that $m(\tilde{z})$ does not really plateau at a "bulk" value away from both the middle of the strip and the walls in either phase. This is due to strong capillary-wave fluctuations, which cause the local interface position to explore the entire strip. In a van der Waals-style mean-field treatment (Sec. 2.2), these fluctuations are absent, and so the profile is very sharp – see the figure for an example of a profile from a mean-field theory [123].

When drive is applied to the system, the shape of the profile changes. In all cases, the profile becomes sharper compared to the equilibrium case: $m(\tilde{z})$ changes sign more rapidly in the interfacial region, and the absolute value $|m(\tilde{z})|$ near the walls is larger. In the case of boundary drive, this effect increases with increasing f_w up to a saturation point at $f_w \approx 5$, beyond which there are no further changes to the profile, within error bars. Fig. 9.4a shows

this limiting behaviour, for $f_w = 50$ (essentially infinite, since particle moves against the field are suppressed by a factor of the order e^{-50}). For weak shear-like drive, $\gamma = 0.025$, we see that the effect on $m(\tilde{z})$ is rather similar to that of the boundary drive. For larger γ, the profile is very strongly affected: for $\gamma = 1.0$, $m(\tilde{z})$ becomes almost kink-like, which is reminiscent of the mean-field profile obtained by *neglecting* CW fluctuations. It also mimics the effect of a reduced temperature (the zero-temperature profile is a strict step function) in an equilibrium system. The other types of drive illustrated in Fig. 9.4b show similar effects on $m(\tilde{z})$. Comparing the shear-like and V-shaped drive, we find that for given γ, the V-shaped field produces a slightly larger effect on the profile than its odd-symmetric counterpart. For uniform and step-like drive, the situation is not so simple: we find that at small field strength f, the latter has a stronger effect, but as f increases, the uniform "catches up", and for $f \gtrsim 0.25$, shows a greater effect than the step field. For these bulk-driven cases (i.e., all except the boundary drive), the limiting behaviour of the profile for strong drive appears to be almost step function-like – the profile shape attains its limiting form. This is in contrast to the boundary-driven case, where the maximum effect is limited by the fact that the system is only driven in two layers next to the walls. What *is* common to all cases is that capillary-wave fluctuations, which broaden the profile, seem to be suppressed, to a greater or lesser degree. This finding is in agreement with the KLS simulations of Leung *et al.* [103], where the magnetisation profile was also measured. Similar behaviour is also seen in the energy bond profiles between the walls; we have also presented [68] data for these quantities in our system.

A natural question to ask is: what is the *microscopic* physical mechanism responsible for this behaviour? Part of the answer lies in the competition between advection and diffusion. In the system there are always "intruders" of one phase into the other. These may be single spins, or clusters. In equilibrium, a cluster of two or more intruders is much less mobile than a lone intruder – this is because bond(s) must be broken in order to move any member of the cluster. The driving field helps to break up clusters into their constituents, because its effect can counteract the cost of bond-breaking, if the move is in the favoured direction. The resulting lone intruders can diffuse *freely* in the other phase, and finally coalesce with their own phase. This reduction (on the average) in intruders will contribute to the sharpening of the magnetisation profiles. However, this argument is certainly not the whole answer, at least for the bulk-driven cases – it does not address the interfacial fluctuations themselves directly. Unfortunately, we are not able to provide a

quantitative microscopic argument for how the bulk drive suppresses capillary waves. It is physically plausible, however, that the drive detaches particles from the "leading edge" of a fluctuation, which then become intruders – the previous mechanism could then be applied. What is missing is a calculation to make the details precise – unfortunately, attempts at this either by a dynamic mean-field approach, or considering microsopic transitions, have not yielded a solution.

Rescaling and effective confinement

However, we do have a strong and appealing physical *interpretation* of the effect of drive on the profile, as well as on other structural observables. This is that the drive acts to produce an *effective increase in confinement* of the *equilibrium* system, by reducing the effective distance between the walls [123]. In terms of the finite-size scaling function for the profile (see Eqn. (3.20)), this argument may be summarized as:

$$\frac{m(z,T,L_z)}{m_{\rm b}(T)} \approx \mathcal{M}_{\rm eq}\left(\frac{z}{L_z^*},\frac{L_z*}{\xi_b(T)}\right) + \mathcal{M}_{\rm corr}(z) \qquad \text{with } L_z^* < L_z. \tag{9.3}$$

Here $\mathcal{M}_{\rm eq}$ is the equilibrium finite-size scaling function of Eqn. (3.20), L_z is the actual wall separation, L_z^* is the effective wall separation under drive, and $\mathcal{M}_{\rm corr}$ is a boundary correction that decays away from the walls on the scale of the bulk correlation length ξ_b. Eqn. (9.3) says that the non-equilibrium profile $m(z)$ is controlled by the equilibrium scaling function, with a smaller wall separation. For the simulation data, this corresponds to the scaling $m(a_\perp z) \approx m_{\rm eq}(z)$, where $a_\perp = L_z^*/L_z$ is the ratio of the effective and actual wall separations. In the $2d$ system, we neglect the boundary correction term, and use the full range of the profile data in the rescaling. In the $3d$ system we treat the process rather more systematically, as will be explained later, but this is not critical to the conclusions. For limiting boundary drive, rescaling the driven profile to the equilibrium one is possible, as shown in Fig. 9.5, with $a_\perp = 0.83$; interestingly, this value is the same for all values of T and L_z tested. Rescaling is also possible for the other drive types. In Fig. 9.5 we give examples for shear-like drive for a wide variety of γ – note that rescaling is possible for the profile even in the strongly-driven case $\gamma = 1$, where the effective wall separation L_z^* is greatly reduced ($a_\perp = 1/3.4 \approx 0.29$ for $\gamma = 1.0$). For shear and the other bulk driven cases, $a_\perp$ does depend on the temperature and wall separation, unlike for boundary drive. With increasing wall separation L_z at fixed T and drive strength, $a_\perp$ decreases, showing that the confinement effect of drive becomes larger. This will be seen again when we discuss the

interface width in the next section. For fixed L_z and drive strength, increasing T to $0.85T_c$ leads to a slightly weaker confinement effect, while decreasing the temperature to $0.6T_c$ increases the effect fairly significantly. These changes are greater for weak driving fields: in the case of shear-like drive with $\gamma = 0.025$, $a_\perp = 0.93, 0.87$, and 0.67 for $T/T_c = 0.85, 0.75$ and 0.6, respectively. Next, we investigate other observables in order to develop the effective-confinement idea further.

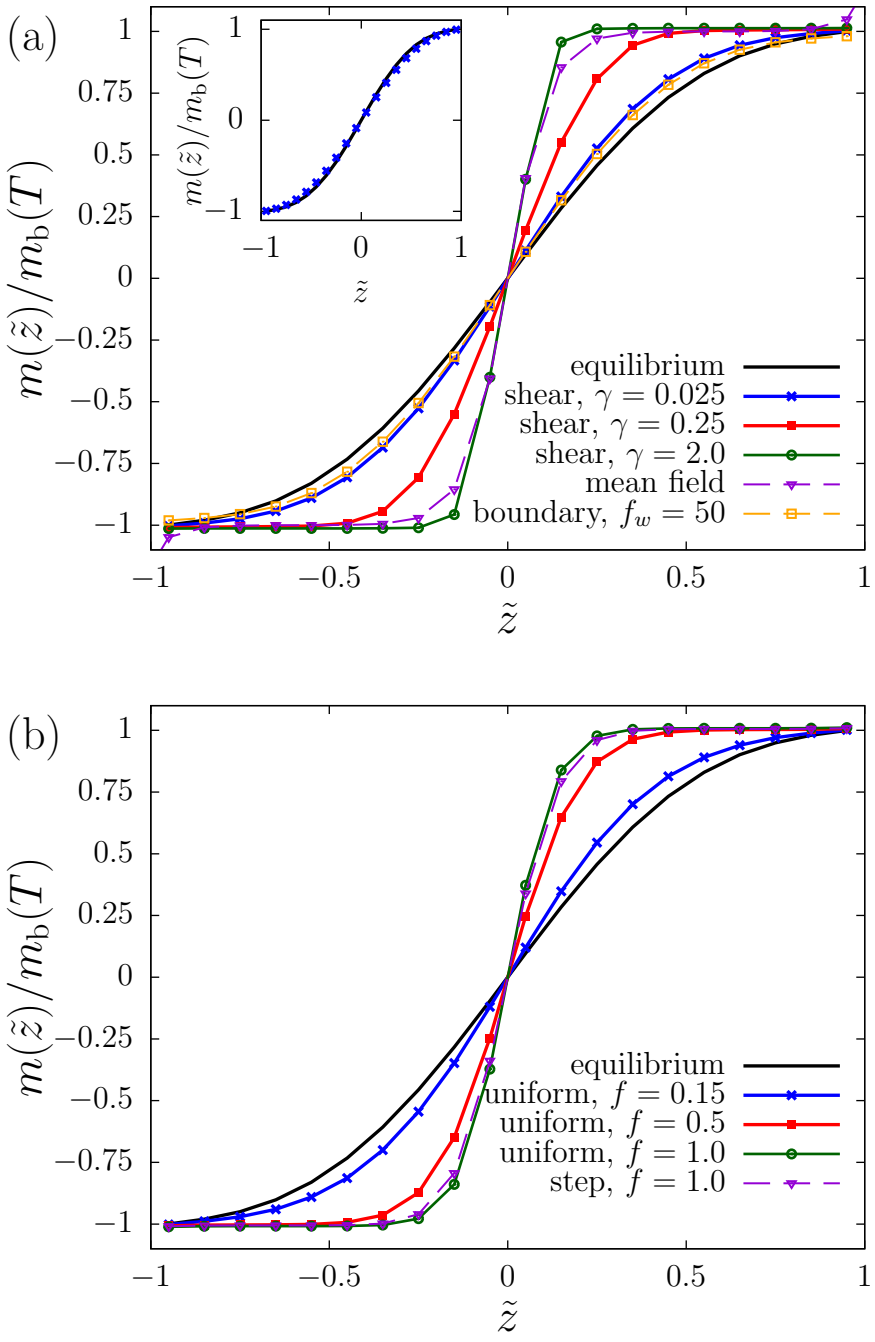

Figure 9.4: Magnetisation profiles $m(\tilde{z})$ scaled by the spontaneous (bulk) magnetisation $m_b(T)$, as a function of the scaled coordinate $\tilde{z}$. The system is $L_x = 200$, $L_z = 20$ at temperature $T/T_c = 0.75$. (a) Results for Kawasaki dynamics in equilibrium, as well from (equilibrium) mean-field theory, and both boundary and shear-like drive. Inset: comparison of the exact result from transfer matrix diagonalization, and from Kawasaki dynamics simulations. (b) Results for the uniform and step-like bulk drive variants, compared to the equilibrium result. Error bars are of order or smaller than the symbol size.

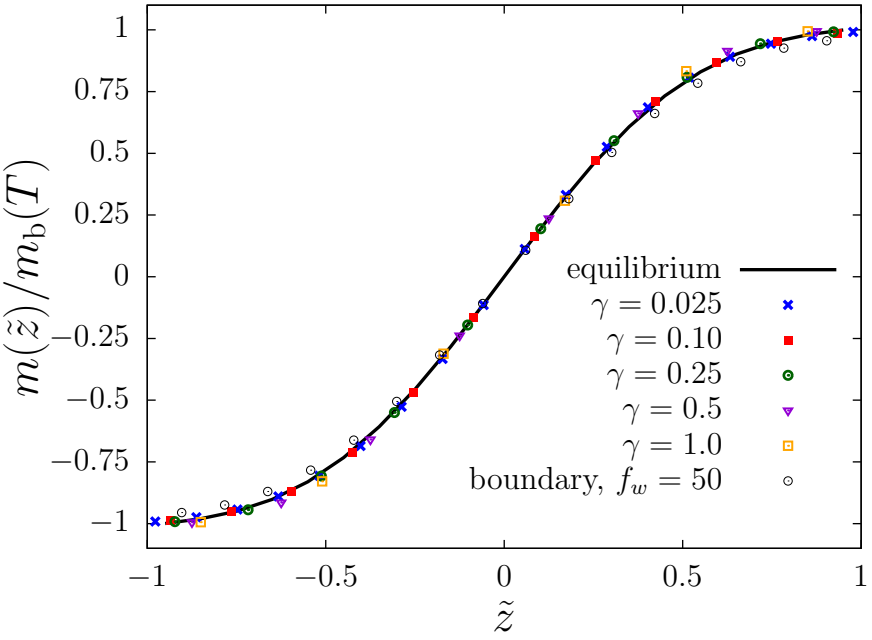

Figure 9.5: Results of rescaling on the magnetisation profile according to $m(z) \approx m_{\rm eq}(a_\perp z)$. The system size and temperature are the same as in Fig. 9.4. The equilibrium profile with Kawasaki dynamics is shown, as well as the results of rescaling the data from several values of shear-like drive, as indicated, and also the boundary drive data. The values of $a_\perp$ are 1/1.15, 1/1.7, 1/2.05, 1/2.5 and 1/3.4, for γ increasing as in the figure. For the limiting boundary drive, $a_\perp = 0.83$.

9.3.2 Interface width

These results for the profile have implications for the width of the interface. Previously in Sec. 2.3.1 we defined the (squared) interfacial width w^2 by $C(\mathbf{r} = 0)$, the zero-separation value of the static height-height correlation function. An alternative definition may be made from the second moment of $\partial m(z)/\partial z$:

$$w^2 \equiv 2\frac{\int dz\, z^2 \frac{\partial m(z)}{\partial z}}{\int dz\, \frac{\partial m(z)}{\partial z}}, \tag{9.4}$$

where the integrals extend between the walls. From earlier, Eqn. (2.35), we have $w \propto L_z$ for equilibrium confined Ising interfaces. We therefore expect the width to reduce when drive is applied (this is also obvious from visual inspection of the driven configurations and profiles). Fig. 9.6a, where we plot w versus driving strength parameter (γ or f) for several system sizes and temperatures, shows that this is indeed the case. The trend is rather similar in all shear-like cases shown with $L_z > 10$. The gradient is nonlinear, as the width reduces rapidly as the drive is increased from zero, and then falls more slowly in the strongly driven region. This is to be expected from the results for the profile – the effect of the drive (on this quantity, at least) begins to saturate as we approach $\gamma \approx 1$. For $L_z = 10$, the variation is closer to linear, since the system is already quite strongly confined in equilibrium, so again we experience "diminishing returns". Increasing the temperature to $0.85T_c$ increases the interfacial width, since thermal fluctuations are stronger, but the effect of the drive is qualitatively the same.

The rescaling and effective-confinement idea which we applied to the magnetisation profile says that the structure of the driven system should be like that of an equilibrium system with a smaller wall separation. According to this, the width should vary linearly with the effective wall separation L_z^* – a prediction we can test here. Indeed, a plot of w against L_z^* for fixed actual wall separation L_z may be well-fitted by a straight line, albeit with a non-zero intercept (this is not a big concern, because at extremely small L_z, the whole concept of an interface is not particularly meaningful). This result strengthens the effective-confinement picture, and is a rather more stringent test than rescaling the profile, since $w \propto L_z^*$ would seem harder to find fortuitously.

Unexpectedly, we are also able to obtain data collapse for the width from several different system sizes and shear-like drive strengths for given temperature, when w/L_z is plotted as a function of a scaling variable $\theta = L_z\gamma^s$, see Fig. 9.6b. Here s is an

adjustable exponent; data collapse is achieved for $s = 0.3$. The division of the width by L_z corresponds to the equilibrium scaling, as long as the system is in the confined regime $L_x \gg L_z$. Thus as $\theta \to 0$, the $w/L_z \to$ constant. As shown in the figure, the data collapse is rather good over a wide range of γ from 0.025 to 1.0 and several values of L_z from 10 to 40 (as detailed in the figure caption). The equilibrium data themselves deserve comment: clearly $w/L_z =$ const. does not hold for this whole range of L_z (10 to 40) – this is shown by the inset of Fig. 9.6b, where w/L_z does not vary much with L_z for $L_z \leq 20$, but drops sharply for $L_z = 30$, 40. This suggests that the system is no longer fully in the confined regime for $L_z \gtrsim 20$ when $L_x = 200$ – there should be some crossover region where w is still dependent on L_z (unlike for fully free, unconfined, interfaces – Eqn. (2.18) with $g \to 0$), but with a different functional dependence. In any case, for $L_z \leq 20$, the driven data available do seem to be approaching the equilibrium limit.

Although the origin of this scaling is mysterious, the existence of a scaling variable coupling L_z and γ is intriguing. It seems likely that the scaling is part of the effective-confinement picture of the action of drive on the system, but it is not clear whether this is indeed true, and if so, what the physical meaning of the scaling variable θ is. To cloud the issue further, it seems to be possible to include the reduced temperature $|t| \equiv |(T - T_c)/T_c|$ in the scaling variable, so that θ becomes $L_z(\gamma|t|)^s$; again $s = 0.3$. See Fig. 9.7, which demonstrates data collapse for a variety of L_z and γ, as before, and now also a second temperature $T/T_c = 0.85$ ($|t| = 0.15$). Data from $T/T_c = 0.6$ do not follow the scaling, suggesting that it only applies in reasonably close proximity to the critical point. It is interesting to compare our findings for the width to the KLS results of Leung *et al.* [103]. Firstly, as discussed in Sec. 4.2.5, the interface width was also found to be reduced by driving in that study (recall that their system was not strongly confined, so there is some difference from the uniform field case in the present work). Furthermore, those authors found a similar data collapse for the width results, as a function of a scaling variable involving L_x, their (uniform) driving field strength E (equivalent to f in our notation), and the temperature. On the scaling plot the width data were also scaled differently, by L_x, and w^2 rather than w was used. The appearance of L_x and w^2 rather than L_z and w is due to the absence of strong confinement for their system geometries, so that the lateral correlation length $\xi_{\|}$ is limited by the finiteness of L_x, and $w^2 \propto L_x$ [7]. Despite the differences, it seems likely that the scaling in [103] is related to the one shown here (indeed, inspiration for investigating this aspect came from that paper!).

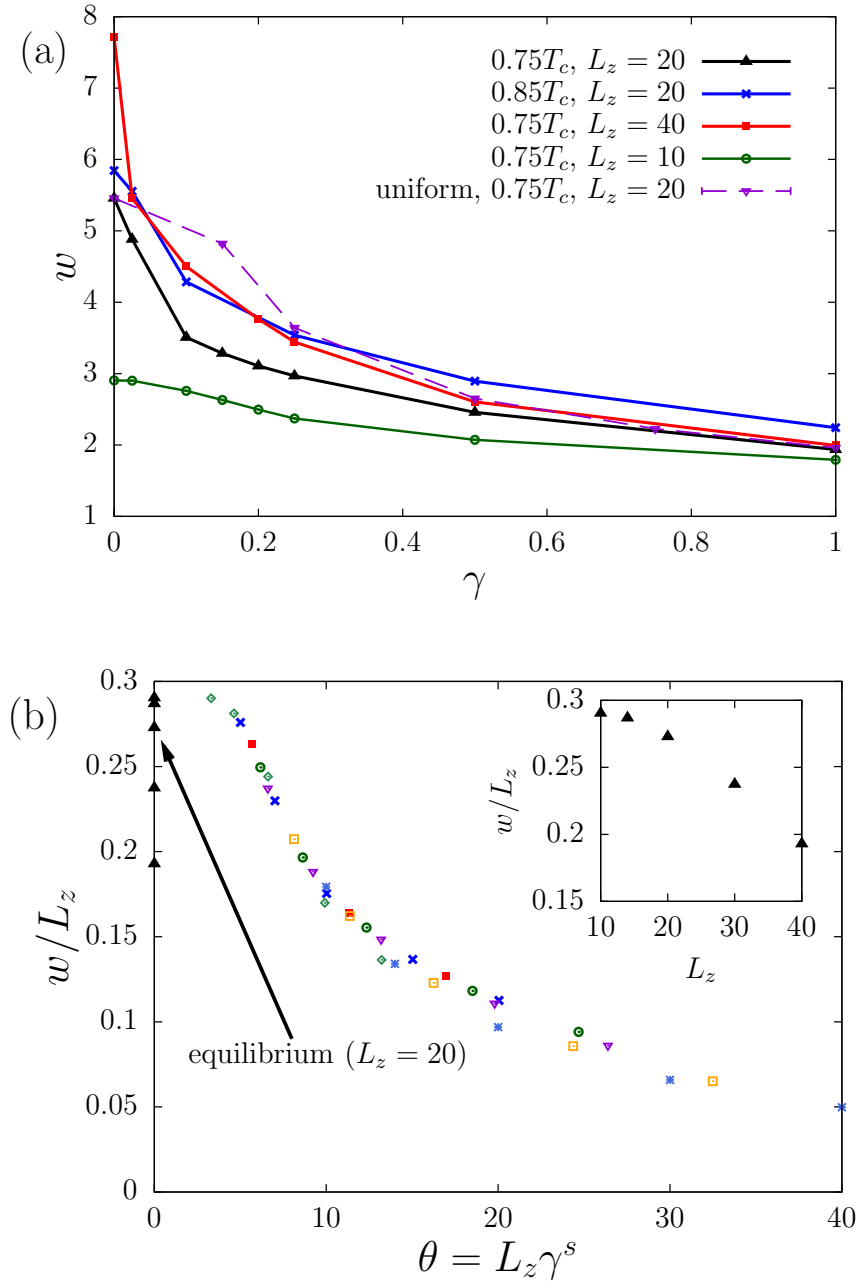

Figure 9.6: (a) Interface width w plotted against driving strength parameter (γ for shear, f for uniform drive) for various L_z values and two temperatures $T/T_c = 0.75$, 0.85. The lateral system length $L_x = 200$ in all cases. (b) Variation of the scaled interfacial width w/L_z as a function of the scaling variable $\theta = L_z\gamma^s$, with $s = 0.3$. Data are shown for systems with $L_z = 10$, 14, 20, 30 and 40, and shear-like drive strengths $\gamma = 0.025$ (green diamonds), $\gamma = 0.1$ (blue crosses), $\gamma = 0.15$ (filled red squares), $\gamma = 0.2$ (green open circles), $\gamma = 0.25$ (violet triangles), $\gamma = 0.5$ (orange open squares), and $\gamma = 1.0$ (blue stars). Also shown, intersecting with the y-axis, are the equilibrium results. Inset: equilibrium data plotted as a function of L_z – the infinite-strip result is $w/L_z = \text{const}$.

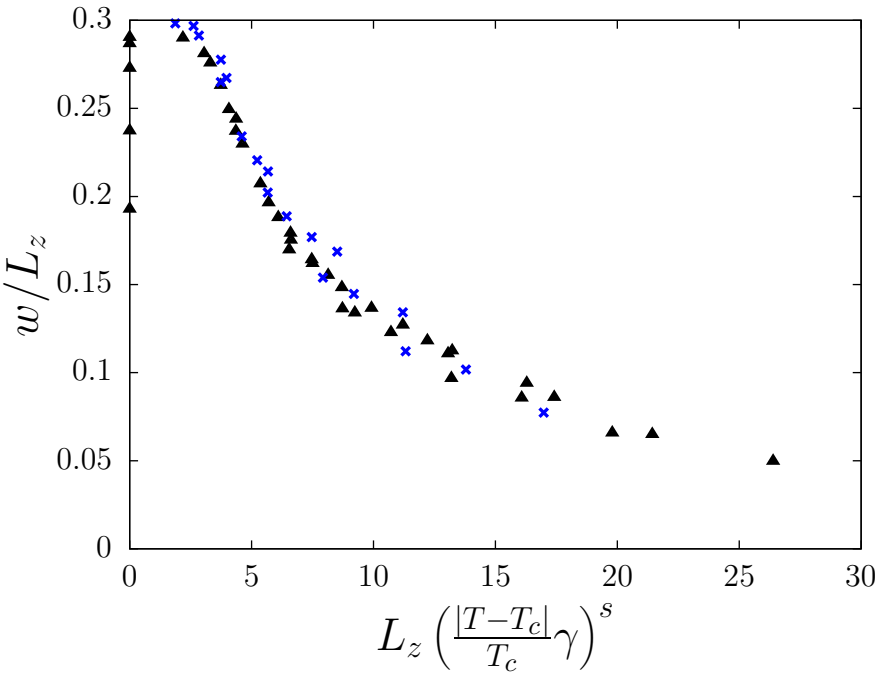

Figure 9.7: Variation of the scaled interfacial width w/L_z as a function of the scaling variable $\theta = L_z(\gamma|\frac{T-T_c}{T_c}|)^s$, with $s = 0.3$. Data are shown for the same values of wall separation L_z and shear-like drive strength γ as in Fig. 9.6b; here data from a second temperature $T/T_c = 0.85$ are also included (blue crosses), in addition to that from $T/T_c = 0.75$ (black triangles).

9.3.3 Spin-spin correlation function at the interface

More information about the structure of the interface under drive can be gained by studying *two-body* quantities, which measure the correlations between spatially separated parts of the system. We first consider the microscopic interface pair correlation function, which is the spin-spin correlation function evaluated at the mean interface position (the middle of the system). In $2d$ this is defined as

$$G(x, z = 1/2) = \frac{1}{L_x} \left\langle \sum_{x'} \sigma(x', z = 1/2)\sigma(x' + x, z = 1/2) \right\rangle . \tag{9.5}$$

We focus on this function since it should reveal the interface-mediated correlations most clearly. Note that there is a two-fold degeneracy in the choice of the z value, for a half-filled ($m = 0$) system with even L_z. Since the $T = 0$ (flat) interface lies *between* two lattice rows, one may measure G at either of the layers just above and below; due to the symmetry in the system, the choice does not matter. Note that due to the measurement location, G as defined in (9.5) will not quite decay to zero, even in an infinite system, since it approaches $\langle \sigma(z = \pm 1/2) \rangle^2 \neq 0$ for $x \to \infty$. Independent measurements of this latter quantity from the simulations showed it to be consistently extremely small, so we neglect it.

The results in Fig. 9.8a show that when shear-like drive is applied, $G(x)$ (we suppress the constant z value) decays more quickly with distance than in equilibrium, with the effect becoming stronger for larger γ. The same is true for the boundary drive, with $f_w = 50$ having a similar effect to shear-like drive with $\gamma = 0.025$. These trends hold for the other drive types, as for the magnetisation profile, see Fig. 9.8b; the shapes of the correlation functions are similar for all variants. In the equilibrium case, $G(x)$ displays significant anti-correlations, becoming negative at $x/L_x \approx 0.2$. This can be attributed to strong finite-size effects, which we discuss in Sec. 9.4. When drive is applied, the negative regions become less deep, and for shear-like drive with $\gamma \gtrsim 0.25$ or uniform drive with $f \gtrsim 0.5$, disappear entirely. Thus it seems that driving reduces the severity of the finite-size effects.

Furthermore, the idea of drive acting as effective confinement can also be successfully applied to $G(x)$, this time by rescaling the *lateral* coordinate x:

$$G(a_{\parallel} x) \approx G_{\mathrm{eq}}(x) \tag{9.6}$$

with

$$a_{\parallel} = \xi_{\parallel} / \xi_{\parallel}^{\mathrm{eq}}, \tag{9.7}$$

where $\xi_\parallel$ is the (non-equilibrium) lateral correlation length, and $\xi_\parallel^{\rm eq}$ its equilibrium counterpart. This relationship comes about by assuming that the non-equilibrium correlation function is a function of $x/\xi_\parallel$, and then requiring equality with the equilibrium correlation function. The parameter $a_\parallel$, the ratio of the lateral correlation lengths in and out of the equilibrium, is the fitting parameter in the procedure. Fig. 9.9 shows some example results of the rescaling; the procedure only works well for boundary drive and *weak* bulk drive (e.g., $\gamma \leq 0.1$ for shear). The failure for stronger drive is perhaps to be expected, given the shapes of $G(x)$ in those cases (Fig. 9.8), which are markedly different from that of the equilibrium data. In the cases where rescaling applies, we find $a_\parallel < 1$, implying that the lateral correlation length is reduced by the application of drive – this tallies with the faster decay already observed. Example values of the rescaling parameter $a_\parallel$ are given in the caption to Fig. 9.9.

How does the reduction of $\xi_\parallel$ relate to increased confinement? In equilibrium confined Ising systems, or from capillary wave theory, $\xi_\parallel \propto L_z^2$ (see Eqn. (2.34) and Sec. 3.5.2). If the effective wall separation is reduced to L_z^*, then this relation predicts a reduction of the correlation length. This of course assumes that the equilibrium result approximately holds when the system is driven out of equilibrium (we already assumed that the profile is controlled by the equilibrium scaling function). Note that the one-body rescaling worked for strong as well as weak bulk drive, which is not the case here – this suggests that a violation of Eqn. (2.34) may be the "culprit". Finally, one observes that the rescaling does not work for large x/L_x – this is mainly due to the equilibrium finite-size effects already mentioned, and tests for driven systems with larger aspect ratios L_x/L_z show better agreement at large separations; see Sec. 9.4 for a comparison of the equilibrium $G(x)$ at different aspect ratios.

We also measured the spin correlations in the x-direction at z values away from the interface: $G(x, z \neq \pm 1/2)$. These show much less structure than the interfacial correlations: even a few lattice spacings away from the interface, the short-range bulk correlations are dominant, resulting in faster decay of G. This is especially striking in the driven cases, e.g., for shear-like drive with $\gamma = 1$, measuring at three lattice spacings away from the centre, G decays to its asymptotic value only only two lattice spacings. This occurs because the strong drive suppresses interfacial fluctuations to such an extent, that even quite near the centre of the system, they cannot be felt. For equilibrium, there is a much smaller effect, because the far stronger interfacial fluctuations exert an influence well into the two phases.

Finally, the aysmptotic value of G increases as we move further from the midline – this is just because $\langle\sigma(z)\rangle^2$ (the squared magnetisation profile) increases towards the walls.

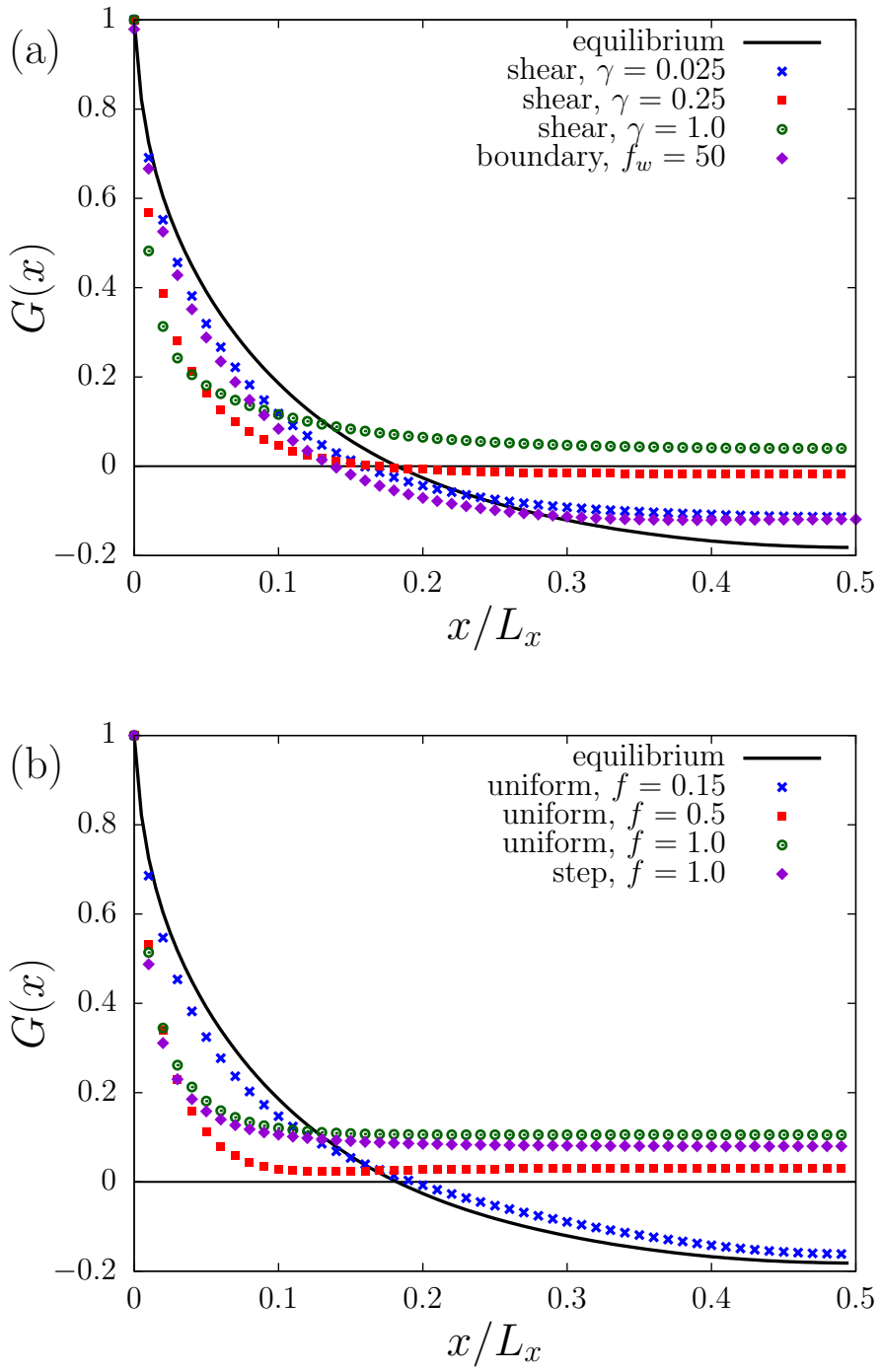

Figure 9.8: Spin-spin correlation function at the interface, $G(x, z = 1/2)$ as a function of scaled coordinate x/L_x, for a 200×20 system at temperature $T/T_c = 0.75$. Error bars are of order or smaller than the symbol size. (a) Results for equilibrium, for limiting boundary drive, and for three values of shear-like drive gradient γ, as indicated. (b) The same equilibrium result is compared to data for uniform and step-like driving fields.

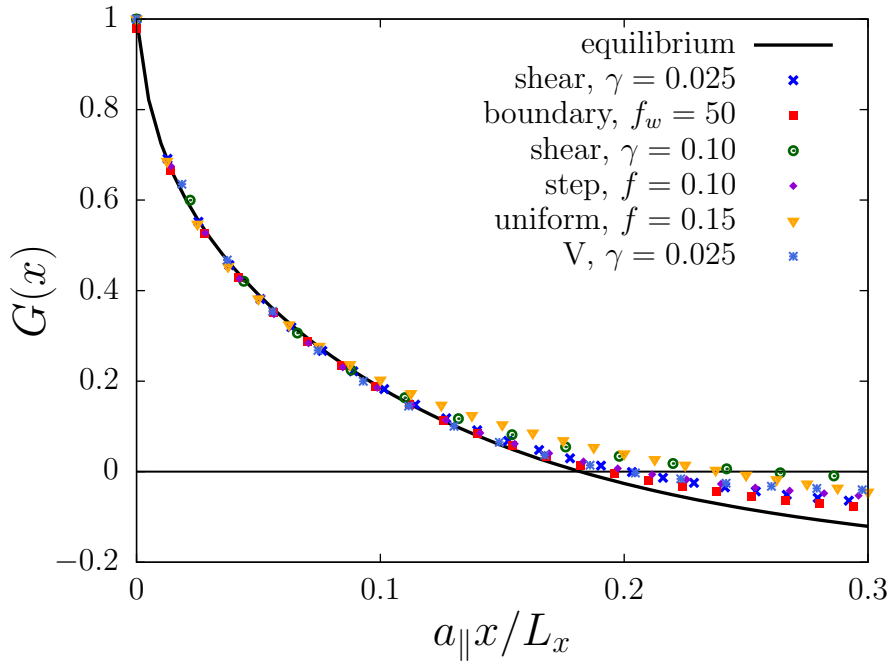

Figure 9.9: Results of the rescaling $G(a_\parallel x) \approx G_{\rm eq}(x)$, for limiting boundary drive and weak shear-like, step, and V-shaped driving fields, where $a_\parallel = \xi_\parallel/\xi_\parallel^{\rm eq}$. The system is again 200×20 at temperature $T/T_c = 0.75$. In the case of boundary drive, $a_\parallel = 1/1.4 \approx 0.7$; for shear-like drive, $a_\parallel = 1/1.27$, $1/2.2$ for $\gamma = 0.025, 0.10$ respectively; for step drive with $f = 0.10$, $a_\parallel = 1/1.41$; for uniform drive with $f = 0.15$, $a_\parallel = 1/1.25$, and for V-shaped drive with $\gamma = 0.025$, $a_\parallel = 1/1.86$.

9.3.4 Interface height-height correlation function

In our discussion of equilibrium interfaces in Sec. 2.3, the interface was described by a height variable $h(\mathbf{r})$, where $\mathbf{r}$ are the coordinates in the plane of the interface. The height also appeared in the KLS model with an interface in Sec. 4.2.5, and in the experimental work described in Chapter 5. We would therefore like to be able to measure the correlations of some suitably-defined height variable in the driven Ising system. As discussed in the context of the SOS and DG models in Sec. 3.5.1, no *direct* measure of the height from the microscopic Ising configurations is generally possible, due to bubbles and overhangs, so one must *coarse-grain* the system in some way. Coarse-graining involves tracing over (eliminating) some degrees of freedom to produce a cruder, larger scale picture. Here, we use two methods to obtain the interface height h.

The first method is to simply define the height at x by a sum over the spins in that column:

$$h(x,t) = -\frac{1}{2m_\mathrm{b}} \sum_z \sigma(x,z,t), \tag{9.8}$$

where the height is measured with reference to the midline between the walls, and so the $1/2$ factor ensures that the maximum height is $\pm L_z/2$. Since the '+' phase is in the upper half of the system, the negative sign is also required. When there are equal numbers of '+' and '−' spins in a column, $h(x) = 0$, while when there is a majority of one species, $h \neq 0$. The presence of the bulk magnetisation m_b may be justified by viewing $h(x,t)$ as the solution of an ideal equation for the magnetisation of a column: $m_\mathrm{col} = m_\mathrm{b}(L_z - h) - m_\mathrm{b}h$. This equation assumes that the two phases have their respective bulk magnetisations $\pm m_\mathrm{b}$ throughout, which is clearly not the case – however, it is appropriate for the purpose of coarse-graining. For the second method, we follow the method of Ref. [7]. In this method, for each column we evaluate the sum

$$v(h) = \sum_z \left[\sigma(x,z) - \Theta(z-h)\right]^2, \qquad \Theta(\zeta) = \pm 1 \quad \text{for} \quad \zeta \gtrless 0. \tag{9.9}$$

The value of h which minimizes $v(h)$ defines the position of the interface in this column x. Essentially one places the interface at a "trial" position, and then penalizes the appearance of "intruder" spins; the choice with the smallest penalty is the final height h. This method is clearly more complicated than the first, but deals with bulk intruders in a more robust fashion. For instance, given an initial "ideal" column with no intruders, if we introduce a single '+' intruder into the '−' phase (by swapping one spin's sign), then by (9.9), the

optimal interface position will be unchanged, as seems most reasonable. This is because moving h down would create an additional '$-$' intruder, which is penalized in (9.9). By contrast, using (9.8), h would indeed be reduced by one unit. Despite this, in fact we will find that the two methods give very similar results for most quantities (though not all). In the following, we use the simple sum definition unless otherwise stated, but for all height-dependent quantities we check the effect of the choice of definition.

The general height-height correlation function in $2d$ depends on spatial separations x and on temporal displacement t:

$$C(x,t) = \frac{1}{L_x}\left\langle \sum_{x'} h(x',t')h(x'+x,t'+t)\right\rangle, \tag{9.10}$$

where the angles indicate an average over time. Note that $\langle h\rangle = 0$ always for the COP Ising model with $m = 0$ (by either height definition), so no $\langle h\rangle^2$ is subtracted in the definition (9.10). We first consider the equal-time correlations $C(x, t = 0)$, which we abbreviate to $C(x)$; this is directly related to the spin-spin correlation function: $C(x) = (4m_{\rm b}^2)^{-1}\sum_{z,z'} G(x,z,z')$. The zero-separation value, $C(0) = \langle h^2\rangle$, is a measure of the squared width w^2 of the interface; indeed this is the definition used in the capillary-wave description. We can check the reliability of the results for the width shown earlier, by substituting this definition; when this is done, the same trends are seen, including the scaling of Figs. 9.6 and 9.7. This shows that those findings were not just the result of some peculiarity in the second-moment definition of w.

Turning to the full $C(x)$, we see from Fig. 9.10a that when boundary drive is applied to the system, $C(x)$ decays more quickly with separation than in equilibrium. As for the other quantitites, shear-like drive with $\gamma = 0.025$ has a similar effect to strong boundary drive. Larger values of γ produce a much stronger effect; $C(0)$ is greatly reduced, and $C(x)$ decays significantly more quickly. Results for other drive types in Fig. 9.10b show the same trend, with the V-shaped drive showing a slightly stronger effect than the shear-like field (as was the case for the magnetisation profile) – compare the $\gamma = 0.1$ results in (a) and (b). Comparing the uniform and step-like drive, we also find the same trend as we did for the magnetisation profile: at small field strength f, the step-like field suppresses correlations more strongly (see Fig. 9.10b), but beyond $f \gtrsim 0.25$, the uniform drive shows the greater effect. These results are consistent with the behaviour of the spin-spin correlation function, and indicate that driving the system either at the boundaries or in bulk suppresses capillary-wave fluctuations.

The anti-correlations of $G(x)$ present in equilibrium also persist to $C(x)$. The statistical errors on $C(x)$ for equilibrium and for weak drive are relatively rather larger than for the previous quantities, although still small in absolute terms. For stronger drive, the errors are much smaller, due to the reduced interfacial fluctuations – it is a general trend that the system is "easier" to simulate when more strongly driven.

From the scaling of $m(z)$ and $G(x)$, we might expect that rescaling might be possible for the height correlations too. What sort of form might this take? To answer this, we appeal to the (Weeks) scaling of $C(x)$ in equilibrium [27]:

$$C_{\rm eq}(x) \approx w_{\rm eq}^2 \mathcal{C}(x/\xi_{\parallel}^{\rm eq}), \tag{9.11}$$

where $\mathcal{C}$ is a scaling function, and $w_{\rm eq}$ the width in equilibrium. In confined $2d$ Ising systems, we know $w_{\rm eq} \propto L_z$. Assuming that the scaling form (9.11) applies out of equilibrium, we can rescale the driven results to equilibrium as follows:

$$a_{\perp}^{-2} C(a_{\parallel} x) \approx C_{\rm eq}(x), \tag{9.12}$$

where we have also invoked $a_{\perp} = L_z^*/L_z \sim w/w_{\rm eq}$, which was tested in Sec. 9.3.2. Note that the values of the parameters $a_{\perp}$ and $a_{\parallel}$ are obtained from the rescaling of the profile and spin correlation function, respectively, so when we rescale $C(x)$, there are no free parameters. This therefore provides quite a strong test as to how well the "effective-confinement" picture works. Fig. 9.11 shows some example results. The procedure works well for small and intermediate separations, in the cases of boundary drive and weak bulk drive, as expected from experience with $G(x)$. The success of the rescaling for the height certainly reinforces the idea that the interface of the boundary driven or weakly bulk driven Ising lattice gas behaves like an equilibrium interface under a greater degree of confinement (smaller distance between the walls). While the rescaling for the profile could perhaps be regarded as "accidental", combining it with the result from $G(x)$ to produce a testable prediction for $C(x)$, suggests that this is not the case. The rescaling of $C(x)$ is rather sensitive to changes in both $a_{\perp}$ and $a_{\parallel}$, so the fact that the values obtained earlier "work" provides further evidence that the argument has a physical basis.

Comparing the behaviour of $C(x)$ to the experimental results of Ref. [13] discussed in Chapter 5, we find both similarities and differences. The reduction of the interfacial width $C(0)$ when drive is applied is in agreement with experiment; in both cases, the effect is greater for stronger drive. These findings also agree with the KLS simulations

of Leung *et al.* [103], see also Sec. 4.2.5. However, Derks *et al.* found an *increase* of the lateral correlation length $\xi_{\parallel}$ for the sheared system, whereas the rescaling results shown here imply a reduction of this quantity in the driven Ising system. Of course, the experimental system is three-dimensional, and dimensionality plays an important role in interfacial fluctuations. Also, the correlation length in the experiment was obtained via a fitting to the ($3d$) CWT for $C(x)$ – a different procedure to that used here. Finally, the experimental system is of course much more complex than our simple driven Ising lattice gas, and effects not accounted for in our model could be at work in determining interfacial correlations. Nevertheless, the mix of agreement and disagreement between the simulations and experiment is intriguing, and raises the question of which features of driven interfaces are universal, and which are special to a particular dimensionality or system. At this stage, we may hypothesize that the suppression of interfacial roughness by lateral drive is a universal feature, and given that the qualitative effect is the same for *all* drive types considered, it seems likely that its presence does not depend on the specific form of field. The strength of the effect *does* depend on $F(z)$ – compare the boundary and bulk driven cases; also, the symmetry of the field seems to have a small effect. In the light of these findings and questions, it seems natural to investigate the structure of the interface in a $3d$ driven Ising system – indeed we shall do this in Chapter 10. For now, however, we remain in two dimensions, since novel features remain to be discussed.

Finally, as stated earlier, the results shown above are based on the sum definition of the height; however, in all cases $C(x)$ was also calculated for the other height definition (9.9). Fig. 9.12 compares results for equilibrium and shear-like drive from the two definitions; as per the earlier assertion, the data agree rather closely. Indeed, one should expect the specific method of coarse-graining to be unimportant, at least for static quantities, since any valid method should pick up the same large length- and time-scale features.

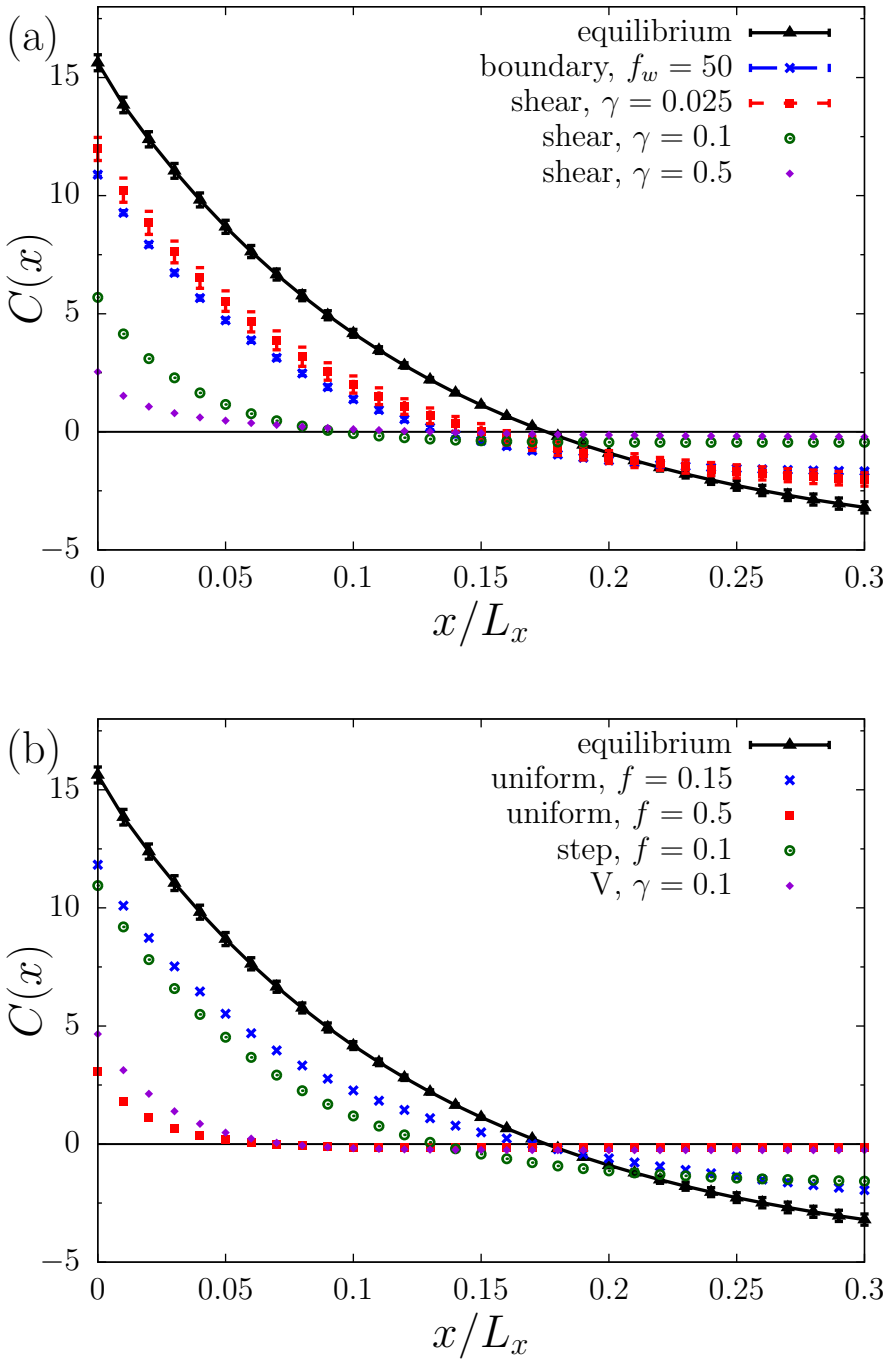

Figure 9.10: Spatial height-height correlation function $C(x, t = 0) \equiv C(x)$, for an $L_x = 200$, $L_z = 20$ system at $T/T_c = 0.75$, as a function of scaled coordinate x/L_x. (a) Data for equilibrium, as well as boundary and shear-like drive of various strengths, as indicated. (b) Results for uniform, step-like, and V-shaped driving fields, as well as the equilibrium result for reference. The effect of the $f = 0.1$ step field is slightly greater than the $f = 0.15$ uniform field; as discussed in the text, this reverses at larger f.

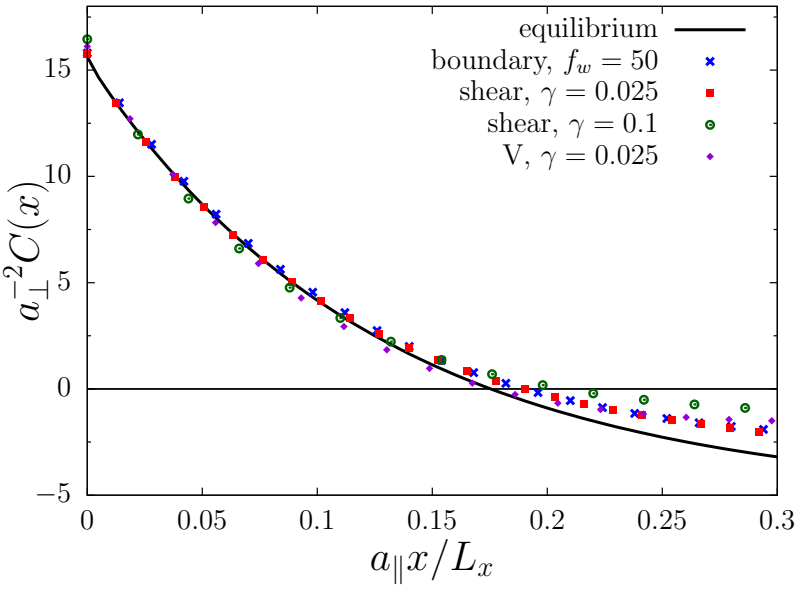

Figure 9.11: Results of rescaling the data for the driven spatial height correlation function back to the equilibrium result, according to $a_\perp^{-2} C(a_\parallel x) \approx C_{\rm eq}(x)$, where $a_\perp$ and $a_\parallel$ were obtained from the rescaling of $m(z)$ and $G(x)$, respectively. The system parameters are the same as in Fig. 9.10; the procedure works for all boundary drive strengths and for weak fields in the bulk driven cases.

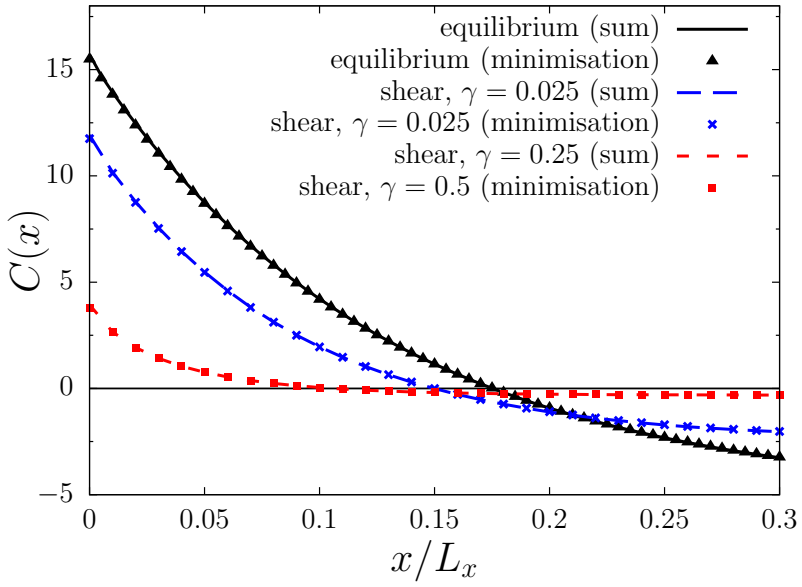

Figure 9.12: Comparison of the height correlation function $C(x)$ obtained from the sum definition of the height, Eqn. (9.8), and the "minimization" definition, Eqn. (9.9). The system parameters are $L_x = 200$, $L_z = 20$, $T/T_c = 0.75$; results are shown for equilibrium and for shear-like drive.

9.4 Kawasaki and Glauber dynamics in equilibrium

We now change tack slightly and concentrate on equilibrium systems. In spin systems, the most common type of dynamics are non-conserving *spin-flip* or Glauber dynamics, mentioned in Chapter 6. One may use any acceptance rates satisfying detailed balance, the most common choice being Metropolis rates; another are Glauber rates [132]; the latter, unlike the Metropolis rates, are continuous in the internal energy change for a move, ΔH. Note that the nomenclature can be a little confusing (and indeed inconsistent in the literature!) – here we use the term *Glauber dynamics* to mean non-conserving spin-flip dynamics, as opposed to *Glauber rates*, which are a particular choice of transition rate. Glauber dynamics generate microstates of an ensemble where the total magnetisation can fluctuate; in lattice gas language, this corresponds to a grand canonical description. Kawasaki exchange dynamics sample an ensemble with fixed total magnetisation, corresponding to a lattice gas in the canonical ensemble (see also Sec. 3.4), and so may be used to simulate the conserved order parameter (COP) Ising model. We have previously discussed (Secs. 3.4 and 6.2) the equivalence of ensembles in the thermodynamic limit: static (but not dynamic) observables must attain the same averages in the normal and COP Ising models for infinite systems. However, in MC simulations we fall some way short of this limit(!), so one should not necessarily expect agreement. In particular, for systems with an interface, the constraint on m in the Kawasaki case restricts the mean interface position to be at the centre of the system, which is not the case for spin-flip dynamics. Unfreezing this "zero mode" may lead to significant differences in *static* observables. We note that results for time-dependent quantities also depend on dynamics, but this is to be expected, whereas for statics, the issue is more subtle. Here we compare and contrast the results for one- and two-body functions obtained from equilibrium simulations using Kawasaki and Glauber dynamics (with Metropolis update rates). We have already described the method for the former case in Chapters 7 and 8. For the latter, a single-spin implementation was used; the algorithmic steps are similar to the Kawasaki case, though simpler, since one only has to consider one spin and its neighbours, rather than a pair. Further details be found in standard Monte Carlo references [54, 55].

A selection of results for the magnetisation profile is shown in Fig. 9.13 where $L_x = 200$ is fixed and L_z is varied, and in Fig. 9.14 where $L_z = 20$ is fixed and L_x is varied. As a benchmark we compare to results from the exact diagonalisation of the transfer matrix

for an infinite strip, $L_z = \text{const}$ and $L_x = \infty$. We have also tested the effect of changing the temperature of the system (not shown for the profiles). In general, we find that with *decreasing* scaling variable (see Eqn. (3.20)) $L_z/\xi_b(T) \sim L_z t^\nu$ at fixed L_x, where the reduced temperature $t = |T - T_c| / T_c$, and ν is the bulk correlation length critical exponent introduced in Sec. 3.2, the shape of the profiles for the two dynamics agree more closely. For example, for $L_z = 40$ in Fig. 9.13a, the Glauber and infinite-strip results agree well, but the Kawasaki profile shows a pronounced difference in shape; by contrast, for $L_z = 10$ in Fig. 9.13b, the profiles coincide. It is also interesting to note that effects on the magnetisation profiles due to L_x being finite are rather strong – see Fig. 9.14. For $L_z = 20$ at $T/T_c = 0.75$ one has to consider strips as long as $L_x = 800$ to find an agreement with the transfer matrix results for infinite strips! On the one hand this might not seem surprising because of the very large lateral correlation length; for infinite strips $\xi_\parallel \sim L_z^2$ in two dimensions. On the other hand, for Glauber dynamics the limit of the infinite strip at the same temperature and the same width of the strip is already achieved for $L_x = 200$ (not shown), so the nature of the dynamics seems to be important.

The differences between results from Glauber and from Kawasaki dynamics are even more pronounced on the level of two-body functions. Results for the spin-spin correlation function at the interface, $G(x)$, are shown in Fig. 9.15. As observed in the earlier results for $G(x)$, a striking feature of the correlation functions for Kawasaki dynamics is that they cross zero at some $x = x_0$ and saturate at a negative value G^{sat} for larger values of x. Both x_0 and G^{sat} depend on the temperature and on the size of the system. At fixed L_x and T, a wider (larger value of L_z) strip gives a larger value of x_0 and a more negative saturation value (Fig. 9.15c). At fixed L_z and T, a longer (greater L_x) strip gives a smaller x_0 and a less negative saturation value (Fig. 9.15a). At fixed L_x and L_z, the higher the temperature, the smaller x_0 and the less negative G^{sat} (Fig. 9.15b). As mentioned earlier, we associate these negative correlations with finite-size effects; on a coarse-grained level, these cause the interface to cross the mid-line $z = 0$ on average at intervals in lateral separation of $x = x_0$.

For Glauber dynamics, the results are rather different – negatively correlated regions are absent for all parameter combinations investigated. For shorter systems at fixed L_z and T (Fig. 9.15a), $G(x)$ decays much more slowly, and significant correlations are evident even at the maximum separation. Note that as in Sec. 9.3.3, $\langle \sigma(z = 1/2) \rangle^2$ was measured independently to be small in all cases, so these large asymptotic values are not simply the

result of a large average (squared) magnetisation at the interface. In Glauber dynamics simulations, the interface may sweep up and down in z as a whole, so at a particular time, $\sigma(z = 1/2)$ may be significant, but over the course of the simulation, equal positive and negative contributions should be recorded, so on that the average $\langle\sigma(z = 1/2)\rangle^2 \ll 1$. The large asymptotic values of $G(x)$ indicate that finite-size effects are still significant in the Glauber dynamics simulations, although they take a very different form to those in the Kawasaki case. This effect is also found for larger wall separations L_z at fixed L_x and T (Fig. 9.15c) – the larger L_z causes a greater lateral correlation length $\xi_\parallel$ via Eqn. (2.34), and this becomes of order L_x for $L_z \gtrsim 20$ (we saw this also when discussing the results for the interface width in Sec. 9.3.2).

As expected, $G(x)$ from the two types of dynamics becomes similar only when the finite-size effects are not severe. This occurs for long strips ($L_x = 800$) in Fig. 9.15a, and to a lesser extent for small L_z in Fig. 9.15c. Unlike in the case of the magnetisation profiles, there is still a significant difference in the results even for $L_x = 800$, with the Kawasaki data showing a small negative correlation (this also occurs in Figs. 9.15b and c) – this would seem to suggest that the finite-size effects are more severe for Kawasaki dynamics. For even longer systems, the agreement should become better. Moreover, we observe that the differences in $G(x)$ at fixed L_x and L_z reduce as we approach T_c, where the interface becomes more diffuse and interfacial fluctuations become less important relative to bulk fluctuations. Indeed for both dynamics $G(x)$ decays more quickly at higher temperatures, and the negative regions in the Kawasaki case reduce – for $T/T_c = 0.95$ in Fig. 9.15b, the results are more similar than at $T/T_c = 0.75$.

These results show that even for *static* observables, Kawasaki and Glauber dynamics can give quite different results for the same system sizes and temperatures, due to the change in the nature of interfacial fluctuations when the restriction of fixed magnetisation is imposed by using exchange dynamics. In Ref. [68], results are also shown for the height-height correlation function, for which similar conclusions apply. The disagreements are larger for simulation parameters where finite-size effects are strong, and so could be controlled and minimised if necessary. Finally, we note that for *driven* Kawasaki dynamics, as we have already observed, finite-size effects are less severe – however, lacking an equivalent way of applying drive in the spin-flip case, we are unable to generate "driven Glauber" results for a like-for-like comparison.

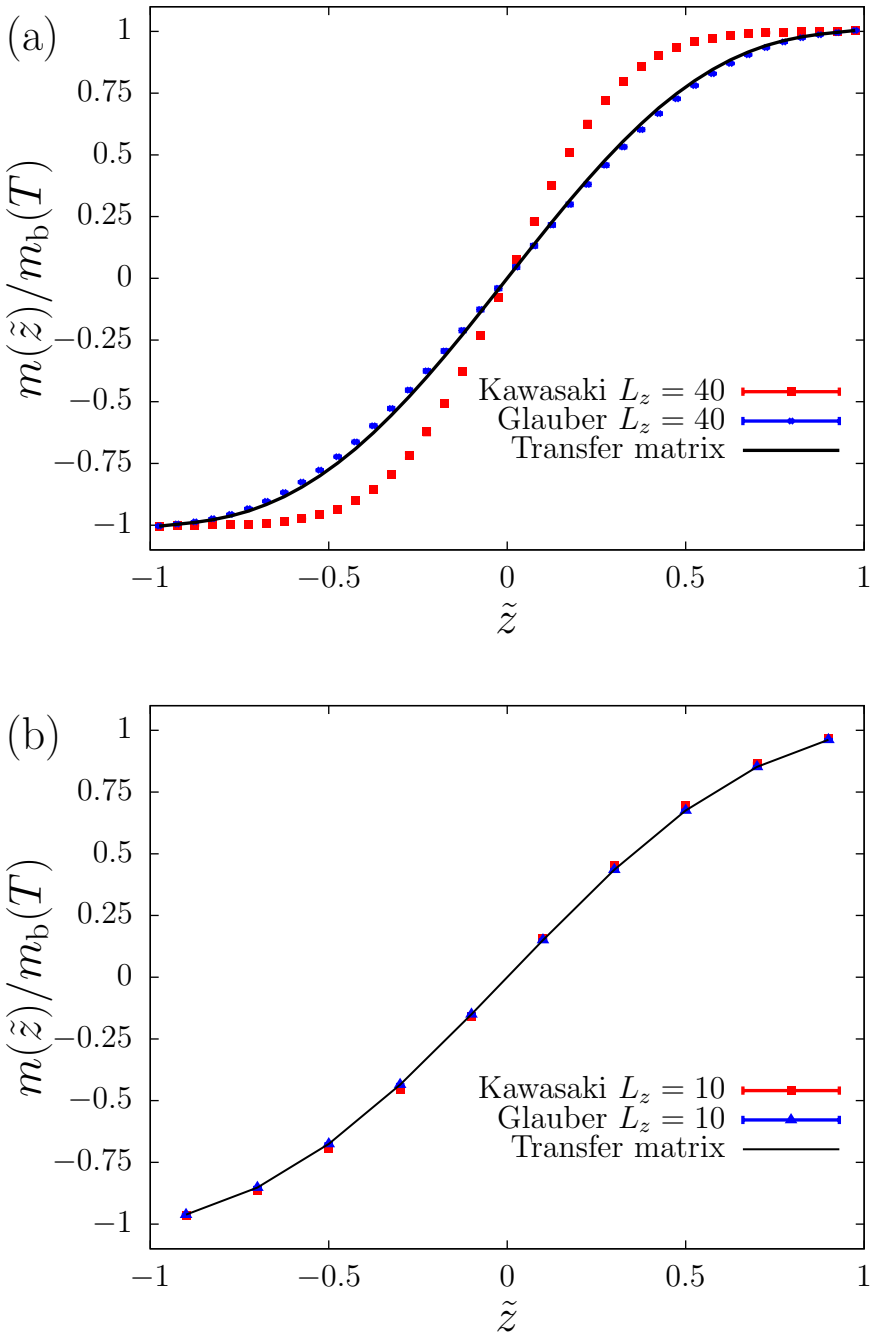

Figure 9.13: Magnetisation profiles $m(\tilde{z})$, scaled by the bulk magnetisation in equilibrium $m_{\mathrm{b}}(T)$, obtained from equilibrium simulations with Kawasaki and Glauber dynamics, for $L_x = 200$ and $T/T_c = 0.75$, for two different wall separations $L_z = 40$ in (a) and $L_z = 10$ in (b). The simulation results are compared to profiles obtained via exact diagonalization of the transfer matrix for infinite strips $L_x = \infty$.

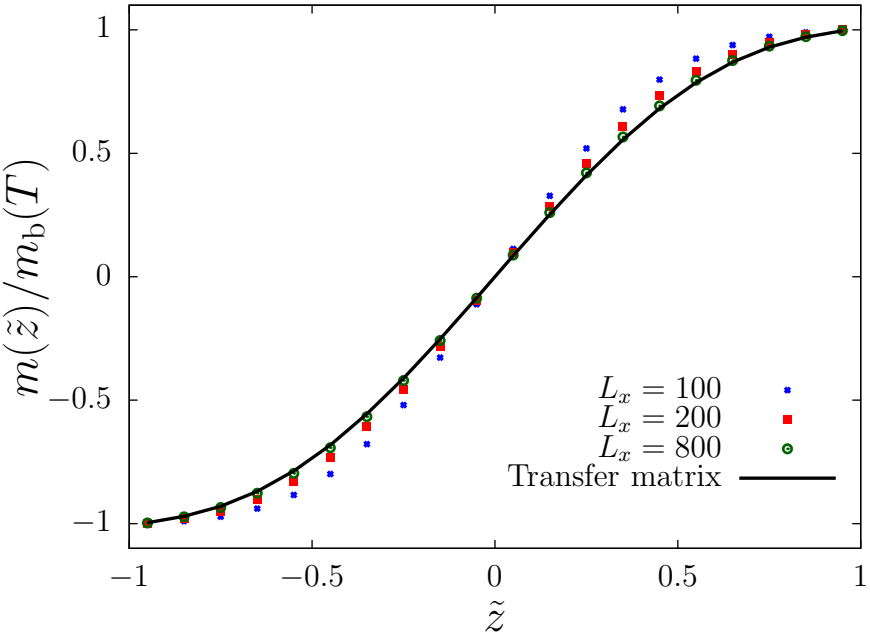

Figure 9.14: Magnetisation profiles $m(\tilde{z})$ obtained from simulations with Kawasaki dynamics, for fixed $L_z = 20$ and $T/T_c = 0.75$, and varying lateral system extent L_x, as indicated. The simulation results are compared to profiles obtained via exact diagonalization of the transfer matrix for infinite strips $L_x = \infty$; close agreement (to within statistical uncertainty) between the simulation and exact results is only attained for an $L_x = 800$ simulation system.

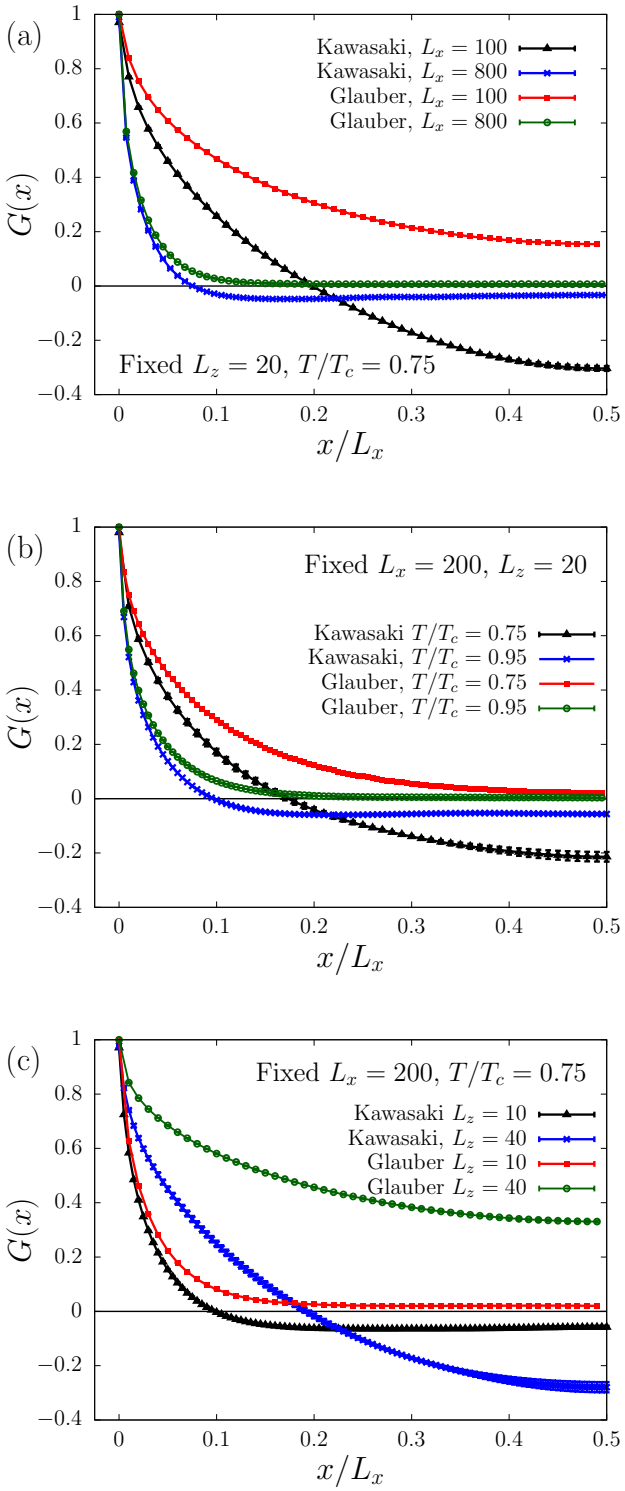

Figure 9.15: Interfacial spin-spin correlation functions $G(x)$ obtained from simulations with Kawasaki and Glauber dynamics, plotted as a function of scaled separation x/L_x. In (a), the temperature $T/T_c = 0.75$ and wall separation $L_z = 20$ are fixed, and the effect of varying the system length L_x is shown. In (b), $L_x = 200$ and $L_z = 20$ are fixed, and data are shown for two different temperatures. Finally in (c), we have fixed $L_x = 200$, $T/T_c = 0.75$, and two wall separations $L_z = 10$ and 40.

9.5 Dynamics of the driven interface

9.5.1 Space-time height correlations

We now investigate the effects of the driving field upon the dynamics of confined Ising interfaces, via the full space-time height correlation function $C(x,t)$, Eqn. (9.10). This measures correlations between the interface height at spatially and temporally displaced points. Due to translational invariance in the x direction, $C(x,0) = C(-x,0)$ (negative x separations were therefore not plotted in Sec. 9.3.4). Additionally, in *equilibrium*, we expect this to hold for time separations $t > 0$, since there is nothing to break the symmetry. $C(x,t)$ was measured for time displacements of up to approximately 10^5MCS, so as to assess both short- and long-time dynamics. In order to show the behaviour clearly, in Fig. 9.16a we plot $C(x,t)$ as a function of x, for several fixed values of time difference t, for the case of shear-like drive with $\gamma = 1.0$. At $t = 0$, the curves correspond to the $C(x,0)$ results already discussed, and exhibit the expected reflection symmetry across $x = 0$. For time differences $t > 0$, the position of the peak *moves* towards negative values of x, while its height decays, and its width increases; at $t > 0$ the strongest correlations are between points displaced in both time and space, and the spatial separation increases with time. This clearly indicates the existence of damped *propagating* thermal capillary waves on the interface, which move in the negative x direction [131]. The decay of the correlations with increasing time difference is due to the random rearrangements (noise) in the MC simulation. The position of the peak varies linearly with time, enabling us to infer a velocity v_{peak} by plotting the position of the maximum against time, and measuring the gradient. For the parameters in the figure, $v_{\mathrm{peak}} = 0.009$ in units of the lattice constant per MCS. We find that transport occurs for all strengths of shear-like drive, with v_{peak} varying approximately linearly with γ.

Very different behaviour occurs for V-shaped drive – see Fig. 9.16b. Here the peak decays and broadens *without* lateral motion, so the symmetry around $x = 0$ is preserved at all times. The decay rate is similar to shear-like drive (slightly greater). These results are similar to the equilibrium case, shown in the inset: as required, the peak shows no motion in this case. The decay is extremely slow in equilibrium – the peak has only decayed to approximately three-quarters of its initial value at $t \approx 5 \times 10^4$MCS; this reflects the slow nature of Kawasaki dynamics. The boundary drive (not shown) shows behaviour very similar to equilibrium. For step-like drive, the situation is different again – we observe

wave motion similarly to shear-like drive, see Fig. 9.17; to "complete the set", with uniform drive we find that no transport occurs, and the results (not shown) are similar to those for V-shaped drive. These findings also hold for the alternative (minimization) definition of the height, Eqn. (9.9); as in the case of the static height correlation function $C(x, 0)$, the results from the two definitions show good agreement.

We now ask: what are the criteria for capillary wave transport? Clearly the phenomenon is not linked to a specific functional form of driving field $F(z)$, but it *does* seem to depend on the symmetry of the field with respect to z: motion occurs for cases of *odd* symmetry. The symmetry of the field is directly inherited by the current profile $j^x(z)$ in the Ising model, so in fact we may talk in terms of symmetry of the current – this is appealing, since we relate the large-scale transport phenomenon to the microscopic motion. Let us make the following conjecture: [131] *the lateral order parameter current at a planar interface induces lateral motion of the thermal capillary waves, provided that $j(z)$ has a component which is an odd function of distance z from the interface.* This is quite a general proposal: we do not specialise to a particular model or dimensionality, and so it requires testing on systems besides the $2d$ driven Ising lattice gas – we shall do this in subsequent sections. Note that the above conjecture does not require *purely* odd current profiles, but instead only profiles which are not even in z; the justification for this generalisation was based on tests for fields with both odd and even components, which give rise to transport in $C(x, t)$. We cover this further in the context of the $3d$ driven Ising model in Chapter 10. For now, we consider more closely the symmetries of the model in order to shed light on the transport. In particular, the equilibrium system is invariant under the combined operation of species inversion $\sigma_i \to -\sigma_i$, and spatial reflection $x \to -x$, $z \to -z$. When drive is applied, this also holds for the even current cases (i.e., uniform and V-shaped fields). The sequence of operations is illustrated in Fig. 9.18: after the combined operation, the '+' species (say) move in the same (positive) x-direction as they did originally. For the odd current profiles, the situation is different: the '+' spins have reversed their directions, so that in their phase ($z > 0$), they move in the *negative* x-direction. Therefore, in the cases where we observe CW transport, there is a broken symmetry under species inversion and spatial (x and z) reflection, as compared to the non-transport cases. These symmetry considerations come directly from the definition of our model, and do not depend on any simulation results – in contrast with the motion conjecture above, which depends explicitly on the current profile results (but not a particular model).

Another way to express the difference is in terms of the movement directions of the "intruders" in the system. In the cases where capillary-wave transport occcurs, the '−' spin intruders in the region $z > 0$ (the '+' phase) move in the same negative x direction as '+' spins do in the region $z < 0$ (the '−' phase). Thus intruders move in the same direction throughout the system (which is also the direction of wave motion, and opposite to that of the "velocity profile" of the order parameter, $j^x(z)/m(z)$, which is positive for all z), whereas for even current profiles, the directions are opposite in the upper and lower halves. This coherent movement of intruders seems to be important in the transport of interfacial fluctuations. On an idealised level, it means that the positive and negative fluctuations ("troughs" and "humps") move in the same direction, and thereby show net transport. However, although this is a hint towards a fully microscopic mechanism for CW motion, one must remember that the Ising spins have no inertia, and spin/particle movement occurs only by exchanges, so it is not obvious that "pushing" on one side of a hump or trough induces motion of the whole object. This simple nature of the lattice gas means care is required in carrying over concepts familiar in real, inertial systems – there is of course always a trade-off between retaining a connection to the dynamics of real fluid interfaces, and the complexity of the model.

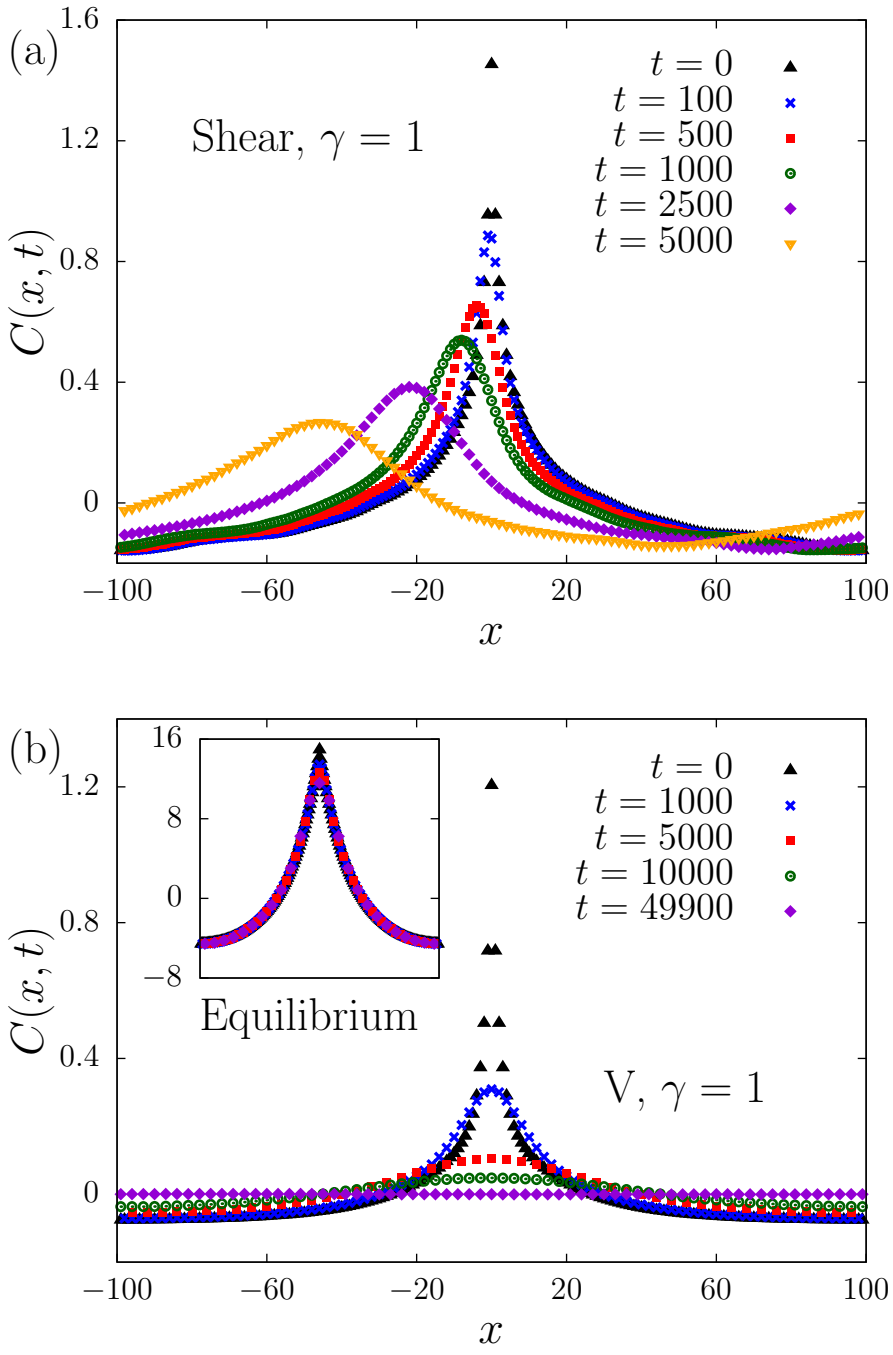

Figure 9.16: Space-time height correlation function $C(x,t)$, for an $L_x = 200$, $L_z = 20$ system at temperature $T/T_c = 0.75$, plotted as a function of spatial separation x, at various fixed time separations t, as indicated. (a) Results for shear-like drive with $\gamma = 1.0$, showing capillary wave transport. (b) V-shaped drive with $\gamma = 1.0$, where no transport occurs; in the inset, the equilibrium result is shown for the same time displacements as the main figure.

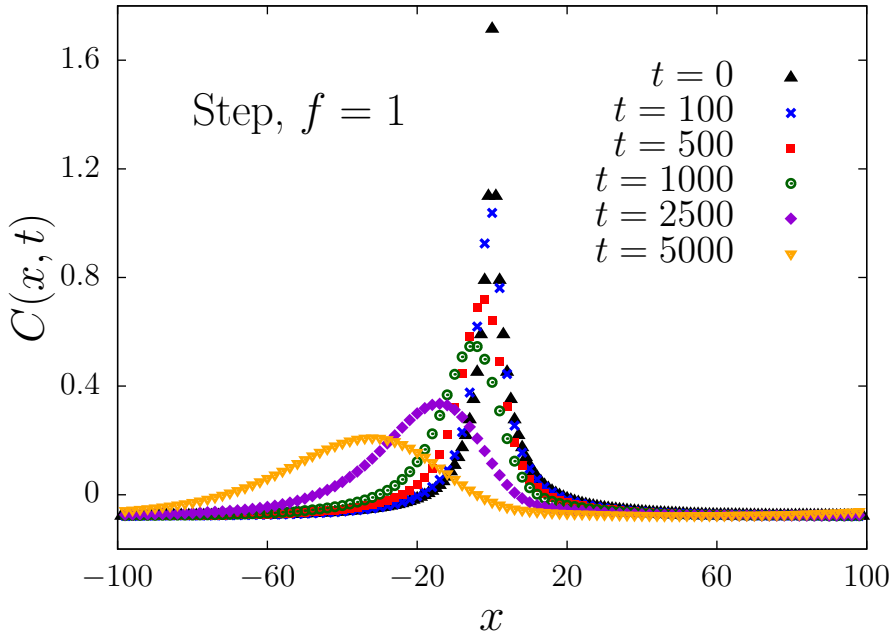

Figure 9.17: Space-time height correlation function $C(x,t)$, for the same system as in Fig. 9.16, but driven by a step-like field $f = 1$. Capillary wave transport occurs as in the shear-like case.

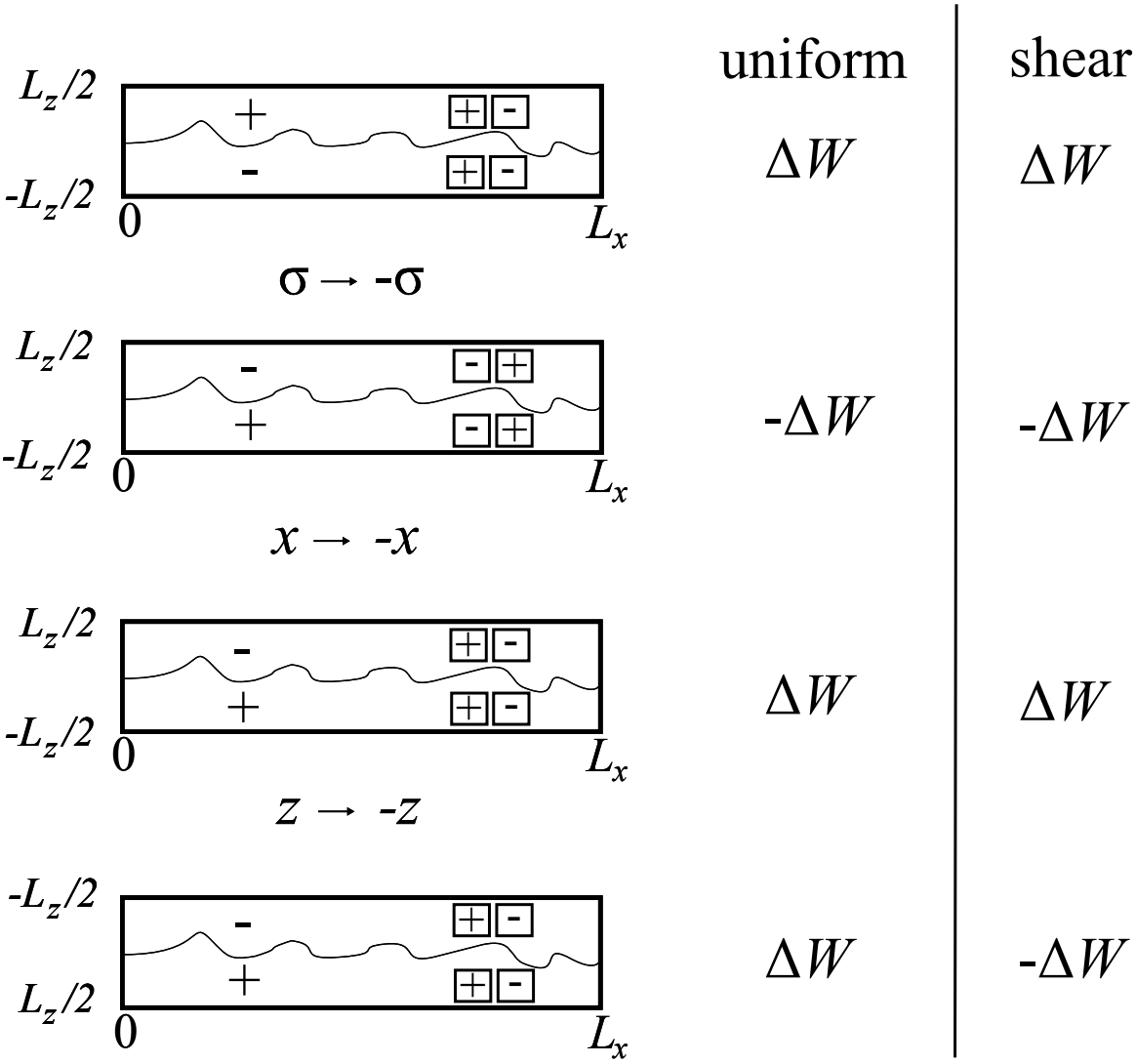

Figure 9.18: The effect of the sequence of operations $\sigma_i \to -\sigma_i$, $x \to -x$ and $z \to -z$ upon the driven Ising model for uniform and shear-like drive. At the top, the initial system is shown, with the phases marked, and individual $+-$ pairs in the upper and lower halves picked out. The work terms $\Delta W = -J\ \boldsymbol{\delta} \cdot \mathbf{F}(z)(\sigma_i - \sigma_j)/2$ are shown for both drive types. The first operation is species inversion, after which the orientation of the $+-$ pairs has changed, and ΔW has changed sign for both drive types, according to the above equation. After spatial reflection $x \to -x$ (third system down), the orientation of the $+-$ pairs is restored, and ΔW reverses again, due to $\boldsymbol{\delta}$ changing sign. Finally, reflection in z is performed. Now the '+' phase is in the $z > 0$ half of the system, as originally, and the pair orientation is also unchanged. For uniform drive, ΔW is also invariant through this step, since $F(z) \equiv f$; however, for shear-like drive $F(z) = \gamma z$, so ΔW swaps sign once more, thus reversing the directions of movement of each species with respect to the original system. In this way, the odd-current cases, where capillary-wave transport is seen, have a broken symmetry under this sequence of operations.

9.6 Wave propagation in the driven discrete Gaussian model

In order to test the conjecture on the criteria for occurrence of capillary wave transport, we now consider the $1d$ discrete Gaussian (DG) model with conserved dynamics under drive. The equilibrium DG model was discussed in Sec. 3.5.1, and the driven variant we simulate here was introduced in Sec. 7.2. The results in this section are from systems of length $L_x = 200$ (which proved sufficient to prevent noticeable finite-size effects) at a temperature $T = 0.75T_c^{\mathrm{Ising},2d}$, where $T_c^{\mathrm{Ising},2d}$ is the bulk, equilibrium $d = 2$ Ising critical temperature encountered earlier. Most of the simulations were therefore carried out at the same temperature as the majority of those in the driven Ising system – this seems a reasonable choice, given that the DG and SOS models may be viewed as coarse-grained Ising models, and that they have no equivalent critical point of their own. We have checked, however, that the findings discussed below apply across a range of temperatures from $0.5T_c^{\mathrm{Ising},2d}$ to $0.85T_c^{\mathrm{Ising},2d}$. Before investigating whether transport itself occurs, we first consider the current in the system, as well as the magnetisation profile.

In the conserved height DG model, the elementary move consists of a single unit of height moving from one column to one of its nearest neighbours – in this way, the interface configuration defined by the set of heights $\{h_i\}$ evolves in time. The current in the x direction at a particular height, $j^x(h)$, is just the average net flux of "height units" at that height. However, there is some ambiguity here, because two columns are involved – at which height should the contribution be recorded? In order to avoid asymmetry around $h = 0$ in the measured current profiles (which we expect to have either even or odd symmetry, depending on the driving field), we can record the contribution at the *average* of the two heights – we therefore apply this method. Fig. 9.19 shows results for $j^x(h)$ for the DG model under shear-like (linearly height-dependent) drive, and spatially uniform drive. The current was recorded for heights $|h| \leq 100$, but beyond the displayed region, $j^x(h)$ is essentially zero, because individual heights reach these values extremely rarely (the constraint $\sum_i h_i = 0$ makes it especially difficult for such events to occur, since for example a strong positive region must be balanced by strong and/or numerous negative regions). For the linearly height-dependent drive, the current has opposite signs for positive and negative h, and is strongly peaked at two values of h close to and either side of the $h = 0$ line. These peaks reflect the fact that the rms height is rather small, only a few height units – as for the Ising model, there is competition between carrier availability (column

with the correct height) and drive strength; however, in the DG model the current always shows strong peaks near the centre and no plateaus. The peaks move slightly towards the midline for stronger drive, as in the Ising model. For uniform drive, the sign is constant throughout, and the maximal current occurs at the midline, since carrier availability is the only factor in this case.

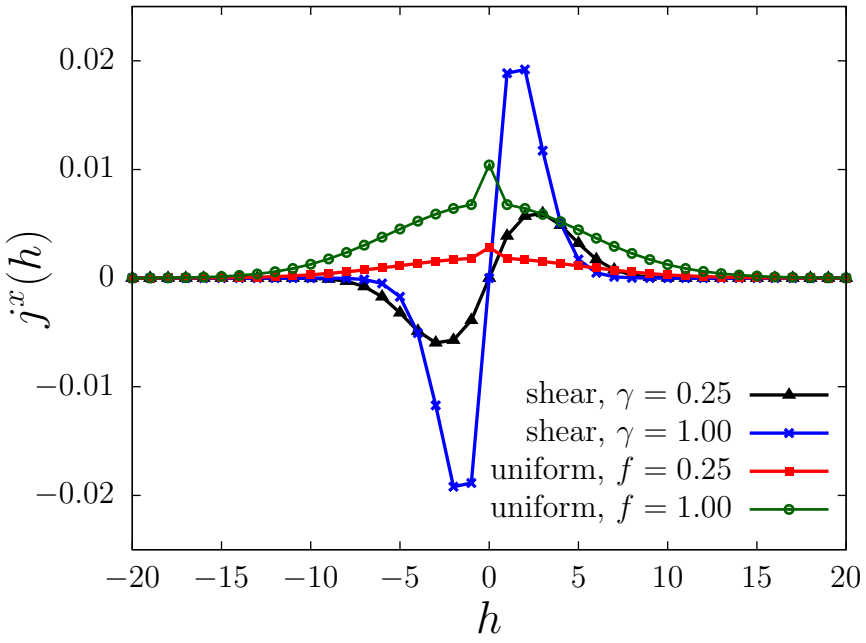

Figure 9.19: Current profiles $j^x(h)$ for the driven discrete Gaussian model with conservative dynamics, as a function of height h. The h axis is cut off at $|h| = 20$, beyond which the current is essentially zero. In all cases, the system has length $L_x = 200$ and is at a temperature $T/T_c^{\mathrm{Ising},2d} = 0.75$. Data for shear-like and uniform drive are shown, the former with odd symmetry around $h = 0$, and the latter with even symmetry.

Structural information in the DG model may be gleaned from the magnetisation (density) profile. The definition of this quantity is perhaps less obvious than for microscopic models, since we do not have any microscopic density variable. However, the height h at a particular position defines an interface dividing an upper and a lower phase ('+' and '-' respectively in our Ising wall convention), so at a particular height $h = z$, we record a positive contribution to the magnetisation profile if the column height $h_i < z$ (since we are in the '+' phase at z), and a negative contribution if $h_i > z$. In this way we generate a magnetisation profile as a function of height, for which results are shown in Fig. 9.20;

as for the current, the displayed region is limited to $|h| \leq 20$. When the interface is subject to weak or intermediate shear-like drive, the profile becomes sharper, reminiscent of the results for the Ising model. However, beyond a certain drive strength (approximately $\gamma = 2$), the profile begins to become *more diffuse*, and for very strong drive, eventually crosses back past the equilibrium result - the figure shows this for $\gamma = 20$. This phenomenon also occurs, if rather than using the average of the two column heights in the work term, as in Eqn. (7.13), we use just one of the heights (in fact, the effect sets in for smaller γ in this case). For uniform drive, the situation is similar – for weak drive there is a (very slight) sharpening of the profile, but for larger f, the driven $m(h)$ becomes more diffuse than the equilibrium case. An interpretation of these results is that the interface is somehow *destabilised* by strong driving fields, so that the width increases with respect to equilibrium (direct measurement of $\langle h^2 \rangle$ confirms this). Further evidence for destabilisation is found in simulations of the same dynamical model but with the SOS Hamiltonian, where the driven interface width appears to be larger than the corresponding result for equilibrium even for weak drive. Fig. 9.20b shows the SOS equilibrium profile, which itself has a large width, and varies almost linearly with h. The larger width in equilibrium in the SOS case is consistent with the weaker energetic penalty for height differences greater than unity (recall that the SOS Hamiltonian is linear in height differences, while the DG is quadratic).

The above issues of interface instability are certainly interesting, if somewhat murky, and deserve further investigation. For now we return to our primary aim, and study the behaviour of the space-time height-height correlation function $C(x,t)$, for choices of parameters where the interface is stable under drive. Fig. 9.21a shows that, as for the Ising model, capillary wave transport occurs for a system driven by a shear-like field [131]. For given γ, the peak velocity v_{peak} is much greater in the DG model (0.103 lattice constants per MCS for $\gamma = 1$) – indeed, by $t = 1000$MCS, the peak has wrapped around the periodic boundaries in the figure. The function also exhibits much shorter tails than for the Ising model, and the lateral spreading with time is slower. For uniform drive with $f = 0.25$, Fig. 9.21b, wave motion is absent, and $C(x,t)$ decays (slowly) while remaining peaked at $x = 0$, consistent with the findings in the Ising model. The amplitude in this case is much greater, as expected from the results for $m(h)$ – the interface width is very close to the equilibrium value. Since the symmetry of the current $j(h)$ in the DG model is the same as that of the applied field, these findings support our earlier conjecture: for odd current

profiles, capillary wave transport occurs. We may also apply similar symmetry arguments to those in the driven Ising model, to differentiate between the cases where motion does and does not occur. Here, the model is one-dimensional, and we have only heights rather than spins, so the sequence of operations is different. The equilibrium system is invariant under the spatial reflections $h \to -h$, $x \to -x$ and exchange of source and destination columns x and x'. For uniform drive, the work term ΔW changes sign twice, due to the last two operations, to return to its original sign, whereas for shear, an additional reversal is incurred due to the h dependence of the field. Thus for uniform drive, the system as a whole is invariant under these operations (as in equilibrium), but this is not the case for shear-like drive, where CW transport is found.

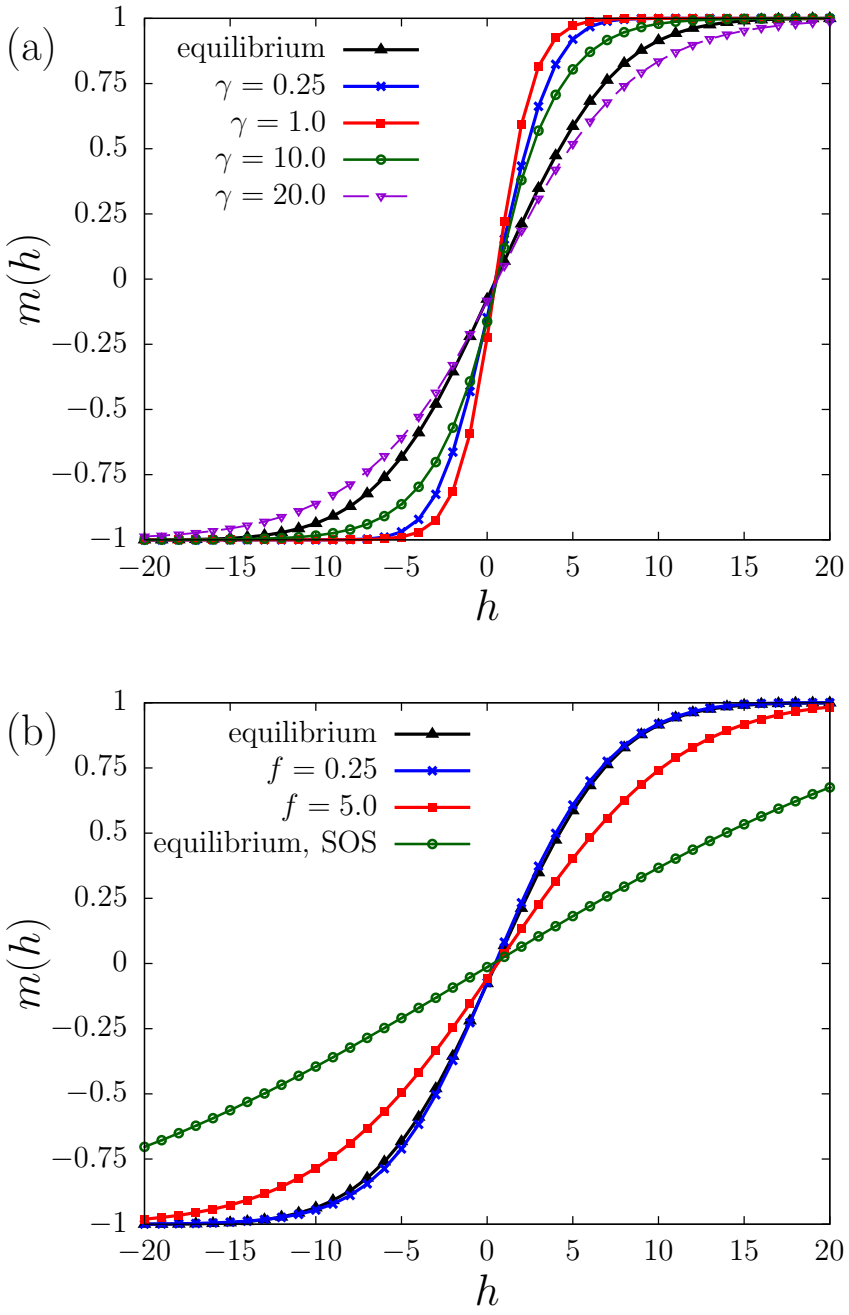

Figure 9.20: Magnetisation profiles $m(h)$ for the discrete Gaussian model simulated with conservative dynamics, as a function of height h. As in Fig. 9.19, the system has length $L_x = 200$, and is at a temperature $T/T_c^{\text{Ising},2d} = 0.75$. In (a), the equilibrium profile is compared to the profiles obtained from systems driven by various strengths of shear-like drive. For weak and intermediate drive, the profile becomes sharper than in equilibrium, but for very large γ, it crosses back, becoming more washed-out. (b) The same effect is seen for a uniform driving field, although the re-crossing occurs for much weaker drive. The equilibrium profile from simulating with the SOS Hamiltonian is also shown – this is almost linear in h, and very diffuse.

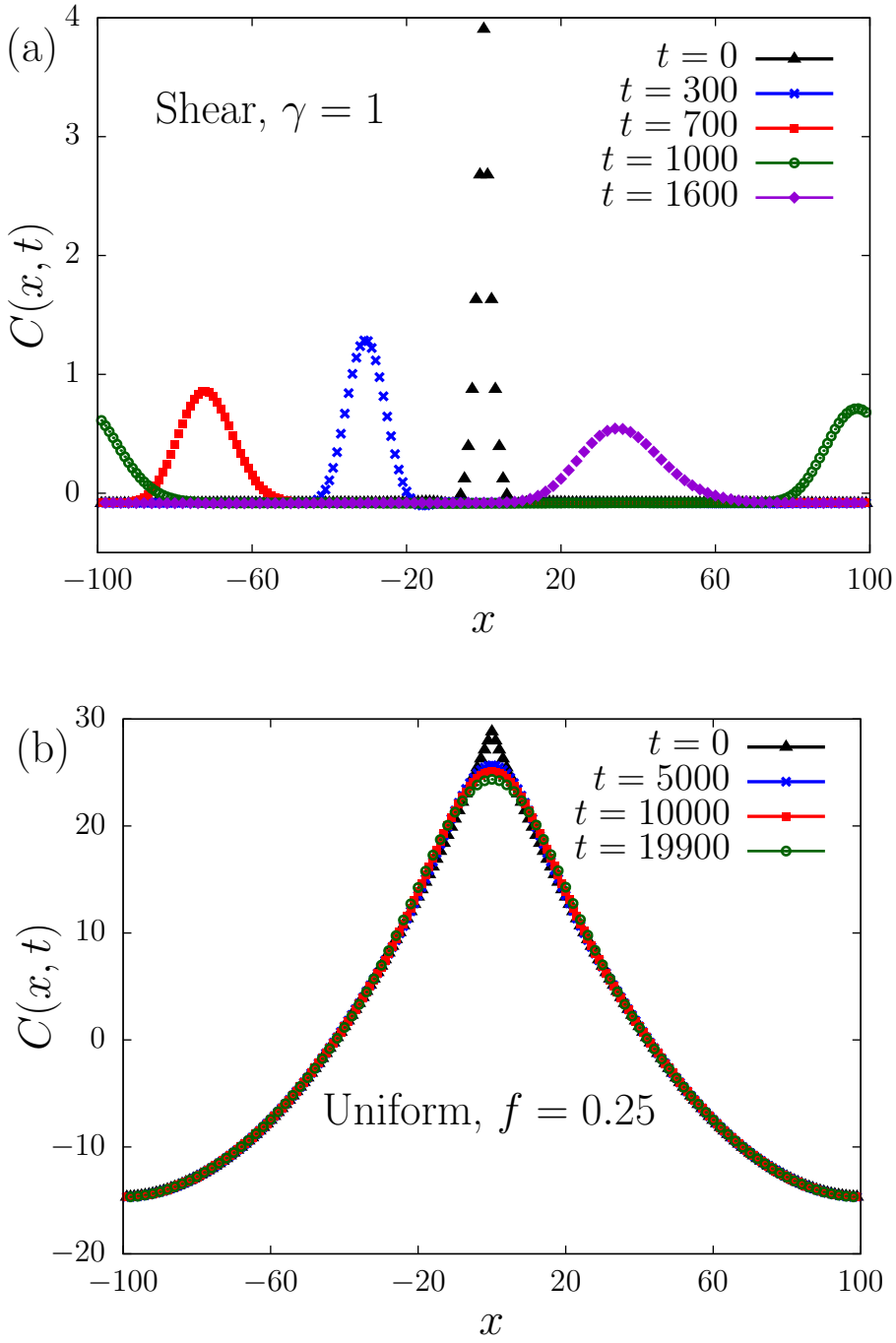

Figure 9.21: Space-time height correlation function $C(x,t)$ for the driven discrete Gaussian model, for various fixed time differences t, as a function of spatial separation x. The system size and temperature are the same as Figs. 9.19 and 9.20. In (a), results for shear-like show evidence of capillary-wave transport, as observed in the Ising model. Note that for the last two times t, the peak has crossed through the periodic boundary to appear at the other end of the system. Results for a uniform field $f = 0.25$ are shown in (b): as for the Ising model, no movement occurs.

9.7 Dispersion relation for travelling capillary waves

In order to characterize the dynamics of the capillary waves in both the Ising and DG models, we consider the evolution of the spatial Fourier modes $\tilde{h}(n_x, t)$ of the height function $h(x, t)$, defined by:

$$h(x,t) = \sum_{n_x=1}^{L_x} e^{2\pi i (n_x/L_x)x}\, \tilde{h}(n_x, t). \tag{9.13}$$

The summation is over integer n_x from 1 to L_x; because $h(x, t)$ is a real function, the Fourier transform has the conjugate symmetry $\tilde{h}(n_x, t) = \tilde{h}^*(L_x - n_x, t)$, i.e., there are $L_x/2$ independent terms in (9.13). Defining the scaled wave number $k_x = (2\pi n_x/L_x)$, each complex Fourier component $\tilde{h}(k_x, t)$ can be written in terms of its modulus and its phase $\phi(k_x, t)$:

$$\tilde{h}(k_x, t) = |\tilde{h}(k_x, t)| e^{i\phi(k_x,t)}, \tag{9.14}$$

where $-\pi \leq \phi(k_x, t) \leq \pi$. The form $\phi(k_x, t) = \omega(k_x)t$ corresponds to a travelling wave at constant velocity, with dispersion relation $\omega(k_x)$. In a steady state, the phase shift of each mode is a fluctuating quantity, with a distribution which when measured with increasing time intervals spreads and decays quickly to zero due to noise. However, at short times, we are able to measure its mean value in unit time to obtain the dispersion relation of the frequency ω as a function of k_x as:

$$\omega(k_x) = \arg\left(\langle \tilde{h}^*(k_x, t)\tilde{h}(k_x, t + dt)\rangle\right)/dt. \tag{9.15}$$

In the simulation one calculates the Fourier transform of the heights $h(x, t)$ at time t, and stores the phases of these complex numbers. At time $t + dt$, the procedure is repeated, and the difference in phase in the interval dt can be calculated; $\omega(k_x)$ is then the average of this difference, normalised to unit time. The interval dt must be rather short, otherwise we cannot reliably measure the phase shift: ϕ may "wrap around" from $+\pi$ to $-\pi$ between measurements, and if the shift is too large, then it can become ambiguous. Here we use the value $L_x/10$ attempted spin exchanges (for a 200×20 Ising system, this corresponds to 0.005 MCS). Fig. 9.22 shows results for waves induced by shear-like drive of strength $\gamma = 1.0$, for both the Ising, using the simple sum height definition, and the DG model.

In the case of the DG model, $\omega(k_x)$ shows linear behaviour at small k_x, and is symmetric around $k_x = \pi/2$. The data can be fitted excellently by the simple form [131]

$$\omega(k_x) = v^{\mathrm{DG}} \sin(k_x), \tag{9.16}$$

which for small k_x reduces to the linear form $\omega(k_x) = v^{\mathrm{DG}} k_x$. The fitting parameter $v^{\mathrm{DG}} = 0.760(1)$ is in reasonable agreement with the peak velocity (0.08) measured from $C(x,t)$.

For the Ising model, the dispersion relation is non-linear even for small k_x; indeed we find that $\omega(k_x)$ may be fitted to the form

$$\omega(k_x) = (v + 2u)\sin(k_x) - u\sin(2k_x) + s\sin^2(k_x), \tag{9.17}$$

as shown in Fig. 9.22. The values of the fitting parameters are $v = 0.0175(1)$, $u = 0.0402(4)$, $s = 0.0262(0)$. Expanding (9.17) for small k_x, we have

$$\omega(k_x) = vk_x + sk_x^2 + (u - v/6)k_x^3, \tag{9.18}$$

showing that the quadratic and cubic terms are indeed important. In order to investigate the origin of the fitting forms, the dynamics were modelled by a linear transport operator (propagator) $\hat{L}$ acting on plane-wave modes $h(x,t) \propto \exp(i(\omega t + k_x x))$. In the case of the DG model, the simple form

$$\hat{L} = \partial_t - v^{\mathrm{DG}}\partial_x, \tag{9.19}$$

with *continuous* time derivative but *discrete* (mid-point) spatial deriative

$$\partial_x h(x,t) = \frac{[h(x+1,t) - h(x-1,t)]}{2}, \tag{9.20}$$

yields the fitting form (9.16). For the Ising model, the first two terms in the dispersion relation (9.17) may be obtained from the operator

$$\hat{L} = \partial_t - v\partial_x + u\partial_x^3, \tag{9.21}$$

where a 5-point stencil is used for ∂_x^3:

$$\partial_x^3 h(x,t) = \frac{h(x+2,t) - 2h(x+1,t) + 2h(x-1,t) - h(x-2,t)}{2} \tag{9.22}$$

However, the third term, which for small k_x gives the quadratic dependence in (9.18) cannot be generated by a linear transport operator with purely real coefficients. It may be obtained by allowing an imaginary contribution $is(\partial_x^2 + \partial_x^4/4)$ (with 3- and 5-point stencils) to $\hat{L}$.

In the Ising model, the prescription of interface height $h(x,t)$ is not unique. Using the minimization procedure rather than the column-sum as input for the calculation of $\omega(k_x)$

yields a dispersion relation which can be fitted by (9.17) with $s = 0$, and different values of v and u: $v = 0.0133(1)$, $u = 0.0128(49)$. Thus in this case no imaginary contributions to the transport operator are required. For previous quantities we have studied, both static and time-dependent, the two height definitions gave consistent results, but here this is not the case. The difference is due to the very short time scales involved in the measurement of the phase shift – small differences in the heights from the two procedures can have a significant effect, because the system configuration changes very little from one measurement to the next (on a strictly microscopic level rather than larger rearrangements). What then is the origin of the s term in the sum-height dispersion relation? A possible argument is that the sum is more susceptible to picking up *bulk* rearrangements in $h(x,t)$; this will be amplified when measuring at short time intervals. The minimization definition is less sensitive to bulk movements, since typically (say) a few exchanges will not change the value of h which minimizes the quantity v in Eqn. (9.9). By this argument, the $s\sin^2(k_x)$ term may be in fact a bulk effect, or a sign of bulk-interfacial coupling – however, these arguments are somewhat speculative. We defer further discussion of the presence of complex coefficients in the transport operator to the three-dimensional Ising results (Sec. 10.2.3).

For those cases where capillary wave transport does not occur (i.e., even order parameter current profiles), the average phase shift was measured to be zero – this is expected, since there is no lateral motion on the average. According to earlier results, we should however see a non-zero average phase shift for step-like drive $F_x(z) = f \cdot \mathrm{sgn}(z)$. Indeed, for the Ising model, using the column-sum height and $f = 1.0$, this produces a dispersion relation which can be fit by the same form (9.17) as for shear, with $v = 0.0100(4)$, $u = 0.01802(2)$, and $s = 0.0071(2)$. Varying the strength of the shear- or step-like field alters the magnitude of $\omega(k_x)$, but not the shape, and the same fitting form applies, with a reduced value of v for smaller γ or f, as expected from the trend observed in the peak velocity v_{peak} of $C(x,t)$. However, unlike v_{peak}, the dependence of v upon γ does not seem to be linear – although the data available are limited.

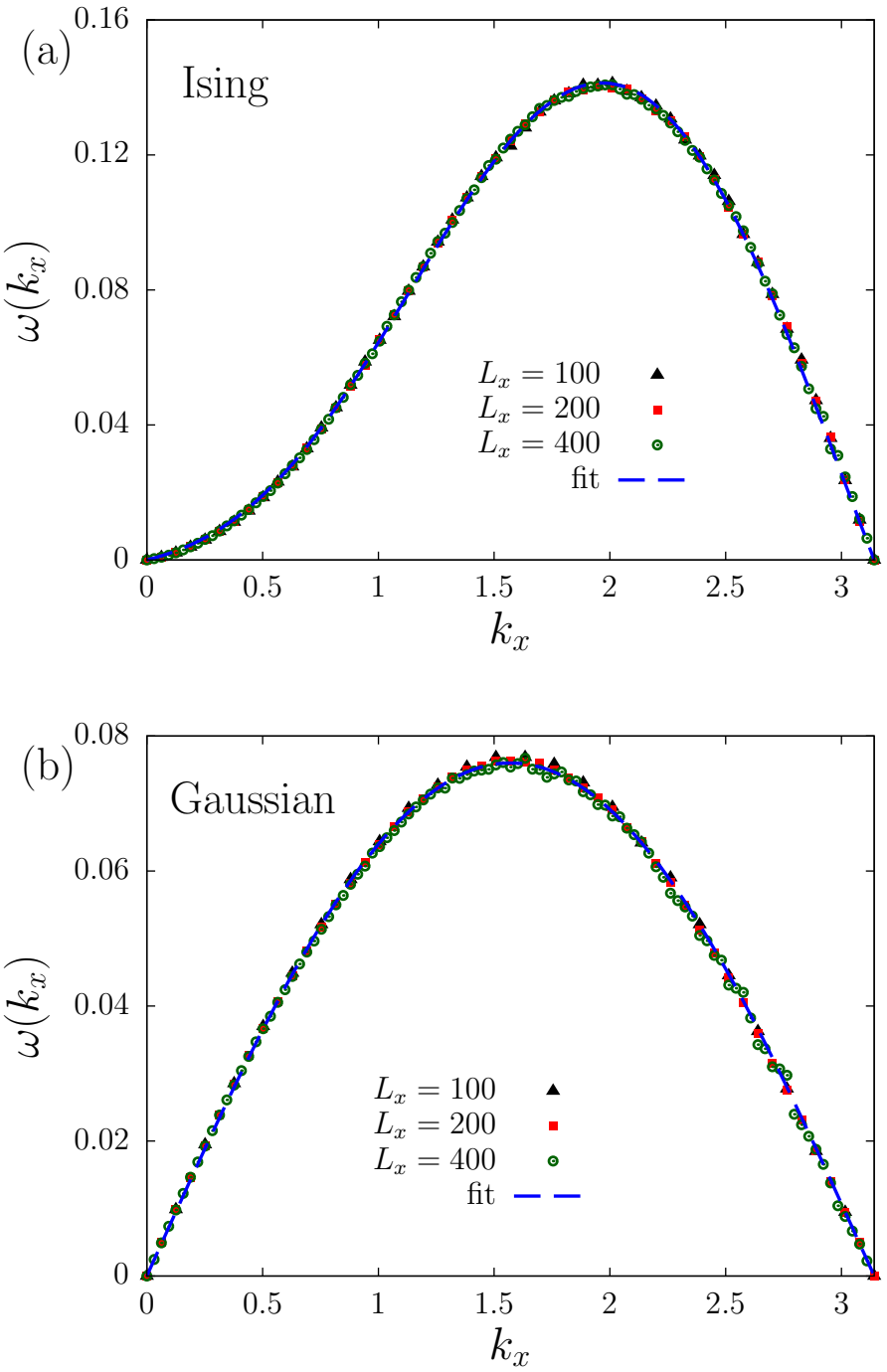

Figure 9.22: Dispersion relation $\omega(k_x)$ for the travelling capillary waves in the Ising lattice gas and discrete Gaussian models driven by a shear-like field with $\gamma = 1$, as a function of scaled wave number $k_x = (2\pi n_x/L_x)$. Data for systems with $L_x = 100$, 200, and 400 (with fixed $L_z = 20$ in the Ising case) collapse on top of each other. The fitting forms described in the text are also plotted in both cases.

Finally, we return to the simple DG transport operator (9.19). We may in fact derive this form, for a shear-like field, via an approximate microscopic approach, in the strong-drive limit [131]. As defined in Sec. 7.2, an elementary move consists of a column at x losing a unit of height to one of its neighbours, at position x'. In the strong-drive limit, the work done by the driving field is much greater than the work to overcome surface tension: $\Delta W \gg \Delta H$. Thus the Metropolis update rate becomes

$$p(x \to x') = \min\left\{1, \exp\left[-\beta \Delta W\right]\right\}. \tag{9.23}$$

The change of height at position x per unit time is given by the net flux of "height units" into x:

$$\partial_t h(x) = 2 \cdot \frac{1}{4}\left[p(x-1 \to x) - p(x \to x-1) + p(x+1 \to x) - p(x \to x+1)\right]. \tag{9.24}$$

The pre-factor of 2 accounts for the fact that each p term can come about in two different ways, by swapping x and x'. Now, the work ΔW for shear-like drive is given by Eqn. (7.13), which involves the expression $[h(x)+h(x')]/2$, the average of the heights in the source and destination columns. We may re-write this in terms of discrete derivatives of $h(x)$:

$$h(x) + h(x \pm 1) = \frac{1}{2}\partial_x^2 h(x) \pm \partial_x h(x) + 2h(x), \tag{9.25}$$

where, as above, we use the mid-point (two-point stencil) first derivative formula, and a three-point stencil for the second: $\partial_x^2 h(x) = h(x+1) - 2h(x) + h(x-1)$. At this point we introduce the abbreviation $\alpha \equiv \beta J \gamma$, and substitute the rates (9.23) into (9.24), dealing with the cases $h(x)$, $h(x \pm 1) > 0$ and $h(x)$, $h(x \pm 1) < 0$ separately:

$$\partial_t h(x) = \begin{cases} \frac{1}{2}\left(1 - e^{-\frac{\alpha}{2}(h(x)+h(x-1))} + e^{-\frac{\alpha}{2}(h(x)+h(x+1))} - 1\right), & h(x) > 0 \\ \frac{1}{2}\left(e^{-\frac{\alpha}{2}\mathrm{sgn}(h(x))(h(x)+h(x-1))} - 1 + 1 - e^{-\frac{\alpha}{2}\mathrm{sgn}(h(x))(h(x)+h(x+1))}\right), & h(x) < 0, \end{cases} \tag{9.26}$$

or simply

$$\partial_t h(x) = \frac{1}{2}\mathrm{sgn}(h(x))\left[-e^{-\alpha\frac{\mathrm{sgn}(h(x))(h(x)+h(x-1))}{2}} + e^{-\alpha\frac{\mathrm{sgn}(h(x))(h(x)+h(x+1))}{2}}\right]. \tag{9.27}$$

Note that we have assumed that both involved columns have the *same* sign, and we do not consider the case where they have opposite signs – this is, of course, a potentially serious restriction, since this is a common case. Using (9.25) yields

$$\begin{aligned} \partial_t h(x) =& \frac{1}{2}\mathrm{sgn}(h(x)) e^{-\alpha\left(|h(x)| + \frac{1}{4}\mathrm{sgn}(h(x))\partial_x^2 h(x)\right)}\left[-e^{+\frac{\alpha}{2}\mathrm{sgn}(h(x))\partial_x h(x)} + e^{-\frac{\alpha}{2}\mathrm{sgn}(h(x))\partial_x h(x)}\right] \\ \approx& -\frac{1}{2}\alpha e^{-\alpha\left(|h(x)| + \frac{1}{4}\mathrm{sgn}(h(x))\partial_x^2 h(x)\right)}\partial_x h(x) \end{aligned} \tag{9.28}$$

for $\alpha\partial_x h(x) \ll 1$. To linear order in h (we assume $\partial_x^2 h(x) \ll h(x)$), one finally obtains

$$\partial_t h(x) = -\frac{\alpha}{2}\partial_x h(x), \tag{9.29}$$

which is the form of the transport equation produced by the operator (9.19). In arriving at this form, we did impose several restrictions: in particular, the strong drive limit, the condition that both column heights have the same sign, and the assumption of small height gradients. Consequently, in this form the above is not a general derivation of the transport operator, but rather a plausibility argument; its appeal is its origin in the *microscopic* dynamics, as opposed to coming from a continuum description. For the more complex Ising model, the type of approach we have used here would be far more difficult – one would have to account for how individual spin exchanges from a given configuration affect the height, which involves dealing with many more degrees of freedom.

9.8 Interface structure and dynamics in the driven Blume-Capel model

The addition of the third spin state (or vacancy in binary mixture language) $\sigma = 0$ in the Blume-Capel (BC) model has important effects on the structure and dynamics of the interface. In equilibrium, simulations on (non-conserved) phase-separated systems (with magnetic field $B = 0$) below the critical temperature for given crystal field D show adsorption of $\sigma = 0$ spins at the interface [137, 152] – this layer provides a "buffer" between the ± 1 species, and so lowers the energy of the system. The thickness of the layer depends on D, as well as system size and temperature. We observe the same phenomenon to occur in the BC system evolving under conservative dynamics, where the numbers of $\sigma = +1, -1, 0$ spins are fixed at all times, in both the equilibrium and driven cases. This is demonstrated by the simulation snapshot in Fig. 9.23a, and confirmed by the vacancy density profile $\rho_0(\tilde{z})$ in Fig. 9.24a, which exhibits a peak at the centre of the system. In both the figure and the snapshot, the vacancy concentration is 20%, the system dimensions are $L_x = 128$, $L_z = 16$, and the temperature is $k_BT/J = 0.75$ (absolute), far below the equilibrium critical point. The system is driven by a *co-drive* uniform field of strength $f = 0.125$ - recall from Sec. 7.1 that in this case, both the ± 1 species are driven in the *same* direction, in contrast to the Ising model. The density profiles for the ± 1 species in Fig. 9.24a are mirror images of one another across the $\tilde{z} = 0$ line, since we fix their total densities to be equal, $\rho_+ = \rho_-$ ($= 0.4$ each in this case). Also shown is the order parameter profile

$$\Phi(\tilde{z}) = \rho_+(\tilde{z}) - \rho_-(\tilde{z}), \tag{9.30}$$

the equivalent of the magnetisation profile in the Ising model, which varies from a negative value in the bulk '$-$' phase to a positive one in the '$+$' phase, passing through zero at the interface.

The sharpening of the order parameter profile observed in the driven Ising model also occurs in the BC system, as shown in the main panel of Fig. 9.24b, where order parameter profiles for co-driven systems are compared to the equilibrium result. In all cases, the vacancy concentration is 20%, so the system is significantly different from the Ising model even in equilibrium. For these co-driven systems, the sharpening of $\Phi(\tilde{z})$ increases with stronger driving fields. However, when the system is subject to *counter-drive*, where the ± 1 species move in opposite directions, it transpires that the interface

can become destabilized, for sufficiently large vacancy concentrations. Fig. 9.23b shows a simulation snapshot for parameters where this phenomenon occurs; the corresponding time-averaged density profiles are shown in the inset of Fig. 9.24b. The vacancy density is almost constant for all z, due to the block-like structures visible in the snapshot. The phase separation is severely affected, with large regions of the ± 1 species in contact with the opposite wall (i.e., '+' next to the '-' wall, and vice-versa). We explore these strange effects further in Appendix B; for now, we confine our attention to the cases where the system is stable under drive.

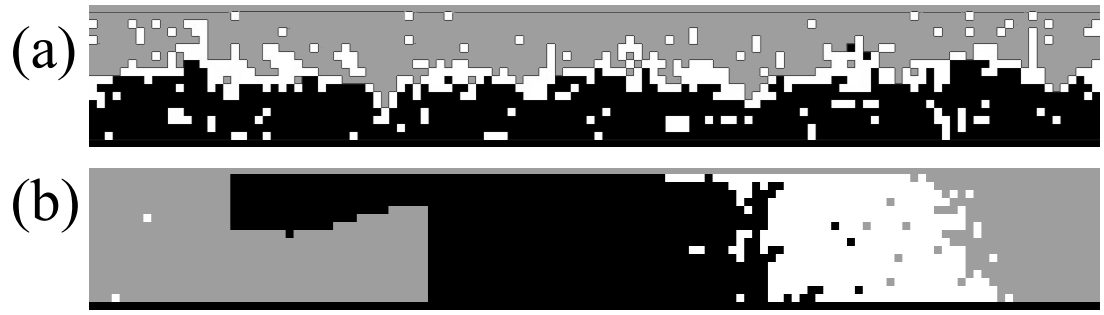

Figure 9.23: Snapshots from Monte Carlo simulations of the driven, conservative Blume-Capel model. In both cases the system has dimensions $L_x = 128$, $L_z = 16$, the temperature is $k_B T/J = 0.75$, and the vacancy concentration is 20%. The '+' spins are shown in grey, the '$-$' in black, and the vacancies are white. (a) Uniform co-drive field of strength $f = 0.125$: the interface is stable, and vacancies ($\sigma = 0$ spins) form a buffer layer between the ± 1 phases. (b) Uniform counter-drive with $f = 0.25$ – the interface is unstable, and the vacancies form a long-lived block or plug-like structure, which travels through the system.

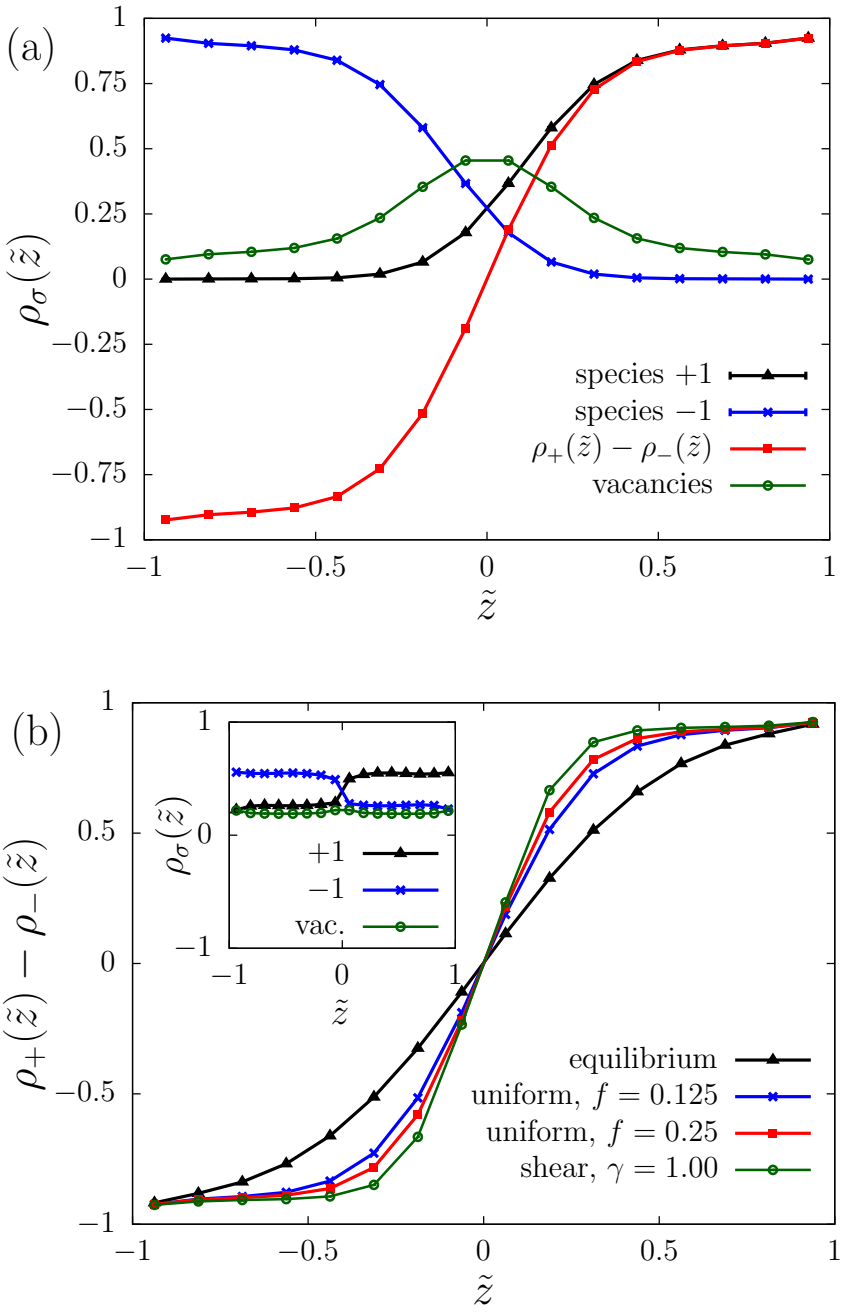

Figure 9.24: Density profiles for the Blume-Capel model with driven, conservative dynamics. (a) Results for an $L_x = 128$, $L_z = 16$ system at temperature $k_BT/J = 0.75$, driven by a co-drive uniform field of strength $f = 0.125$, with vacancy concentration 20%, and equal concentrations of the ± 1 species. The individual species' density profiles $\rho_\sigma(\tilde{z})$, as well as the order parameter profile $\Phi(\tilde{z}) = \rho_+(\tilde{z}) - \rho_-(\tilde{z})$, are shown. (b) Order parameter profiles for the same system, but driven by different field strengths and types, including zero field (equilibrium). In the inset, density profiles for a *counter-drive* uniform field with $f = 0.125$ show the instability of the system for this combination of parameters.

A key difference between co-driven BC systems and the driven Ising model concerns the symmetry of the order parameter current $j_+(\tilde{z}) - j_-(\tilde{z})$ (cf. Eqn. (9.1)). Fig. 9.25 shows current profiles for the cases of uniform and shear-like driving fields. For a uniform field in (a), the individual currents for the ± 1 species are always positive (due to co-drive) – consequently, the vacancy/hole current is negative, since the vacancies are effectively driven in the opposite direction via exchanges with the ± 1 species. The ± 1 species' currents are strong in their own phase, where there is a large carrier density. The order parameter current therefore attains an *odd* symmetry in this case, in contrast to the situation in the Ising model. For shear-like drive in (b), $j_+(\tilde{z}) - j_-(\tilde{z})$ is even in $\tilde{z}$, again opposite to the Ising case. This means that our choice of the appearance of the symmetry of the current, rather than the field, in the earlier conjecture for the occurence of travelling capillary waves, may be tested.

We do this by coarse-graining the BC model in the same way as the Ising model, via the simple sum definition of the interface height, and measuring the space-time height correlation function $C(x,t)$. Based on the symmetry of the order parameter current profile, we expect motion to occur for uniform co-drive, but not for shear-like co-drive. This is indeed the case: in the main plot of Fig. 9.26, where results for uniform drive are shown, the peak moves to the right with increasing time, whereas for shear-like drive in the inset, there is no evidence of motion. As in the Ising model, the direction of movement is the same as that of the "intruders" – in this case, the intruders move in the same direction as the local majority species (the positive x direction). The relevance of the direction of motion of the vacancies is not clear, but seems difficult to assess, due to the nature of the exchange dynamics on the lattice: if one species is driven in a particular direction, another species which does not explicitly interact with the field (as for the vacancies here) will effectively feel a force in the opposite direction. Thus co-driving the vacancies with the ± 1 species is not possible (just as we could not co-drive the ± 1 spins in the Ising model). The peak velocity v_{peak} is larger than in the Ising model – for example, with vacancy concentration 20% and $f = 0.25$, $v_{\text{peak}} \approx 0.009$, whereas for step-like drive in the Ising model with $f = 1$ (as in Fig. 9.17), $v_{\text{peak}} \approx 0.0064$. For smaller vacancy densities, we observe that v_{peak} is smaller – this is natural, since the action of the drive depends entirely upon the presence of vacancies in the case of co-driving. The nature of the drive also means that if we consider the same symmetry arguments applied to the Ising model in Sec. 9.5.1, we find that for uniform co-drive (where CW motion occurs), the directions of movement

of the ± 1 species are *unchanged* after species inversion and x, z spatial reflection – in contrast with the cases where motion occurs in the Ising model. This highlights the fact that the symmetry considerations are strongly model-dependent, whereas the relationship between the order parameter current and CW motion is less so.

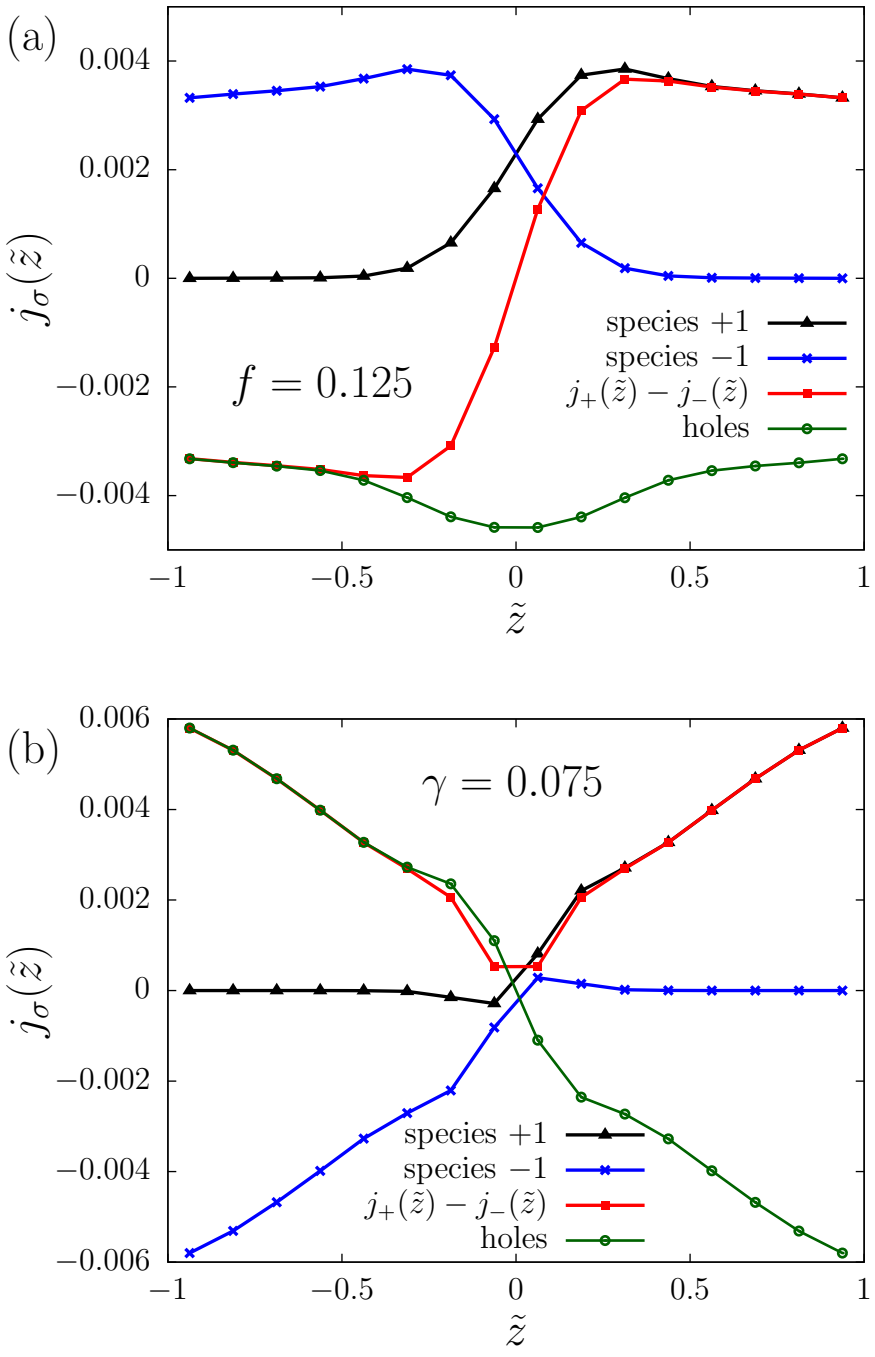

Figure 9.25: Current profiles for the co-driven Blume-Capel model. As for Fig. 9.24, the system is $L_x = 128$, $L_z = 16$ with $k_BT/J = 0.75$, and the vacancy concentration is 20%. (a) Results for uniform drive of strength $f = 0.125$, showing individual species' currents, as well as the order parameter current profile $j_+(\tilde{z}) - j_-(\tilde{z})$; the latter has odd symmetry in $\tilde{z}$. (b) Profiles for shear-like drive with $\gamma = 0.075$; the order parameter current is now even.

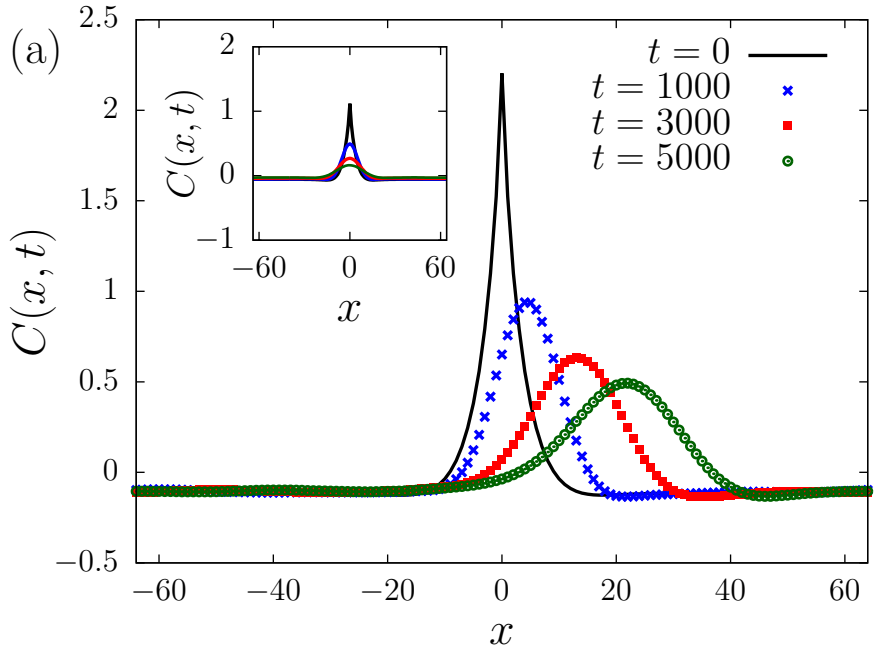

Figure 9.26: Space-time height correlation function $C(x,t)$ for the Blume-Capel model with conservative dynamics, for different time differences t, as indicated, as a function of spatial separation x. In the main plot, results for uniform co-drive of strength $f = 0.125$ and vacancy concentration 20% are shown: the peak decays and moves to the right, indicating lateral capillary wave motion. In the inset, data for shear-like co-drive with $\gamma = 0.075$ and vacancy concentration of 8% show that for this case, no transport occurs. In both plots, the system has dimensions 128×16, and $k_BT/J = 0.75$.

Chapter 10

Results in three dimensions

We now consider the driven Ising lattice gas in three dimensions on a simple cubic lattice, as introduced in Chapter 7. We wish to investigate whether the suppression of capillary waves, and the transport phenomenon, which we discovered in $2d$, persist in three dimensions; simulating a $3d$ system enables a more direct comparison with the experimental results of Ref. [13]. Furthermore, the problem of non-equilibrium fluctuations of a liquid-liquid interface in a $3d$ system under shear has recently been addressed theoretically [122] within the framework of fluctuating hydrodynamics. This approach leads to a mode-coupling equation for the interface height which was solved using a perturbation theory. Results for the interfacial width are in agreement with the experiment of Ref. [13], but the results for the interfacial correlation length in the flow direction are not. The theoretical height-height correlation function and the structure factor imply a decrease of the correlation length in the direction of flow. Interestingly, in the direction perpendicular to the flow (vorticity direction), the correlation length seems to *increase*. In light of these theoretical results, studying the $3d$ driven Ising system is all the more valuable.

The majority of the results shown here are for a system size $L_x = L_y \equiv L = 128$ and $L_z = 10$ or $L_z = 20$, at a temperature $T/T_c^{3d} = 0.75$, where $k_B T_c^{3d} \approx 4.5115$ ($\beta_c^{3d} = 1/k_B T_c^{3d} \approx 0.22165$) is the bulk critical temperature of the equilibrium $3d$ Ising system [57]. We abbreviate T_c^{3d} to T_c in the rest of this chapter except when this notation is ambiguous. The effect of going to larger values $L \leq 192$ was checked, and generally found to be small, except for the largest wall separations (recall that the lateral correlation length $\xi_{\|}$ grows exponentially with L_z; once this becomes comparable to L, the effects of finite L will be noticeable). We will see evidence of this when we discuss the interfacial

width. We also vary the temperature, firstly to investigate the effect of an increase to $T/T_c = 0.90$, and secondly to study the behaviour near and below the roughening transition. For an equilibrium system in the thermodynamic limit, the roughening temperature is $k_B T_R \approx 2.454J$ [90]. In a finite system, the (pseudo-)transition will occur at a shifted value of temperature $T_R(L, L, L_z)$, governed by the system size [153]. As temperature is increased in the smooth regime, either the interfacial width will reach the scale of L_z, or the lateral correlation length will reach L_x or L_y – in either case, the interface reaches the rough regime. We therefore cover a range of temperatures around the roughening temperature in the simulations, from $T/T_c = 0.4$ to $T/T_c = 0.6$. As mentioned in Sec. 3.5.4, the roughening transition belongs to the universality class of the Kosterlitz-Thouless transition [84]. The renormalization group method of Kosterlitz [154] showed that the lateral correlation length $\xi_\parallel$ diverges very rapidly as $T \to T_R$ from below:

$$\xi_\parallel = A \exp\left[\frac{B}{\sqrt{(T_R/T - 1)}}\right], \tag{10.1}$$

where A and B are non-universal parameters. The numerical values for these constants obtained from MC simulation studies of the Ising interface in $3d$ are $A = 0.80(1)$ and $B = 1.01(1)$ [90]. The shift of the pseudo-roughening temperature can be estimated from the condition $\xi_\parallel \simeq L_x (= L_y = L)$, which yields $(T_R - T_R(L, L, L_z))/T_R(L, L, L_z) \equiv \Delta T \simeq (B/\ln(L/A))^2$. This is a very weak dependence on L and for our system size it gives $\Delta T \simeq 0.04$. At the same time the width of the interface diverges upon approaching the bulk roughening temperature, as $w^2 \sim \ln(\xi_\parallel)$. The condition $w \simeq L_z$ yields $\Delta T \simeq \left(B/(L_z^2 - \ln A)\right)^2$, which is a much stronger dependence on the finite dimension L_z than that obtained on L from the condition involving $\xi_\parallel$. For $L_z = 10$, $\Delta T \simeq 10^{-4}$, therefore we conclude that the shift of the roughening transition is governed by $\xi_\parallel$. Using that estimate of ΔT gives $T_R(L, L, L_z)/T_c \simeq 0.52$, so the range of simulation temperatures should include the equilibrium pseudo-transition temperature.

As in two dimensions, the time for the system to reach a steady state was estimated, and run lengths chosen accordingly. Results reported here are from total run lengths of $2 - 4 \times 10^7$ MCS ($L_x \times L_y \times L_z$ trial moves in the $3d$ system), of which the last $1 - 2 \times 10^7$ MCS were used for capturing data. These run lengths are much shorter than in $2d$ – even allowing for some over-estimation in the relaxation time in that case, it is clear that the slow evolution of Kawasaki dynamics to a steady state is less of a problem in $3d$ than in $2d$. Errors were estimated in the same ways as they were in two dimensions.

10.1 Statics: interface structure

10.1.1 Magnetisation profile

We first investigate the interfacial structure of the driven $3d$ Ising model in order to see whether in three dimensions the effective action of drive is to increase the confinement of the interface, as it was in two. The magnetisation profile $m(z)$ between the walls is calculated in the $3d$ system as

$$m(z) = \frac{1}{L_x L_y} \left\langle \sum_{x,y} \sigma(x,y,z) \right\rangle, \tag{10.2}$$

where the angles denote an average in the steady state (see also Eqn. (9.2)). In Fig. 10.1a we plot profiles from both equilibrium and driven systems, making use of the same scaled variable $\tilde{z} = 2z/L_z$ as before in $2d$. Upon applying drive to the system, the magnetisation profile becomes sharper: $m(\tilde{z})$ changes sign more rapidly in the interfacial region, and there is a more extended flat region near either wall. The size of this effect increases with increasing driving strength, γ or f. These trends are the same as in two dimensions, but for given driving strength, the magnitude of the effect is smaller in $3d$. This latter finding is consistent with the fact that in equilibrium, CW fluctuations at interfaces in $d = 3$ systems are much weaker than in $d = 2$ (for example, the interface width follows $w \propto \sqrt{L_z}$ in $d = 3$, while $w \propto L_z$ in $d = 2$). Therefore there are fewer large-scale CW fluctuations for the drive to destroy in the $3d$ system; the destruction of such fluctuations is the biggest contributor to the profile sharpening / interface smoothening when drive is initially applied.

As in two dimensions, it is possible to rescale the driven profiles to collapse back onto the equilibrium result: see Fig. 10.1b. We again interpret this as the drive acting to reduce the effective distance between the walls from L_z to L_z^*, and thus to effectively increase the confinement of the system. As mentioned in Sec. 9.3.1, the estimation of the rescaling factor $a_\perp = L_z^*/L_z$ was obtained systematically for the $3d$ system. This was done by rescaling the driven data to spline-interpolated equilibrium curves and minimizing the associated chi-squared statistic by varying $a_\perp$ – the value of $a_\perp$ at the minimum being the optimal value. Points near the upper and lower walls, where wall-interaction effects are important (which would ideally be handled by the unknown $\mathcal{M}_{\rm corr}(z)$ term in Eqn. (9.3)) were excluded from the procedure, although this was observed to have a rather minor effect on the resulting optimal $a_\perp$ values. Applying the crude "manual" rescaling procedure used

for the $2d$ system also gave similar results to the more systematic procedure, although clearly the latter should be preferred.

For shear-like drive with $\gamma = 1.0$, we find $a_\perp = 0.71(8)$, whereas for two dimensions, for the same value of γ and L_z we had $a_\perp^{2d} = 1/3.4 = 0.29$ (Sec. 9.3.1) – this highlights the greater effect of drive in the $2d$ case. Although the lateral dimensions of the $2d$ and $3d$ systems are different ($L_x = 200$ in $2d$, while $L_x = L_y = 128$ here), this should not be especially important, since the controlling length scale in the confined regime is the wall separation L_z. For given γ at $T/T_c = 0.75$, shear-like and V-shaped drive yield rather similar rescaling factors. More pronounced differences are observed for smaller values of γ and lower temperatures, suggesting that effective confinement is stronger for the V-shaped drive – this was also observed in $2d$. Rescaling fails for lower temperatures closer to and below the equilibrium bulk roughening transition temperature. For these temperatures, the equilibrium profile is already almost step-like, since thermal capillary-wave fluctuations are much weaker; driving the system therefore has a much smaller effect on the profile than at higher temperatures.

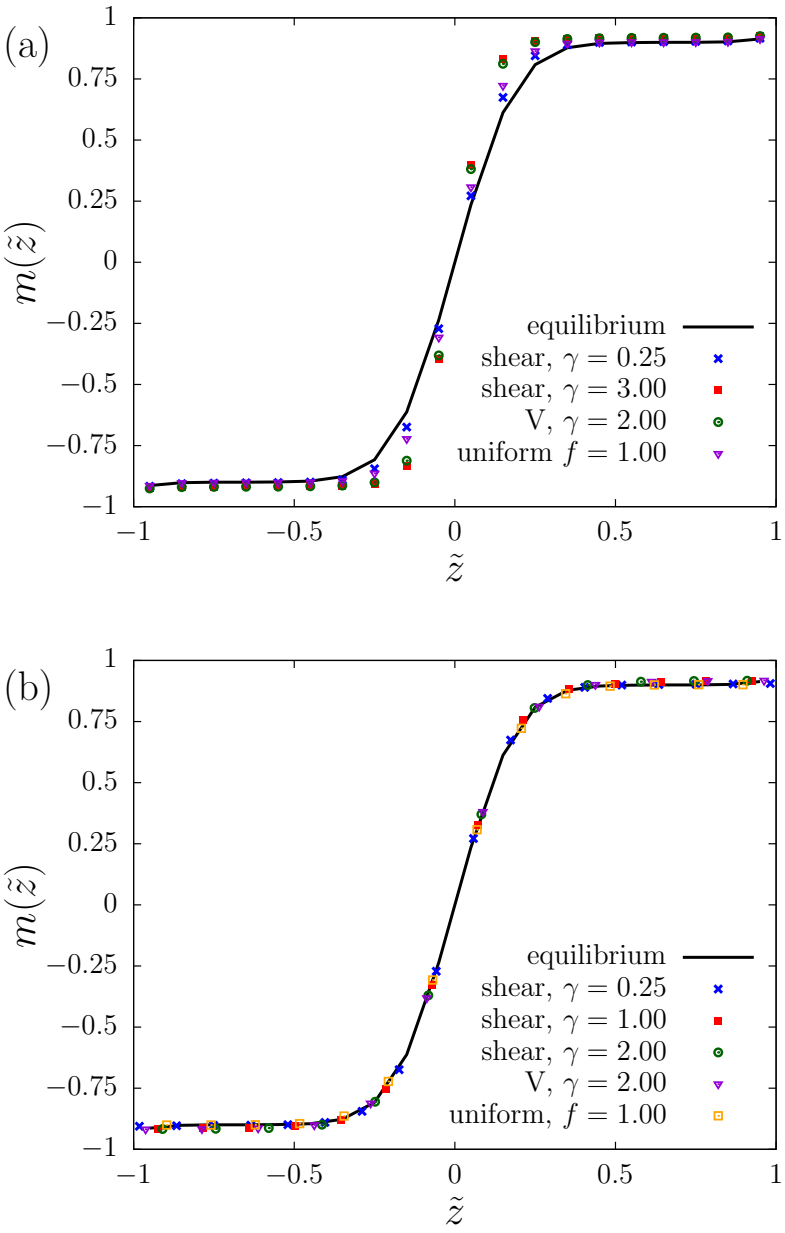

Figure 10.1: Magnetisation profiles $m(\tilde{z})$ as a function of the scaled coordinate $\tilde{z}$ between the walls. The system is $L_x = L_y = 128, L_z = 20$, at a temperature $T/T_c = 0.75$. Results for equilibrium simulations ($\gamma = 0$) with Kawasaki dynamics (solid line) are shown in (a), as well as for shear-like, V-shaped and uniform drive (symbols). In (b) results of rescaling to equilibrium are plotted; rescaling factors are $a_\perp = 0.87, 0.70, 0.60$ for shear with $\gamma = 0.25, 1.0, 2.0$, respectively, $a_\perp = 0.57$ for V drive with $\gamma = 1.0$, and $a_\perp = 0.72$ for uniform drive with $f = 1.0$. Error bars are of order or smaller than the line thickness or symbol size.

10.1.2 Interface width

As in $2d$, we measure the width via the second moment of $\partial m/\partial z$ and study its variation with driving strength, wall separation L_z, and temperature. Upon increasing driving strength γ or f, the width reduces, as expected from the results for the full profile. For shear-like and V-shaped drive, we are also able to obtain data collapse for the behaviour of $w/\sqrt{L_z}$ as a function of the same scaling variable $\theta = L_z\gamma^s$ as in the $2d$ driven Ising system with, remarkably, the *same* exponent $s = 0.3$. The division of the width by $\sqrt{L_z}$ corresponds to the expected $d = 3$ equilibrium behaviour (Sec. 2.3.1, Sec. 3.5.3), so that for $\theta \to 0$, $w/\sqrt{L_z} \to$ constant. The scaling behaviour of the width is shown in Fig. 10.2, for fixed temperature $T/T_c = 0.75$, and a variety of wall separations and drive gradients in the ranges $10 \leq L_z \leq 20$, $0 < \gamma \leq 2$. From Fig. 10.2 we see that for small γ at the larger values of $L_z = 16$ and 20, the data collapse is lost – we believe that this is because the system starts to move out of the confined regime with $w \sim \sqrt{L_z}$ for these parameters. For these wall separations, the lateral correlation length $\xi_\parallel$ becomes comparable to the linear dimension L of the interface, and the system begins to cross over to the regime where the dominant length scale is L. This does not require a large increase in L_z, because from Eqn. (2.31), $\xi_\parallel \simeq \exp(\kappa L_z/4)$, where the transverse length scale κ^{-1} is of order the bulk correlation length ξ_b. Data collapse is regained for larger values of γ, because the effective wall separation $L_z^* < L_z$ is the controlling length scale (from the discussion of the magnetisation profile above), and L_z^* is small enough for the system to be in the "confined regime". The inset of Fig. 10.2 shows the variation of the width with drive gradient γ for shear-like and V-shaped drive. The trends are rather similar, with the width for given γ very slightly smaller for V-shaped drive – this is consistent with the previous conclusion that confinement is stronger for this drive type.

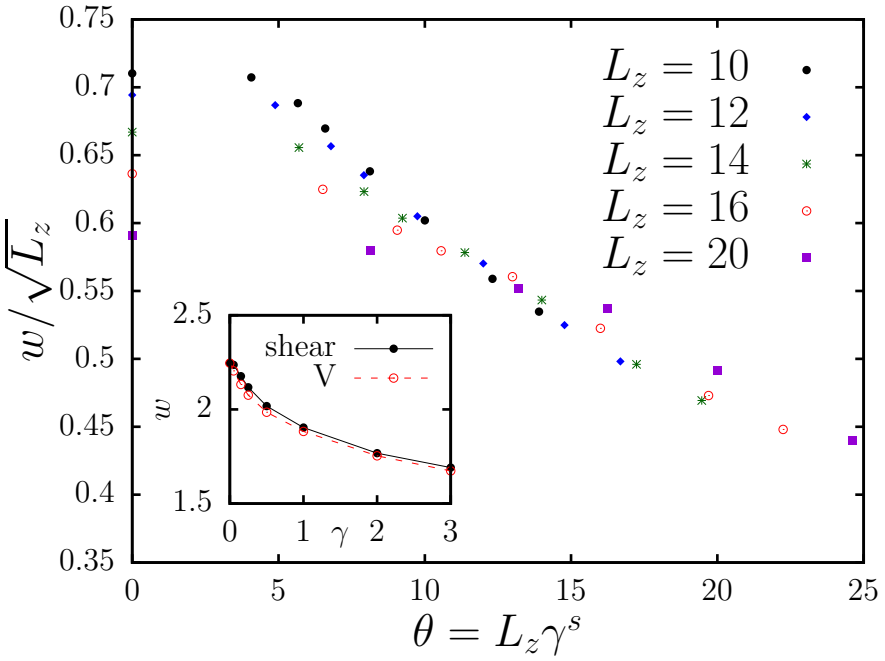

Figure 10.2: Scaling behaviour of the interfacial width w, as a function of the scaling variable $\theta = L_z\gamma^s$, with $s = 0.3$, for systems driven by a shear-like field. The width is scaled by $\sqrt{L_z}$ according to the equilibrium relation $w/\sqrt{L_z} = \text{const.}$, as discussed in the text. Different point types correspond to differing values of L_z, from 10 to 20, as indicated. In all cases, the lateral system length is $L = 128$, and the temperature is $T/T_c = 0.75$. Inset: variation of the width with drive gradient γ, for shear-like drive (filled circles, solid line) and V-shaped drive (open circles, dashed line), at fixed $L_z = 10$.

10.1.3 Interfacial spin-spin correlation function

The spatial spin-spin correlation function at the midplane is defined in the $3d$ system as

$$G(x, y, z = 1/2) = \frac{1}{L_x L_y} \left\langle \sum_{x',y'} \sigma(x', y', 1/2)\sigma(x' + x, y' + y, 1/2) \right\rangle, \tag{10.3}$$

which depends on separations in both the x and y directions. We suppress the fixed z coordinate in the following. Comparing the specific cases $G(x, y = 0)$ and $G(x = 0, y)$ provides information on the anisotropy between the x and y directions. In equilibrium, the system should be isotropic in the lateral plane, so $G(x, 0) = G(0, y)$ for $L_x = L_y$, but for driven systems, the two functions may differ. Results in Fig. 10.3a show that shear-like drive causes *both* $G(x, 0)$ and $G(0, y)$ to decay more quickly and for larger separations to saturate at larger asymptotic values than in equilibrium. In the x direction, this finding is in agreement with recent hydrodynamics results [122]; however in that study, the correlation length in the y direction was found to *increase* under shear, contrary to the trend in our system. We defer further exploration of this difference to the discussion of the height correlations below, since the height variable provides a more direct point of comparison between the systems.

As in the $2d$ case, the spin correlation functions at intermediate separations may be transformed to the equilibrium result via a rescaling of the lateral coordinate, x or y: $G(a_\parallel^x x, 0) \approx G_{\rm eq}(x, 0)$ and $G(0, a_\parallel^y y) \approx G_{\rm eq}(0, y)$, see Sec. 9.3.3. In the driven $3d$ system, separate parameters $a_\parallel^x$ and $a_\parallel^y$ are required for the x and y directions due to the anisotropy: the lateral correlation lengths in the two directions may be different. Fig. 10.3b shows rescaling results for $G(x, 0)$ in the main figure, and for $G(0, y)$ in the inset, from an $L = 128$, $L_z = 10$ system at $T/T_c = 0.75$ at various driving strengths. The rescaling factors were obtained via the same method as for the magnetisation profile; in this case, very small values of x or y were cut off in the procedure, as were the tails of the functions, so that the rescaling procedure was carried out over $2 \leq x, y \leq 16$. As in $2d$, the $a_\parallel$ parameters may be interpreted as ratios of lateral interfacial correlation lengths in and out of equilibrium: $a_\parallel^x = \xi_\parallel^x / \xi_\parallel^{x,\rm eq}$ and $a_\parallel^y = \xi_\parallel^y / \xi_\parallel^{y,\rm eq}$ Rescaling the driven data produces $a_\parallel^x < 1$ and $a_\parallel^y < 1$, so that the correlation length is reduced under drive – this tallies with the faster decay evident from Fig. 10.3a. The x-y anisotropy may be measured by the ratio $a_\parallel^y / a_\parallel^x$; this is consistently slightly smaller than unity, leading to the surprising conclusion that the correlations are slightly *more* suppressed in the y (vorticity) direction. As with the

magnetisation profile, the effect of drive is much weaker in three dimensions than in two – for example, in $2d$, $a_{\parallel}^{x} = 1/1.27$ for $\gamma = 0.025$, while in $3d$, $a_{\parallel}^{x} = 0.78 \approx 1/1.28$ for $\gamma = 0.25$: a ten times larger field gradient is required to produce a comparable confinement. As a result, the rescaling procedure works for much larger values of γ than in $2d$ – a stronger drive is required to push the system into a regime which is too far from equilibrium for rescaling to be possible. The V-shaped drive has a similar effect on the interfacial correlations: for example, with $\gamma = 0.25$, $a_{\parallel}^{x} = 0.74$, corresponding to a slightly stronger confinement effect than with shear, consistent with the findings for the magnetisation profile.

Fig. 10.4 shows the effect of varying the temperature on the interfacial correlations. Lowering the temperature to $T/T_c = 0.5$ (below the roughening transition in a bulk equilibrium system) in equilibrium results in correlations $G(x, 0)$ that decay to only ~ 0.6 for the largest separations. Since on the lattice the average interface position lies *between* two lattice points (for zero overall magnetisation), one measures the correlations just either side of the interface (which side does not matter, due to symmetry). Thus at zero temperature, $G(x, y, z = 1/2) = 1$ for all x, y, since the interface is perfectly flat at $T = 0$. This explains the observed increase of asymptotic values of $G(x, 0)$ for low T. Moreover, the width of smooth interfaces is of order of the bulk correlation length, which at low temperatures is $\sim$ 2-3 lattice spacings. Therefore, for low temperatures $G(x, 0)$ essentially measures correlations in the bulk-like phase. We also see from Fig. 10.4 that driving the system enhances the asymptotic value further for $T/T_c = 0.5$, which indicates that at fixed temperature the bulk-like phase is more ordered under drive than in equilibrium. As for the magnetisation profile, rescaling does not work for the low temperatures – the drive affects the asymptotic value more than the decay rate for these temperatures.

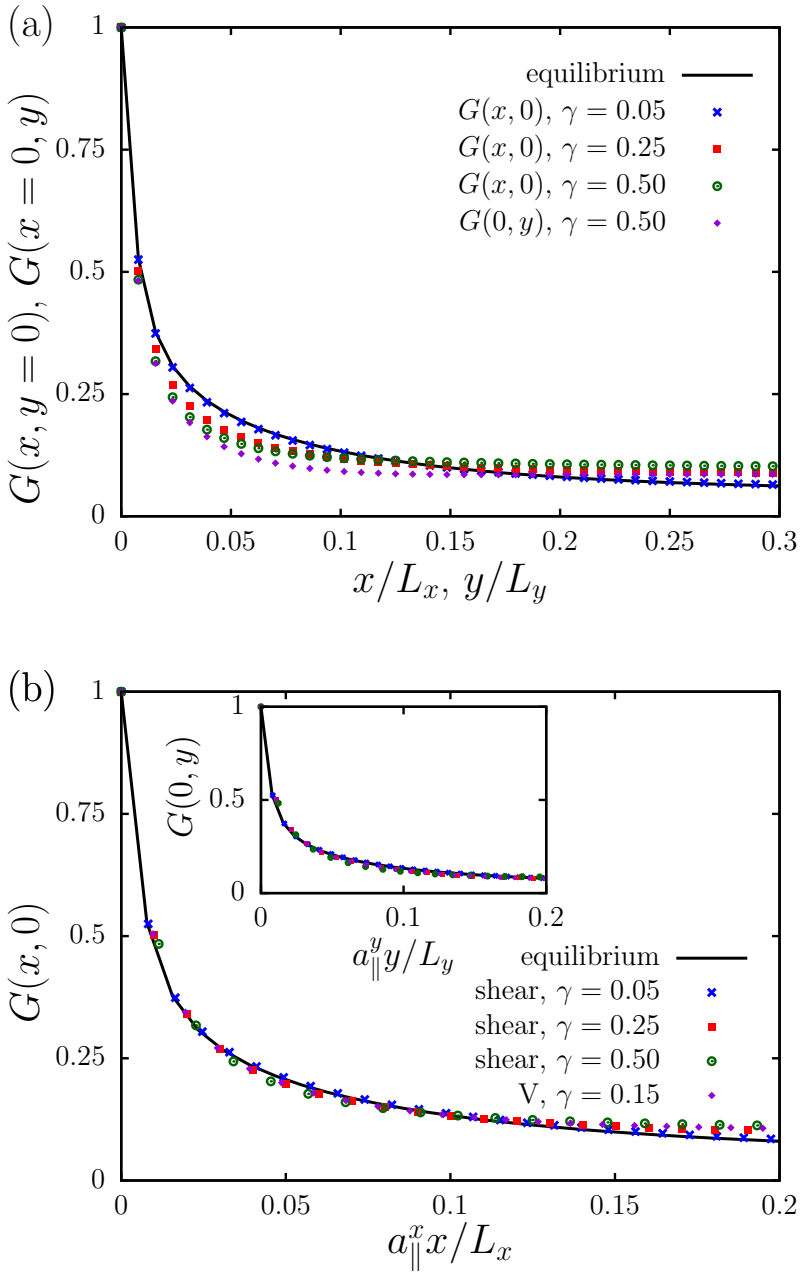

Figure 10.3: Spin-spin correlation functions $G(x, y = 0)$ and $G(x = 0, y)$ as a function of scaled separation x/L_x or y/L_y. (a) Results for a $128 \times 128 \times 10$ system at $T/T_c = 0.75$. The equilibrium result is shown, as well as driven results for shear-like drive at several values of drive gradient γ, as indicated. The behaviour of $G(x, 0)$ and $G(0, y)$ for $\gamma = 0.5$ may be compared. In the main panel of (b), the driven results for $G(x, y = 0)$ are rescaled via the parameter $a^x_\parallel = \xi^x_\parallel / \xi^{x,\mathrm{eq}}_\parallel$, as described in the text; rescaling factors are $a^x_\parallel = 0.95$, 0.78, 0.69 for shear-like drive with $\gamma = 0.05, 0.25, 0.5$, respectively, and $a^x_\parallel = 0.80$ for V drive with $\gamma = 0.15$. In the inset, the corresponding rescaling results for $G(x = 0, y)$ are shown; $a^y_\parallel = 0.95$, 0.74, 0.64 for the same values of shear-like drive, implying a slightly greater reduction in correlation length $\xi^y_\parallel$.

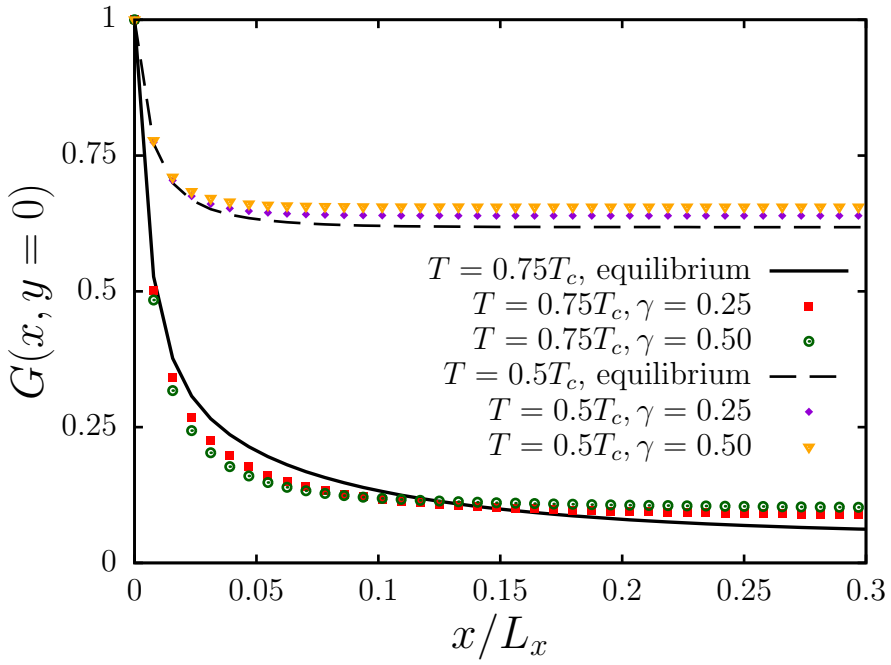

Figure 10.4: Results for $G(x, y = 0)$ for $128 \times 128 \times 10$ systems at $T/T_c = 0.75$ and $T/T_c = 0.5$, for equilibrium and two strengths of shear-like drive. Below the equilibrium roughening temperature, i.e., for $T/T_c = 0.5$, the asymptotic value is large, and increases for stronger drive.

10.1.4 Height-height correlation functions

We now turn to the interfacial height-height pair correlation function. Motivated by the success of the simple column-sum coarse-graining method used in the two-dimensional driven Ising system, we adopt the same method here, such that $h(x, y, t) = -(1/2)\sum_z \sigma(x, y, z, t)$. The height-height correlation function in $3d$ depends on spatial separations x and y in the drive and vorticity directions respectively, and on temporal displacement t:

$$C(x, y, t) = \frac{1}{L_x L_y} \left\langle \sum_{x',y'} h(x', y', t')h(x' + x, y' + y, t' + t) \right\rangle, \tag{10.4}$$

where the angles indicate an average over time. We first consider the equal-time correlations, with one of the spatial separations set to zero: Fig. 10.5 shows results for $C(x, y = 0, t = 0)$; in the rest of this section we suppress the (zero) time coordinate. In two dimensions, we saw that $C(x)$ (also $G(x)$) in equilibrium exhibited strong anti-correlated regions for medium-to-large separations, presumed to be finite size effects. These features are not present in $3d$ for the system sizes considered – the functions decay to zero without becoming significantly negative, indicating less severe finite size effects; an explanation may be the following. With conservative dynamics, a positive-height 'bump' must be accompanied by one with negative height, since $\sum h \equiv 0$. In $2d$, these must lie on the same x-z layer (the only one), so an anti-correlation is measured in $C(x)$. However in $3d$ there are L_y x-z layers, so the pair may be located in different layers, meaning $C(x, y = 0)$ does not necessarily display anti-correlations.

Turning to the driven cases, we see from both the main plot and the inset of Fig. 10.5a that applying shear-like or V-shaped drive leads to a more rapid decay of $C(x, 0)$, as well as a smaller initial value $C(0, 0)$ (a measure of the interfacial width). The magnitude of this effect increases with increasing γ. Comparing the results from the two drive types at $\gamma = 0.5$, we see that the effects are very similar, though slightly greater for the V-shaped drive. This trend seems to hold for all values of γ. In the vorticity direction the findings are similar to those for the spin-spin correlation function: we see correlation-suppression in $C(0, y)$, and this effect is slightly *greater* than for $C(x, 0)$. As for other quantities, rescaling to the equilibrium result is possible in the same manner as in $2d$. For the height correlations, the rescaling takes the form $a_\perp^{-2} C(a_\parallel^x x) \approx C_{\mathrm{eq}}(x)$. The values of $a_\perp$ and $a_\parallel$ are those obtained from the rescaling of the magnetisation profile and the spin-spin correlation function for given simulation parameters. In $2d$ this procedure was

motivated by the scaling form Eqn. (9.11) for the equilibrium height correlation function from capillary wave theory in $d = 2$. In $d = 3$, this scaling form does not hold, because the width does not appear as a multiplicative factor with the scaling function; nevertheless, the rescaling procedure works reasonably well for $\gamma \lesssim 0.5$. As with the spin correlations, this range of validity is much greater than in two dimensions.

Furthermore, we are able to fit the results for $C(x, 0)$ and $C(0, y)$ for small-to-intermediate separations to the *equilibrium* capillary wave result for the height correlation function in $3d$: see Fig. 10.6 for results for shear-like drive. This procedure was used previously by Derks et *al.* to describe their experimental data, where an excellent fit was obtained [13]. For reference we quote the CWT result for $C(x, 0)$ in the limit $L_x = L_y \to \infty$, cf. Eqn. (2.24):

$$C(x,0) = \frac{k_B T}{2\pi\sigma} K_0 \left(\sqrt{\left(\frac{x}{\xi_\parallel}\right)^2 + \lambda^2} \right). \tag{10.5}$$

From the discussion around Eqn. (2.24) in Sec. 2.3.2, the shift $\lambda \approx 1/(k_{\max}\xi_\parallel)$. Combining (10.5) with the CWT result for the interface width, Eqn. (2.17), we are able to substitute for the (unknown) $k_{\max}$ in terms of the (measurable) width, and obtain a fitting form with two parameters: the correlation length $\xi_\parallel$ and the pre-factor $k_{\rm B}T/\sigma$. Note that in (10.5), we have specialised to separations in x rather than the radial distance r usual in CWT, since isotropy is broken in the non-equilibrium situation. For separations in y, the form for $C(0, y, 0)$ is the same, but different values of the parameters are expected – i.e., the correlation length ($\xi_\parallel^y$) will be different, as will the pre-factor. The interpretation of the latter quantity is difficult. Indeed, the interface tension is an *equilibrium* concept and cannot be carried over directly to non-equilibrium situations, so the meaning of the pre-factor is not initially clear – here we just note its anisotropy.

The equilibrium fit in Fig. 10.6 wanders off the data for larger separations; this may be due to a (less serious) manifestation of the finite size effects encountered in $2d$, which were mentioned above, and the conserved order parameter. (This is most obvious for the equilibrium data on the log scale, where the data diverge as they approach zero and become negative). For the driven cases, as drive becomes stronger, the fit works for a smaller range of separations – the example of shear-like drive with $\gamma = 1$ is given in Fig. 10.6. This trend is expected from the findings for the rescaling procedures applied above – initially the system is "close enough" to equilibrium for CWT to be approximately applicable, but as drive increases, this ceases to be true. From the fits we obtain the

equilibrium and non-equilibrium correlation lengths in the x and y directions, $\xi_{\parallel}^{x}$ and $\xi_{\parallel}^{y}$– see the inset of Fig. 10.6 for their variation with γ in the case of shear-like drive. The trend of decreasing correlation length with increasing drive strength mirrors the one found in $2d$, although there we were not able to obtain the correlation length reliably, due to the difficulty of fitting the correlation function data over a reasonable range. We also note that $\xi_{\parallel}^{y}$ is consistently smaller than $\xi_{\parallel}^{x}$, in agreement with the earlier conclusions, based on the behaviour of the spin-spin correlation functions, that correlations are slightly more strongly suppressed in the vorticity direction than in the driving direction.

The suppression of correlations we find in the drive (x) direction is in agreement with the hydrodynamics work of Thiébaud and Bickel [122], who studied phase separated fluids between two walls under shear. This trend is also the same as in the $2d$ Ising system, and both microscopic ($G(x)$, spin-spin) and coarse-grained ($C(x)$, height) measures of correlations give the same conclusion. Both the theoretical and simulation findings disagree, however, with the experimental results of Derks et *al.* [13], who found an *increase* of correlation length in the flow direction when shear was applied to a phase-separated colloid-polymer mixture. The fact that we have used the same method of fitting the height correlation data to the equilibrium capillary wave form as Ref. [13], makes the method of comparison the same, at least.

Finally, we consider the pre-factor resulting from the fit of the height correlation data to the CWT form (10.5). In equilibrium, the pre-factor is proportional to $k_B T/\sigma$, where σ is the surface tension (or more generally, surface stiffness Γ, which allows for anisotropy in the lattice axis directions, and for a continuum fluid becomes the surface tension) – in an equilibrium statistical-mechanical description, this is the free energy associated with the interface. Out of equilibrium, this free energy is not defined, so the meaning of the pre-factor resulting from the fit is not clear from the standpoint of equilibrium statistical mechanics. If, however, we think more generally, then the tension is a force per unit length – this force can be measured in an experiment, whether or not the system is in equilibrium – therefore, in this view, the pre-factor is better defined. The problem with this argument is that the CW results come from equilibrium statistical mechanics, so we cannot simply divorce ourselves from it! Of course, there is also the practical problem of identifying and measuring a quantity in the driven diffusive lattice system which is the analogue of the experimental force. Numerically, we find that the pre-factor from fitting $C(x, 0, 0)$ is a decreasing function of drive gradient γ for shear-like drive. If one *defines* a

"non-equilibrium surface tension" (keeping in mind the above discussion) from the CWT fit, and further takes the temperature T to be fixed (i.e., the value of the parameter in simulations), the conclusion is then that this tension increases as the system is more strongly driven. This procedure of defining an effective non-equilibrium surface tension via the CWT fit was the approach taken in the analysis of the experiments of Derks *et al.* [13], who also found this tension to be an increasing function of shear rate. The CWT fits of experimental data in Ref. [13] show that an increase in this surface tension is accompanied by an *increase* in correlation length, but our simulations show the opposite relationship – a decreasing correlation length as the effective interfacial tension increases. Our findings seem to be inconsistent with the general CWT result Eqn. (2.28), $\xi_{\|} \propto \sqrt{\sigma}$. However, in our system at equilibrium $\xi_{\|} \propto \sqrt{\sigma}\exp(L_z/(4\xi_b))$ (Eqn. (2.31)), so that the effective increase of the confinement due to driving (reduction of L_z) wins over the effective increase of σ.

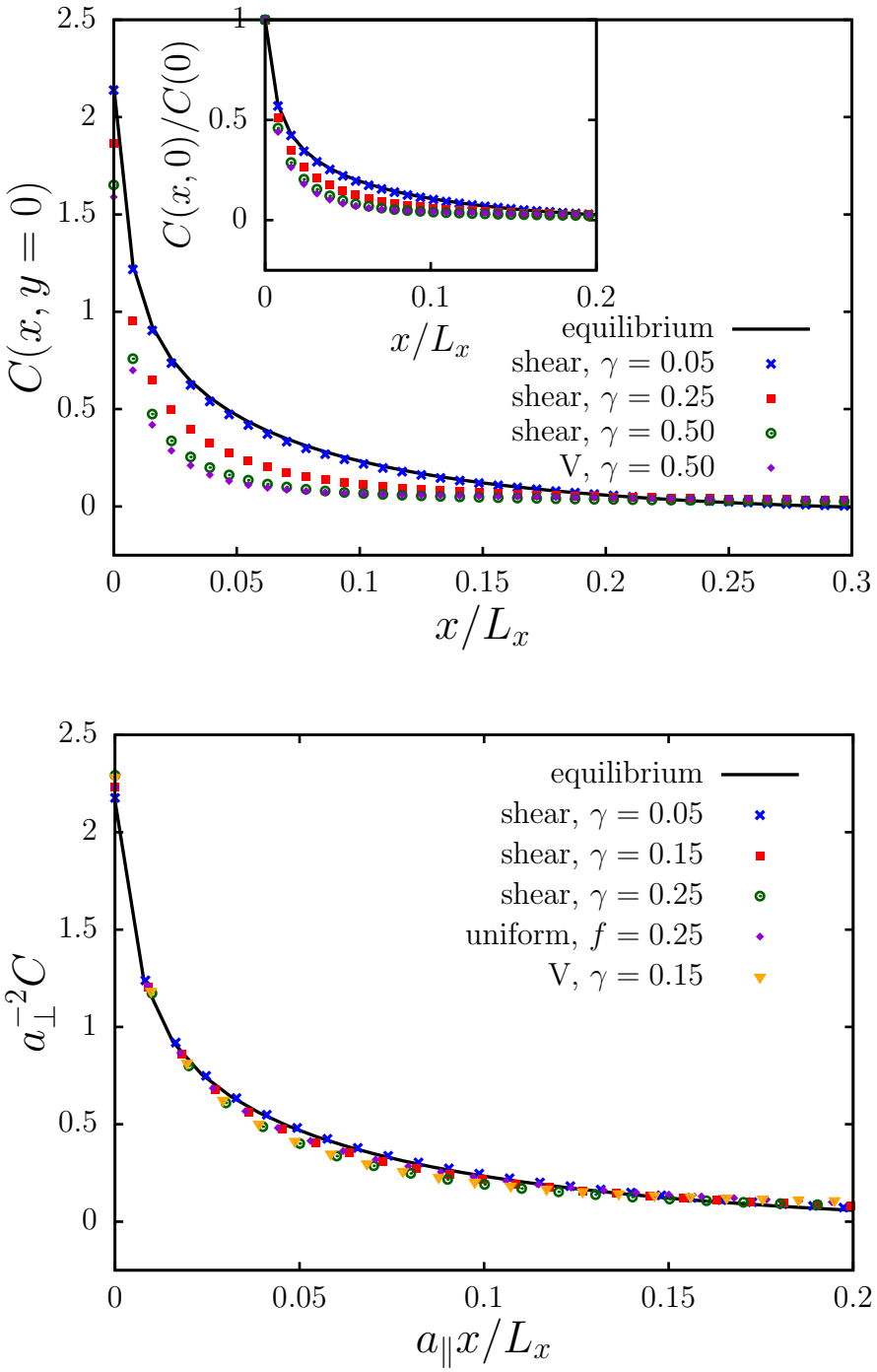

Figure 10.5: (a) Height-height correlation function $C(x, y = 0, t = 0)$ as a function of scaled separation x/L_x, for a $128 \times 128 \times 10$ system at $T/T_c = 0.75$. In the inset, the data are re-plotted, scaled by the respective zero-separation values $C(0, 0, 0)$, showing the increased decay rate under drive. (b) Data for non-zero drive are rescaled to the equilibrium result via the relation $a_\perp^{-2} C(a_\parallel^x x) \approx C_{\rm eq}(x)$ given in the text, where the values of $a_\perp$ and $a_\parallel^x$ are obtained from the rescaling of the magnetisation profile and spin-spin correlation functions, respectively.

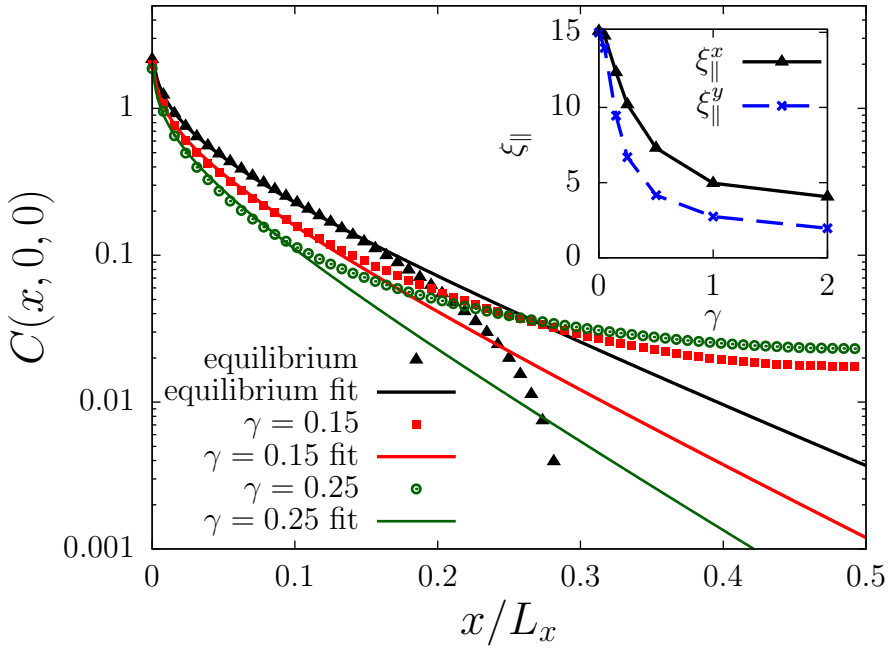

Figure 10.6: Fits (log-lin scale) of the equilibrium and non-equilibrium height correlation data for $C(x, y = 0)$ to the asymptotic capillary wave prediction given in the text. The system parameters are the same as in Fig. 10.5. Inset: correlation lengths $\xi_\parallel^x$ and $\xi_\parallel^y$ (the latter via fitting $C(0, y)$ data) obtained from the fits, as a function of shear-like drive gradient γ.

10.1.5 Structure factor

To further complicate the situation, our finding of a decrease of correlation length in the vorticity (y) direction is in disagreement with Ref. [122], where an *increase* was found. Intriguingly, Thiébaud and Bickel found the structure factor $S(\mathbf{k}) = S(k_x, k_y)$ to be *unaffected* in the k_y direction by the application of shear [122]. The same was concluded for the uniformly driven system from the analytic approach based on a time-dependent Landau-Ginzburg functional by Leung [105]. The static structure factor in the $3d$ system is accessible via a two-dimensional spatial Fourier transform of the equal-time height correlations, $C(x, y, t = 0)$:

$$S(\mathbf{k}) = \left|\mathcal{F}\left\{C(x, y, t = 0)\right\}\right|^2, \tag{10.6}$$

where $\mathcal{F}\{\}$ denotes a two-dimensional spatial Fourier transform, $\mathbf{k} = (2n_x\pi/L_x, 2n_y\pi/L_y)$, and $n_{x,y} = 0, 1 \ldots ((L_{x,y}/2) - 1)$, so that k_x and k_y lie on the range $0 \ldots (\pi - (2\pi/L_{x,y}))$. In Fig. 10.7 we plot $1/S(\mathbf{k})$ for equilibrium and driven systems, along either the k_x or k_y direction, as a function of $k^2 = |\mathbf{k}|^2$. From Eqn. (2.14), in equilibrium, one expects $1/S(k) \propto (\sigma/k_\mathrm{B}T)\left[k^2 + \xi_{\|}^{-2}\right]$; the equilibrium data are fitted to this form in Fig. 10.7. The data shown are along the direction with $k_y = 0$, although we have checked that the equilibrium structure factor behaves the same along the k_y direction, as expected. For $k_x \lesssim 1$, this behaviour is indeed observable in the simulations, except at very small k_x, which we attribute to finite-size effects. For $k_x \gtrsim 1$, the data diverge from the CWT prediction, when other powers of k_x presumably become important. We note that this crossover makes a comprehensive fitting of the structure factor inherently tricky (especially in the presence of drive), so we have concentrated on a limited regime.

Turning to the non-equilibrium behaviour, we see that for shear-like drive, $S(\mathbf{k})$ is affected (suppressed) in both the drive (x, blue crosses) *and* vorticity (y, red squares) directions, but the effect is smaller in the vorticity direction. These results are in disagreement with the hydrodynamics results [122]; however, since the effect in the drive direction is stronger than in the vorticity direction, the latter effect could possibly be of higher order than was considered in Ref. [122]. The data for shear-like drive along $k_y = 0$ are also fit to the equilibrium CWT form in Fig. 10.7; we see that as for equilibrium, the fit is reasonable for $k_x \lesssim 1$. Additionally, the intercept at $k_x = 0$ is greater, indicating a smaller lateral correlation length, as found in real space above. Indeed, one can compare the parameters resulting from the CWT fits in real and Fourier space. We find that the

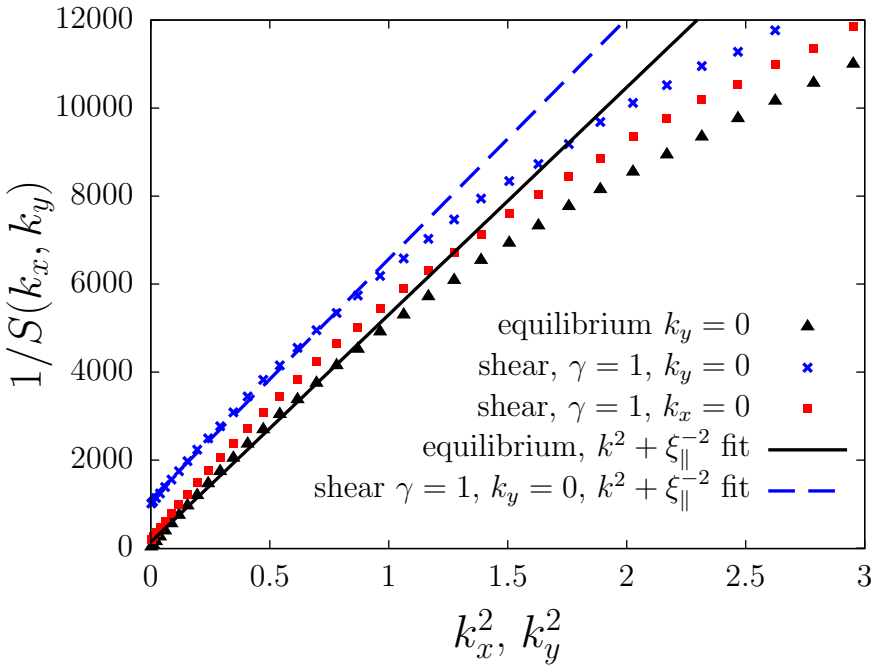

Figure 10.7: Structure factor $S(\mathbf{k})$, as defined in (10.6). Data are shown for $S(k_x, k_y = 0)$ and $S(k_x = 0, k_y)$, as a function of the squared norm of the wave vector, $k^2 = k_x^2$ or k_y^2, respectively. As before, the system dimensions are $128 \times 128 \times 10$, and the temperature is $T/T_c = 0.75$. Equilibrium data are shown, as well as for shear-like drive with $\gamma = 1$, and fits to the CWT form are displayed for equilibrium and for $S(k_x, 0)$ with $\gamma = 1$, up to $k_x^2 = 1$.

qualitative trend for the correlation length is the same, but do not obtain quantitative agreement – the values obtained from the real space fits are consistently larger. These differences are expected – for equilibrium, they can be caused by the finite system size and lattice discretization effects. For non-zero drive, the effect of deviations from CWT can be different in real and Fourier space. Additionally, the fits in Fourier space are for small k (long wavelengths), while the real-space fits are for small separations, so the length scales the fits are applicable to are not necessarily the same. For V-shaped drive, we find that for given drive gradient γ, the results are similar to those for shear-like drive, with slightly greater suppression of the structure factor at small k.

10.2 Capillary wave transport in the driven $3d$ Ising system

We now return to the topic of capillary wave transport in the driven Ising system, and test whether the conjecture made in Sec. 9.5.1 for the occurrence of motion holds in three dimensions. Firstly we investigate the order parameter current profile in the system, since the symmetry of this quantity should determine whether or not we observe transport.

10.2.1 Order parameter current

The order parameter current in the $3d$ system $\mathbf{j}(z)$ is again defined by Eqn. (9.1). In principle, this can now have a y-component $j^y(z)$ in addition to the x-component $j^x(z)$; however to keep the situation relatively simple, we do not consider driving fields with a y component, so $j^y(z)$ measured in the simulations is zero (within fluctuations). As shown in Fig. 10.8, the shear-like drive $F_x(z) = \gamma z$, $F_y(z) = 0$ gives a purely odd order parameter current component $j^x(z)$. For the V-shaped drive, the current is an even function of z, since $F_x(z) = \gamma |z|$; these symmetries are the same as in the $2d$ Ising system, as one would reasonably expect. We should therefore see transport along x for shear-like drive, but none for the V-shaped drive, just as in $2d$. For the same value of γ, the currents for the two drive types almost coincide in the region $z > 0$, where the driving fields are the same in magnitude and direction.

In Figs. 10.8a and 10.8b, $j^x(z)$ is shown for various drive gradients γ, for temperatures above and below the (equilibrium) roughening transition. Looking at the high temperature data in Fig. 10.8a we see that for small γ, $|j^x(z)|$ has maxima at the walls; as γ is increased, plateaus develop with the maximum current shifted slightly from the wall. Eventually for strong drive the maxima become localized near the interface. This reflects the competing effects of local drive strength and current carrier availability ($+-$ pairs): for large γ, the drive strength is essentially saturated at the walls, so the greater carrier density at the interface eventually becomes more important. Below the bulk roughening temperature ($T = 2.4$, Fig. 10.8b), the current $|j^x(z)|$ also has maxima at the walls for small γ, and quickly develops maxima at the middle two layers as γ is increased. These maxima appear for much weaker drive (approximately six times smaller γ) than they do for $T/T_c = 0.75$. They are also localised to the two middle layers either side of the interface, and are much more pronounced than at the higher temperature; this indicates that at low temperatures the interface region is very sharp, reduced to approximately two lattice spacings. For

strong drive, the greater carrier density at the interface again 'wins', and these maxima become global. We also note that $|j^x(z)|$ is roughly five times smaller than that at the higher temperature, since the carrier density is much smaller due to the increased bulk and interfacial order.

Finally, Fig. 10.8a also shows an example of *mixed* symmetry in the current profile. The driving field is of the 'V' type, but with different values of γ in the upper and lower halves of the system: $\gamma_l = 0.25$ in the lower half, $\gamma_u = 0.5$ in the upper. Thus the total driving field can be written in the form $F(z) = \gamma_1 |z| + \gamma_2 z$, with $\gamma_1 = 0.75/2$, $\gamma_2 = 0.25/2$, showing the even and odd components explicitly. The current profile reflects the asymmetry in the drive: in the lower half of the system, the current matches that for a (symmetric) V-shaped drive with $\gamma = 0.25$, while in the upper half, it matches that for either V or shear with $\gamma = 0.5$ (see Fig. 10.8a) – the crossover occurs over a single lattice spacing.

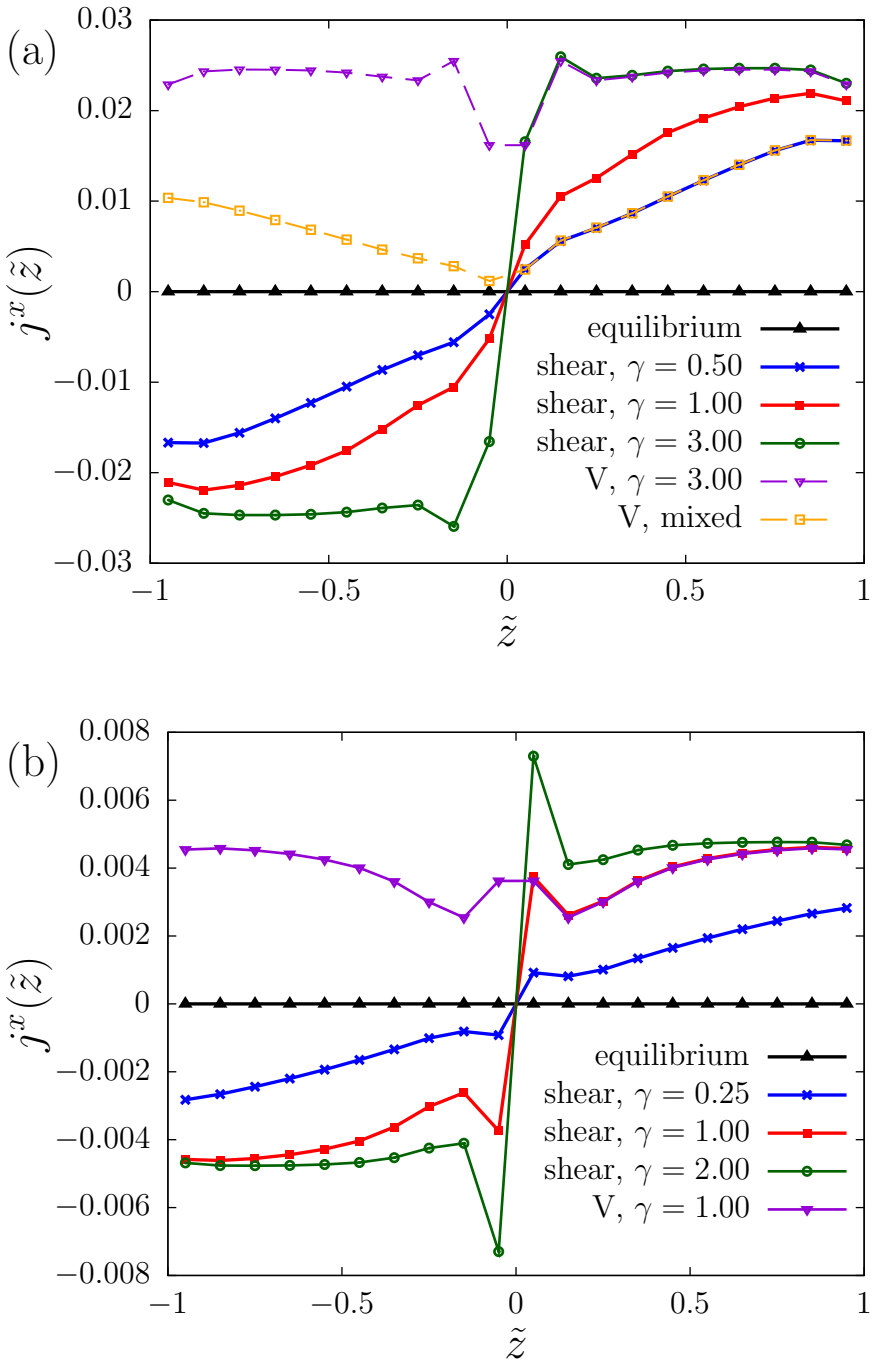

Figure 10.8: Order parameter current profile component $j^x(\tilde{z})$, for the system parameters $L_x = 128$, $L_y = 128$, $L_z = 20$. (a) Temperature $T/T_c = 0.75$. Results are shown for equilibrium (zero current), shear-like and V-shaped drive, and the case of mixed symmetry in the driving field. In the latter case the lower and upper-half γ values are $\gamma_l = 0.25$, $\gamma_u = 0.5$. For $z > 0$, the currents resulting from shear-like and V-shaped drive with $\gamma = 3$ coincide, as do those from mixed symmetry and shear with $\gamma = 0.5$. (b) $T = 2.4$. Results are shown for equilibrium, as well as shear-like and V-shaped drive with various values of γ.

10.2.2 Space-time height correlations

We investigate whether the conjecture for the occurrence of capillary wave motion holds for the $3d$ driven Ising system by measuring $C(x, y = 0, t)$ for different forms of driving field. Fig. 10.9a shows that this is indeed the case – see the main panel for results for $C(x, y = 0, t)$ for shear-like drive, and the inset for V-shaped drive. For time difference $t = 0$, the peak lies symmetrically around $x = 0$ in both cases, due to the translational invariance ensured by the periodic boundaries along x. However, at time differences $t > 0$, the peak moves to negative x values for shear-like drive, indicating that now the greatest correlations are between spatially-displaced points. As in the $2d$ system, we interpret this to mean that wave-like height fluctuations are being coherently transported along the interface by the drive. For the V-shaped drive, the peak remains at $x = 0$ for all t, showing the absence of wave motion. In both cases, correlations decay with increasing time difference, due to thermal noise. We note that the rate of decay of correlations is much faster when drive is applied than it is for equilibrium Kawasaki dynamics (data not shown), as we also found in the $2d$ system.

The results for the uniform ($F_x \equiv f = \text{const}$) and step-like ($F_x(z) = f \cdot \text{sgn}(z)$) driving fields are also consistent with the conjecture: the former produces an even order parameter current profile whereas the latter produces an odd one, and results for $C(x, 0, t)$ (not displayed) show that wave motion does not occur for a uniform drive but does for step-like drive. For the case of the asymmetric V-like drive discussed in the previous section, which has mixed symmetry, we expect to see wave movement, since the current profile is not purely even, but like the driving field itself, can be written as a sum of even and odd components. Indeed we find this is the case, with the peak of $C(x, 0, t)$ moving with time. From these results we conclude that the criteria for capillary wave motion are the same in the $2d$ and $3d$ Ising systems.

Having established the occurrence of wave motion, it is natural to investigate the dependence of the wave velocity on system parameters. We measure the speed of the peak of $C(x, 0, t)$, v_{peak}, and vary the driving strength (γ for shear-like drive, f for step-like drive), temperature and wall separation L_z. As shown in Fig. 10.10, v_{peak} shows linear variation with γ or f for fixed temperature and system size, for $\gamma, f \lesssim 2$. For shear-like drive, the gradient of $v_{\text{peak}}(\gamma)$ is close to 2 in this range. We also see that varying L_z has a rather small effect on the peak velocity – doubling L_z from 10 to 20 reduces the gradient

of $v_{\rm peak}(\gamma)$ by only a few percent. Changing the temperature from $0.75T_c$ to $0.90T_c$ also has small effect, in the other direction – the peak moves faster for the higher temperature at given L_z, γ. For the step drive, $v_{\rm peak}$ also seems to be linear in driving strength f for small f, with a reduced gradient compared to shear-like drive. For both forms of drive, non-linearity appears to set in for $\gamma \gtrsim 2$. For the mixed symmetry case, where the driving field could be written as $F_x(z) = \gamma_1 |z| + \gamma_2 z$, we find that the velocity of motion is smaller than that for a purely odd field with $\gamma = \gamma_2$ – the velocity in the mixed case is linear in γ_2 and approximately 80% that of the pure case for $\gamma, \gamma_2 \lesssim 2$. For lower temperatures near and below the equilibrium roughening temperature, we find that the interfacial motion still occurs, with a much reduced velocity; correlations also decay much more quickly with time, as shown in Fig. 10.9b.

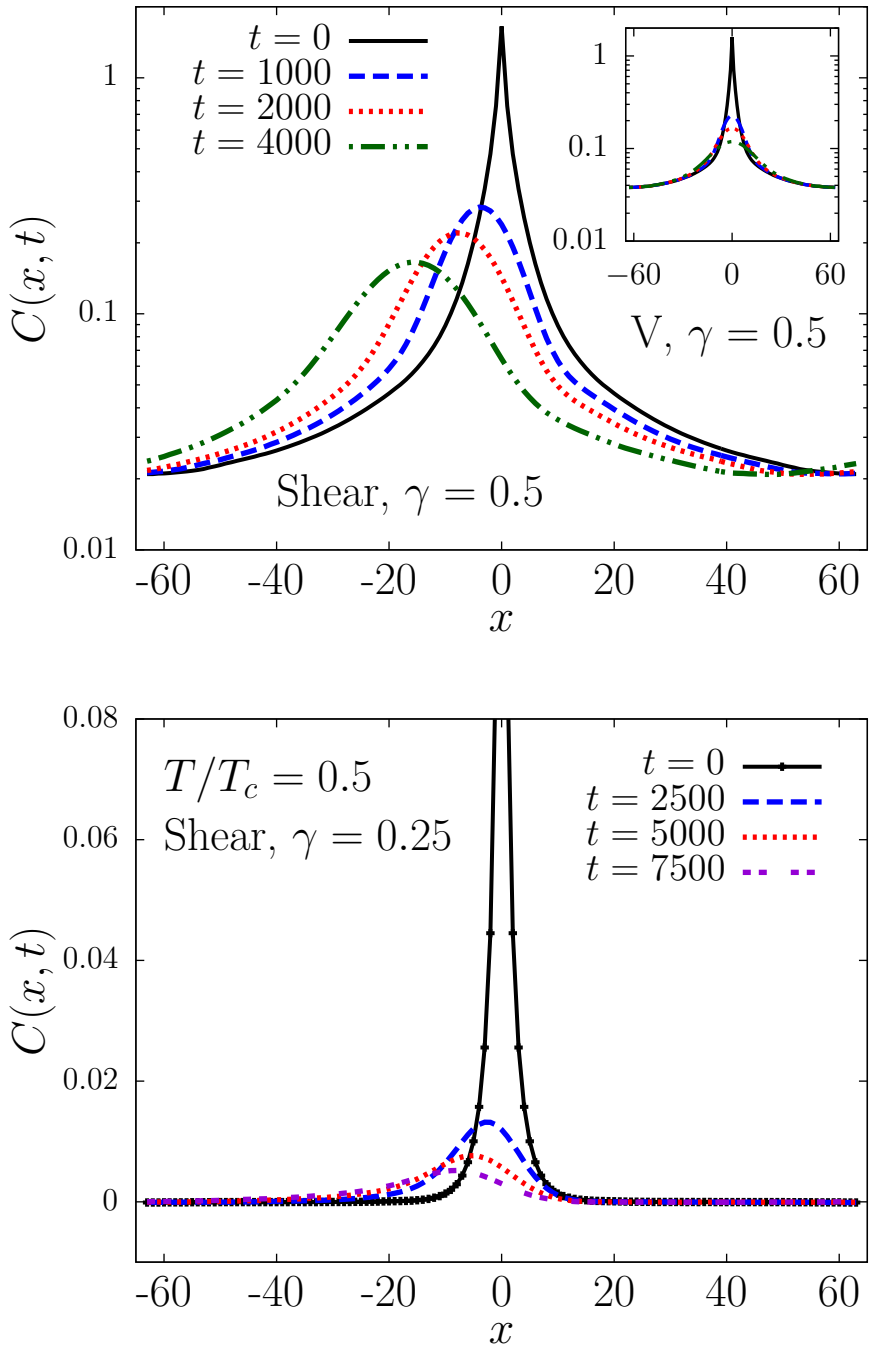

Figure 10.9: Time-displaced height-height correlation function $C(x, y = 0, t)$ for a $128 \times 128 \times 10$ system at temperature $T/T_c = 0.75$ in (a), and $T/T_c = 0.5$ in (b). "Snapshots" are plotted at time displacements t, as indicated. In the main plot of (a), results for shear-like drive with gradient $\gamma = 0.5$ are shown; the peak of the correlation function moves to the left with increasing time difference, indicating capillary wave motion. Inset: results for V-shaped drive with strength $\gamma = 0.5$. Correlations decay without movement of the peak. In (b), we see that the capillary wave motion persists at temperatures below the equilibrium roughening temperature T_R.

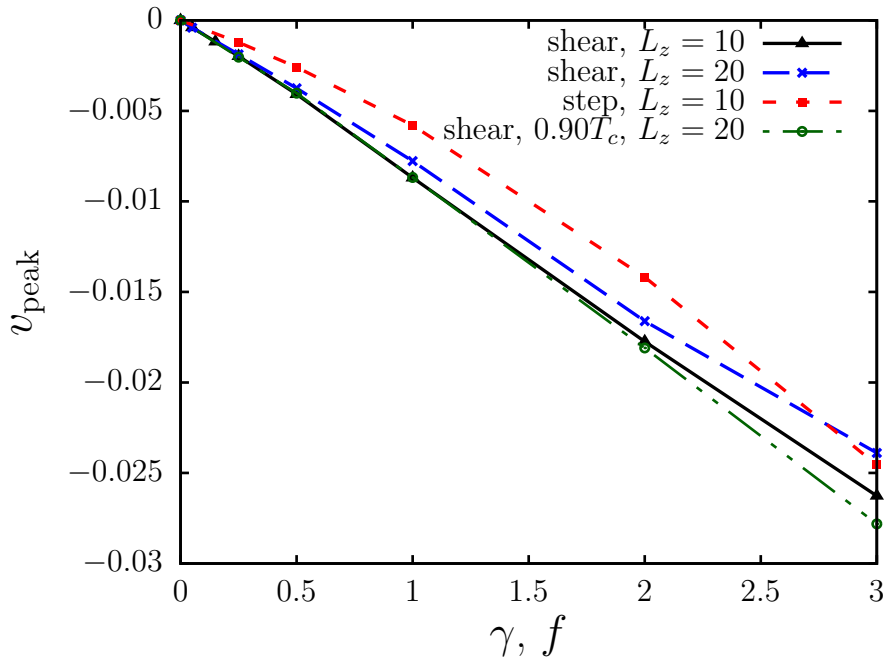

Figure 10.10: Speed of movement of the peak of $C(x, 0, t)$, v_{peak}, as a function of driving strength, γ or f, for shear- and step-like drives, respectively. Shown is the effect of varying L_z for fixed driving strength and temperature, and also the effect of increasing the temperature from $T/T_c = 0.75$ to 0.9.

10.2.3 Dispersion relation

We measure the dispersion relation of the travelling capillary waves in the $3d$ driven Ising model via the same method as in $2d$, see Sec. 9.7, straightforwardly generalised to include the third dimension. The sum over modes, Eqn. (9.13), now becomes double sum over n_x and n_y, with $L_x/2 \times L_y/2$ independent terms. The phase now depends on two wave numbers, $\phi = \phi(k_x, k_y, t)$, and consequently the dispersion relation $\omega = \omega(k_x, k_y)$. In the simulation a two-dimensional Fourier transform of the height variables is now required at each measurement time; we set the measurement interval dt equal to $1/10$ of an MC sweep. This is rather larger than the value used in the $2d$ system – the extra computational cost of the double Fourier transform makes some concession necessary (recall from Sec. 9.7 that a smaller interval is preferable, so that the measurement of the phase difference is reliable). However, this value of dt still proved to be sufficiently small to yield trustworthy data, which was consistent between runs.

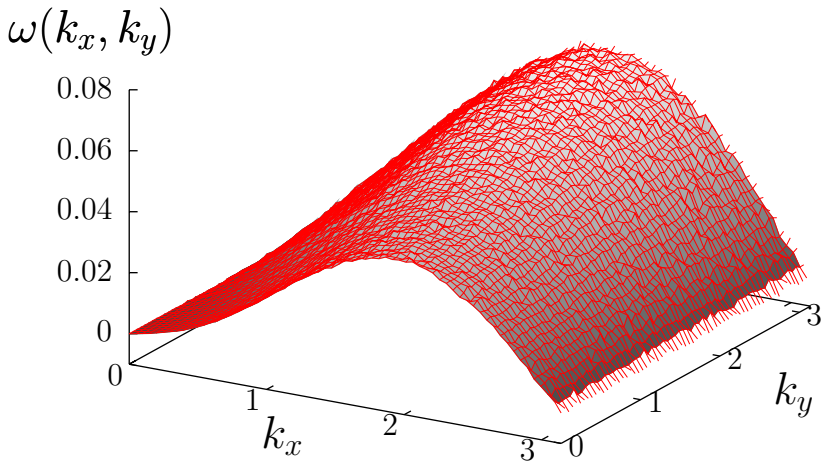

Figure 10.11: Surface plot of the dispersion relation $\omega(k_x, k_y)$ for shear-like drive with $\gamma = 1$ as a function of k_x and k_y. Data are for the system parameters $L_x = 128$, $L_y = 128$, $L_z = 10$ at temperature $T/T_c = 0.75$.

Results for $\omega(\mathbf{k}) = \omega(k_x, k_y)$, where $k_x = 2\pi k_x/L_x$, $k_y = 2\pi k_y/L_y$, are shown in Fig. 10.11, from a $128 \times 128 \times 10$ system subject to shear-like drive with $\gamma = 1$ at temperature $T/T_c = 0.75$, using the simple sum height definition. In Fig. 10.12, cross-sections of $\omega(k_x, k_y)$ are also plotted as a function of k_x for several fixed values of k_y. From Fig. 10.12, we see that the shape of $\omega(k_x, 0)$ is very similar to that obtained in the two-dimensional

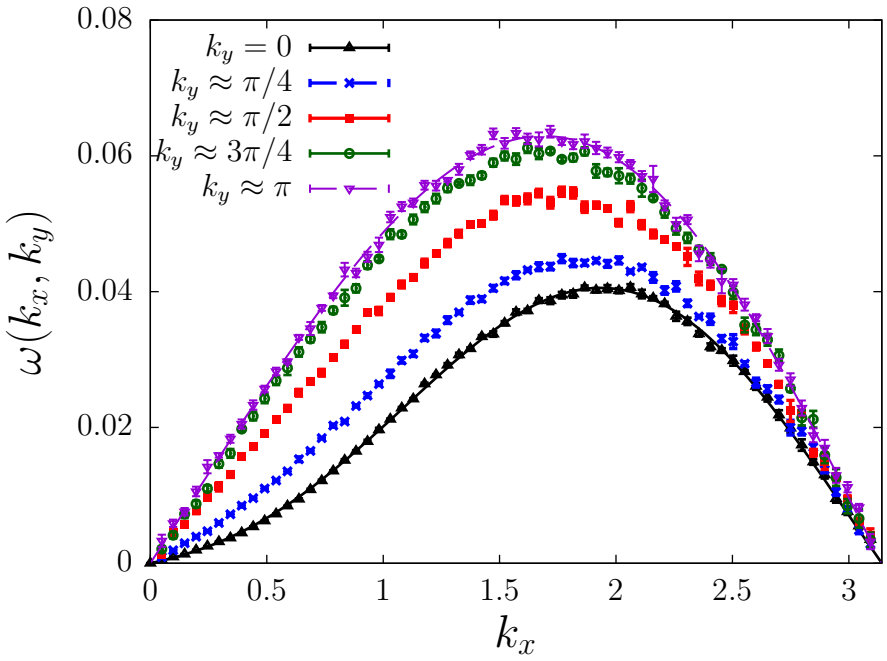

Figure 10.12: Dispersion relation $\omega(k_x, k_y)$ for the same system parameters as Fig. 10.11 as a function of the wave number k_x for several values of k_y. Solid lines are fits to the analytical formula (10.7).

system, cf. Fig. 9.22a, which suggests to use the same analytical formula for describing the dispersion relation:

$$\omega(k_x, k_y = \text{const}) = (v + 2u)\sin(k_x) - u\sin(2k_x) + s\sin^2(k_x). \tag{10.7}$$

Indeed, as can be seen by the solid line in Fig. 10.12, the data for $\omega(k_x, 0)$ fit well with $v = 0.0073(7), u = 0.0104(3), s = 0.0082(8)$. Waves with larger k_y are less dispersive in the sense that the corresponding coefficients u and s are smaller, so that the curves in Fig. 10.12 become more symmetric around $\pi/2$. The fastest mode is the one with $k_y = \pi$, or a wavelength of two lattice spacings; $\omega(k_x, \pi)$ can also be fitted using (10.7) with $v = 0.0525(9), u = 0.0039(2), s = 0.0020(3)$. The variation of ω with k_y for any particular k_x may also be seen in a continuous manner from Fig. 10.11. As discussed in Sec. 9.7, if the dynamics of the height function are modelled by the linear transport operator (9.21), then the Ansatz in the form of a travelling wave $A\exp(i(\omega t + \mathbf{k}\cdot\mathbf{r}))$ yields the first and the second terms in the fit function (10.7), whereas the third term (in s) requires an imaginary contribution to $\hat{L}$.

One may be able to understand the presence of complex coefficients in the transport equation for the height function $h(\mathbf{r}, t)$, by recognising that the plane wave solution above neglects the dependence of the amplitude A on the wave number. In fact the average modulus $|\tilde{h}(\mathbf{k}, t)|$ of each complex Fourier component varies significantly with $k = |\mathbf{k}|$, even in the absence of driving (see the plot for the structure factor Fig. 10.7). Taking this into account, it should be possible to derive an equation for the amplitude as well as the phase – this may aid in understanding the presence of real and imaginary parts in the transport operator. The $t \to \infty$ limit of the solution of the amplitude equation should yield the static structure factor, which may be compared to simulation data. We leave the interesting and difficult problem of deriving the full transport equation from these considerations to future work.

Chapter 11

Conclusions and outlook

In this thesis, we have explored a few of the aspects of the behaviour of interfaces in simple models of non-equilibrium confined fluid systems. Hopefully, we have at least highlighted the richness and variety of phenomena exhibited by these systems driven out of equilibrium. Even in the simple systems studied here, we have seen interesting behaviour, which is in some ways entirely different to equilibrium, but in others shows a definite connection to it.

The first main finding from the laterally driven confined Ising model simulations is that interfacial fluctuations are suppressed by drive, and that the static properties of the system may be well-described by an *equilibrium* system with a smaller effective wall separation. In this way, the non-equilibrium system may be viewed as an equilibrium system subject to a greater degree of confinement. Evidence for this conclusion is based on both one- and two-body observables: the magnetisation (density in fluid language) profile (also the energy bond profiles [68]), the interface width, and both microscopic and coarse-grained interface correlation functions. For the magnetisation profile between the walls, $m(z)$, the driven data were rescaled to equilibrium using the known equilibrium finite-size scaling form, implying that the same scaling function is applicable out of equilibrium. This procedure yielded the rescaling parameter $a_\perp = L_z^*/L_z < 1$, where L_z^* is the reduced effective wall separation, and L_z is the actual separation. For the two-body microscopic spin-spin correlation function $G(x)$ ($G(x, y = 0)$ in $3d$) for lateral separations x along the interface, the rescaling was based on a modified lateral correlation length $\xi_\parallel^x$, and gave the rescaling parameter $a_\parallel^x = \xi_\parallel^x/\xi_\parallel^{\rm eq} < 1$, implying a reduction of the correlation length. For $3d$ systems, this could also be applied to $G(x = 0, y)$ in the y (vorticity)

direction, with, surprisingly, a slightly greater effect due to drive. We also found that the coarse-grained height correlation function $C(x, t = 0)$ ($C(x, y = 0, t = 0)$ in $3d$) could be rescaled to equilibrium, using the already-fixed values of $a_\perp$ and $a_\parallel$. In two dimensions, the rescaling form was inspired by the equilibrium Weeks scaling form; in three dimensions, the connection to equilibrium is not so clear. The successful rescaling of the height correlations solidifies the effective-confinement idea, by providing quite a strong test of self-consistency, without free parameters. This picture is not special to a particular form of driving field, but works for all the forms of drive tested – both spatially uniform, and linearly varying with z, and with both even and odd symmetries around the mid-point between the walls, $z = 0$. The one-body rescaling seems to apply for arbitrarily strong driving fields, but on the two-body level, it only works for weak-to-intermediate drive. The range of validity of the rescaling is much greater in $3d$ than in $2d$, since for given field strength, the drive has a smaller effect on the system's structure.

Thus, overall, we can conclude that the effect of lateral drive upon on the structure of the phase-separated, conserved order parameter Ising system may be viewed as an increase in the degree of confinement of the corresponding equilibrium system. This holds as long as the drive is not too strong – beyond a certain point, the driven system is too far from equilibrium for this picture to apply. This separation into a close-to-equilibrium regime, and another, strongly driven regime, is quite common in work on non-equilibrium systems, so the breakdown of rescaling does not come as a great surprise. It would be interesting to try to define the separation more systematically – this would presumably be based on a theoretical approach, with some suitably-defined parameter measuring the "distance from equilibrium". In the $3d$ case, we also looked at the behaviour of the driven system nearer (and also below) the bulk equilibrium roughening temperature. The effect of the drive upon the structure is reduced for these low temperatures, since there are no large fluctuations to "smoothen out"; the effective-confinement picture no longer seems to apply here. A proper study of the interplay between drive and the roughening transition would be valuable, in view of possible practical applications.

The scaling behaviour of the interface width does not directly fall into the increased-confinement idea, but it seems likely that a connection does exist – the physical interpretation of the scaling variable $\theta = L_z\gamma^s$ is not yet clear. Exploring this avenue could be interesting, particularly because the exponent s has the same value in $2d$ and $3d$ – a common scaling form across dimensions is quite unusual. The fitting of the height cor-

relation function in three dimensions to the capillary wave theory (Bessel function) form also clearly shows a connection between driven and equilibrium systems, and the trend of decreased lateral correlation length under drive agrees with that from the rescaling procedure. The Fourier-space description provided by the structure factor complements the real-space CWT fits. As before, these inherently *equilibrium* descriptions break down for strong driving fields. Some of the difficulty in applying both rescaling and CWT fitting to the simulation data arises from finite-size effects, which are rather strong in the $2d$ equilibrium and weakly-driven systems, and weaker, but still non-negligible, in the $3d$ equilibrium case. These effects may be reduced by simulating systems with larger aspect ratios $L_x, L_y/L_z$, such that a better approximation to an infinite strip (in $2d$; infinite "slab" in $3d$) is obtained. Qualitatively, however, the conclusions seem to be unchanged; there is certainly scope for a more systematic finite-size scaling study.

In the case of shear-like drive, our findings for the decay of the height-height correlation functions and for the structure factor are in partial agreement with recent results from fluctuating hydrodynamics [122]. In both cases, a decrease of the lateral correlation $\xi_{\parallel}$ in the flow direction is seen. The discrepancy concerns the behaviour in the vorticity direction. We have found a decrease of the correlation length in this direction whereas hydrodynamic calculations predict an increase. Also, our data show that the structure factor is suppressed in both the drive and the vorticity directions. In Ref. [122] it is concluded that $S(q_x, q_y)$ is unaffected in the vorticity direction. Moreover, our results for the interfacial width are in agreement with the experiment of Ref. [13], but the results for the lateral correlation length in the flow direction are not: in the experiment, $\xi_{\parallel}$ increased upon the application of shear to the system. For spatially uniform drive, the trends in our system agree with those found by Leung *et al.* in their KLS simulations, but we have supplied a new interpretation in terms of increased confinement. This partial agreement between theory, simulation and experiment (albeit for different systems!) is intriguing, and it would certainly be desirable to carry out more studies, experimental, theoretical and simulation-based, to clarify these discrepancies. It may be the case that the systems are simply too different to expect the responses to drive to be similar; indeed, the lattice model studied here has no hydrodynamics and a simple Ising nearest-neighbour Hamiltonian. From this viewpoint, it is perhaps surprising that there is any similarity at all in the results! To sum up, an overarching question is which features of the structure of driven interfaces are universal, and which are peculiar to a particular model. Hopefully,

the murky waters will be illuminated by further investigations.

The second main result is dynamical in nature: for certain forms of driving field, we have observed lateral transport of capillary-wave (CW) fluctuations along the interface. Specifically, motion occurs for cases where the order parameter current profile $j^x(z)$ has a component which is an odd function of distance z from the mid-line between the walls. We have shown evidence for this phenomenon in the space-time height correlation function $C(x,t)$, whose peak moves from $x = 0$ as a function of increasing time difference t, for both $2d$ and $3d$ driven Ising systems. When transport does not occur (i.e., for equilibrium systems, or where the order parameter current is even), $C(x,t)$ remains symmetric around $x = 0$, and simply decays with time. In order to test whether the CW motion is special to the Ising lattice gas, we simulated a driven discrete Gaussian (DG) effective-interface model, and a driven Blume-Capel (BC) model. In both cases, transport was observed, with the same criterion for motion as in the Ising model. The DG and BC models provide complementary testing grounds – the former "boils down" the system to a purely interfacial description, devoid of bulk contributions, while the latter allows for new ways of driving, by virtue of the third spin species (vacancies in a binary mixture description). This last point is important, because we were able to confirm that it is the symmetry of the order parameter current, rather than the driving field, that determines whether CW motion occurs. Based on these results, it seems likely that this phenomenon should occur in other driven lattice models. Whether any similar result holds for continuum systems is an open question. We were also able to measure the dispersion relation $\omega(\mathbf{q})$ of the moving waves in the simulations. For the DG model, the observed form of $\omega(q_x)$ may be produced by a simple linear transport operator $\partial_t - v\partial_x$, which we were able to motivate by an approximate microscopic argument. The behaviour for the Ising model is more complex, and the requirement of imaginary contributions to the transport operator is not fully understood. Investigating the dynamics of the capillary waves further in order to ultimately try and derive the transport operator for the driven Ising model, and so understand the various terms better physically, would definitely be worthwhile. Such a treatment should in principle include non-linear effects, and include the time and wave-vector dependence of the Fourier amplitude. Further insight, especially into the effect of coupling between bulk and interfacial degrees of freedom, could be gained by considering theoretical models based on the order parameter [155, 156].

Finally, the previously-claimed richness of behaviour in non-equilibrium statistical-

mechanical systems is highlighted by our observation of instabilities and strange phenomena in the DG and BC systems. Some qualitative results for the BC instability may be found in Appendix B; we suspect that these represent but the tip of an iceberg of interesting phenomenology, even in this restricted system. To conclude, it is hoped that the investigations presented here will contribute positively to the understanding of non-equilibrium interfaces, by making a connection to equilibrium systems, by exploring the common elements of different driven lattice systems, and suggesting further avenues of research.

Appendix A

Full expressions for the multispin exchange probabilities

A.1 Full expression for against-drive S_1 moves in $d = 3$

This expression extends Eqn. (8.5), and takes the form

$$\begin{aligned} p_a = p_{\rm eq} \wedge \big\{ &\big[\overline{Q_1} \wedge V_0\big] \\ &\vee \big[Q_1 \wedge \overline{Q_2} \wedge ((P_5 \wedge V_1) \vee (\overline{P_5} \wedge V_0))\big] \\ &\vee \big[Q_2 \wedge \overline{Q_3} \wedge ((P_5 \wedge V_2) \vee (\overline{P_5} \wedge P_4 \wedge V_1) \vee (\overline{P_4} \wedge V_0))\big] \\ &\vee \big[Q_3 \wedge \overline{Q_4} \wedge ((P_5 \wedge V_3) \vee (\overline{P_5} \wedge P_4 \wedge V_2) \vee (\overline{P_4} \wedge P_3 \wedge V_1) \vee (\overline{P_3} \wedge V_0))\big] \\ &\vee \big[Q_4 \wedge \overline{Q_5} \wedge ((P_5 \wedge V_4) \vee (\overline{P_5} \wedge P_4 \wedge V_3) \vee (\overline{P_4} \wedge P_3 \wedge V_2) \vee (\overline{P_3} \wedge P_2 \wedge V_1) \vee (\overline{P_2} \wedge V_0))\big] \\ &\vee \big[Q_5 \wedge ((P_5 \wedge V_5) \vee (\overline{P_5} \wedge P_4 \wedge V_4) \vee (\overline{P_4} \wedge P_3 \wedge V_3) \vee (\overline{P_3} \wedge P_2 \wedge V_2) \vee (\overline{P_2} \wedge P_1 \wedge V_1) \vee (\overline{P_1} \wedge V_0))\big]\big\}, \end{aligned} \tag{A.1}$$

where V_0 and V_1 were already defined in Sec. 8.3.1, and the other V_i continue this series logically. Explicitly, each bit in V_i is on with probability

$$p(V_i) = \min[1, \exp(-\beta(-4i + \Delta W))]. \tag{A.2}$$

A.2 Full expression for with-drive S_1 moves in $d = 3$

This expression extends Eqn. (8.7):

$$\begin{aligned} p_w = (S_1 \oplus S_2) \wedge \\ \{ \left[\overline{Q_1} \wedge ((P_5) \vee (\overline{P_5} \wedge P_4 \wedge U_1) \vee (\overline{P_4} \wedge P_3 \wedge U_2) \vee (\overline{P_3} \wedge P_2 \wedge U_3) \vee (\overline{P_2} \wedge P_1 \wedge U_4) \vee (\overline{P_1} \wedge U_5)) \right] \\ \vee \left[\overline{Q_2} \wedge Q_1 \wedge ((P_4) \vee (\overline{P_4} \wedge P_3 \wedge U_1) \vee (\overline{P_3} \wedge P_2 \wedge U_2) \vee (\overline{P_2} \wedge P_1 \wedge U_3) \vee (\overline{P_1} \wedge U_4)) \right] \\ \vee \left[\overline{Q_3} \wedge Q_2 \wedge ((P_3) \vee (\overline{P_3} \wedge P_2 \wedge U_1) \vee (\overline{P_2} \wedge P_1 \wedge U_2) \vee (\overline{P_1} \wedge U_3)) \right] \\ \vee \left[\overline{Q_4} \wedge Q_3 \wedge ((P_2) \vee (\overline{P_2} \wedge P_1 \wedge U_1) \vee (\overline{P_1} \wedge U_2)) \right] \\ \vee \left[\overline{Q_5} \wedge Q_4 \wedge ((P_1) \vee (\overline{P_1} \wedge U_1)) \right] \\ \vee [Q_5] \} \, . \end{aligned} \tag{A.3}$$

The general expression for the U_i was already given after Eqn. (8.6). Although both these expressions are rather long and require many operations, these bitwise operations are computationally cheap, so the total cost is reasonable.

Appendix B

Instability in the driven Blume-Capel models

In Sec. 9.8, we saw that for the counter-driven (i.e., such that the ± 1 species are driven in opposite directions) Blume-Capel model, the system can become unstable. In the example given earlier, the density profiles of both the ± 1 and the vacancies became almost flat, with the vacancies forming a "block" spanning the two walls. Here we investigate this phenomenon further, in particular the dependence on vacancy density and driving strength. In Fig. B.1, snapshots are shown for three different unstable BC systems under uniform counter-drive. In all cases, $k_BT/J = 0.75$, well below the equilibrium bulk BC critical temperature, and the system dimensions are $L_x = 128$, $L_z = 16$. The simulation systems were quenched from an initial $T = \infty$ state. In (a), the drive strength is $f = 0.1$, while the vacancy fraction is $\rho_v = 0.02$ – this is much smaller than the case shown in Fig. 9.23b. Despite this, the general features of the system are the same: regions of '+' and '−' spins span the system from wall to wall (this is surprising, given the energetic cost of the "wrong" phase contacting a wall), and the vacancies tend to form a buffer at the vertical interface between the '−' on the *left* and '+' on the *right* (as opposed to at the other interface). For the same ρ_v and stronger drive $f = 1.0$ in (b), the overall structure is again the same, but the $+-$ spin interfaces tend to be microscopically flat. This is a general trend – as drive strength increases, the sharper the vertical domain boundaries become. Finally in (c) we see that for $\rho_v = 0.005$ and $f = 0.075$, the instability persists to extremely small vacancy concentrations, and quite weak drive. In this case, there is not a sufficiency of vacancies to span the walls at the $+-$ interface; nevertheless this is still the

same interface as in the other cases.

This preference of the vacancies to sit here is due to both the drive and energetic considerations: firstly, as we have discussed before, the vacancies provide screening between the energetically unfavourable $+-$ spin interactions, causing them to be found at $+-$ interfaces. The reason for the particular choice of interface here is due to the drive – if we placed the vacancies at the other vertical interface, then exchanges with '+' spins would tend to drive them in the negative x direction, while exchanges with '$-$' would drive them the other way. In both cases, these directions are away from the interface, so the vacancies are effectively *repelled* from it. By contrast, there is an effective attraction to the interface where they are found to sit.

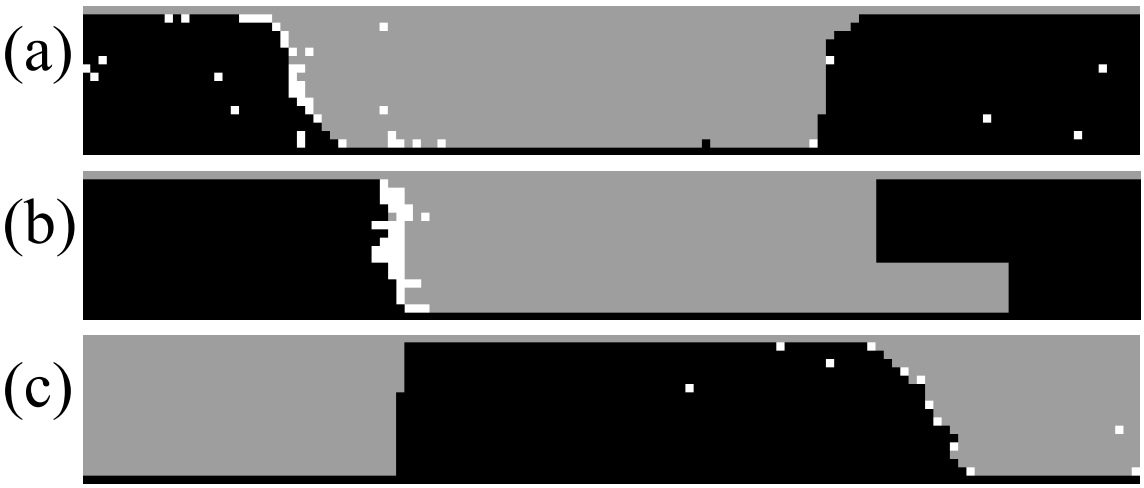

Figure B.1: Simulation snapshots of the driven Blume-Capel model with conservative dynamics, under uniform counter-drive. The system dimensions are $L_x = 128$, $L_z = 16$ and the temperature $k_BT/J = 0.75$ in all three systems. The '+' spins are shown in grey, the '$-$' in black, and the vacancies are white. (a) Vacancy concentration $\rho_v = 0.02$ and drive strength $f = 0.1$. (b) Vacancy concentration $\rho_v = 0.02$ and drive strength $f = 1.0$. (c) Vacancy concentration $\rho_v = 0.005$ and drive strength $f = 0.075$.

Once the system has reached this kind of block-like state, which it does by $\mathrm{O}(10^7)$ MCS for the temperature and system size above, it does not appear to return to the "normal" state, at least on simulation timescales $\mathrm{O}(10^8)$ MCS – if the states are in fact metastable, their lifetime is rather long. The behaviour within the block-like state appears to be cyclic: the system will resemble the snapshots in Fig. B.1 for a reasonably long period, of order 10^7 MCS, but then develop a "finger" of '+' spins which grows from the $+-$ vertical

interface where the vacancies do not sit – indeed the initial stages of the finger formation may be seen on the right hand side of Fig. B.1b. This structure grows laterally, and then vertically, to occupy the full extent of the system between the walls – the connection with the main '+' region becomes thinner. At some point the new structure finally breaks off, but then rather quickly re-coalesces with the the main phase, by being transported through the vacancy buffer – the system is then back to its initial state. This whole process takes approximately 5×10^6 MCS for the system in Fig. B.1b, with the timescale increasing for weaker driving fields.

The system's behaviour in the block-like state is certainly interesting, but the central question is *how* the system evolves into this state, rather than the normal phase-separated state we would expect. Inspection of simulation snapshots in the first few million MCS reveals that for weak drive, the system actually does initially phase separate in the normal way, but then destabilises. The time-series of snapshots in Fig. B.2, for a system driven with $f = 0.075$ and with just two vacancies, shows how this occurs on the large scale. To set off the process, a large interfacial fluctuation is required – a "hump" of '$-$' phase in the '+' (accompanied by a neighbouring '+' trough, due to the conservative dynamics). The interface to the left of this feature then becomes increasingly inclined, as '+' spins are transported towards the feature. On the right-hand side of the feature, the $+-$ boundary becomes also becomes increasingly inclined, eventually becoming vertical. The '+' region then continues to shrink in lateral extent, reducing the interface area, until we obtain the block-like structures already seen.

At first sight, it appears extremely strange that such extremely small vacancy concentrations can have such a profound effect on the system's structure. However, recall that the system temperature we have used is rather low, $k_B T/J = 0.75$, less than half the bulk BC critical temperature, and even further below the Ising critical point. The lack of intruders into the bulk phases, as evident in the snapshots, is a sign of the relative weakness of thermal fluctuations in the system: creating intruders means performing an exchange across the interface (detaching spins from their phases), which costs energy $\Delta H = 12J$ for a locally flat interface. At low temperatures, due to the $\exp(-\beta\Delta H)$ factor in the Metropolis acceptance rates, these exchanges thus occur very rarely for the Ising case ($\rho_v = 0$). Therefore, the action of the drive, and the role of the vacancies in enhancing probabilities for otherwise heavily suppressed moves, become more important at low T. In particular, a vacancy in contact with the inclined $+-$ interface in the second snapshot

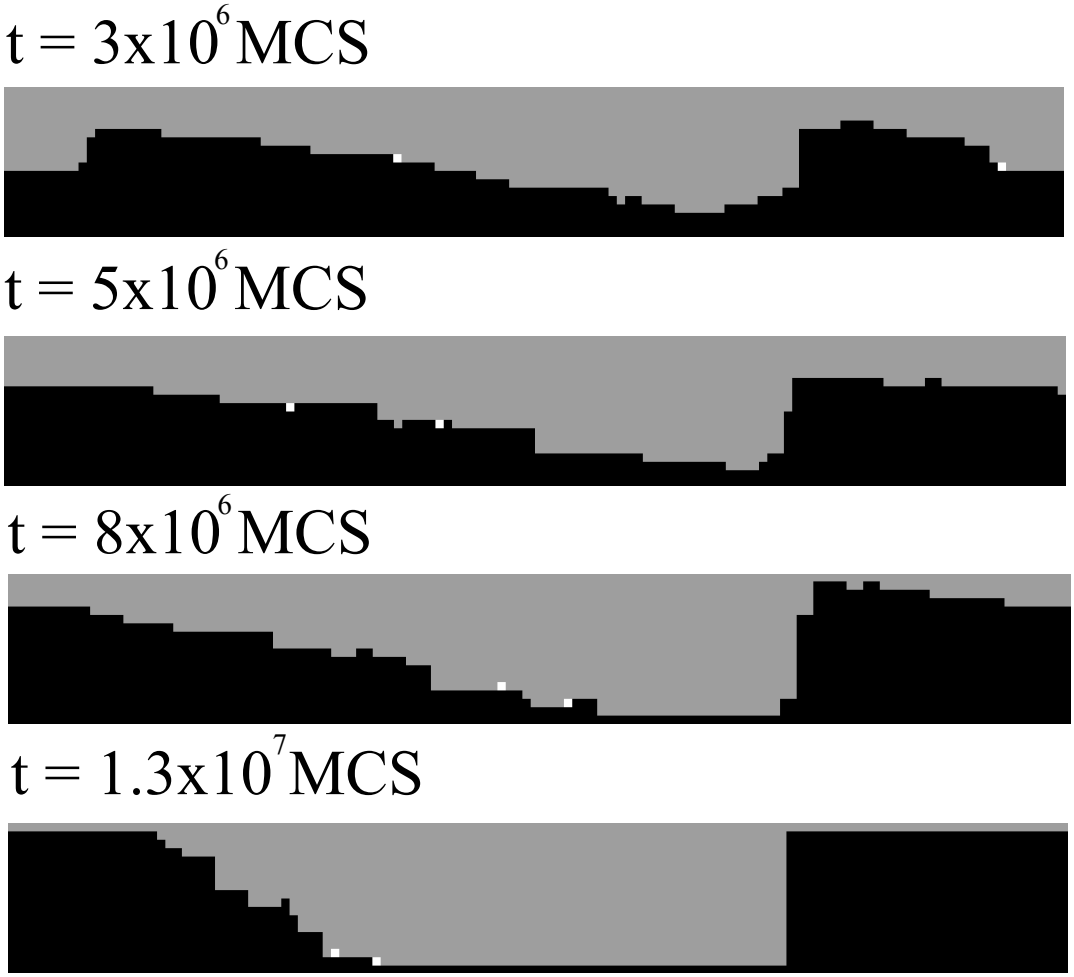

Figure B.2: Evolution of the uniformly counter-driven Blume-Capel model towards the block-like state. As before, the system is 128×16, at temperature $k_BT/J = 0.75$. The drive strength is $f = 0.075$, and there are just two vacancies in the system.

of Fig. B.2 greatly enhances the probability of detaching a '+' spin from its phase (compared to performing a $+-$ exchange, up to three fewer bonds are broken), to allow it to be transported along the interface. Via this transport mode, '+' spins may be deposited at the fluctuation, thereby growing it downwards. The $+-$ interface on the right hand side is stable, since performing exchanges across it typically costs $12J$, and so these are heavily suppressed, and as discussed above, the vacancies are *repelled* from this region, so are not available to enhance the probabilities. It seems plausible that the evolution shown in Fig. B.2 could occur by this process; with a larger ρ_v, the approach to the block-like state happens more quickly. Importantly, when $\rho_v = 0$ (Ising), the symmetry between the

left and right $+-$ interfaces is restored, and so the above process does not apply. This would explain why we have never observed these block-like structures in the driven Ising model. Furthermore, for higher temperatures, we observe the BC system to become more stable, since thermal fluctuations become stronger, and the effect of the vacancies is less important – indeed, for the system of Fig. B.2 but at $k_BT/J = 1.6$, normal phase separation is regained. Finally, the above findings have been checked to hold for larger systems $L_x = 256$, $L_z = 32$, although the timescales are longer in this case.

From the above discussion, it should be clear that the driven conservative Blume-Capel model can exhibit rich phenomenology, due to the interplay of the vacancies, drive, and thermal fluctuations of the interface and bulk. In Sec. 9.8, we concentrated on the case of co-driving the ± 1 species, where the system is "well behaved", and observed capillary wave motion as in the driven Ising model. Here we have explored some of the strange phenomena that can occur when the system is subjected to counter-drive – as always in non-equilibrium statistical physics, much remains to be investigated and understood.

Bibliography

[1] J. Atencia and D. Beebe, Nature **437**, 648 (2005).

[2] P. Kenis, R. Ismagilov, and G. Whitesides, Science **285**, 83 (1999).

[3] W. Jeong, J. Kim, S. Kim, S. Lee, G. Mensing, and D. Beebe, Lab on a Chip **4**, 576 (2004).

[4] Barabási, A.L. and Stanley, H.E., *Fractal Concepts in Surface Growth* (Cambridge Univ. Press, 1995).

[5] S. Dietrich, in *Phase Transitions and Critical Phenomena*, edited by C. Domb and J. L. Lebowitz (Academic Press, 1988), vol. 12.

[6] K. Binder, R. Evans, D. Landau, and A. Ferrenberg, Phys. Rev. E **53**, 5023 (1996).

[7] A. De Virgiliis, E. V. Albano, M. Müller, and K. Binder, Physica A **352**, 477 (2005).

[8] E. Chacón and P. Tarazona, Phys. Rev. Lett. **91**, 166103 (2003).

[9] J. D. Weeks, J. Chem. Phys. **67**, 3106 (1977).

[10] P. Hurtado, J. Marro, P. Garrido, and E. Albano, Phys. Rev. B **67**, 14206 (2003).

[11] F. Gallet, S. Balibar, and E. Rolley, J. de Phys. **48**, 369 (1987).

[12] D. Aarts, M. Schmidt, and H. Lekkerkerker, Science **304**, 847 (2004).

[13] D. Derks, D. G. A. L. Aarts, D. Bonn, H. N. W. Lekkerkerker, and A. Imhof, Phys. Rev. Lett. **97**, 038301 (2006).

[14] M. E. Fisher, in *Statistical Mechanics of Membranes and Surfaces*, edited by D. Nelson, T. Piran, and S. Weinberg (World Scientific, 1989).

[15] J. Hansen and I. McDonald, *Theory of Simple Liquids* (Academic Press, 2006).

[16] R. M. L. Evans, R. A. Simha, A. Baule, and P. D. Olmsted, Phys. Rev. E **81**, 051109 (2010).

[17] M. Plischke and B. Bergersen, *Equilibrium Statistical Physics* (World Scientific, 2006), 3rd ed.

[18] J. Percus and G. Williams, in *Fluid Interfacial Phenomena*, edited by C. A. Croxton (Wiley, 1986).

[19] E. Chacón, E. Fernández, D. Duque, R. Delgado-Buscalioni, and P. Tarazona, Phys. Rev. B **80**, 195403 (2009).

[20] J. D. Van der Waals, Z. Phys. Chem. **13**, 657 (1894).

[21] J. Rowlinson and B. Widom, *Molecular Theory of Capillarity* (Dover, 2002).

[22] R. Evans, Adv. Phys. **28**, 143 (1979).

[23] M. V. v. Smoluchowski, Ann. Phys. **33**, 205 (1908).

[24] L. Mandelstam, Ann. Phys. **41** (1913).

[25] F. P. Buff, R. A. Lovett, and F. H. Stillinger, Phys. Rev. Lett. **15**, 621 (1965).

[26] D. Aarts, M. Schmidt, H. Lekkerkerker, and K. Mecke, Adv. in Solid State Physics **45**, 15 (2005).

[27] D. Bedeaux and J. D. Weeks, J. Chem. Phys. **82**, 972 (1985).

[28] A. Vrij, Adv. Colloid Interface Sci. **2**, 39 (1968).

[29] M. Boas, *Mathematical Methods in the Physical Sciences* (Wiley, 1983), p. 229, 2nd ed.

[30] K. Mecke and S. Dietrich, Phys. Rev. E **59**, 6766 (1999).

[31] N. Goldenfeld, *Lectures on Phase Transitions and the Renormalization Group* (Addison-Wesley, 1992).

[32] M. Abramowitz and I. Stegun, *Handbook of Mathematical Functions with Formulas, Graphs, and Mathematical Tables* (Dover, 1964).

[33] J. Stecki, J. Chem. Phys. **108**, 3788 (1998).

[34] R. Lipowsky, Phys. Rev. B **32**, 1731 (1985).

[35] T. Smith, O. Vasilyev, A. Maciolek, and M. Schmidt, Phys. Rev. E **82**, 021126 (2010).

[36] T. Kerle, J. Klein, and K. Binder, Eur. Phys. J. B **7**, 401 (1999).

[37] K. Binder, M. Müller, F. Schmid, and A. Werner, Adv. Colloid Interface Sci. **94**, 237 (2001).

[38] A. Parry and R. Evans, Physica A **181**, 250 (1992).

[39] M. Schmidt, A. Fortini, and M. Dijkstra, J. Phys. Condens. Matter **15**, S3411 (2003).

[40] R. Vink, K. Binder, and J. Horbach, Phys. Rev. E **73**, 56118 (2006).

[41] R. Evans, J. Phys. Condens. Matter **2**, 8989 (1990).

[42] R. Vink, A. De Virgiliis, J. Horbach, and K. Binder, Phys. Rev. E **74**, 31601 (2006).

[43] A. Fortini, M. Schmidt, and M. Dijkstra, Phys. Rev. E **73**, 51502 (2006).

[44] D. Landau, A. Ferrenberg, and K. Binder, Braz. J. Phys. **30**, 748 (2000).

[45] E. Albano and K. Binder, J. Stat. Phys. **135**, 991 (2009).

[46] A. De Virgiliis, R. Vink, J. Horbach, and K. Binder, Europhys. Lett. **77**, 60002 (2007).

[47] K. Binder, J. Horbach, R. Vink, and A. De Virgiliis, Soft Matter **4**, 1555 (2008).

[48] K. Binder, D. Landau, and M. Müller, J. Stat. Phys. **110**, 1411 (2003).

[49] M. Niss, Arch. Hist. Exact Sci. **59**, 267 (2005).

[50] M. Niss, Arch. Hist. Exact Sci. **63**, 243 (2009).

[51] L. Onsager, Phys. Rev. **65**, 117 (1944).

[52] D. Chandler, *Introduction to Modern Statistical Mechanics* (Oxford Univ. Press, 1987).

[53] P. Chaikin and T. Lubensky, *Principles of Condensed Matter Physics* (Cambridge Univ. Press, 2000).

[54] D. Landau and K. Binder, *A Guide to Monte Carlo Simulations in Statistical Physics* (Cambridge Univ. Press, 2005), 2nd ed.

[55] M. E. J. Newman and G. T. Barkema, *Monte Carlo Methods in Statistical Physics* (Oxford Univ. Press, 1999).

[56] M. Allen and D. Tildesley, *Computer Simulation of Liquids* (Clarendon Press, 1989).

[57] A. Talapov and H. Blöte, J. Phys. A: Math. Gen. **29**, 5727 (1996).

[58] J. Cardy, *Scaling and Renormalization in Statistical Physics* (Cambridge Univ. Press, 1996).

[59] L. P. Kadanoff, Physics **2**, 263 (1966).

[60] K. Wilson, Phys. Rev. B **4**, 3174 (1971).

[61] G. Baker Jr, B. Nickel, M. Green, and D. Meiron, Phys. Rev. Lett. **36**, 1351 (1976).

[62] M. Fisher, Rep. Prog. Phys. **30**, 615 (1967).

[63] M. Kastner, J. Stat. Phys. **109**, 133 (2002).

[64] D. Fraiman, P. Balenzuela, J. Foss, and D. Chialvo, Phys. Rev. E **79**, 61922 (2009).

[65] S. Katz, J. Lebowitz, and H. Spohn, Phys. Rev. B **28**, 1655 (1983).

[66] C. Nonaka and M. Asakawa, Physical Review C **71**, 44904 (2005).

[67] M. Sahimi and D. Stauffer, Phys. Rev. Lett. **71**, 4271 (1993).

[68] T. H. R. Smith, O. Vasilyev, D. B. Abraham, A. Maciołek, and M. Schmidt, J. Phys. Condens. Matter **20**, 494237 (2008).

[69] R. Swendsen, Phys. Rev. B **15**, 689 (1977).

[70] R. Swendsen, Phys. Rev. B **15**, 5421 (1977).

[71] S. Chui and J. Weeks, Phys. Rev. B **14**, 4978 (1976).

[72] T. Schultz, D. Mattis, and E. Lieb, Rev. Mod. Phys. **36**, 856 (1964).

[73] D. Abraham and A. Martin-Löf, Comm. Math. Phys. **32**, 245 (1973).

[74] J. Stecki, Phys. Rev. B **47**, 7519 (1993).

[75] J. Stecki, A. Maciołek, and K. Olaussen, Phys. Rev. B **49**, 1092 (1994).

[76] A. Maciołek, J. Phys. A: Math. Gen. **29**, 3837 (1996).

[77] A. Maciołek and J. Stecki, Phys. Rev. B **54**, 1128 (1996).

[78] M. Fisher and P. De Gennes, Sci., Paris, Ser. B **287**, 207 (1978).

[79] J. Bricmont, A. El Mellouki, and J. Fröhlich, J. Stat. Phys. **42**, 743 (1986).

[80] T. Kerle, J. Klein, and K. Binder, Phys. Rev. Lett. **77**, 1318 (1996).

[81] R. Vink, J. Horbach, and K. Binder, J. Chem. Phys. **122**, 134905 (2005).

[82] W. Burton and N. Cabrera, Discuss. Faraday Soc. **5**, 33 (1949).

[83] W. Burton, N. Cabrera, and F. Frank, Phil. Trans **243**, 299 (1951).

[84] J. Kosterlitz and D. Thouless, J. Phys. C: Solid State Phys. **6**, 1181 (1973).

[85] R. Savit, Rev. Mod. Phys. **52**, 453 (1980).

[86] J. Weeks, G. Gilmer, and H. Leamy, Phys. Rev. Lett. **31**, 549 (1973).

[87] S. T. Chui and J. D. Weeks, Phys. Rev. Lett. **40**, 733 (1978).

[88] J. José, L. Kadanoff, S. Kirkpatrick, and D. Nelson, Phys. Rev. B **16**, 1217 (1977).

[89] M. Hasenbusch, S. Meyer, and M. Pütz, J. Stat. Phys. **85**, 383 (1996).

[90] M. Hasenbusch and K. Pinn, J. Phys. A: Math. Gen. **30**, 63 (1997).

[91] P. Nozières, in *Solids Far From Equilibrium*, edited by C. Godrèche (Cambridge Univ. Press, 1991).

[92] S. Katz, J. Lebowitz, and H. Spohn, J. Stat. Phys. **34**, 497 (1984).

[93] M. Salamon and H. Beyeler, *Physics of Superionic Conductors* (Springer, 1979).

[94] B. Schmittmann and R. K. P. Zia (Academic Press, 1995), vol. 17 of *Phase Transitions and Critical Phenomena*.

[95] K. Kawasaki, Phys. Rev. **145**, 224 (1966).

[96] N. Metropolis, A. Rosenbluth, M. Rosenbluth, A. Teller, E. Teller, et al., J. Chem. Phys. **21**, 1087 (1953).

[97] M. Kardar, *Statistical Physics of Fields* (Cambridge Univ. Press, 2007).

[98] R. Dickman, Phys. Rev. A **38**, 2588 (1988).

[99] N. C. Pesheva, Y. Shnidman, and R. K. P. Zia, J. Stat. Phys. **70**, 737 (1993).

[100] J. Marro, J. Lebowitz, H. Spohn, and M. Kalos, J. Stat. Phys. **38**, 725 (1985).

[101] K. Leung and J. Cardy, J. Stat. Phys. **44**, 567 (1986).

[102] K. t. Leung, K. K. Mon, J. L. Vallés, and R. K. P. Zia, Phys. Rev. Lett. **61**, 1744 (1988).

[103] K.-t. Leung, K. K. Mon, J. L. Vallés, and R. K. P. Zia, Phys. Rev. B **39**, 9312 (1989).

[104] K. t. Leung and R. K. P. Zia, J. Phys. A: Math. Gen. **26**, L737 (1993).

[105] K. Leung, J. Stat. Phys. **50**, 405 (1988).

[106] R. K. P. Zia and K. t. Leung, J. Phys. A: Math. Gen. **24**, L1399 (1991).

[107] C. Yeung, J. Mozos, A. Hernánez-Machado, and D. Jasnow, J. Stat. Phys. **70**, 1149 (1993).

[108] R. K. P. Zia, K. Hwang, B. Schmittmann, and K. t. Leung, Physica A **194**, 183 (1993).

[109] D. H. Boal, B. Schmittmann, and R. K. P. Zia, Phys. Rev. A **43**, 5214 (1991).

[110] G. Saracco and E. Albano, Phys. Rev. E **78**, 31132 (2008).

[111] R. K. P. Zia, J. Stat. Phys. **138**, 20 (2010).

[112] C. K. Chan and L. Lin, Europhys. Lett. **11**, 13 (1990).

[113] E. Cirillo, G. Gonnella, and G. Saracco, Phys. Rev. E **72**, 26139 (2005).

[114] D. Langevin, ed., *Light Scattering by Liquid Surfaces and Complementary Techniques* (Marcel Dekker, New York, 1992).

[115] J. Penfold, Rep. Prog. Phys. **64**, 777 (2001).

[116] T. Seydel, A. Madsen, M. Tolan, G. Grübel, and W. Press, Phys. Rev. B **63**, 73409 (2001).

[117] D. Aarts and H. Lekkerkerker, J. Fluid Mech. **606**, 275 (2008), ISSN 0022-1120.

[118] D. Derks, Ph.D. thesis, Utrecht Univ. (2006).

[119] S. Asakura and F. Oosawa, J. Polym. Sci. **33**, 183 (1958).

[120] A. Vrij, Physica A **235**, 120 (1997).

[121] V. Villeneuve, J. Leeuwen, J. Folter, D. Aarts, W. Saarloos, and H. Lekkerkerker, Europhys. Lett. **81**, 60004 (2008).

[122] M. Thiébaud and T. Bickel, Phys. Rev. E **81**, 31602 (2010).

[123] T. H. R. Smith, O. Vasilyev, D. B. Abraham, A. Maciołek, and M. Schmidt, Phys. Rev. Lett. **101**, 067203 (2008).

[124] U. Jeng, L. Esibov, L. Crow, and A. Steyerl, J. Phys. Condens. Matter **10**, 4955 (1998).

[125] D. McLeish, *Monte Carlo Simulation and Finance* (Wiley, 2005).

[126] S. van Gemmert, G. T. Barkema, and S. Puri, Phys. Rev. E **72**, 046131 (2005).

[127] P. Rikvold and M. Kolesik, J. Phys. A: Math. Gen. **35**, L117 (2002).

[128] P. Rikvold and M. Kolesik, Phys. Rev. E **66**, 66116 (2002).

[129] P. Rikvold and M. Kolesik, Phys. Rev. E **67**, 66113 (2003).

[130] K. Park, P. Rikvold, G. Buendia, and M. Novotny, Phys. Rev. Lett. **92**, 15701 (2004).

[131] T. H. R. Smith, O. Vasilyev, A. Maciołek, and M. Schmidt, Europhys. Lett. **89**, 10006 (2010), 0904.3668.

[132] R. Glauber, J. Math. Phys. **4**, 294 (1963).

[133] C. Shida and V. Henriques, arXiv:cond-mat/9703198v28 (1997).

[134] M. Blume, Phys. Rev. **141**, 517 (1966).

[135] H. Capel, Physica **32**, 966 (1966).

[136] H. Capel, Physica **33**, 295 (1967).

[137] W. Selke and J. Yeomans, J. Phys. A: Math. Gen. **16**, 2789 (1983).

[138] P. Fox and A. Guttmann, J. Phys. C: Solid State Phys. **6**, 913 (1973).

[139] P. Beale, Phys. Rev. B **33**, 1717 (1986).

[140] *RandomLib*, http://randomlib.sourceforge.net/html/.

[141] M. Matsumoto and T. Nishimura, ACM Transactions on Modeling and Computer Simulation (TOMACS) **8**, 3 (1998).

[142] W. Press, W. Vetterling, S. Teukolsky, and B. Flannery, *Numerical recipes in C: The Art of Scientific Computing* (Cambridge Univ. Press, 1992), 2nd ed.

[143] D. Butenhof, *Programming with POSIX Threads* (Addison-Wesley, 1997).

[144] *Blitz++: Object-Oriented Scientific Computing*, http://www.oonumerics.org/blitz/.

[145] *Boost*, http://www.boost.org/.

[146] *FFTW: "Fastest Fourier Transform in the West"*, http://www.fftw.org/.

[147] *RapidXML*, http://rapidxml.sourceforge.net/.

[148] *CImg Library: C++ Template Image Processing Toolkit*, http://cimg.sourceforge.net/.

[149] B. Efron and G. Gong, Amer. Statistician **37**, 36 (1983).

[150] H. Flyvbjerg and H. Petersen, J. Chem. Phys. **91**, 461 (1989).

[151] P. Broersen, IEEE Trans. Instrum. Meas. **47**, 1085 (1998).

[152] W. Selke, D. Huse, and D. Kroll, J. Phys. A: Math. Gen. **17**, 3019 (1984).

[153] M. N. Barber, in *Phase Transitions and Critical Phenomena*, edited by C. Domb and J. L. Lebowitz (Academic Press, 1983), vol. 8.

[154] J. Kosterlitz, J. Phys. C: Solid State Phys. **7**, 1046 (1974).

[155] A. Bray, A. Cavagna, and R. Travasso, Phys. Rev. E **64**, 12102 (2001).

[156] A. Bray, A. Cavagna, and R. Travasso, Phys. Rev. E **65**, 16104 (2001).